Section 4:
Session 4: Crack Growth Rate Studies for the Disposition of Flaws

US REGULATORY EXPERIENCE AND PROGNOSIS WITH RPV HEAD DEGRADATION AND VHP NOZZLE CRACKING

Allen L. Hiser, Jr.

Assistant Branch Chief
Materials Engineering Branch
Office of Nuclear Regulatory Research
U.S. Nuclear Regulatory Commission

Cracking in Alloy 600 penetration nozzles in the reactor pressure vessel upper heads of pressurized water reactors (PWRs) has been an issue in the U.S. nuclear industry for more than 10 years. Since the first identification of leaking vessel head penetration (VHP) nozzles in US pressurized water reactors (PWR) in 2000, the US Nuclear Regulatory Commission (NRC) has used several generic communications to elicit those inspections necessary to provide a reasonable assurance of adequate protection of the public health and safety. This approach was modified recently with the issuance of orders to all PWR plants to require the implementation of visual and non-visual examinations. This paper reviews the recent regulatory history, describes the examination methods and frequency of examinations mandated by the recently-issued orders, and provides a prognosis for future inspection requirements.

Introduction

Alloy 600 is used to fabricate various parts in nuclear power plants, including reactor vessel top head penetrations for control rod drive mechanism (CRDMs), control element drive mechanisms (CEDMs), in-core instruments (ICIs) and thermocouples, reactor vessel bottom head bottom mounted instruments (BMIs), pressurizer heater sleeves, and various other instrumentation ports. Related weld materials Alloy 82 and Alloy 182 are used to join these Alloy 600 parts to the ferritic steel components and also as a bi-metallic weld joining ferritic base materials to austenitic stainless steel base materials. Alloy 600 and its associated weld filler metals were originally used because of expectations of resistance to service-induced cracking. However, parts fabricated from these materials have demonstrated a susceptibility to primary water stress corrosion cracking (PWSCC), also referred to as low potential stress corrosion cracking (LPSCC). This paper focuses on the recent experience in the U.S. with PWSCC of upper head penetrations, with descriptions of other findings (excluding steam generator applications) to provide context.

A schematic cross-section of an upper head is provided in Fig. 1. This schematic is for a head fabricated by Babcock and Wilcox. A schematic cross-section of a CRDM nozzle is provided in Fig. 2., illustrating the J groove weld, the counterbored region just above the J-groove weld (and the annulus between the RPV head and the CRDM nozzle), and the shrink fit region of the head and the CRDM nozzle.

Formerly, Senior Materials Engineer, Materials and Chemical Engineering Branch, Office of Nuclear Reactor Regulation.

Early Findings of PWSCC in Alloy 600

In the United States, PWSCC of Alloy 600 became an issue following a leakage event of a pressurizer heater sleeve nozzle at Calvert Cliffs Unit 2 in 1989. Other instances of leakage in pressurizer instrument nozzles were identified in both domestic and foreign PWRs, as described in Information Notice 90-10 (Ref. 1). As described in this Information Notice:

> PWSCC of Inconel 600 is not a new phenomenon. However, very little special attention has been given to the inspection for PWSCC in Inconel 600 applications other than that associated with the steam generator tubing. As a result of the recently reported instances of PWSCC in the pressurizer heater thermal sleeves and instrument nozzles in several domestic and foreign PWRs, it may be prudent for licensees of all PWRs to review their Inconel 600 applications in the primary coolant pressure boundary, and when necessary, to implement an augmented inspection program.

As described in Reference 2, the first indication of cracking in upper head Alloy 600 penetrations was identified in France at Bugey Unit 3 in 1991 during the ten-year primary system hydrostatic test. The leak rate was low, < 1 liter/hr (0.004 gpm), for the through-wall crack identified in an outer row CRDM nozzle. Further examinations indicated that the leakage was from an axial flaw that had initiated on the nozzle inside surface near the elevation of the J-groove weld. This flaw was also found to have a small extension in the nozzle base material that was inclined ~ 30° from the nozzle axis, and a small extension into the J-groove weld. In addition, several other partial depth axial cracks were identified at a similar elevation in this nozzle. Failure analysis confirmed that the cracking was due to PWSCC, and identified the following contributing factors:

- Stress concentration at a counterbore on the nozzle inside surface at the J-groove weld elevation.
- High hardness of the cold-worked machined surface.
- High residual stresses in the nozzle resulting from the welding.

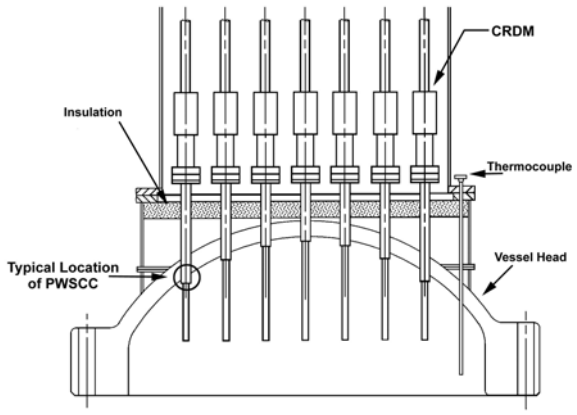

Figure 1 Schematic cross-section of an upper RPV head for a B&W plant.

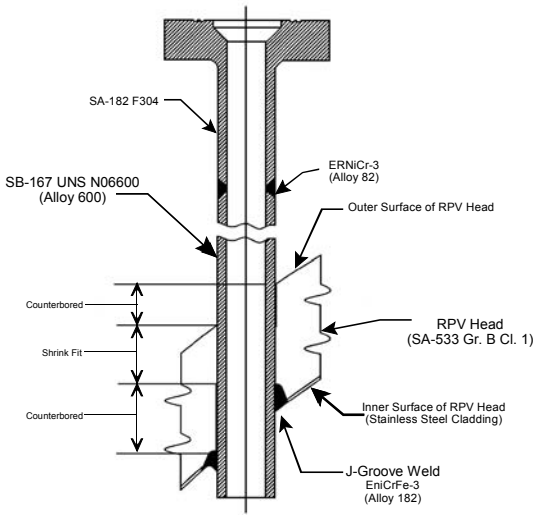

Figure 2 Schematic cross-section of a CRDM nozzle in an upper RPV head.

The first U.S. inspection of vessel head penetration (VHP) nozzles took place in the spring of 1994 at the Point Beach Nuclear Generating Station, and no indications were detected in any of its 49 CRDM penetrations (Ref. 3). The eddy current inspection at the Oconee Nuclear Station (ONS) in the fall of 1994 revealed 20 indications in one penetration. Ultrasonic testing (UT) did not reveal the depth of these indications because they were shallow. UT cannot accurately size defects that are less than one mil deep (0.03 mm). These indications may be associated with the original fabrication. A limited examination of eight in-core instrumentation penetrations conducted at the Palisades plant found no cracking. An examination of the CRDM penetrations at the D. C. Cook plant in the fall of 1994 revealed three clustered indications in one penetration. The indications were 46 mm (1.81 in.), 16 mm (0.63 in.), and 6 to 8 mm (0.24 to 0.31 in.) in length, and the deepest flaw was 6.8 mm (0.27 in.) deep. The tip of the 46-mm (1.81 in.) flaw was just below the J-groove weld. Virginia Electric and Power Company inspected North Anna Unit 1 during its spring 1996 refueling outage. Some high-stress areas (e.g., upper and lower hillsides) were examined on each outer ring CRDM penetrations and no indications were observed using eddy current testing.

Generic Letter 97-01

On April 1, 1997, the NRC issued Generic Letter 97-01 (Ref. 3) to request PWR licensees submit descriptions of their programs for inspecting CRDM and other VHP nozzle penetrations. As described in a generic response to NRC requests for additional information (Ref. 4), the industry used a histogram grouping of plants, in combination with completed inspections and planned inspections as its approach for managing this issue. The plant grouping used probabilistic crack initiation and growth models to estimate the amount of time remaining (in effective full power years, EFPYs) until the plant reached a limiting condition for a reference plant. This limiting condition was the time for the plant to reach the same probability of having a crack 75% through-wall as D.C. Cook Unit 2 had at the time a 6.5 mm deep crack was identified in 1994. These models included differences in operating time and temperature, water chemistry environment, surface stress, component geometry, material yield strength and microstructure, and fabrication practices (amount of cold work during machining) between the subject plant and the reference plant in determining a plant's susceptibility. The industry cited inspection results from six plants (D.C. Cook Unit 2, North Anna Unit 1, ONS-2, Millstone Unit 2, Point Beach Unit 1, and Palisades) and inspection plans at five plants (Farley Unit 2, Crystal River Unit 3, Diablo Canyon Unit 2, Ginna, and San Onofre Unit 3) as key information that would inform the need for any additional actions to manage the issue.

These inspections continued into the fall of 2000, with no significantly adverse results. As described in Reference 2, the most significant crack identified in these inspections was a 6.8 mm (0.27 in.) deep crack found at D.C. Cook Unit 2. This flaw was repaired by a process that involved partial removal (by grinding) and and overlay weld to isolate the remnant of the original flaw from the environment. Three of the plants identified shallow "craze cracks," generally found as cluster of shallow, less than 0.2 mm deep (0.008 in.) and axially oriented. At Millstone Unit 2, one nozzle with seven such indications in a single nozzle were removed by flapper wheel grinding to a depth of 0.8 mm (0.032 in.).

Worldwide, inspection activities were finding PWSCC in VHP nozzles, and in some cases RPV heads were being replaced. Common characteristics of these findings were the flaws originating in the nozzle base material and located on the inside surface of the nozzles.

In the fall of 2000, the inspection findings in the U. S. became more significant. At Oconee Unit 1 that fall, boron deposits were identified on the RPV head at one CRDM nozzle and at five (of the eight) thermocouple nozzles (one of only two plants with small diameter thermocouple nozzles). Contrary to expectations, the boron deposits were very small (less than 1 $in.^3$ total volume), as illustrated in Fig. 3. Analysis of the CRDM nozzle identified an axial-radial PWSCC crack that initiated in the J-groove weld and propagated part way into the outer diameter surface of the nozzle. The crack in the J-groove weld was arrested when it encountered the RPV head base material, consistent with expectations.

In February 2001, Oconee Unit 3 identified nine nozzles with leaks (again small boron deposits). Additional inspections, including ultrasonic, eddy current and liquid penetrant examinations, identified numerous part- and through-wall axial cracks, generally initiated on the outer diameter surface of the nozzles below the J-groove weld. During the repair of these nozzles, two of the nozzles were found to have single through-wall circumferential cracks extending 165° around the nozzle, although the cracks were not through-wall for their entire circumferential extent. These cracks were identified as having initiated on the nozzle outer diameter surface. The findings at Oconee Unit 3 were the subject of NRC Information Notice 2001-05, issued on April 30, 2001 (Ref. 5).

In March 2001, Arkansas Nuclear One Unit 1 (ANO-1) identified boron deposits on a single CRDM nozzle. Examination of this nozzle identified an axial part-through wall crack that initiated on the nozzle outer diameter surface below the J-groove weld and propagated to a distance 33 mm (1.3 in.) above the J-groove weld.

In April 2001, Oconee Unit 2 identified boron deposits on four CRDM nozzles. Eddy current examinations of these nozzles identified clusters of shallow axial indications on the nozzle inside surfaces, ranging in depth from 0.35 to 0.8 mm (0.014 to 0.032 in.) and in length from 23 to 79 mm (0.9 to 3.1 in.). Ultrasonic examination of these nozzles identified numerous axial flaws on the nozzle outer diameter surfaces, including one circumferential crack above the J-groove weld. The latter was reported as 32 mm (1.25 in.) long and 1.8 mm (0.07 in.) deep. Leakage from these nozzles was identified as originating from cracks on the outer diameter surface of the nozzle that propagated along the weld to nozzle interface from below the J-groove weld to above the weld.

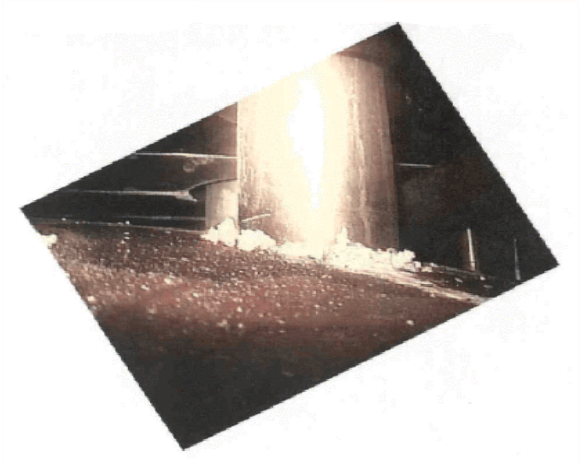

Figure 3 Leakage at Oconee Unit 1 identified fall 2000.

Bulletin 2001-01

With these findings, the NRC took action by issuing Bulletin 2001-01 in August 2001 (Ref. 6). The focus of this Bulletin was the safety issue of circumferential cracking in VHP nozzles, with a goal of providing assurance that no such cracking existed in plants. Because of the time frame involved in the development of a circumferential crack that could be subject to nozzle ejection, visual inspections of the RPV head outer surface, where the nozzle intersected the RPV head, was considered at that point to be an adequate inspection. As described in this Bulletin,

> Cracking due to PWSCC in PWR CRDM nozzles and other VHP nozzles fabricated from Alloy 600 is not a new issue; axial cracking in the CRDM nozzles has been identified since the late 1980s. In addition, numerous small-bore Alloy 600 nozzles and pressurizer heater sleeves have experienced leaks attributable to PWSCC. Generally, these components are exposed to high temperatures (greater than 550°F) and a primary water environment. However, circumferential cracking from the nozzle OD to the ID, above the weld, and cracking of the J-groove weld have not been previously identified in PWRs.

As described in Bulletin 2001-01, the generic responses of licensees to Generic Letter 97-01 were predicated on the development of susceptibility ranking models to relate the operating conditions (in particular the operating temperature and time) for each plant to the plant's relative susceptibility to PWSCC. The generic responses committed to surface examinations of the VHP nozzles at the plants identified as having the highest relative susceptibility ranking. Consistent with the expectations expressed by the NRC staff in Generic Letter 97-01, the surface examinations conducted prior to November 2000 identified only limited axial cracking, and circumferential cracking below the weld in the base metal of CRDM nozzles, but no circumferential cracking above the nozzle welds and no cracking in the Alloy 182 welds.

However, as described in Bulletin 2001-01, the identified CRDM nozzle degradation phenomena from the spring 2001 outage season raised several issues regarding the resolution approach taken in Generic Letter 97-01:

(1) Cracking of Alloy 182 weld metal has been identified in CRDM nozzle J-groove welds for the first time. This finding raises an issue regarding the adequacy of cracking susceptibility models based only on the base metal conditions.

(2) The identification of cracking at ANO-1 raises an issue regarding the adequacy of the industry's Generic Letter 97-01 susceptibility model. ANO-1 cracking was predicted to be more than 15 effective full power years (EFPY) beyond January 1, 1997, from reaching the same conditions as the limiting plant, based on the susceptibility models used by the industry to address base metal cracking in response to Generic Letter 97-01.

(3) Circumferential cracking of CRDM nozzles, located outside of any structural retaining welds, has been identified for the first time. This finding raises concerns about the potential for rapidly propagating failure of CRDM nozzles and control rod ejection, causing a loss of coolant accident (LOCA).

(4) Circumferential cracking from the CRDM nozzle outer diameter to the inner diameter has been identified for the first time. This finding raises concerns about increased consequences of secondary effects of leakage from relatively benign axial cracks.

(5) Circumferential cracking of CRDM nozzles was identified by the presence of relatively small amounts of boric acid deposits. This finding increases the need for more effective inspection methods to detect the presence of degradation in CRDM nozzles before the nozzle integrity is compromised.

This Bulletin was an information request for licensees to identify their VHP nozzle inspection plans. Based on industry input (Ref. 2), the Bulletin grouped the plants based upon a time-at-temperature model that quantified the time for each plant to achieve the same calculated time-at-temperature as ONS-3 when that plant identified circumferential cracks. The Bulletin then described inspections, including inspection method and inspection timing, that would be effective in identifying nozzle cracking in plants in each grouping, based upon the level of expectation for cracking in the group. This Bulletin introduced two new terms to describe visual examinations, a "qualified visual examination" (for plants with a high susceptibility to PWSCC) and an "effective visual examination" (for plants with a moderate susceptibility to PWSCC). The effective visual examination was described in Reference 6 as an examination

> of 100% of the VHP nozzles that is capable of detecting and discriminating small amounts of boric acid deposits from VHP nozzle leaks, such as were identified at ONS-2 and ONS-3, may be sufficient to provide reasonable confidence that PWSCC degradation would be identified prior to posing an undue risk. The effective visual examination should not be compromised by the presence of insulation, existing deposits on the RPV head, or other factors that could interfere with the detection of leakage."

The qualified visual examination was described in Reference 6 as an examination that is

> able to reliably detect and accurately characterize leakage from cracking in VHP nozzles considering two characteristics. One characteristic is a plant-specific demonstration that any VHP nozzle exhibiting through-wall cracking will provide sufficient leakage to the RPV head surface (based on the as-built configuration of the VHPs). Secondly, similar to the effective visual examination for moderate susceptibility plants, the effectiveness of the qualified visual examination should not be compromised by the presence of insulation, existing deposits on the RPV head, or other factors that could interfere with the detection of leakage.

One implication from the Bulletin was the identification of a group of thirteen plants that either had experienced VHP nozzle cracking or leakage (at the time this included the three Oconee units, ANO-1, and DC Cook Unit 2), and additional plants that were calculated to be within five years of operating time from the ONS-3 calculated time-at-temperature. For this group of plants, the Bulletin suggested that inspections should be performed by December 31, 2001. These thirteen plants included seven Babcock and Wilcox plants (including the three Oconee units, ANO-1, Crystal River 3, Three Mile Island Unit 1, and Davis-Besse) that tended to operate at higher temperatures than the other PWR plants.

Of the thirteen plants that were of particular interest to the Bulletin, five had received recent inspections that were considered to be consistent with the expectations of the Bulletin. Four of the remaining eight had refueling outages scheduled prior to December 31, 2001. Two of the remaining four were the second unit at dual unit sites where the first unit was scheduled to be inspected, and the licensee in this case decided to perform an inspection at all units consistent with the schedule outlined in the Bulletin. The two remaining units are Davis-Besse, which is described below, and D.C. Cook Unit 2. Cook 2 was scheduled for refueling in fall 2001, but operational issues in the summer of 2001 pushed their planned outage back until mid-January 2002. After numerous interactions with the licensee and additional justification by the licensee, the NRC staff concluded that the licensee's schedule was acceptable.

Of the plants that did inspections in fall 2001, Crystal River Unit 3 identified a nozzle with boron deposits, and ultrasonic examination revealed a through-wall circumferential crack that extended ~ 90° around the nozzle (Fig. 4). This nozzle was repaired.

ONS-3 identified another five nozzles with leaks, seven that required repair, including one nozzle with a circumferential crack.

Three Mile Island Unit 1 identified five CRDM nozzles with leaks and all eight thermocouple nozzles with leaks. Additional ultrasonic and penetrant tests identified an additional three nozzles with cracks. All of the thermocouple nozzles were repaired (plugged) and six of the eight cracked CRDM nozzles were repaired.

North Anna Unit 1 identified nine nozzles with shallow cracks that were found by the licensee to be acceptable for continued operation. North Anna Unit 2 identified three leaking nozzles that were repaired.

Surry Unit 1 identified four nozzles with leaks and repaired a total of six nozzles. Surry Unit 2 identified no leaking nozzles from a bare metal visual examination.

The inspection at D.C. Cook Unit 2 identified no unacceptable indications.

Figure 4 Boric acid deposits identified at Crystal River Unit 3 during its fall 2001 outage.

Davis-Besse

The Davis-Besse refueling outage began on February 16, 2002. The licensee planned to perform a visual inspection of the outer surface of the RPV head looking for signs of boron deposits, and ultrasonic inspection of all CRDM nozzles. The inspection identified five nozzles with indications, including three with through-wall cracks, and the licensee decided to repair all five nozzles. During machining to facilitate repair of nozzle #3, the equipment rotated and was removed from the head. Upon removal, the licensee found that the nozzle had tipped, with the CRDM flange (located above the head) contacting the flange of an adjacent CRDM. The licensee cleaned the surface of the RPV head and found a large cavity adjacent to nozzle #3 (Fig. 5), where the RPV head base material had been corroded down to the stainless steel cladding. Subsequent investigation revealed an additional much smaller degraded area near nozzle #2, located within the wall thickness (no cladding was exposed).

The licensee completed a root cause analysis (Ref. 7). One of the new pieces of information in that report was a photograph of the head from the 2000 refueling outage (Fig. 6). A similar photograph, albeit without the reddish tinting from corrosion product, has subsequently been identified from the 1998 outage.

After the initial finding of the cavity at Davis-Besse, the NRC issued Information Notice 2002-11 (Ref. 8), "Recent Experience with Degradation of Reactor Pressure Vessel Head," on March 12, 2002. After some of the evidence began to be accumulated regarding secondary indications of a serious ferritic corrosion event, the NRC issued Information Notice 2002-13 (Ref. 9), "Possible Indicators of Ongoing Reactor Pressure Vessel Head Degradation," on April 4, 2002.

Bulletin 2002-01

In response to the findings at Davis-Besse, the NRC issued Bulletin 2002-01 (Ref. 10) on March 18, 2002. The focus of this Bulletin was to assess licensee inspections and other information that could provide a basis for conclusions on the condition of the RPV head. The Bulletin also addressed boric acid corrosion of other parts of the reactor coolant system. Following issuance of this Bulletin, inspection findings in spring 2002 were relatively quiet. The exception was an inspection at Millstone Unit 2, which identified three nozzles (no leaks) requiring repair, with axial outer diameter surface cracks that extended from below the J-groove

Figure 5 Cavity identified at Davis-Besse during its spring 2002 outage.


Figure 6 Boric acid and corrosion products identified on the RPV head flange of Davis-Besse during its 2000 outage.

into the weld zone. This finding is significant because this plant had the lowest susceptibility of any plant that had identified cracking.

Bulletin 2002-02

Since the initial findings of circumferential cracking at ONS-3, the nuclear industry has been working to develop inspection recommendations (and justification for the recommendations) that would provide effective management of the issue. This effort was continually challenged by new findings, e.g., Davis-Besse upper head wastage, and the industry did not have a proposal available for consideration by the summer of 2002. To address cracking and wastage on the upper RPV head, the NRC issued Bulletin 2002-02 in August 2002 (Ref. 11). This Bulletin provided a description of a comprehensive inspection program that identified a combination of visual and non-visual examinations on a graded approach consistent with a variety of plant susceptibilities to PWSCC. This Bulletin used a parameter referred to as effective degradation years (EDY) to characterize plant susceptibility to PWSCC. Calculation of this parameter requires information on the RPV head operating temperature(s) and the operating time (i.e., effective full power years, EFPY) at each operating temperature. These data are used to integrate the effects of operating temperature, normalized to 316°C (600°F). The standard Arrhenius activation energy dependence on temperature is applied to each time period with a distinct head temperature:

$$EDY = \sum_{j=1}^{n} \left\{ \Delta EFPY_j \exp\left[-\frac{Q_i}{R}\left(\frac{1}{T_{head,j}} - \frac{1}{T_{ref}} \right) \right] \right\}$$

where:

EDY	=	effective degradation years
n	=	the number of distinct operating temperatures used at the plant
Qi	=	activation energy for crack initiation (50 kcal/mole)
R	=	universal gas constant (1.103x10-3 kcal/mol-°R)
Thead,j	=	RPV head operating temperature at 100% power during time period j (°R = °F + 459.67)
ΔEFPYj	=	the effective full power years of operation at temperature Thead,j
Tref	=	reference temperature (600°F = 1059.67°R)

Notable inspection findings were prevalent during the fall 2002 outages. North Anna Unit 2 identified two leaking nozzles. One of these leaks was from a nozzle that had received a weld over-lay repair at the previous outage. Failure of the repair was attributed to the weld over-lay repair not completely covering the original Alloy 182 weld butter, with cracking then occurring in the original weld at the periphery of the repair weld. Surface examinations of the J-groove welds identified more than half of the welds with cracks. Ultrasonic testing of the nozzle base material identified twenty nozzles with axial indications. Several nozzles were identified with circumferential cracks on the nozzle outer diameter surface within the zone of the J-groove weld, just below the root of the weld. With the myriad of repairs necessary due to these findings, this plant became the first U.S. plant to install a new RPV head using Alloy 690 nozzle base material and Alloy 52 and 152 welds.

At ANO-1, a leak was identified from the nozzle that had been repaired in the spring of 2001. The failure of the repair was attributed to the weld over-lay repair not completely covering the original J-groove weld, similar to the North Anna Unit 2 finding.

At Sequoyah Unit 2, minor head corrosion was identified from a boron leak located above the RPV head. In particular, the licensee identified a leak from a valve in the reactor vessel level instrument system (RVLIS). Leaking coolant impacted the RPV head insulation below the valve, fell through a seam in the insulation and onto the RPV head. After the RPV head was cleaned up, a corrosion area was identified with dimensions 127 mm (5 in.) long and 8 mm (5/16 in.) wide, with a maximum depth of 3 mm (1/8 in.).

Order EA-03-009

The NRC issued Order EA-03-009 (Ref. 12) to all PWR licensees on February 11, 2003. This Order amends the licenses to provide specific inspection requirements for all PWR plants. This Order requires that plants evaluate their susceptibility to PWSCC using a formula for effective degradation years, EDY. The Order then provides specific inspection requirements based upon the EDY level of the plant. The Order provides requirements for plants with EDY greater than 12 or that have experienced PWSCC. These plants are required to perform a bare metal visual examination and a non-visual examination every refueling outage. Moderate susceptibility plants (those with EDY from 8 to 12) are required to perform either bare metal visual or non-visual examination every outage, alternating the two methods each RFO. Low susceptibility plants (with EDY less than 8) are required to perform a bare metal visual examination by their second refueling outage after issuance of the Order and every third refueling outage or five years thereafter. In addition, low susceptibility plants are required to perform non-visual examination by February 11, 2008, and then repeat every fourth refueling outage or seven years thereafter.

The non-visual examinations described in the Order are ultrasonic examination or surface examination. The ultrasonic examination covers from the bottom of the nozzle to 2 inches above the J-groove weld, and includes an assessment to determine if leakage has occurred in the interference fit zone of the nozzles. The scope of the surface examination includes the surface of the J-groove weld, the outer diameter surface of the VHP nozzle base metal, and the inside surface of the VHP nozzle to a point 2 inches above the J-groove weld.

The Order provides explicit inspection requirements for repaired nozzles and welds, and makes no distinction for heads fabricated from Alloy 600 or Alloy 690.

In addition to the susceptibility based inspections of the RPV head surface and VHP nozzles, the Order requires that all licensees perform visual inspections to identify boric acid leaks from components above the RPV head, with follow-up actions including inspection of potentially-affected RPV head areas and VHP nozzles should any leaks be identified.

The Order also provided means for licensees to request relaxation from its requirements upon demonstration of good cause. As of mid-December 2003, nineteen plants had made specific requests for relaxation. These requests relate to limitations in inspection of the top of the nozzles (above the J-groove welds), the lower end of the nozzles, the bare metal visual examination of the RPV head surface, and the need to inspect all nozzles or parts of the nozzle using a single inspection method.

Relaxation requests for the lower end of the nozzles have been due to the presence of guide funnel threads and tapers on the end of the nozzles. In additional, one licensee highlighted an impediment to a complete volumetric examination for cases in which a transducer with a pair of sensors is used for detection of circumferential cracking. The latter issue results in a lack of coupling at the end of the nozzle that prevents a triangular area with long leg on the nozzle outer diameter surface from being effectively interrogated.

The relaxations related to the bare metal visual examination concern service structure impediments that prevent a 100% examination of the RPV head outer surface. These impediments prevent inspection of less than 5% of the head surface and do not substantially preclude inspection of areas located at head elevations above the outer row of VHP nozzles.

The relaxations related to the nozzle inside surface above the J-groove weld are due to geometric conditions that prevent effective examination of these areas. In one case, the CRDM nozzles had centering tabs and a step on the nozzle inside surface just above the J-groove weld.

Because of the specific wording used in the Order, licensees are required to inspect all VHP nozzles using the same approach, either ultrasonic examination or surface examination. This has proven problematic for certain cases, such as the head vent line that does not have an interference fit (thus preventing the ultrasonic leakage assessment required in conjunction with the ultrasonic examination) and certain situations where approval was sought for a limited scope surface examination to supplement the ultrasonic examination.

For the short term, the NRC staff has revised Order EA-03-009 (Ref. 13) to implement changes that would eliminate the need for many of the relaxation requests that have demonstrated no safety benefit to certain requirements of the Order. This revision to the Order permits the use of multiple inspection types for each nozzle and provides other inspection scope reductions that have no safety implications. In support of this activity, the industry submitted a report (Ref. 14) that provided a generic evaluation of industry-proposed revisions to the scope of the inspections required in Order EA-03-009.

Bottom-Mounted Instrument Cracking

With the focus of attention on PWSCC of Alloy 600 on the upper RPV head and possible boric acid corrosion of ferritic components throughout the reactor coolant system, visual examinations of other applications of Alloy 600 have increased in their thoroughness and effectiveness. One area that was not anticipated to provide short-term PWSCC concerns was the RPV lower head BMIs, due to the cold-leg operating temperature of the RPV lower head. However, in the spring of 2003, the licensee for the South Texas Project Unit 1 (STP-1) identified apparent boron deposits on the lower RPV head near two BMIs (Ref. 15). Characterization of all of the BMI nozzles at STP-1 identified PWSCC in these two nozzles, and no PWSCC in any other nozzle (Ref. 16). The operating temperature of the STP-1 lower head was ~ 294°C (561°F), and the calculated EDY was less than 3. Besides issuance of these Information Notices, the NRC issued Bulletin 2003-02 (Ref. 17) to obtain information on licensee inspection activities and inspection plans for the RPV lower head. Thus far other plants have identified white residue on the lower head, frequently boron traced to refueling seal leakage or other sources above the RPV lower head, but no other plant has identified PWSCC in the BMIs.

Outlook

The long-term goal in this area is for the NRC to adopt at 10 CFR 50.55a permanent requirements for inspections to ensure the integrity of the RPV head and VHP nozzles. It is preferred that the American Society for Mechanical Engineers (ASME Code) adopt acceptable requirements in Section XI of the Code that the NRC could endorse; absent acceptable ASME Code requirements the NRC would seek to enumerate acceptable requirements at 10 CFR 50.55a.

The longer term solution for many plants has been to seek replacement of the RPV head using Alloy 690 nozzles and Alloy 52 and 152 for weld filler metals. At the present time thirty-one plants have expressed an intent to replace their RPV head; eleven had completed vessel head replacement by early 2004.

Regarding the future for other applications of Alloy 600 in PWRs, it is reasonable to expect that all parts, components and joints fabricated from Alloy 600 and weld filler metals Alloys 82 and 182 will continue to crack during operation. The critical aspect of preventing this cracking from leading to challenges to plant safety systems will be the implementation of management programs, including effective inspection activities, to identify and remediate the cracking.

Acknowledgments

The author acknowledges his co-workers for their review and comments on this paper.

References

1. U.S. Nuclear Regulatory Commission, Information Notice 90-10, "Primary Water Stress Corrosion Cracking of INCONEL 600," February 23, 1990.

2. Electric Power Research Institute (EPRI) Report TP-1001491, Part 2, 2001, "PWR Materials Reliability Program Interim Alloy 600 Safety Assessments for US PWR Plants (MRP-44), Part 2: Reactor Vessel Top Head Penetrations."

3. U.S. Nuclear Regulatory Commission, Generic Letter 97-01, 1997, "Degradation of Control Rod Drive Mechanism Nozzle and Other Vessel Closure Head Penetrations."

4. D. J. Modeen (Nuclear Energy Institute), letter to G. C. Lainas (U.S. Nuclear Regulatory Commission), 1998, “Responses to NRC Requests for Additional Information on Generic Letter 97-01.”

5. U.S. Nuclear Regulatory Commission, Information Notice 2001-05, 2001, "Through-Wall Circumferential Cracking of Reactor Pressure Vessel Head Control Rod Drive Mechanism Penetration Nozzles at Oconee Nuclear Station, Unit 3."

6. U.S. Nuclear Regulatory Commission, Bulletin 2001-01, 2001, “Circumferential Cracking of Reactor Pressure Vessel Head Penetration Nozzles.”

7. FirstEnergy, Davis-Besse Nuclear Power Station, 2002, “Root Cause Analysis Report - Significant Degradation of the Reactor Vessel Head.”

8. U.S. Nuclear Regulatory Commission, Information Notice 2002-11, 2002, “Recent Experience with Degradation of Reactor Pressure Vessel Head.”

9. U.S. Nuclear Regulatory Commission, Information Notice 2002-13, 2002, “Possible Indicators of Ongoing Reactor Pressure Vessel Head Degradation.”

10. U.S. Nuclear Regulatory Commission, Bulletin 2002-01, 2002, “Reactor Pressure Vessel Head Degradation and Reactor Coolant Pressure Boundary Integrity.”

11. U.S. Nuclear Regulatory Commission, Bulletin 2002-02, 2002, “Reactor Pressure Vessel Head and Vessel Head Penetration Nozzle Inspection Programs.”

12. U.S. Nuclear Regulatory Commission, Order EA-03-009, 2003, “Issuance of Order Establishing Interim Inspection Requirements for Reactor Pressure Vessel Heads at Pressurized Water Reactors.”

13. U.S. Nuclear Regulatory Commission, First Revised Order EA-03-009, 2004, “Issuance of First Revised NRC Order (EA-03-009) Establishing Interim Inspection Requirements for Reactor Pressure Vessel Heads at Pressurized Water Reactors.”

14. Materials Reliability Program, 2003, “Generic Evaluation of Examination Coverage Requirements for Reactor Pressure Vessel Head Penetration Nozzles (MRP- 95NP).”

15. U.S. Nuclear Regulatory Commission, Information Notice 2003-11, 2003, “Leakage Found on Bottom-mounted Instrumentation Nozzles.”

16. U.S. Nuclear Regulatory Commission, Information Notice 2003-11, Supplement 1, 2004, “Leakage Found on Bottom-mounted Instrumentation Nozzles.”

17. U.S. Nuclear Regulatory Commission, Bulletin 2003-02, 2003, “Leakage from Reactor Pressure Vessel Lower Head Penetrations and Reactor Coolant Pressure Boundary Integrity.”

Stress Corrosion Crack Growth Rates
(SCCGRs) for Alloy 182 and 82 Welds

Steven A. Attanasio, John V. Mullen, John W. Wuthrich,
Weldon W. Wilkening, and David S. Morton

Lockheed Martin Corporation, Schenectady, NY 12301

ABSTRACT

Stress corrosion crack growth rate (SCCGR) tests were conducted on Alloy 182 and Alloy 82 weld metals. Tests were conducted using compact tension specimens, which were either actively-loaded, bolt-loaded, or loaded *via* a novel compliant self-loaded compact tension (CSLCT) specimen technique in which the load is applied using a pre-compressed Alloy X-750 ring. This 'ring-loading' method combines some of the advantages of active-load and bolt-load methods. Specifically, the CSLCT specimens maintain a nearly constant load during testing (due to the compliant design of the ring), and yet are compact enough that a large number of specimens can be tested in a single autoclave.

SCCGRs are reported as the average SCC growth rate ($SCCGR_{AVE}$), rather than the maximum SCC growth rate ($SCCGR_{MAX}$). There is a concern, as discussed in this paper, that the apparent maximum SCCGR in a laboratory test is not constant, but rather changes with test duration. To circumvent the concern regarding $SCCGR_{MAX}$ while still capturing the information obtained in the test related to the maximum SCC extension, a quantity referred to as the RATIO is reported for each data point. This quantity refers to the ratio of the maximum SCC extension (Δa_{MAX}) to the average SCC extension (Δa_{AVE}) – *i.e.*, RATIO $\equiv \Delta a_{MAX}/\Delta a_{AVE}$. Reporting the $SCCGR_{AVE}$ and the RATIO provides a quantitative measure of both the average SCC extension and the maximum SCC extension in a test.

The $SCCGR_{AVE}$ data reported in this study are consistent with $SCCGR_{AVE}$ data reported by other investigators, for both Alloys 182 and 82. The SCCGRs reported herein are more rapid for Alloy 182 than for Alloy 82. This result may be related to the lower chromium content of Alloy 182 (~ 15 wt% Cr compared to ~ 20 wt% Cr for Alloy 82), the different welding processes employed, and/or the higher carbon levels for the Alloy 82 heats. Regressions were performed using several empirical model forms, to estimate SCC parameters such as the temperature and stress intensity factor dependencies.

Although much of the data scatter in the SCCGR response is suspected to be caused by the inherent variability of weld materials, another contributor to the variability is believed to be aqueous hydrogen (H_2) concentration. Aqueous hydrogen concentration was found to influence the SCCGR of Alloy 82. Consistent with the behavior previously reported for Alloy 600 and Alloy X-750, the stress corrosion crack growth rates increase as the measured nickel/nickel oxide phase transition is approached. This factor has not been incorporated into the empirical models discussed above.

BACKGROUND

Primary water stress corrosion cracking (PWSCC) of Alloy 182 and 82 weld metal is a concern, as described in References [1] to [4]. According to Reference [1], an Alloy 600 vessel head penetration crack in the Bugey 3 plant was found to propagate into the Alloy 182 weld material. More recently, from 1994 to 1998, several stress corrosion cracks have been detected in Alloy 182 welds in American plants such as St. Lucie, San Onofre and Calvert Cliffs [1]. According to Reference [2], leakage was detected in an outlet nozzle-to-pipe weld of the V.C. Summer plant in October 2000. Stress corrosion cracking had occurred in both the Alloy 182 buttering and the Alloy 82 weld metal, as shown in Figure 1 [3]. Non-destructive test (NDT) indications in a similar location (outlet nozzle-to-safe end weld) had been observed in June 2000 at Ringhals Unit 3 in Sweden. NDT indications were subsequently found in the same region of Ringhals Unit 4, in the fall of 2000. The cracking in Ringhals 3 and 4 [4] was less severe than the V.C. Summer cracking. The Ringhals welds were fabricated from Alloy 182 weld metal.

EPRI Materials Reliability Program: Given the concerns for primary water stress corrosion cracking of Alloy 600 and its weld metals, the Electric Power Research Institute (EPRI) is sponsoring a Materials Reliability Program (MRP). The MRP group members have developed a recommended stress corrosion crack growth rate curve for PWSCC of thick-wall components fabricated from Alloy 600 material [5]. A similar effort is underway for weld materials. The present work is intended to be a contribution to this effort.

EXPERIMENTAL

Materials

Two heats of Alloy 182 weld metal and three heats of Alloy 82 weld metal were tested. Table 1 shows material compositions for each heat. Two elements that are of specific interest for PWSCC resistance are chromium and carbon. The Alloy 182 heats contain 15 wt% Cr, whereas the Alloy 82 heats contain 17 to 21 wt% Cr. The Alloy 182 heats contain 0.02 to 0.03 wt% carbon, whereas the Alloy 82 heats contain 0.045 to 0.047 wt% carbon. Room temperature yield strength values are given in Table 2.

Alloy 182 and 82 weld metals were deposited using the shielded metal arc welding process and the automatic gas tungsten arc welding process, respectively. Specimen fabrication procedures are illustrated in Figure 2.

Specimens

SCCGR data were obtained using compact tension (CT) test specimens, most of which were side-grooved. Specimens were fatigue precracked in air. Specimens were loaded by one of three methods: (a) actively loaded using a test machine, (b) bolt-loaded, or (c) ring-loaded via the CSLCT specimen method. The latter method is described below. All specimens were tested such that cracking proceeded from the root of the weld to the crown of the weld. This specimen orientation is typical of the crack propagation direction that can occur in plant applications such as pipe welds. Orientation is important since the long axis of the dendrites tends to align roughly parallel to the root-to-crown dimension [1]. It has been shown by prior investigators that SCC growth generally occurs more rapidly in the direction parallel to the long axis of the dendrites [6, 7]. The crack propagation directions can be summarized by adopting ASTM terminology, in which the direction of welding is designated as the L direction, as shown in Figure 2. Using this notation, the present specimens had the load applied parallel to the T

direction, and crack growth occurred in the S direction – according to the ASTM notation, such specimens are designated as having a T-S orientation.

Environment

Testing was conducted in recirculating autoclaves, in deaerated water with a high temperature pH of ~7. The desired H_2 concentrations were obtained by varying the feed tank H_2 overpressure according to Henry's law. The room temperature H_2 calculations were conducted using a Henry's law coefficient of 0.85 psia/(scc/kg).

Post-test Evaluation

Most specimens were heat-tinted in air at 454°C for 16 to 20 hours, to provide a clear demarcation of the SCC crack. Specimens were pulled apart by post-test fatigue loading. An optical microscope was used to measure the crack depths using a measurement technique similar to that of ASTM E813. In general, the present work employed 17 measurement locations rather than the 9 measurement locations in ASTM E813. The measurements are averaged to determine an average SCC extension, Δa_{ave}. Also, the maximum SCC extension at any point along the crack, Δa_{max}, is also identified and recorded.

Data Screening Criteria

All SCCGR specimens were subjected to screening criteria similar to that employed in EPRI MRP-55 [5]. All tests conducted were single condition tests, with careful autoclave water chemistry control (including H_2 control). The data are based on post-test destructive examination. An example of a post-test specimen is shown in Figure 3, in which the air fatigue precrack and SCC regions can be readily distinguished. Data are reported herein only for specimens which met the ASTM E647 size criteria (using the flow strength at test temperature in the validity equation, as employed by the MRP group). A minimum crack extension of 0.2 mm was used in screening the data, and a minimum 'engagement' of 50% was utilized. The term engagement quantifies the percentage of the air fatigue precrack length that has incubated SCC.

RESULTS

CSLCT Specimen Hardware, Loading, and Qualification

The compliant self-loaded CT specimen method combines some of the advantages of active-loaded and bolt-loaded test methods. Similar to active load testing, the specimens can be instrumented and yet maintain a nearly constant load due to the compliant design of the ring. Due to the relatively compact size of the ring fixtures, more specimens can be tested in a single autoclave than in active load test facilities. Up to 10 instrumented CSLCT ring fixtures have been tested in a single 60 liter flowing autoclave. Also, a dedicated actuator is not needed for each autoclave test facility, and each ring can be independently loaded to achieve different K_I values for each specimen.

Hardware: The CSLCT hardware and assembly are shown in Figures 4 (a) and (b), respectively. Hardware components are fabricated from Alloy X-750, which is a high strength corrosion resistant nickel-based superalloy. Sizing is controlled to ensure that stresses are low, to preclude PWSCC of the hardware. The CSLCT specimen hardware is reusable. In addition to the loading apparatus, the 'ring-loaded' specimens are also capable of employing linear variable differential transformers (LVDTs) as *in-situ* instrumentation, which can be used in an

effort to identify the incubation time[1] for the onset of SCC, or to determine whether a steady-state crack growth rate is achieved during a given SCCGR test.

Loading: Each ring is pre-compressed to ~ 15.5 kN (3500 pounds-force) and then unloaded prior to use. This pre-compression step is used to work harden each ring slightly, to ensure that the subsequent ring loading is elastic in nature. The unloaded 'length' (L_U) of the ring is then measured in the direction parallel to the load line. This measurement is made in a specific, machined area in the flat region of the ring (from one outside surface to the other), as shown in Figure 4 (a). Then, the spring constant of the ring is determined by using an actuator to compress the ring while measuring the resulting elastic displacement using a clip gauge placed inside of the ring. In general, the rings compress by ~ 8.8 kN per mm (50 pounds-force per mil) of displacement. The ring spring constant (k_r) must be determined independently for each ring.

The schematic diagram for loading a CT specimen into the CSLCT ring fixture is shown in Figure 5. An actuator applies a load to the ring, which compresses it. The top bolt is then rotated such that ~ 0.45 kN (100 pounds-force) of the axial load applied to the ring is transferred to the CT specimen. The actuator-applied load is then slowly released from the ring, which loads the CT specimen as the ring expands (*i.e.*, the ring acts as a spring). Since both the ring and the specimen are compliant, the final load applied to the specimen is generally 15 to 25 percent less than the load applied to the ring by the actuator. Therefore, it is necessary to increase the applied actuator load by the estimated load reduction during ring loading. Typically, the compressive load applied by the actuator will have a value between ~ 4.5 and 11 kN (*i.e.*, between 1000 and 2500 pounds-force). While the exact final specimen load is not known until after the loading process is complete, experience has shown that the final specimen loads are generally within 3% of the desired load. Determination of the final load is made *via* a post-loading measurement of the 'loaded' ring length, L_L, which is illustrated in Figure 5 (c). It is emphasized that the important parameter to measure is the *change* in ring length – *i.e.*, the change in spring length – relative to the unloaded condition, which is referred to as ΔL (where $\Delta L = L_U - L_L$). Then, the load (P) can be determined using the measured spring constant of the ring:

$$\boldsymbol{P = \Delta L \cdot k_r} \,. \tag{1}$$

Since the rings are loaded at room temperature, the load applied to the specimen decreases as the specimen is heated in the autoclave, due to the change in modulus of elasticity with temperature. The load loss due to the modulus change is accounted for during the loading process, by increasing the applied load (*e.g.*, by ~ 8 to 10% for testing at 338 to 360°C) in order to achieve the desired load at the test temperature.

Note that this apparatus has been used to test 0.4T and 0.6T CT specimens (*i.e.*, specimen thickness of ~ 10 and 15 mm, respectively). Testing of larger specimens would require rings with a larger diameter.

Qualification: Testing was performed on Alloy 600 and Alloy X-750 Condition HTH specimens for which abundant active load SCCGR data were available. Figure 6 shows that the SCCGRs measured using the ring-loaded specimens are within the range of results produced by active load testing.

---

[1] Note that since irregular crack fronts limit the effectiveness of *in-situ* crack detection instrumentation methods, the LVDTs are generally less effective at discerning crack incubation times for weld materials than for wrought materials.

Post-test measurements show that the amount of load loss during testing is relatively minor, even when appreciable SCC occurs. Although SCC leads to displacement at the specimen load line (and hence an increase in the ring length), the load is not very sensitive to minor increases in length due to the compliant nature of the rings. Post-test specimen loads were determined by measuring the ring length after the specimens were removed from the autoclave, both prior to unloading ($L_{L,\ post\text{-}test}$) and after unloading ($L_{U,\ post\text{-}test}$). The maximum load loss during the test for the six specimens tested was 2.2 %. Despite this minor loss in load, ring-loaded specimens generally experience an increasing K_I during an SCCGR test, due to the effect of increasing crack length on K_I. For example, the three Alloy 600 specimens had average pre- and post-test K_I values of 27.1 and 28.1 MPa$\sqrt{m}$, respectively (both are at-temperature K_I values). Note that the increase in K_I with crack growth is lower than it would be for an actively-loaded test.

Use of RATIO and $SCCGR_{AVE}$

All data provided in this study are reported as the average SCC growth rate ($SCCGR_{AVE}$), rather than the maximum SCC growth rate ($SCCGR_{MAX}$). In addition, the maximum-to-average crack extension ratio (*i.e.*, RATIO) is also reported for each data point. This method of data reporting, which is used by Lockheed Martin and by Mills and Brown [8], has some advantages over the traditional practice used by most investigators – *i.e.*, data are typically reported as either $SCCGR_{AVE}$ or $SCCGR_{MAX}$.

RATIO: It is well-known that stress corrosion crack fronts are often uneven (Figure 3), particularly for weld metal. Cracks initially occur as discrete 'fingers' – in the case of weld metal, the initial cracks form along SCC-susceptible dendrites – and then become more uniform as cracking proceeds, though some level of crack front unevenness is typically maintained, as shown in the inset of Figure 7. A method is described herein to quantitatively characterize the crack shape by using the maximum SCC extension (Δa_{max}) and the average SCC extension (Δa_{ave}). The ratio of these quantities is referred to herein as the RATIO:

$$RATIO \equiv \frac{\Delta a_{max}}{\Delta a_{ave}} \tag{2}$$

As shown in Figure 7, it is observed experimentally that cracks with longer average crack extensions have smaller RATIOs. Early in the SCC process, where only isolated dendrites have undergone SCC, the RATIO is expected to be large. Later in the SCC process, the amplitude of the 'unevenness' due to the leading dendrites is only a small fraction of the actual crack extension, and the RATIO approaches 1.

A regression to the combined RATIO data set shown in Figure 7 was developed:

$$ln(RATIO - 1) = 2.48 - 0.762 \cdot ln\left(\frac{\Delta a_{ave}}{\Delta a_{ref}}\right) \tag{3}$$

where Δa_{ref} is a normalizing value (taken as 0.051 mm) that is utilized to maintain dimensionless notation. It is noted that one limitation of this equation form is that it produces physically unreasonable RATIO values for very small values of Δa_{ave}. Thus, equation (3) is judged to be valid only for RATIO values $\geq$ 0.051 mm. [{2}]

[{2}] In Figure 7, some of the data presented do not meet the SCCGR screening criteria outlined above, in order that a wide range of data would be available for the RATIO regression (*e.g.*, including cases where the Δa_{ave} is low).

The data set used in the regression includes published data from Mills and Brown [8], in addition to data from the present study. It is observed that the present data and the Mills and Brown data are in good agreement for cracks with Δa_{ave} greater than ~ 1 mm. Below this point, the RATIO values reported by Mills and Brown are somewhat lower than the present RATIO values. There are two possible reasons for this observation. The most probable reason is that the definitions of Δa_{max} utilized in the two studies are different. Specifically, the present work defines Δa_{max} as the absolute maximum SCC extension at any position along the crack front. In the Mills and Brown work, Δa_{max} is defined as the maximum SCC extension at any of the post-test examination measurement points (either 9 or 25 measurement points were used per specimen [8]). Thus, the Mills and Brown method may provide lower Δa_{max} values than the method used in the present work, since the absolute maximum SCC extension along the crack front will often be located somewhere between two of the measurement locations. This difference in the definition of Δa_{max} likely explains the difference in RATIO values at low Δa_{ave}. It seems reasonable that the impact of the different Δa_{max} definitions should diminish as the cracks grow beyond Δa_{ave} values of 1 mm, since the crack front irregularity diminishes as Δa_{ave} increases.

It is also possible, though less likely, that the difference in RATIO values at low Δa_{ave} is due to the use of unload-reload cycles in some of the Mills and Brown tests. It has been suggested in the past that unload-reload cycles may produce more uniform crack fronts, and thus it is conceivable that such an effect could lead to lower RATIO values. In their work ([8],[9]) Mills and Brown state that the unload-reload cycles used in their tests had no effect on the ratio of maximum SCC extension to average SCC extension – the basis for this statement is the overlap between their unload-reload data (stress ratio ~ 0.65, trapezoidal waveform with hold times of 10 or 100 minutes) and constant load data over the range of ~ 1 mm $\leq \Delta a_{ave} \leq$ 5 mm (Figure 7).

It is noted that the concept of the RATIO is applicable to wrought materials as well, since they also exhibit 'uneven' stress corrosion crack fronts. This point is illustrated by the CSLCT specimen qualification data described in the previous section, in which one of the Alloy 600 specimens experienced an average SCC extension of 0.518 mm and a maximum SCC extension of 1.25 mm, while one of the Alloy X-750 HTH specimens experienced an average SCC extension of 0.434 mm and a maximum SCC extension of 0.810 mm. Thus, the RATIO values for these Alloy 600 and Alloy X-750 specimens are 2.41 and 1.87, respectively.

Use of Average rather than Maximum SCCGR: One consequence of the crack shape evolution with time shown in Figure 7 is that the apparent maximum SCC growth rate is not constant, but rather changes with test duration. This concept is illustrated in Figure 8. In this schematic figure, an average SCC growth rate of 1 mm/yr was assumed for the purposes of illustration. The value of Δa_{max} at different test times was calculated using the RATIO equation in Figure 8. The key concept in Figure 8 is that the $SCCGR_{MAX}$ value obtained from this test depends on when the test is stopped. Specifically, if the test is terminated at 0.25 years, a higher $SCCGR_{MAX}$ value would be obtained, relative to a test terminated at 1 year. To circumvent this concern regarding $SCCGR_{MAX}$, while still capturing the information obtained in the test related to the maximum SCC extension, data are reported herein using both the $SCCGR_{AVE}$ and the RATIO.

It can be argued that the use of $SCCGR_{MAX}$ (rather than $SCCGR_{AVE}$) is 'conservative' since $SCCGR_{MAX}$ is always greater than $SCCGR_{AVE}$. However, the use of $SCCGR_{MAX}$ introduces an unknown (and non-constant) level of conservatism. The present authors believe that to incorporate conservatism, it is more appropriate to perform SCC lifetime estimates using an $SCCGR_{AVE}$ model with a specified (*e.g.*, 95%) upper bound. The final average SCC crack depth

for a given exposure time can be calculated using a numerical integration approach (which is necessary due to the changes in K_I during SCC growth), and then, if desired, the RATIO regression can be used to estimate the corresponding final maximum crack depth. This process provides a better means of controlling the amount of conservatism/risk in the SCC lifetime estimates. A user-selected upper bound can also be applied to the RATIO regression, if desired.

It is noted that the use of $SCCGR_{AVE}$ rather than $SCCGR_{MAX}$ is consistent with the practice utilized for wrought Alloy 600 in MRP-55 [5]. Also note that Appendix A shows two plots that relate the percent engagement criteria used in data screening to the RATIO and to Δa_{ave}. These plots may be used along with Figure 7 to analyze or screen historical data for which the percent engagement is not available.

SCCGR Data

Alloy 182: Figure 9 shows the present Alloy 182 SCCGR data, which are labeled as LM (Lockheed Martin) data. Data are reported for the two heats of Alloy 182 (LM182–1 and –2). Note that there are two variants of heat LM182–2, with somewhat different yield strength values due to variations in welding and material processing (Table 2). Data are also included in Figure 9 from welds fabricated by several different laboratories and reported by Westinghouse [10]. The comparison to published data was intentionally limited to cases in which the $SCCGR_{AVE}$ (rather than $SCCGR_{MAX}$) was reported, in order to provide a fair comparison to the present data. Note also that, in order to compare the data on an equivalent basis, three data points from the Westinghouse study were screened due to SCC crack extensions less than 0.2 mm (*i.e.*, using the same screening criterion applied to the LM data). In general, the present data are in reasonable agreement with the SCCGRs reported by Westinghouse, though the Westinghouse values tend to be slightly higher on average.

The LM data were obtained at 328°C and 338°C. In Figure 9, all data were normalized to a temperature of 325°C, consistent with the practice used in EPRI MRP-55. In the MRP-55 report, the SCCGRs for wrought Alloy 600 were temperature-adjusted (*i.e.*, normalized) using a value of 130 kJ/mole. It appears that this value is also a reasonable thermal activation energy (Q_{SCCGR}) to use for the weld materials, on the basis of literature citations. Specifically, Le Hong *et al*. reported that the Q_{SCCGR} for Alloy 182 is ~ 130 kJ/mole, based on EDF, ETH, and CEA data [1]. Mills and Brown [8] reported that the Q_{SCCGR} for Alloy 82 is ~ 130 to 150 kJ/mole. Therefore, the present work utilizes a Q_{SCCGR} of 130 kJ/mole for both Alloys 182 and 82, for the purposes of temperature normalization. The LM data were obtained at either 35 or 40 scc/kg H_2, while the Westinghouse data were obtained at 25 scc/kg.

Alloy 82: Figure 10 shows the present Alloy 82 SCCGR data, for three heats (LM 82–1, –2, and –3). Data are also included in Figure 10 from Bechtel [8]. Again, the comparison to published data was limited to cases in which the $SCCGR_{AVE}$ was reported. The LM data were obtained at either 20 or 40 scc/kg H_2, while the Bechtel data were obtained at 40 to 60 scc/kg H_2. The LM data were obtained at 316, 328, 338, and 360°C (see Appendix A for details). Figure 10 shows the LM and Bechtel data, normalized to 325°C. In general, the present data are in reasonable agreement with the SCCGRs reported by Bechtel.

It appears that some of the variability in the LM data for heat 82-2 may be caused by dissolved hydrogen effects. Specifically, as shown in Figure 10, the three LM data points with the highest SCCGRs were tested at 20 scc/kg H_2. The other four data points from that heat (three data points located at ~ 28 MPa$\sqrt{m}$ and one at ~ 49 MPa$\sqrt{m}$) were tested at 40 scc/kg H_2 and all exhibit lower SCCGRs. Testing for heat 82-2 was conducted at 338°C, at which 20 scc/kg H_2 is

closer to the measured nickel/oxide phase transition than is 40 scc/kg H_2, which should result in higher SCCGRs. This issue is discussed in detail later in this document.

Comparison of Alloys 182 and 82: Figure 11 shows all of the $SCCGR_{AVE}$ data for Alloys 182 (in blue) and 82 (in green). On average, the crack growth rates for Alloy 182 are more rapid than the crack growth rates for Alloy 82. This result may be related to the lower chromium content of Alloy 182 (typical values of ~ 15 wt% Cr compared to ~ 20 wt% Cr for Alloy 82), the different welding processes employed, and/or the higher average carbon levels for the Alloy 82 heats. Given the known influence of chromium concentration on PWSCC resistance, for example, it is not unreasonable to expect that Alloy 182 might exhibit higher SCCGRs than Alloy 82.

The specific test conditions (temperature, aqueous H_2 level) for each LM heat are described in Appendix A.

SCCGR Modeling

Three empirical model forms were evaluated by fitting each model to the combined LM plus commercial $SCCGR_{AVE}$ data set. All three model forms have an Arrhenius-type dependence on temperature and a power law dependence in K_I. The following approaches were used in developing the three model forms:

- The data from Alloy 182 and 82 were grouped together to determine the 1/T and K_I dependencies. This approach was used because there are insufficient data to determine these parameters for each data set independently – for example, most of the Alloy 182 data are at approximately 325°C.
- Given that the SCCGRs for Alloy 182 are generally higher than the SCCGRs for Alloy 82, it was judged appropriate to account for the differences between the two alloys using an 'offset' (*i.e.*, a multiplicative factor), and forcing common 1/T and K_I dependencies.
- Since there are insufficient data in the combined data set to quantify a threshold, model forms with and without a threshold K_I were evaluated. In cases where a threshold was used, a value of 9 MPa√m was employed, to be consistent with the Alloy 600 model presented in MRP-55 (*i.e.*, the Scott model [11]).
- The stress intensity factor dependence was generally determined by the results of the regression (*i.e.*, the K dependence was not fixed). However, it was also of interest to evaluate the form of the Scott model, since this model was utilized for the wrought Alloy 600 modeling in MRP-55. The Scott model fixes the K dependence at 1.16 – this value is based on an analysis of inspection data for cracks in the roll transitions of steam generator tubes [11].
- Unfortunately, the yield strength range of the present data is fairly narrow (Appendix A). For this reason, a yield strength term was not included in the model forms evaluated, even though the authors believe that SCC of weld materials is likely influenced by yield strength. This statement is based on the known effect of yield strength for wrought Alloy 600 SCCGR, as demonstrated in several publications (*e.g.*, [12]).

The following general model form was used:

$$\frac{da}{dt} = A \cdot B_{material} \cdot \left(\frac{K_I - K_{th}}{K_o} \right)^{\beta} \cdot exp\left[- \frac{Q}{R \cdot T} \right] \quad (4)$$

where *da/dt* is the average SCCGR in meters per second, *A* is the intercept, $B_{material}$ is a multiplicative factor for Alloy 182 (*i.e.*, $B_{material}$ = 1 for Alloy 82), K_I is the applied stress intensity factor (in MPa$\sqrt{m}$), K_{th} is a threshold stress intensity factor (in MPa$\sqrt{m}$), K_o is a normalizing stress intensity factor used to obtain dimensionless quantities ($\equiv$ 1 MPa$\sqrt{m}$), β is the K_I dependence fitting parameter, *Q* is the thermal activation energy in joules per mole, *R* is the universal gas constant (8.314 J/mol-K), and *T* is the temperature in Kelvin. The three model forms can be summarized as follows:

- Model 1: K_{th} = 0 MPa$\sqrt{m}$, K dependence not fixed
- Model 2: K_{th} = 9 MPa$\sqrt{m}$, K dependence not fixed
- Model 3: K_{th} = 9 MPa$\sqrt{m}$, K dependence (β) fixed at 1.16 [Scott form]

Model 1: The regression to model form 1 yields the following results:

$$\frac{da}{dt} = 14.76 \cdot \left\langle \begin{matrix} 4.272 & 182 \\ 1.000 & 82 \end{matrix} \right\rangle \cdot \left(\frac{K_I}{1} \right)^{0.999} \cdot exp\left[- \frac{148{,}300}{8.314 \cdot T} \right] \quad (5)$$

where the SCCGR for Alloy 182 is calculated to be, on average, approximately 4.3 times as fast as the SCCGR for Alloy 82. The stress intensity factor dependence (β) is ~ 1 and the Q_{SCCGR} is ~ 148 kJ/mole. This value is slightly higher than the Q_{SCCGR} employed to normalize all data to 325°C. The fit of this model to the data is shown in Figure 12. The R^2 value for this model is 0.550, and the standard deviation is 0.760.

It is recognized that the approach taken in Model 1 is limited by the fact that the K_I-dependence and 1/T-dependence are taken from several heats (11 heats). It can be argued that a more appropriate method of determining the K_I-dependence, for example, is to evaluate the K_I dependence of a single heat over a wide range of stress intensity factors. In the present combined data set, the heat that most closely approximates this situation is heat C-4 from Bechtel. All of the green triangles in Figure 12 belong to this heat, except for the data point at a K_I of 52.5 MPa$\sqrt{m}$ and a normalized $SCCGR_{AVE}$ of 4.18 x 10^{-10} m/s. If the remainder of the Bechtel data points are considered, it can be observed that the apparent K_I dependence for heat C-4 is slightly steeper than the β value of ~ 1 obtained by regressing to the combined data set. Thus, the decision to not force the β value to equal the power law slope of the Bechtel C-4 heat is not expected to be a significant problem for the model forms evaluated herein. It should also be pointed out that there are a few disadvantages to using a single heat to define the K_I-dependence. One disadvantage is that the obtained value may not be directly applicable to other heats, which may not have the same K_I-dependence. Another issue is that using a subset of the data to define the K_I-dependence means that single data points have more leverage on the result, and that random variation in a single response can significantly alter the value of the fitting parameter. Grouping all of the data reduces the influence of each specific data point on the overall result.

Model 2: The regression to model form 2 yields the following results:

$$\frac{da}{dt} = 71.24 \cdot \left\langle \begin{matrix} 4.267 \\ 1.000 \end{matrix} \middle| \begin{matrix} 182 \\ 82 \end{matrix} \right\rangle \cdot \left(\frac{K_I - 9}{1} \right)^{0.723} \cdot exp\left[- \frac{150{,}200}{8.314 \cdot T} \right] \quad (6)$$

where the 'offset' between Alloys 182 and 82 is similar to the offset determined using model 1. The stress intensity factor dependence is lower than for model 1, and the Q_{SCCGR} is slightly higher. The fit of this model to the data is shown in Figure 13. The R^2 value for this model is 0.549, and the standard deviation is 0.760.

Model 3: The regression to model form 3 (the Scott model form) yields the following results:

$$\frac{da}{dt} = 0.199 \cdot \left\langle \begin{matrix} 4.618 \\ 1.000 \end{matrix} \middle| \begin{matrix} 182 \\ 82 \end{matrix} \right\rangle \cdot \left(\frac{K_I - 9}{1} \right)^{1.16} \cdot exp\left[- \frac{127{,}900}{8.314 \cdot T} \right] \quad (7)$$

where the regression results show a slightly higher offset (4.6x) between Alloys 182 and 82, and a lower activation energy. The fit of this model to the data is shown in Figure 14. The R^2 for this model is 0.520 and the standard deviation is 0.764.[{3}]

Comparison of Models 1, 2, and 3: Figure 15 compares the three models. It is evident that Models 1 and 2 are very similar for $K_I \geq 20$ MPa$\sqrt{m}$. It is important to note that from a flaw disposition viewpoint, these models are expected to result in similar SCC predictions, since once cracks have grown to a detectable size, they are likely to have stress intensity values greater than 20 MPa$\sqrt{m}$. Thus, for most practical purposes, Models 1 and 2 are equivalent. Model 3 is distinguishable from the other two forms, but the SCCGRs predicted by Model 3 are within $\leq$ 1.5x of the other models, over the range of 20 MPa$\sqrt{m} \leq K_I \leq$ 70 MPa$\sqrt{m}$. This difference is contained within the scatter of the experimental data.

Model Summary: Models 1 and 2 provide a viable approach for correlating the data, and Model 3 also appears to be reasonable. Over the range of the three models, Q_{SCCGR} values were ~ 128 to 150 kJ/mole, which is not very different from other values in the literature for Alloy 600 weld [1] and wrought [5] materials. The K_I-dependencies, when not forced to 1.16, are ~ 0.7 to 1.0. These values are somewhat lower than the Scott model value, but are not very different than 1.16. In fact, when the variance of the β values is considered, it can be argued that these values cannot be differentiated from 1.16 (specifically, the 95% confidence intervals on the β values from either Model 1 or 2 include the value 1.16).

Note that it is possible that the K_I-dependence of Alloy 182 is lower than that of Alloy 82. For example, the $SCCGR_{MAX}$ data reported from an EDF study [1] suggests a low K-dependence ($K^{0.1}$). While this K_I-dependence is shallower than that observed in the present combined data set and in the C-4 heat of Alloy 82 from Bechtel, it is possible that the K_I-dependencies of Alloys 182 and 82 are different – there are insufficient data in the present study to resolve this issue.

It is clear from Figures 12 to 14 that weld variability is an issue for all three models (R^2 values ~ 0.55). Since prior work has suggested the possibility of a K_I-temperature interaction in

---

[{3}] Note that in the MRP-55, the Scott model was used in a somewhat different manner than employed herein. In the MRP-55 work, an intercept was determined for each heat. The 75th percentile of the intercept values for all the heats was then used to determine a predictive curve for the wrought Alloy 600 data set [5]. In the present work, it was of interest to simply evaluate the performance of the Scott model form relative to the data, rather than to replicate the upper bound procedure used in MRP-55. No upper bound equations are presented herein for Models 1 to 3.

SCCGR data [13,14] (*i.e.*, the data in [13] suggest that Q_{SCCGR} may be a function of K_I), an attempt was made to improve the fit to the data using a K_I-1/T interaction:

$$\frac{da}{dt} = A \cdot B_{material} \cdot \left(\frac{K_I - K_{th}}{K_o} \right)^{\beta} \cdot exp\left[-\frac{Q}{R \cdot T} \right] \cdot exp\left[\frac{C \cdot \left((K - K_{th}) / K_o \right)}{R \cdot T} \right] \quad (8)$$

where the last term in the equation represents the K_I-1/T interaction. Unfortunately, this model form produced no measurable improvement in either R^2 or in the standard deviation (though it is noted that this is not the only possible equation form to describe stress-temperature interactions).

Possible methods of reducing the scatter are to explicitly account for heat-to-heat differences and/or to normalize the data for aqueous hydrogen concentration. At present, however, the quantitative data are not available to enable such a hydrogen normalization. Additional information relative to dissolved hydrogen effects on SCC is presented in the following section.

Aqueous Hydrogen Effects on SCCGR

Prior work: Testing of nickel-based alloys in several laboratories has revealed the existence of a maximum in PWSCC susceptibility, when testing is conducted over a range of aqueous hydrogen (H_2) concentrations [15-26]. This maximum in SCC susceptibility occurs in proximity to the nickel/nickel oxide (Ni/NiO) phase transition, suggesting that oxide phase stability affects PWSCC resistance.

Contact Electric Resistance (CER) Measurements: Experimental measurements of the Ni/NiO transition have been performed using a CER instrument (Figure 16). The CER is capable of measuring the surface resistance of a metal to determine whether it is oxide-covered or oxide-free at a given condition. The CER setup used in [27] employed nickel (99.5 wt%) as a test specimen and iridium as an oxide-free inert specimen. Resistance measurements were conducted to measure the H_2 concentration corresponding to the Ni/NiO equilibrium at 288, 316, 338 and 360°C (note that changing the aqueous H_2 level can stabilize or destabilize NiO, *via* the reaction $NiO + H_2 \leftrightarrows Ni + H_2O$). Figure 17 shows the CER data – the amount of H_2 required to reduce NiO to Ni increased as the temperature was raised, consistent with the trend predicted by thermodynamic calculations. Figure 17 also shows corrosion coupon data (obtained at 338°C) that were used to spot-check the CER results. A Ni coupon exposed at 20 scc/kg H_2 was essentially oxide-free, while a coupon exposed at 12.5 scc/kg H_2 was oxide-covered. As discussed in Reference [27], the CER data showed an appreciable deviation between the measured Ni/NiO transition and a calculated Ni/NiO transition based on free energy data from the Journal of Solution Chemistry [17].

Implications for Aqueous H_2 Effects on PWSCC: As shown in Figures 18 and 19 (a), the CER-measured location of the Ni/NiO transition is in close agreement with the location of the maxima in PWSCC susceptibility for Alloy X-750 Condition HTH at 360°C and Alloy 600 at 338°C (note that, as shown in [18], the maximum in SCC susceptibility for Alloy X-750 Condition AH resides slightly into the nickel oxide stability regime). These observations provide insight related to extrapolating the effects of aqueous H_2 concentration to lower temperatures. In other words, accelerated testing has been conducted at 338, 360, and 399°C to determine the effect of aqueous H_2 on SCC, but such tests would be time-consuming to perform at reduced temperatures. The measured Ni/NiO transition provides a reasonable basis for estimating the aqueous H_2 levels at which the maxima in SCC susceptibility are likely to be observed at lower temperatures. Support for this statement comes from the work of Totsuka *et al*. [24], in which

the maximum in PWSCC susceptibility of Alloy 600 was found to reside at ~ 33 scc/kg H_2 at 360°C, and at ~ 11 scc/kg H_2 at 320°C. The location of the measured Ni/NiO phase transition is 25 ± 5 scc/kg H_2 at 360°C, and ~ 8 ± 2.5 scc/kg H_2 at 320°C.

Prior work indicates that the H_2 dependency can be fundamentally described by the extent that the electrochemical corrosion potential (EcP) of the alloy deviates from the potential of the Ni/NiO phase transition (*i.e.*, $EcP_{Ni/NiO}$ – EcP), as shown in Figure 19 (b). This potential difference (∆EcP) likely represents the relative stability of oxides that can influence SCC (*e.g.*, crack tip oxides are often of a NiO structure [28]). Correlations of the observed hydrogen functionality were developed for Alloys 600, X-750 HTH and X-750 AH in terms of the parameter ∆EcP [18]. Knowing the location of the Ni/NiO phase transition as a function of temperature, these correlations can be extrapolated to lower temperatures *via* the assumption that the magnitude of the dissolved H_2 effect is temperature independent (*i.e.*, it is assumed that the only effect of temperature is to change the location of the Ni/NiO phase transition). Using these correlations, SCCGR effects can be predicted at a given aqueous H_2 concentration and temperature of interest, for each material.

Aqueous Hydrogen Effects on Alloy 82: Given that the SCCGR increases as the Ni/NiO phase transition is approached for other nickel-based alloys, it is expected that similar behavior should also be obtained for the weld materials tested in this study. Although no hydrogen effects data are available for Alloy 182, limited hydrogen effects data are available for Alloy 82, as shown in Figure 20. Crack growth rate data are available for a single heat (LM82-2) at 338°C. Crack growth rates for all three specimens tested at 20 scc/kg H_2 were higher than the crack growth rates for the four specimens tested at 40 scc/kg H_2. As expected, approaching the Ni/NiO phase transition (located at 13.8 scc/kg H_2 at 338°C) leads to higher stress corrosion crack growth rates. Insufficient data are available at present to adequately quantify the magnitude of the hydrogen effect on Alloy 82. For this reason, the hydrogen effect has not been factored into the empirical SCCGR models discussed in the previous section.

SUMMARY

- CSLCT (ring-loaded) specimens can generate efficient, viable SCCGR data.
- The evolution of crack shape with time is quantitatively well-described by the RATIO ($\equiv \Delta a_{MAX}/\Delta a_{AVE}$).
- SCCGR data can be reasonably reported using $SCCGR_{AVE}$ plus the RATIO.
- LM data for Alloys 182 and 82 are generally consistent with $SCCGR_{AVE}$ data from other researchers.
- Three empirical model forms were evaluated – all model forms seem reasonable, though data scatter leads to an appreciable standard deviation for all three forms.
- Aqueous H_2 level influences SCCGR – more quantification of this effect is desirable.

ACKNOWLEDGEMENTS

Development of the CSLCT specimens was due in large part to the work of Norm Perazzo, Kerry Cotterell, and Bruce Furbeck. Some of the SCCGR testing was conducted by John Schisano, Maureen Schurman, and Brian Gain. Thanks to Bill Mills of Bechtel for providing input to this work. Additionally, the decision to report data as $SCCGR_{AVE}$ rather than $SCCGR_{MAX}$ was developed in part as a result of discussions with our colleagues at Bechtel including Bill Moshier, Doug Symons, and Mac Hall. The authors would like to thank John Hickling of EPRI and Glenn White of Dominion Engineering for providing technical information.

REFERENCES

[1] S Le Hong, JM Boursier, C Amzallag, and J Daret, from *Proceedings of the Tenth International Conference on the Environmental Degradation of Materials in Nuclear Power Systems – Water Reactors*, Lake Tahoe, NV, August 2001.

[2] WH Bamford, J Foster, KR Hsu, L Tunon-Sanjur and A McIlree, from *Proceedings of the Tenth International Conference on the Environmental Degradation of Materials in Nuclear Power Systems – Water Reactors*, Lake Tahoe, NV, August 2001.

[3] Nuclear Regulatory Commission website, *http://www.nrc.gov/NRC/REACTOR/SUMMER/index.htm*

[4] A Jenssen, K Norrgard, J Lagerstrom, G Embring, and DR Tice, from *Proceedings of the Tenth International Conference on the Environmental Degradation of Materials in Nuclear Power Systems – Water Reactors*, Lake Tahoe, NV, August 2001.

[5] G White, *Materials Reliability Program (MRP) Crack Growth Rates for Evaluating Primary Water Stress Corrosion Cracking (PWSCC) of Thick-Wall Alloy 600 Materials (MRP-55) Revision 1*, EPRI, Palo Alto, CA: 2002. 1006695.

[6] WH Bamford, JP Foster, and RS Pathania, *Proceedings of the Ninth International Symposium on the Environmental Degradation of Materials in Nuclear Power Systems – Water Reactors*, Newport Beach, August 2001, p. 279.

[7] R Lindstrom, P Lidar, and J Lagerstrom, *Proceedings of the Eighth International Symposium on the Environmental Degradation of Materials in Nuclear Power Systems – Water Reactors*, Amelia Island, August 1997, p. 422.

[8] WJ Mills and CM Brown, Bechtel report B-T-3435, March 2002.

[9] WJ Mills and CM Brown, *Proceedings of the Eleventh International Symposium on the Environmental Degradation of Materials in Nuclear Power Systems – Water Reactors,* Stevenson Washington, September 2003.

[10] W Bamford and J Foster, *Crack Growth of Alloy 182 Weld Metal in PWR Environments (PWRMRP-21)*, EPRI, Palo Alto, CA: 2000. 000000000001000037.

[11] PM Scott, Presented at *NEA/CSNI Specialist Meeting on Operating Experience with Steam Generators*, Brussels, Belgium, September 16-20, 1991.

[12] WC Moshier and CM Brown, CORROSION/99, Paper No. 449, 1999.

[13] Y Shen and PG Shewmon, *Corrosion*, 47 (1991), p. 712.

[14] MM Hall and DM Symons, from *Chemistry and Electrochemistry of Corrosion and Stress Corrosion Cracking: A Symposium Honoring the Contributions of RW Staehle*, The Materials Society (TMS), New Orleans, February 11-15, 2001.

[15] T Cassagne, B Fleury, F Vaillant, O de Bouvier, P Combrade, *Proceedings of the Eighth International Symposium on Environmental Degradation of Materials in Nuclear Power Systems*, p. 307, 1997.

[16] G Economy, RJ Jacko and FW Pement, *Corrosion*, 43, No. 12, p. 727, 1987.

[17] DS Morton, SA Attanasio, JS Fish and MK Schurman, CORROSION/99 Paper No. 447, April 1999.

[18] DS Morton, SA Attanasio, GA Young, and MA Ando, *Proceedings of the Tenth International Symposium on Environmental Degradation of Materials in Nuclear Power Systems-Water Reactors,* Lake Tahoe, 2001.

[19] JM Boursier, O de Bouvier, JM Gras, D Noel, R Rios and F Vaillant, *Proceedings of the Conference*

on Corrosion Deformation Interactions, p. 117, Les editions de Physique, Paris, France (1992).

[20] DS Morton, SA Attanasio, GA Young, PL Andresen, TM Angeliu, CORROSION/01, Paper No. 117, 2001.

[21] RS Pathania, AR McIlree, *Proceedings of the Third International Symposium on Environmental Degradation of Materials in Nuclear Power Systems-Water Reactors*, p.551, 1987.

[22] T Magnin, JM Boursier, D Noel, F Valliant, *Proceedings of the Sixth International Symposium on Environmental Degradation of Materials in Nuclear Power Systems-Water Reactors*, p.669, 1993.

[23] T Cassagne, A Gelpi, *Proceedings of the Sixth International Symposium on Environmental Degradation of Materials in Nuclear Power Systems-Water Reactors*, p.679, 1993.

[24] N Totsuka, Y Nishikawa, and N Nakajima, CORROSION/2002, Paper 523, 2002.

[25] N Totsuka, E Lunarska, G Cragnolino and Z Szklarska-Smialowska, *Corrosion*, 53, 505 (1997).

[26] PM Scott, "Predictions of Alloy 600 Component Failures in PWR Systems", Proceedings of a Research Topical Symposium at CORROSION/96, p. 135.

[27] SA Attanasio, DS Morton, MA Ando, NF Panayotou and CD Thompson, from *Proceedings of the Tenth International Symposium on Environmental Degradation of Materials in Nuclear Power Systems-Water Reactors,* Lake Tahoe, 2001.

[28] N Lewis, WJS Yang, JS Fish, DJ Perry, C.D. Thompson, *Proceedings of the Eighth International Symposium on Environmental Degradation of Materials in Nuclear Power Systems-Water Reactors*, p.266, 1997.

[29] SA Attanasio, DS Morton, and MA Ando, CORROSION/2002, Paper No. 517, 2002.

Table 1. Alloy Compositions in weight percent.

Heat	Ni	Cr	Fe	C	Mn	Cu	Si	Co	S	P	Ti	Nb +Ta
LM182-1	Bal	15.0	7.2	0.03	5.9	0.00	0.7	0.03	0.005	N/A	0.5	2.0
LM182-2	68.7	15.1	7.0	0.02	6.0	0.00	0.8	0.03	0.005	0.01	0.5	1.9
LM82-1	73.4	17.5	1.7	0.047	3.14	0.05	0.26	0.04	0.005	N/A	0.17	3.64
LM82-2	73.5	19.0	1.46	0.045	2.80	0.05	0.12	0.04	0.001	0.013	0.30	2.32
LM82-3	71.5	20.6	1.27	0.045	2.81	0.31	0.14	0.04	0.002	0.012	0.35	2.44

Table 2. Room Temperature Yield Strengths (YS), in MPa.

Heat	LM182-1	LM182-2a	LM182-2b	LM82-1	LM82-2	LM82-3
YS	503	454	530	439	465	460

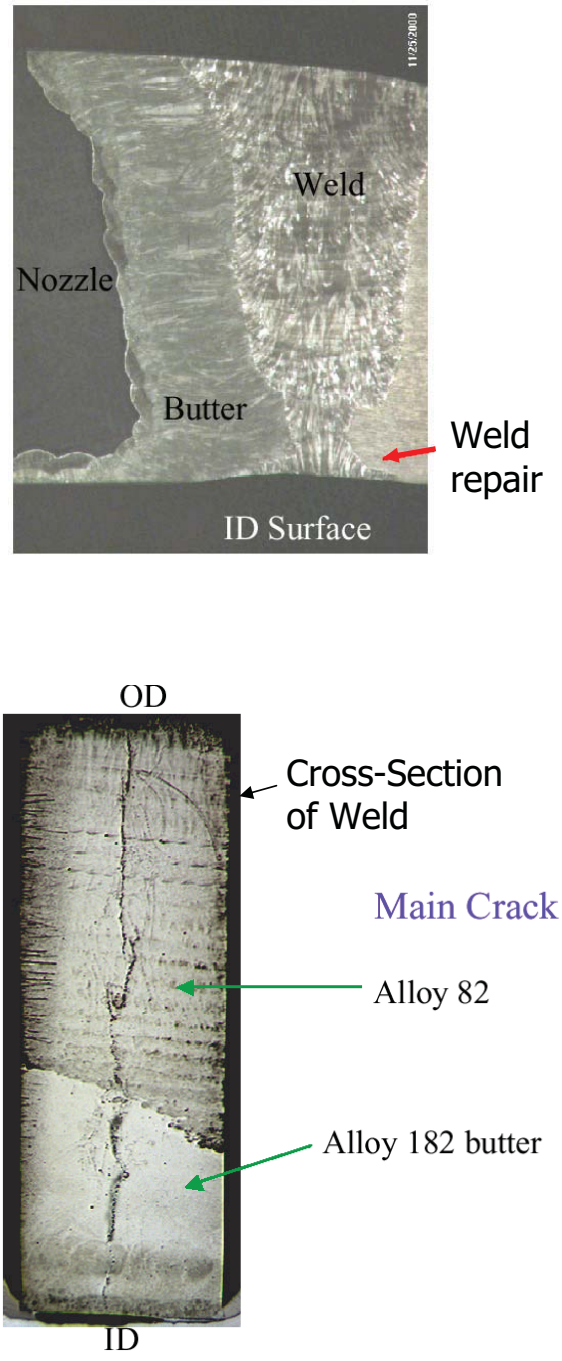

Figure 1. Photographs from the VC Summer hot leg, showing that both Alloys 182 and 82 are susceptible to primary water stress corrosion cracking (source: *http://www.nrc.gov/NRC/REACTOR/SUMMER/index.htm)*.

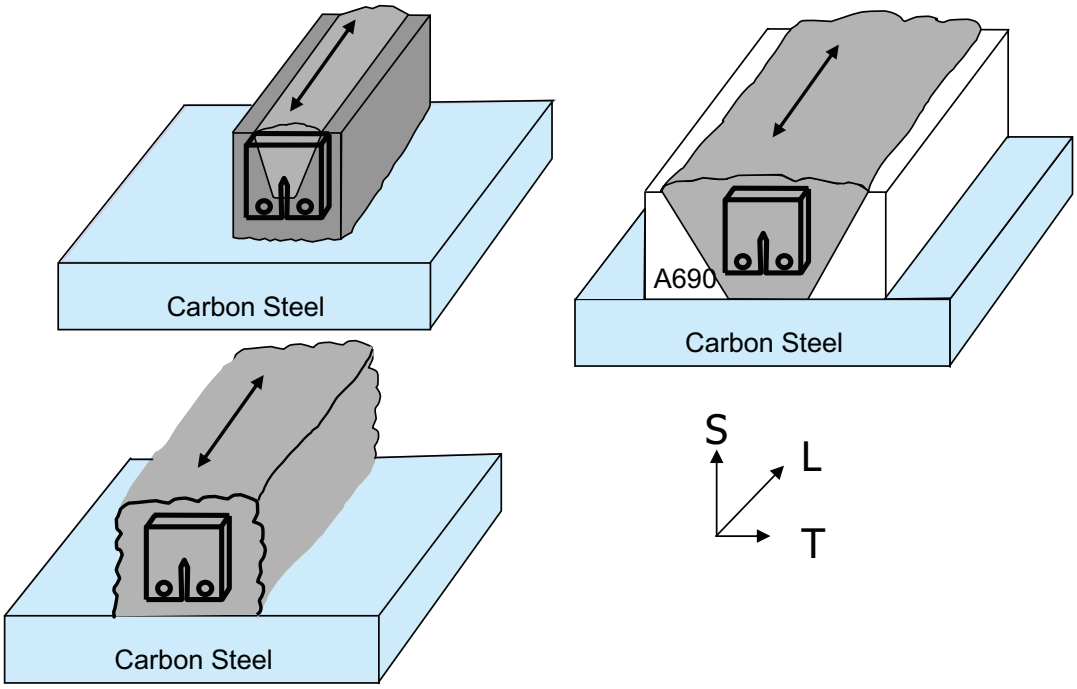

Figure 2. Specimen fabrication methods. Cracks grow from root-to-crown, in the T-S orientation. The arrows denote the welding direction. For the method in the upper left corner, the darker gray weld metal represents Alloy 82 weld buildup, which was subsequently machined to form a groove. Alloy 182 weld metal was then deposited (lighter gray). The end of the notch and the precrack were located in the Alloy 182 material. A similar specimen fabrication method has also been used by Studsvik [7].

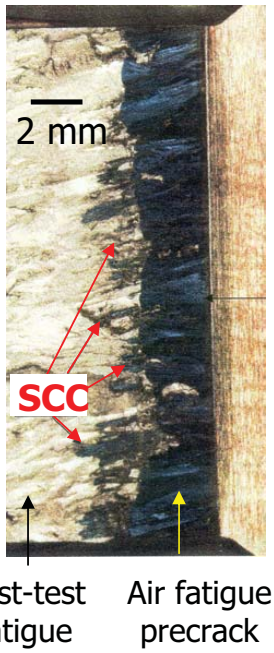

Figure 3. A specimen showing the air fatigue precrack, SCC, and post-test fatigue regions.

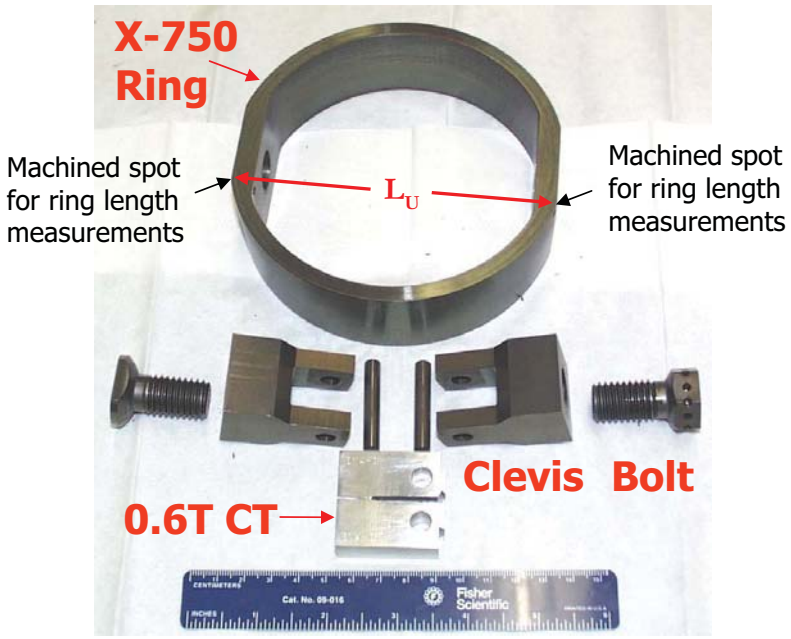

(a)

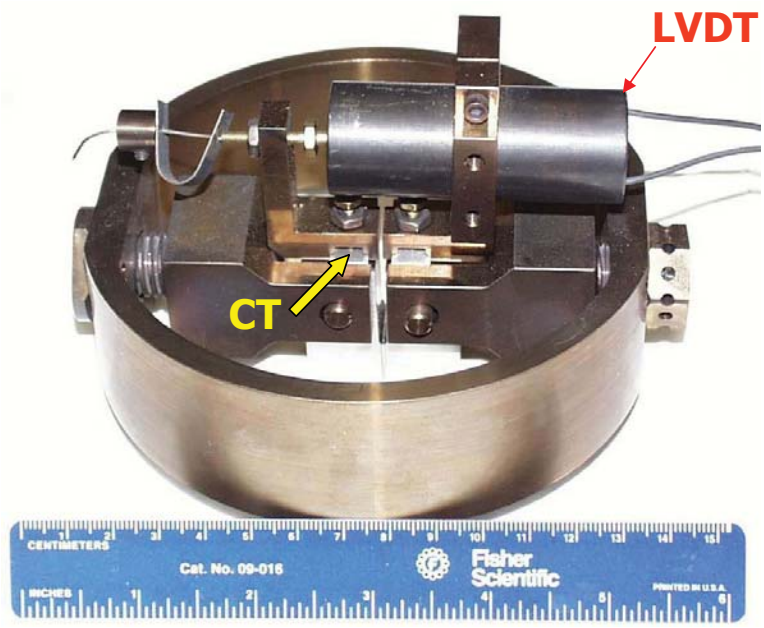

(b)

Figure 4. Compliant self-loaded compact tension (CSLCT) specimen hardware (a) and assembly (b). The unloaded length of the ring (L_U) is shown in (a).

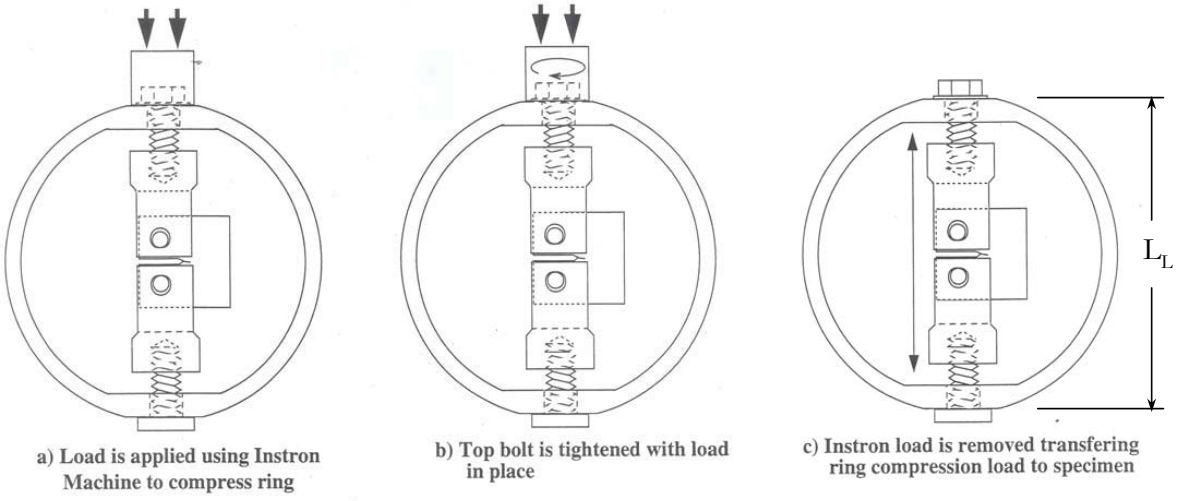

Figure 5. Illustration of CSLCT loading method. The actual load on the specimen is quantified by using the independently-measured spring constant of the ring, plus the change in length of the ring (*i.e.*, $\Delta L = L_U - L_L$). L_U is the 'unloaded' length prior to applying the acutator load, as shown in Figure 4 (a), and L_L is the length after loading.

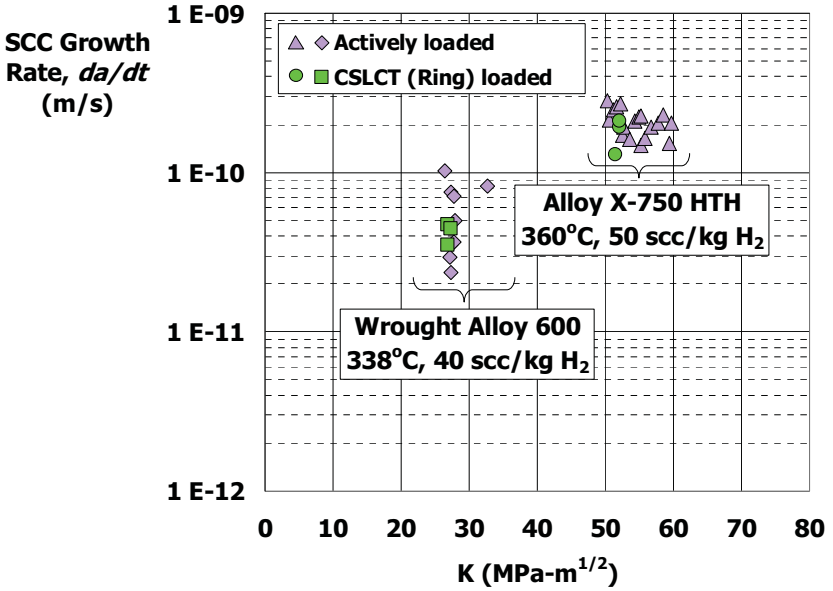

Figure 6. CSLCT specimen qualification test results. The Alloy 600 tests were conducted using 0.6T CT specimens. The tests conducted on Alloy X-750, which has a much greater yield strength than the Alloy 600, utilized 0.4T CT specimens

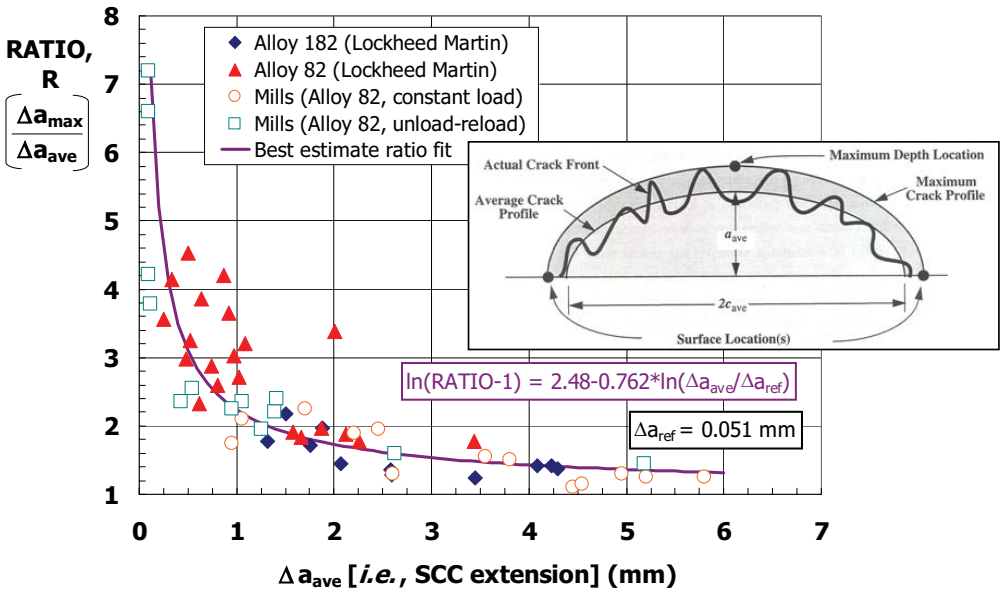

Figure 7. Quantification of the RATIO ($\equiv \Delta a_{max}/\Delta a_{ave}$) as a function of crack depth, based on data from [8] and the present work.

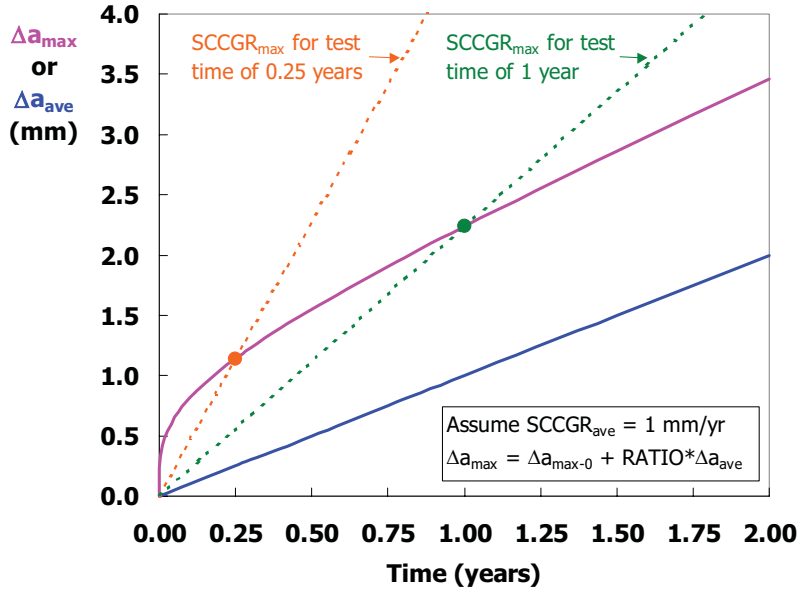

Figure 8. Schematic illustration of the effect of test time on the apparent maximum SCCGR. The Δa_{max} curve (magenta) was obtained by integrating the RATIO data in Figure 7, and by assuming an $SCCGR_{ave}$ of 1 mm/yr.

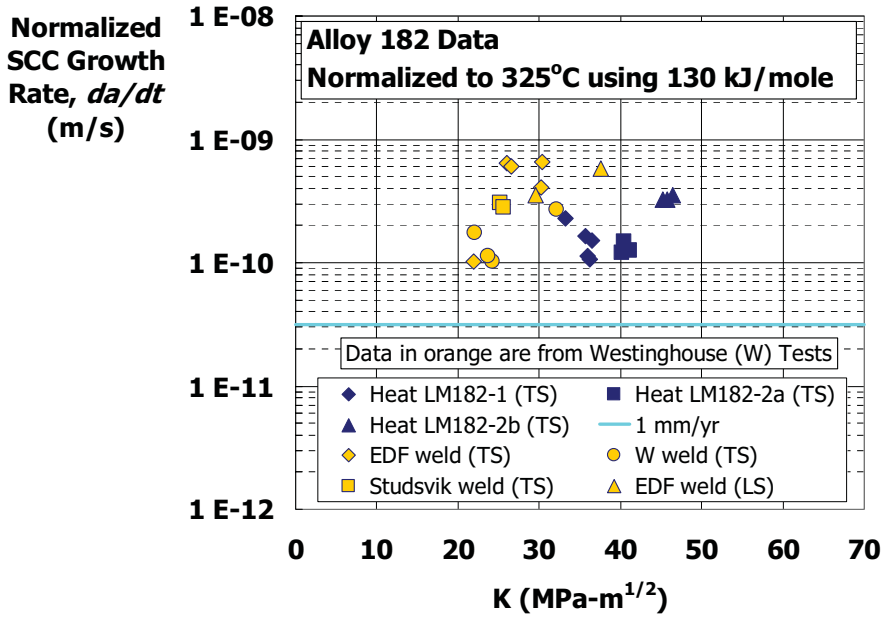

Figure 9. Alloy 182 data from the present study and from a Westinghouse study [10] utilizing welds from several laboratories.

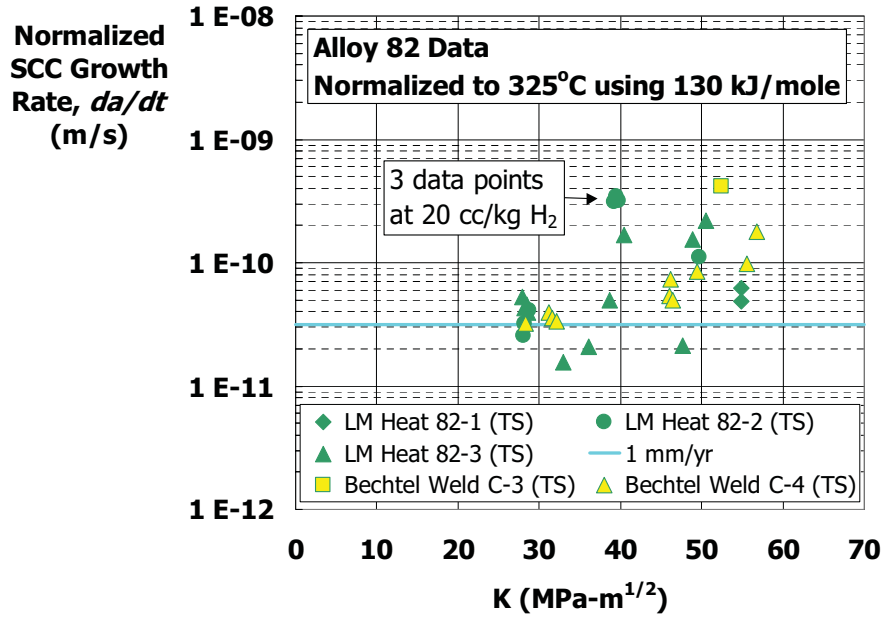

Figure 10. Alloy 82 data from the present study and from a Bechtel study [8].

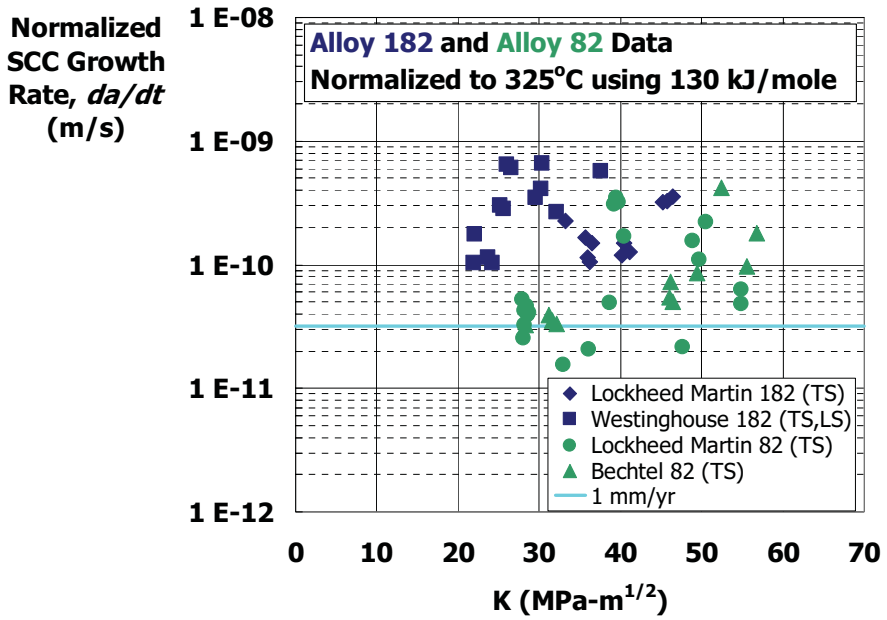

Figure 11. Compilation of Alloy 182 and Alloy 82 data in the combined data set (Lockheed Martin, Westinghouse, and Bechtel).

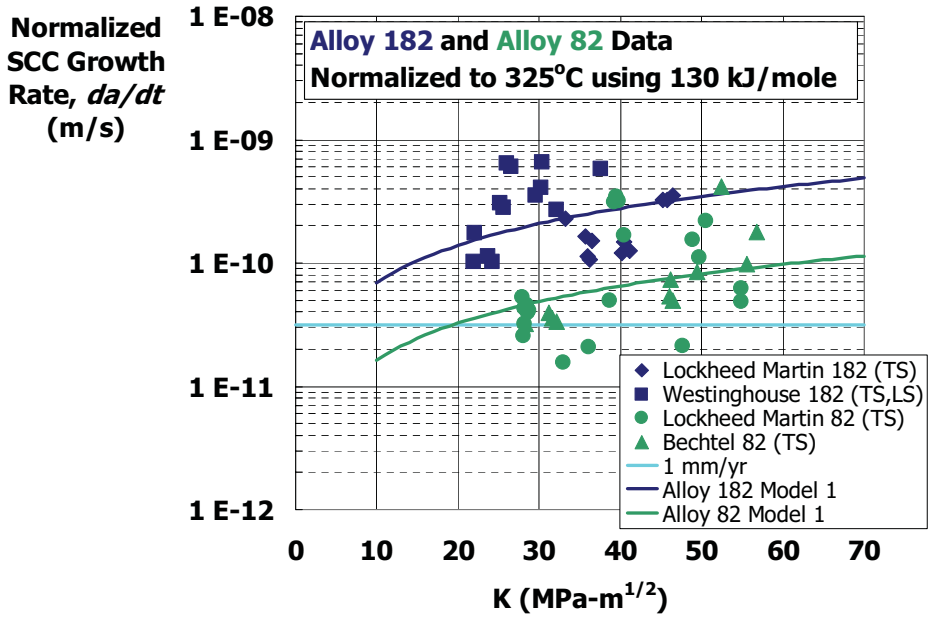

Figure 12. Fit of the SCCGR data to Model 1. This model does not employ a threshold, and the K_I dependency is not fixed.

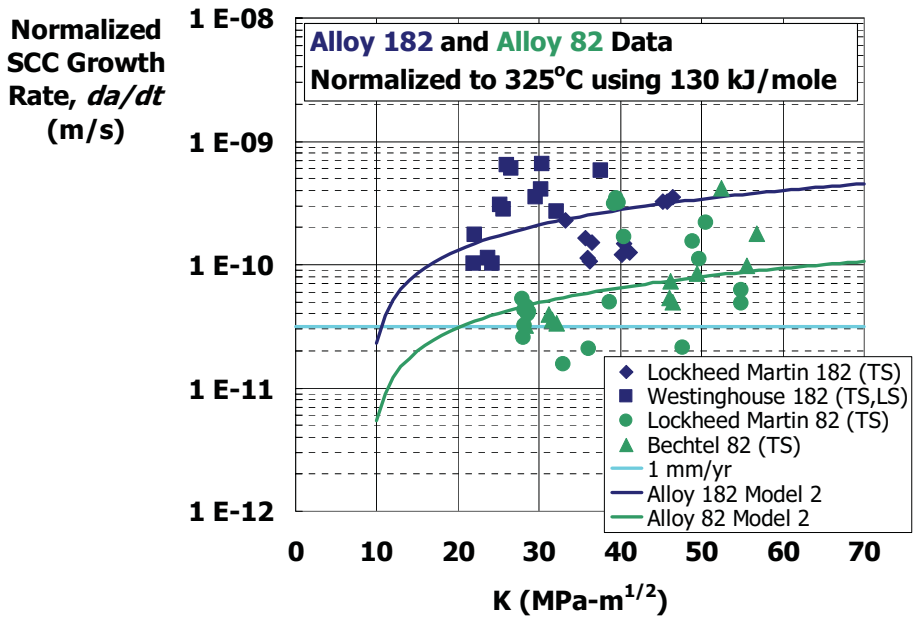

Figure 13. Fit of the SCCGR data to Model 2. This model employs a threshold of 9 MPa√m, and the K_I dependency is not fixed.

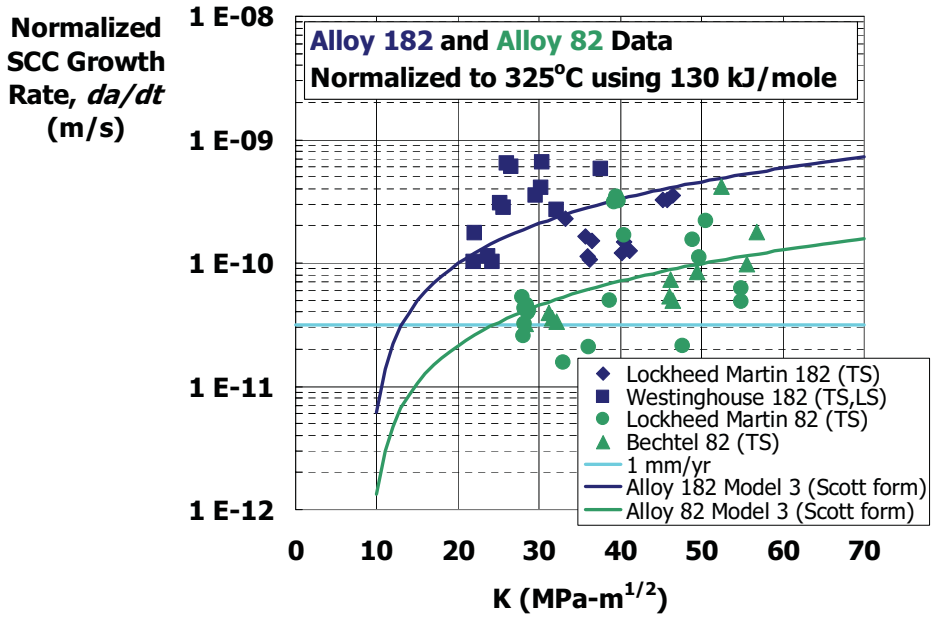

Figure 14. Data fit to Model 3 (Scott form). This model employs a threshold of 9 MPa√m, and the K_I dependency is fixed at 1.16.

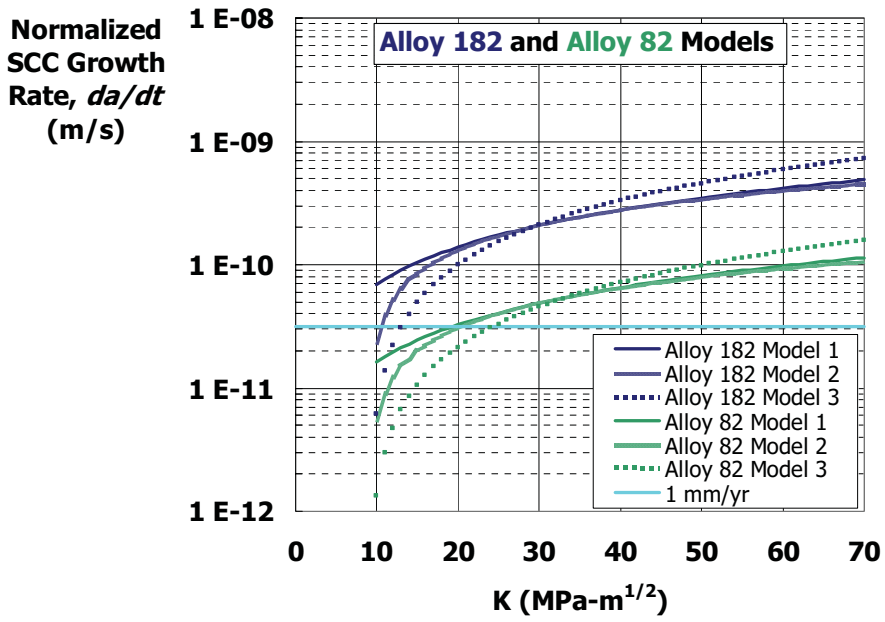

Figure 15. Comparison of Model forms 1, 2, and 3.

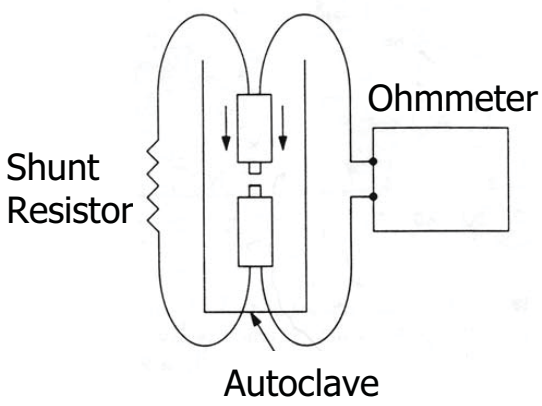

Figure 16. Schematic illustration of the contact electric resistance (CER) setup used to measure the Ni/NiO phase transition in [27].

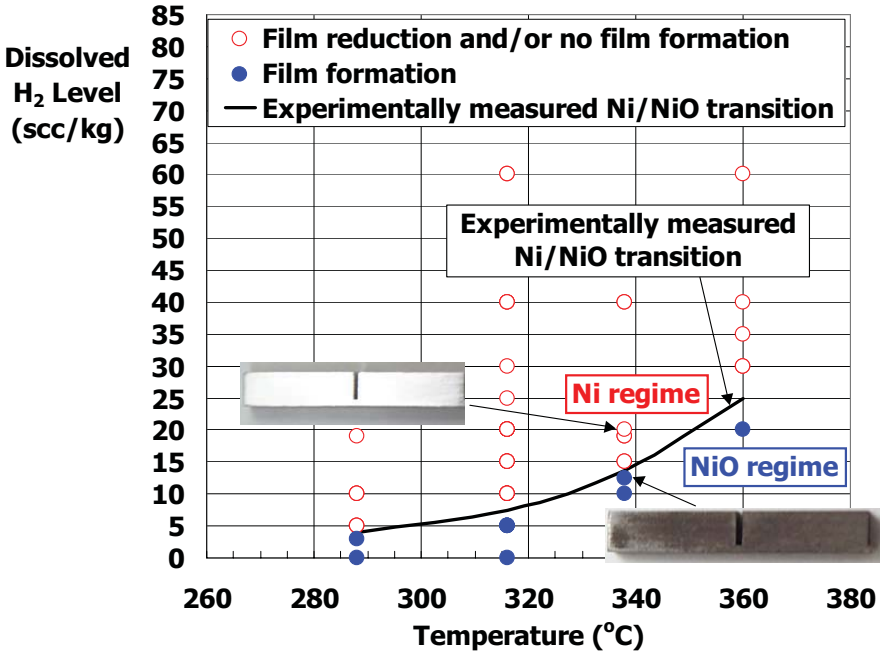

Figure 17. Summary plot of contact electric resistance (CER) and corrosion coupon data [27].

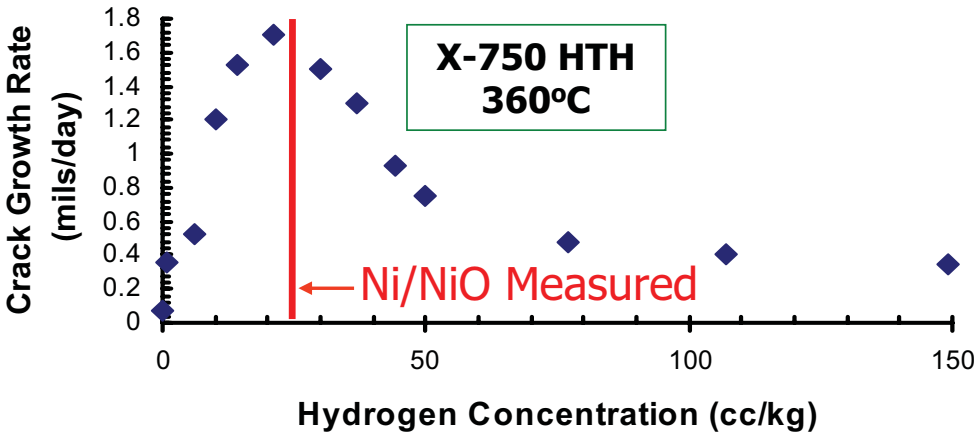

Figure 18. Dissolved hydrogen crack growth rate functionality at 360°C for Alloy X-750 in the HTH heat treatment [18].

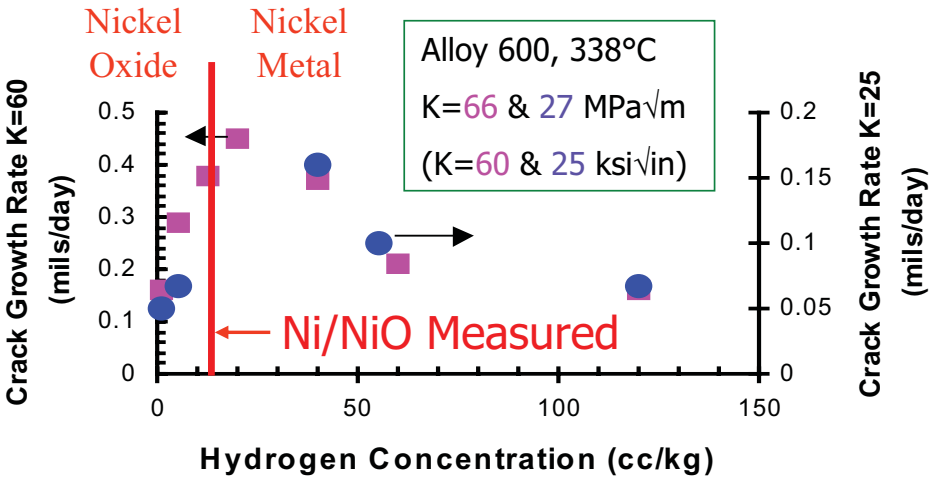

(a)

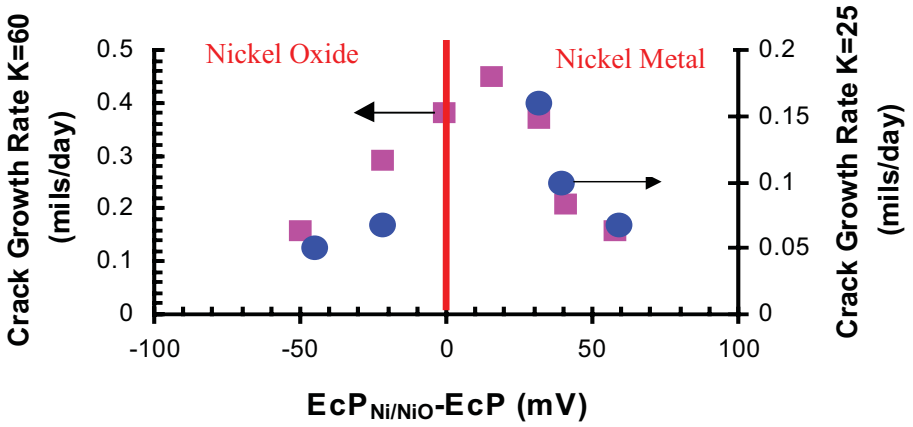

(b)

Figure 19. Alloy 600 dissolved hydrogen crack growth rate functionality at 338°C [18]. A value of 13.8 scc/kg H_2 was used as the hydrogen concentration of the Ni/NiO phase transition at 338°C, as shown in Figure 17. Details for calculating the correlating parameter $EcP_{Ni/NiO}$ – EcP are provided in References [17] and [29].

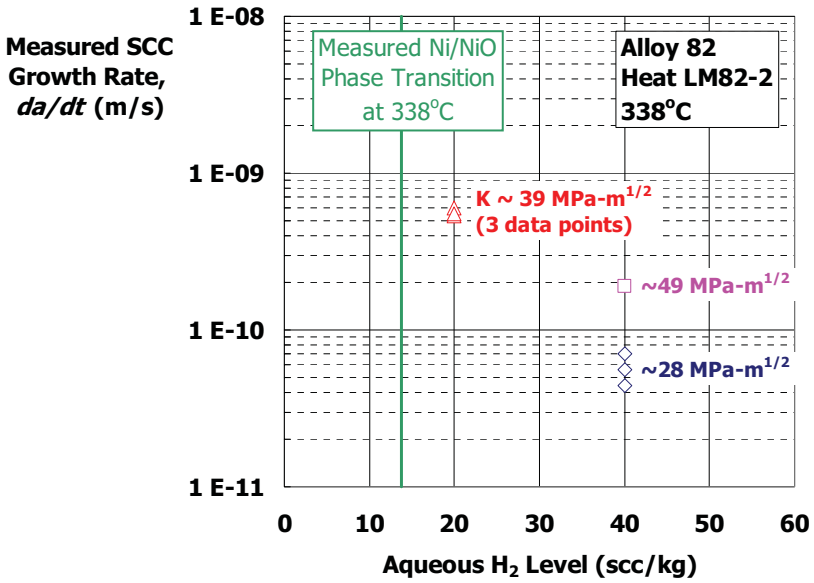

Figure 20. Effect of dissolved hydrogen on SCCGR of Alloy 82 (heat LM82-2) at 338°C. Note that the SCCGRs were not normalized to 325°C.

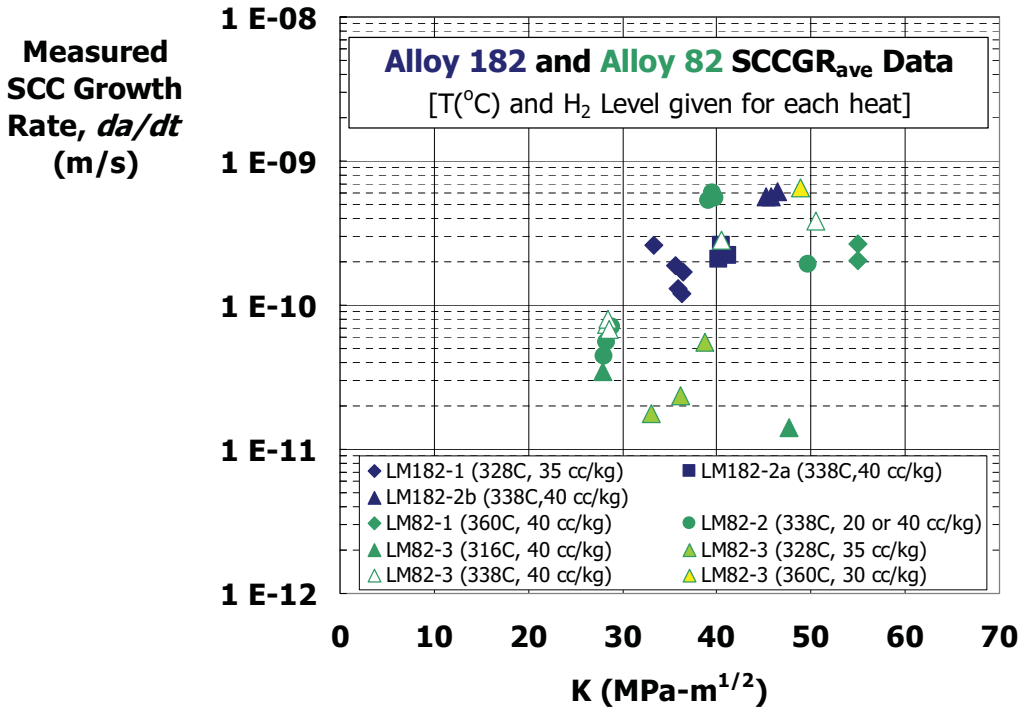

Figure A1. Measured (non-normalized) $SCCGR_{AVE}$ for each of the data points reported in this study. The figure also gives the test temperature and aqueous hydrogen level for each heat tested. All data are in the TS orientation. Stress intensity factor (K) is reported as the average K value during the test.

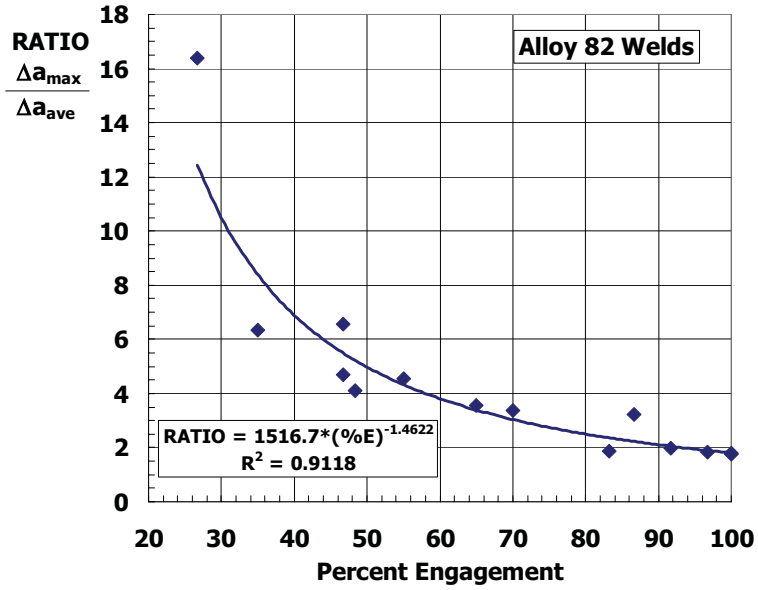

Figure A2. Correlation of maximum-to-average SCC extent ratio with percent engagement (%E). This correlation shows that, consistent with expectations, cracks with high ratios tend to have relatively low engagement. This plot can be used along with Figure 7 to infer the percent engagement for a specimen even if only Δa_{max} is known. This procedure may be of value in screening historical data for which percent engagement is not available.

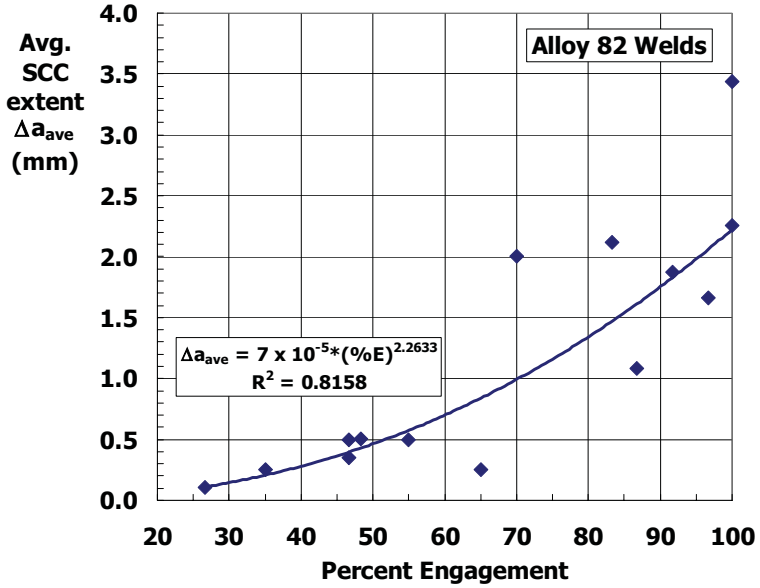

Figure A3. Correlation of average SCC extent (*i.e.*, Δa_{ave}) with percent engagement (%E). This correlation shows that, as expected, cracks with a larger depth of SCC also tend to be closer to full engagement across the precrack. This correlation may also be useful in certain cases for analyzing historical data for which %E is not available.

Influence of Temperature on Primary Water Stress Corrosion Cracking of Alloy 600 Weld Metals

Yoshito Nishikawa, Nobuo Totsuka and Koji Arioka
Institute of Nuclear Safety System, Inc.
64 Sata, Mihama-cho, Mikata-gun, Fukui 919-1205 Japan

ABSTRACT

Influence of temperature on primary water stress corrosion cracking (PWSCC) of Alloy 600 weld metals was studied at temperatures ranging from 330 to 360 °C using slow strain rate technique (SSRT). As the results, it has been revealed that the apparent activation energy of weld metal is about 30 kJ/mol higher than that of heat affected zone, and the PWSCC susceptibility of Alloy 82 is close to that of Alloy 132. It can be thought that the former fact is a reason for that the weld metal suffers PWSCC less frequently than the base metal of 600 alloys in actual PWR plants, though the weld metal suffers PWSCC more frequently in the laboratory conditions at higher temperature.

Key Words: Alloy 600, Alloy 82, Alloy 132, stress corrosion cracking, primary water, SCC, PWSCC, gas tungsten arc welding, shielded metal arc welding, activation energy, SSRT

INTRODUCTION

It is widely known that mill-annealed, nickel-base Alloy 600 is susceptible to stress corrosion cracking in primary cooling water of pressurized water reactors (PWRs) since the studies conducted by Coriou et al.[1,2]. This problem requires consideration in connection with the aging of PWRs[3]. It has been reported recently that primary water stress corrosion cracking (PWSCC) were found in Alloy 182 in PWR nuclear power plants. However, data from the tests conducted on Alloys 82 and 132 are limited.[4] The purpose of this study is to verify the difference of susceptibility between weld metal and heat affected zone (HAZ) of Alloys 82 and 132 on PWSCC behavior using the slow strain rate technique (SSRT) tests.

EXPERIMENTAL PROCEDURE

Material

The specimens used in this test were cut from welded portion on single V groove of mill-annealed Alloy 600 plate as shown in Figure 1. The welding direction is perpendicular to the longitudinal direction of specimen. Alloys 82 and 132 were welded by tungsten inert gas welding and shielded metal arc welding, respectively. The chemical compositions, mechanical properties, weld pass schedule and heat input were as shown in Table 1.

Stress Corrosion Cracking Tests

Stress corrosion cracking tests were conducted by using accelerated SSRT tests[5]. In this method, the central, gauge section of the flat specimen was pressed with a die as shown in Figure 2. This enables PWSCC to develop at a crack growth rate dozens of times higher than that used in the test by the conventional SSRT. As shown in Figure 3 using hump specimen on the weld metal or the HAZ, PWSCC can be initiated at the limited portion with humped specimen, weld metal and HAZ. A schematic diagram of the test system is shown in Figure 4. The water used for the test was simulated primary water used in PWRs (500 ppm B + 2 ppm Li + 2.75ppm H_2), which was the same water reported before[6]. The test was conducted at four levels of temperature: 360 °C, 350 °C, 340 °C and 330 °C. The strain rate in the SSRT test was 5×10^{-7} s^{-1}, assuming 20 mm of gauge length without hump.

TEST RESULTS

The results presented in this study were limited to specimens that had an IGSCC% (Area of intergranular or inter-dendrite fracture / Total area of fracture surface) greater than 5 %. IGSCC% of specimens with less than 5 % had relatively large scatter to evaluate the susceptibility, especially to calculate an activation energy. Figures 5 and 6 show SEM microphotographs of the fractured surface of weld metal after SSRT test at 360 °C. Figures 7 through 9 show ones of HAZ and base metal also. In these tests, intergranular cracks originated and propagated from only the concave side (the bottom in the photo), which was exposed to residual tensile stress due to the cold pressing before the test. The crack propagation rate was obtained by the following equation:

Crack growth rate = Plate Thickness × IGSCC% / Time to fracture

Figures 10 through 13 show the relationship between the temperature and the PWSCC growth rate of weld metal and HAZ in SSRT test. The lines are the approximated curves calculated by least-squares method. And each thin line shows the approximated curve of Alloy 600 base metal. As shown in these figures, the higher the temperature, the higher the crack growth rate. From the temperature dependency of crack growth rate, the apparent activation energy for PWSCC was calculated.[6] The apparent activation energies for PWSCC on Alloy 82 weld metal, Alloy 132 weld metal and HAZs welded by Alloys 82 and 132 are 188 kJ/mol (45 kcal/mol), 179 kJ/mol (43 kcal/mol), 156 kJ/mol (37 kcal/mol) and 148 kJ/mol (35 kcal/mol), respectively. And the one of Alloy 600 base metal is 167 kJ/mol (40 kcal/mol). According to these results, the apparent activation energy for PWSCC of HAZ is lower than that of weld metal regardless of materials and the difference between activation energy of Alloys 82 and 132 is small. And each standard deviations, which are calculated as index numbers of standard deviations of logarithms of deviance of each data from the approximated curves, are 1.43, 1.38, 1.37 and 1.33, respectively. And the one of Alloy 600 base metal is 1.20. These numbers are less than the standard deviation of all data, 1.44.

DISCUSSION

Though there are small differences between activation energies, some trends are recognized. As shown in Figures 10 and 11, the apparent activation energies of weld metals are slightly

higher than those of HAZs. SSRT test is assumed to be affected by both initiation and propagation behavior, but the result of this SSRT test may depend more on initiation. The high activation energy of weld metal indicates crack initiation at lower temperature is difficult. Considering all these results, the initiation stage is more important than propagation stage for evaluating the PWSCC susceptibility of materials.

As shown in Figure 12, the susceptibilities and the apparent activation energies of Alloys 82 and 132 are similar. However the susceptibility of Alloy 82 weld metal is slightly higher than that of Alloy 132 and the apparent activation energy of Alloy 82 is lower in detail. According to this result, it seems that Alloy 82 weld metal would be slightly more susceptible than that of Alloy 132 at lower temperature. On the other hand, in resent studies, the result of reverse U-bends and constant load tests showed that time to cracking in Alloy 82 was 4 to 10 times higher than that in Alloy 182.[4] There are some differences between materials Alloys 82 and 132 on this study and the Alloy 182 used in previous studies with respect to chemical composition, mechanical properties, weld method and weld heat. It is the subject for a future study to determine how these factors affect the PWSCC behavior of Alloys 82, 132 and 182. More studies, which can reveal the difference in PWSCC initiation such as constant load test, are needed.

As shown in Figure 13, the susceptibilities and activation energies of HAZs welded by Alloys 82 and 132 are similar in spite of the difference of welding pass schedule, weld method and grain size. It seems that PWSCC behavior of HAZ depends on the base metal more than welding condition.

CONCLUSIONS

(1) The susceptibilities and the apparent activation energies of Alloys 82 and 132 are almost same.
(2) Weld metal has about 30 kJ/mol higher activation energy than that of HAZ. Therefore, weld metal may be more resistant to crack initiation at lower temperature than the HAZ.
(3) PWSCC behavior of HAZ are close to the base metal more than weld metal. They are similar in different welding conditions.

REFERENCES

1. H.Coriou, L.Grall, M.Pelras and S.Vettier, Third Metallurgy Conference on Corrosion, Saclay, (1959) North Holland Publishing Co., Amsterdam, p.161
2. P.E.MacDonald, V.N.Shah, L.W.Ward and P.G.Ellison, Steam Generator Tube Failures, NUREGICR-6365, INEL-95/0383 (1996)
3. Agency of Natural Resources and Energy, “Fundamental idea about increased aging” Issued in April, 1996
4. R.S.Pathania, A.R.Mcilree and J.Hickling, "Overview of Primary Water Cracking of Alloys 182/82 in PWRs", Fontevraud 5 International Symposium, France (2002)
5. N.Totsuka, E.Lunarska, G.Cragnolino and Z.S.Smialowska, Corrosion, Vol.43 (1987), p.505
6. N.Totsuka, S.Sakai, N.Nakajima and H. Mitsuda, CORROSION/2000, Paper No.212

TABLE 1

CHEMICAL COMPOSITION, MECHANICAL PROPERTIES,

NUMBER OF WELD PASS AND HEAT INPUT OF TEST MATERIALS

(wt%)

Material	C	Si	Mn	P	S	Ni	Cr	Fe	Cu	Nb
Alloy 82	0.017	0.26	2.54	0.006	0.001	72.9	17.95	3.72	0.01	1.93
Alloy 132	0.030	0.30	2.10	0.009	0.002	71.5	15.40	8.50	0.01	1.88
Base Metal*	0.030	0.27	0.29	0.010	0.001	72.9	16.20	-	0.05	-

* Ti is included 0.20% in base metal.

Material	Breakdown strength 0.2%	Tensile strength	Welding pass	Heat input
Alloy 82	306 MPa	625 MPa	4 times	10.1 kJ/cm
	266 MPa	589 MPa	4 times	14.9 kJ/cm
Alloy 132	229 MPa	563 MPa	2 times	10.1 kJ/cm
	200 MPa	534 MPa	2 times	14.9 kJ/cm

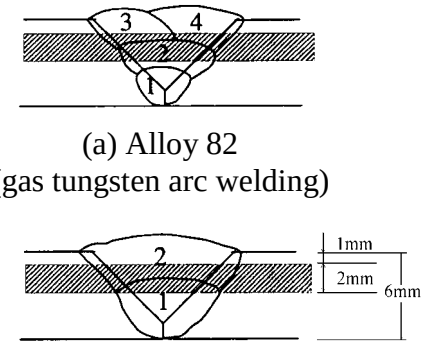

(a) Alloy 82
(gas tungsten arc welding)

(b) Alloy 132
(shielded metal arc welding)

FIGURE 1 - Welding Process and the Part of Specimens of welded metal

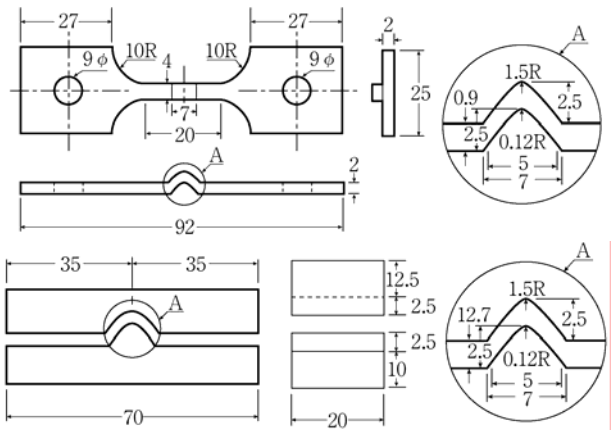

FIGURE 2 - Specimens Used in the Accelerated SSRT test Method

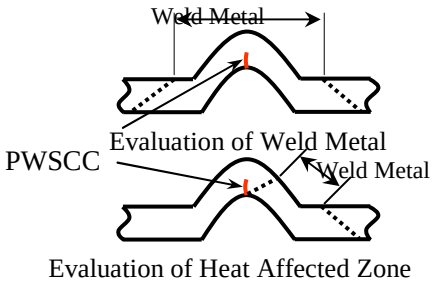

FIGURE 3 - Relationship between the Bending Position and the weld

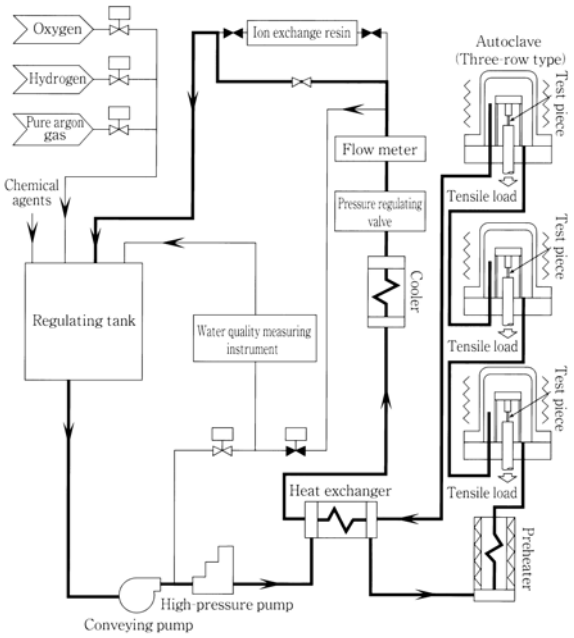

FIGURE 4 - Schematic diagram of SSRT testing machine

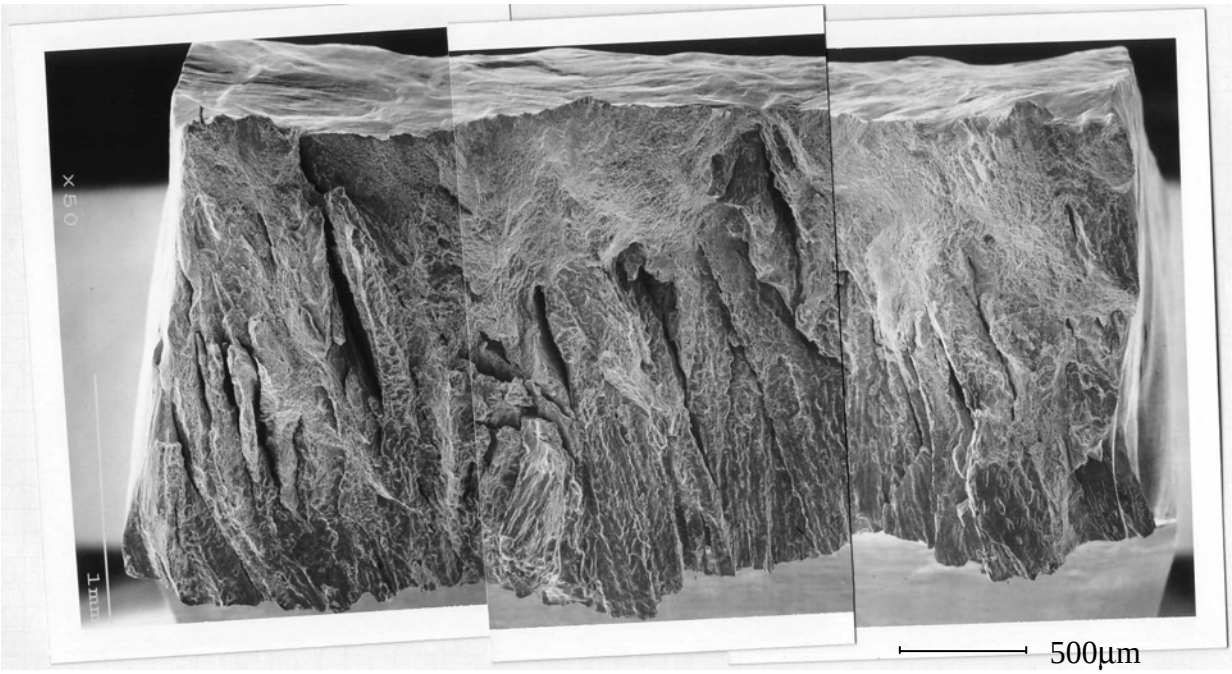

FIGURE 5 - SEM microphotograph of the fractured surface of Alloy 82 weld metal of the SSRT test specimen (Temp.: 360 °C)

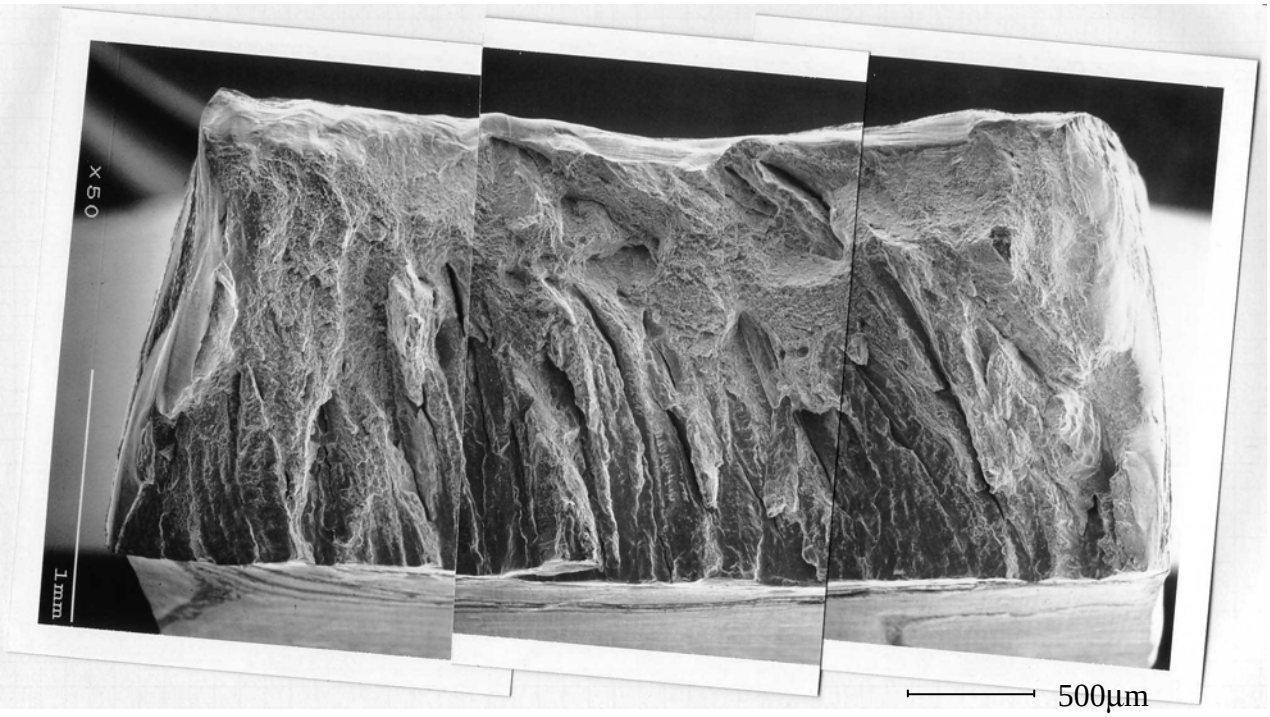

FIGURE 6 - SEM microphotograph of the fractured surface
of Alloy 132 weld metal of the SSRT test specimen (Temp.: 360 °C)

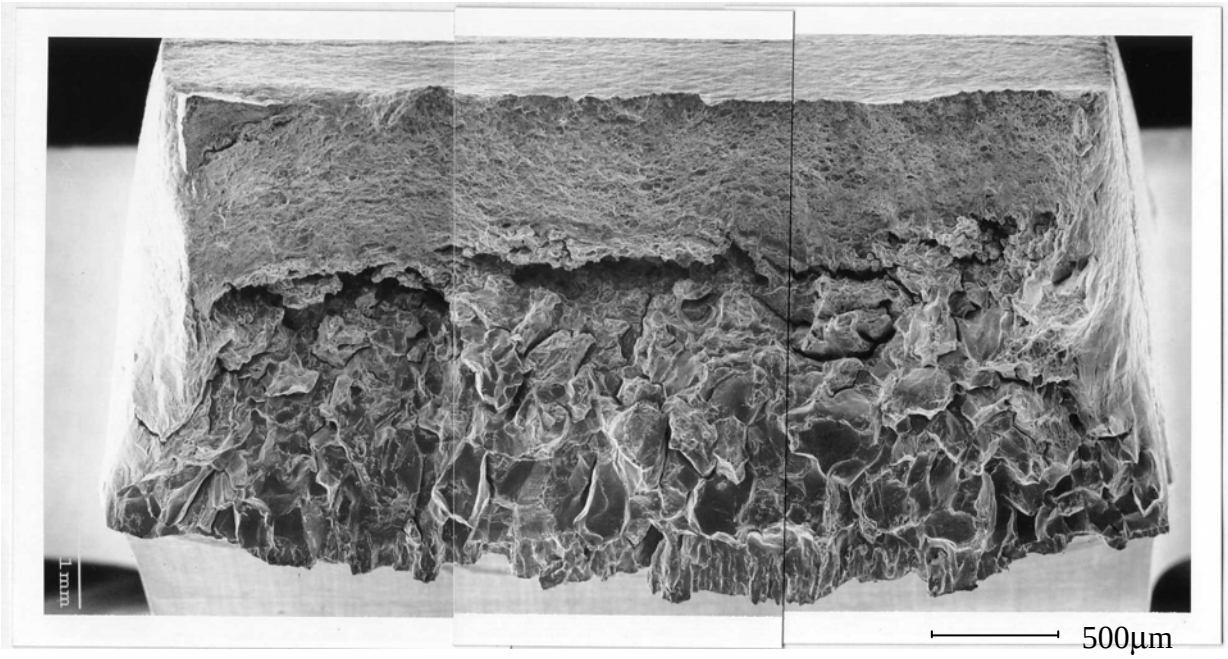

FIGURE 7 - SEM microphotograph of the fractured surface of HAZ
welded by Alloy 82 of the SSRT test specimen (Temp.: 360 °C)

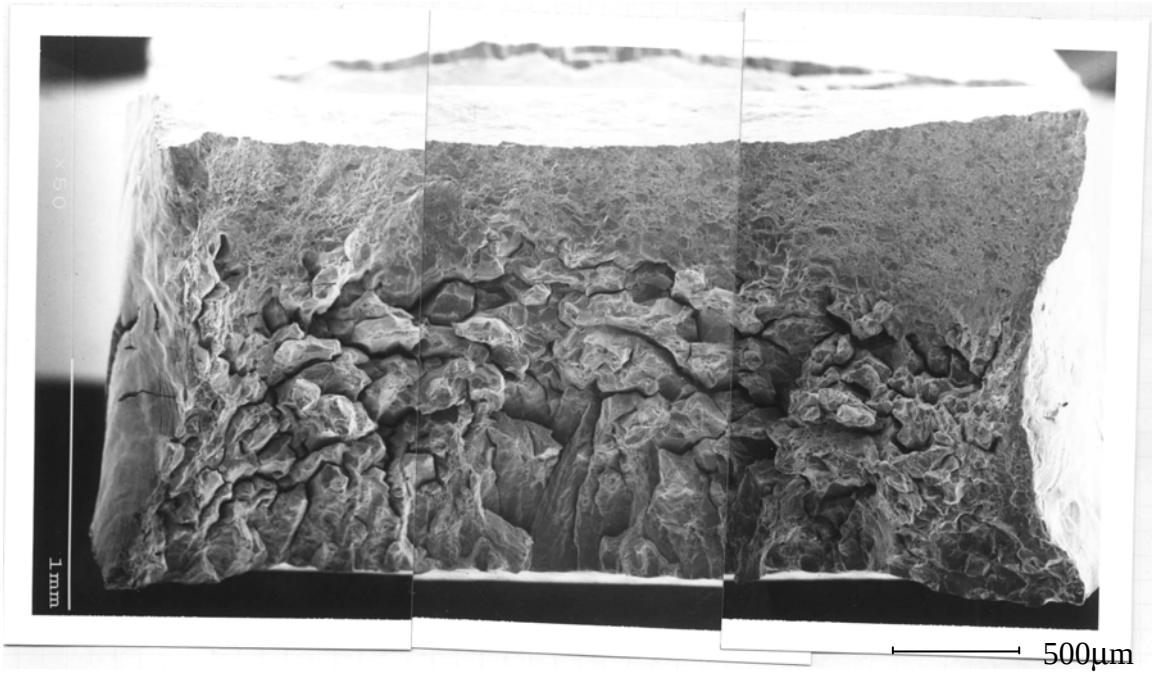

FIGURE 8 - SEM microphotograph of the fractured surface of HAZ welded by Alloy 132 of the SSRT test specimen (Temp.: 360 °C)

FIGURE 9 - SEM microphotograph of the fractured surface of Alloy 600 base metal of the SSRT test specimen (Temp.: 360 °C)

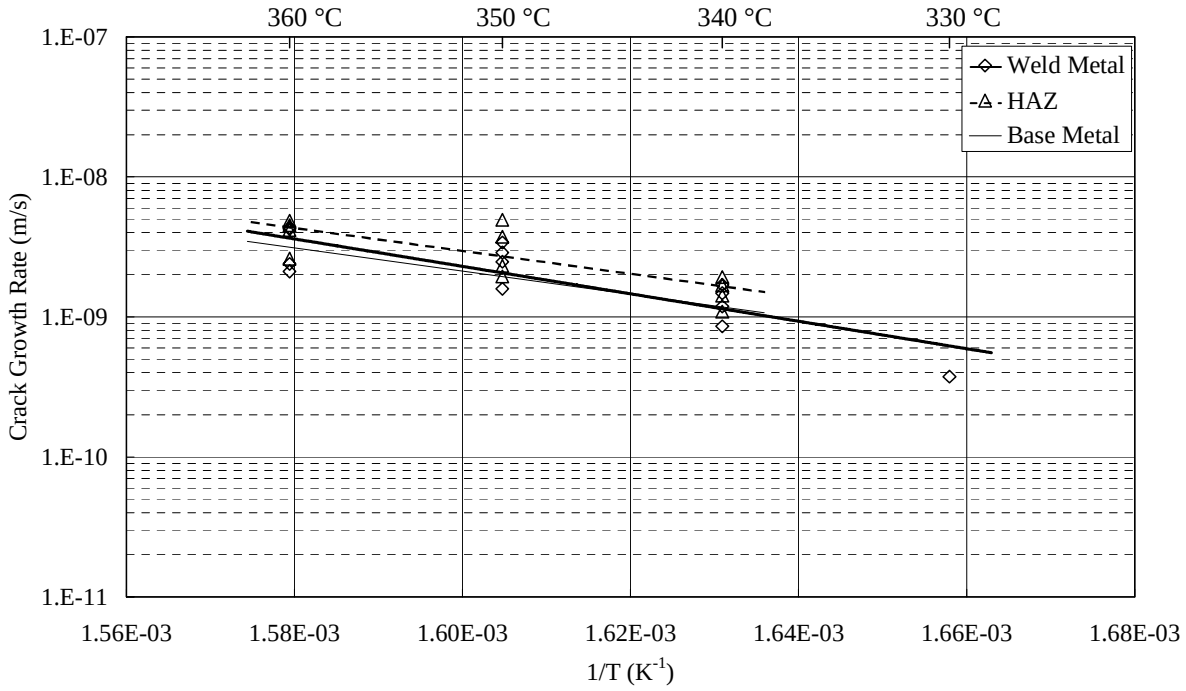

FIGURE 10 - Relationship between Temperature and Crack Growth Rate of Alloy 82 Weld Metal and HAZ in SSRT

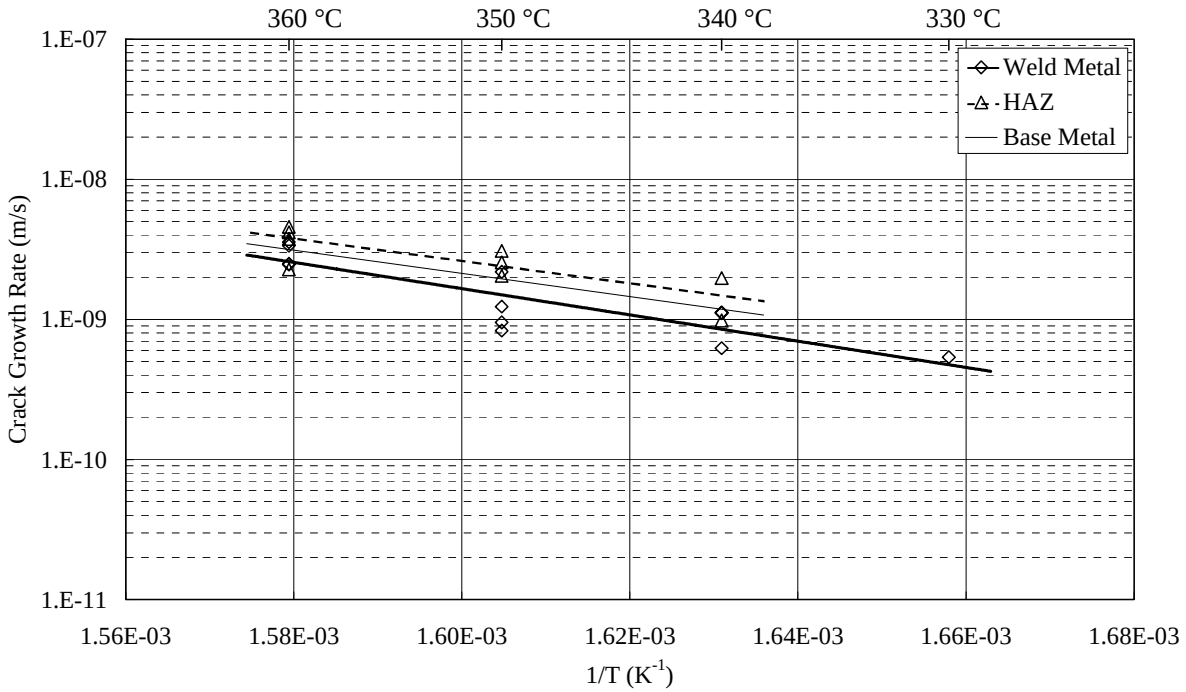

FIGURE 11 - Relationship between Temperature and Crack Growth Rate of Alloy 132 Weld Metal and HAZ in SSRT

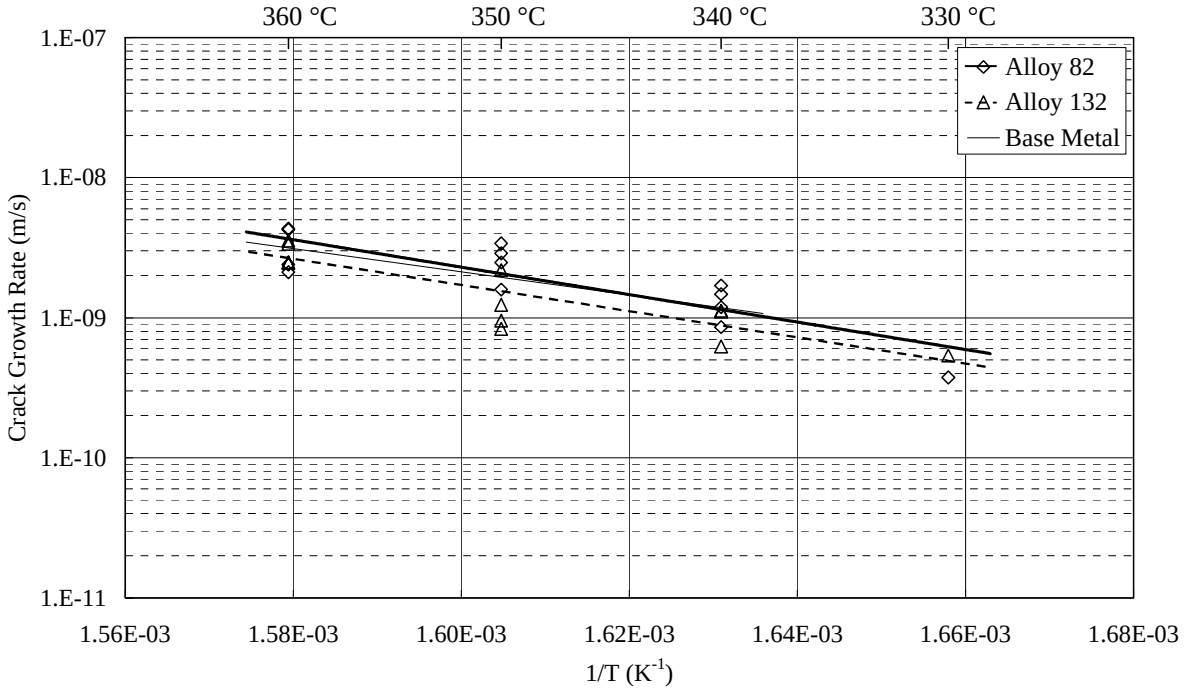

FIGURE 12 - Relationship between Temperature and Crack Growth Rate of Weld Metal in SSRT

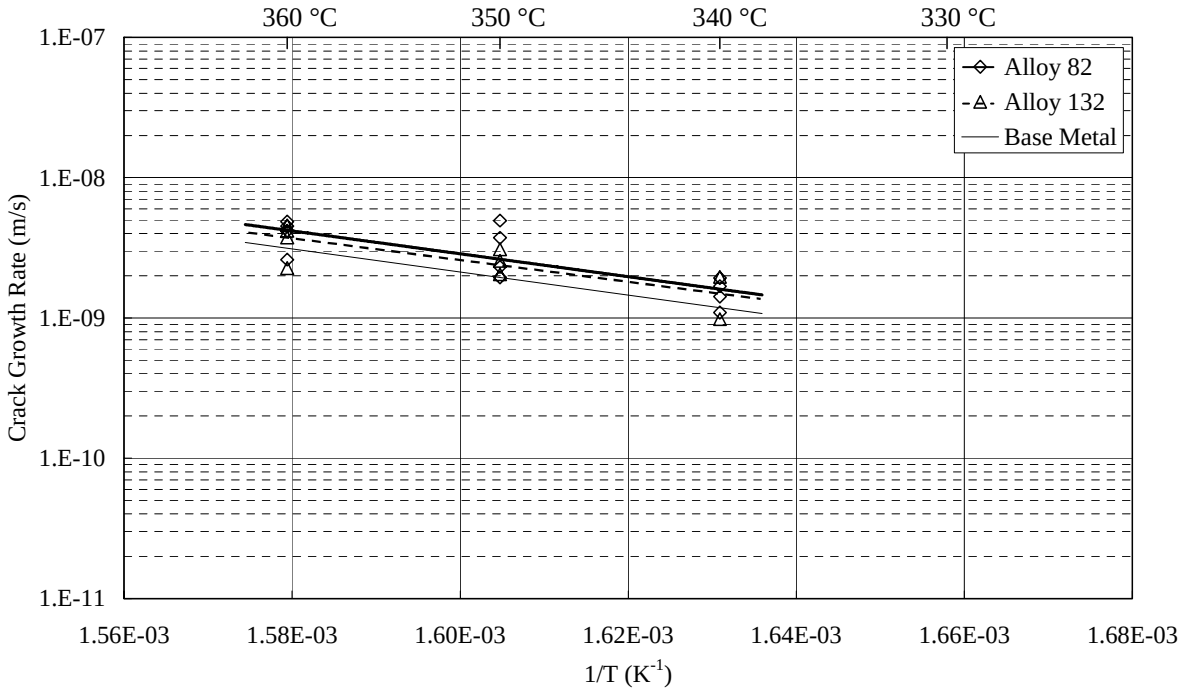

FIGURE 13 - Relationship between Temperature and Crack Growth Rate of HAZ in SSRT

Experimental and Numerical Approaches for Characterizing the Crack Growth Rate of Alloy 600 in PWR Primary Water and Lifetime Prediction for Welded Structures

T. Shoji, Z.P. Lu and Q.J. Peng

Fracture Research Institute, Tohoku University, Sendai 980-8579, Japan

ABSTRACT

In order to evaluate the lifetime of vessel head penetrations (VHP) in PWR, it is critical to fully understand the crack growth behavior of Ni-based alloys such as alloy 600 and alloy 182, taking into account the effects of temperature, the degree of cold work or warm work, and the stress intensity factor, K. Also, in order to predict the crack growth behavior of those alloys near a HAZ or of weld metal subjected to weld residual stress, the variation of K with crack growth, in other words, the effects of changes of K with time, dK/dt, on crack growth rates should be carefully examined. The model proposed by T. Shoji et al suggests changes in crack growth rate as a function of dK/dt. Especially, the crack growth behavior caused by negative dK/dt that occurs when a crack grows in an area of compressive residual stress is well recognized in SCC incidences such as VHP cracking in PWR plants.

In this work, the implications derived from a crack growth model based upon oxidation kinetics and crack tip strain rate in both BWR and PWR environments will be described. The significant effects of yield strength and of dK/dt on da/dt versus K diagrams will be demonstrated by numerical analysis based upon a theoretical equation.

First, the significance of yield strength for crack growth enhancement will be demonstrated by numerical analysis and by the experimental data available in the literature on alloy 600 of various yield strengths. The dependence of crack growth rate on the logarithmic value of K will be emphasized. The proposed growth curves will be compared to existing crack growth curves.

Second, crack growth rate diagrams calculated for the condition of positive dK/dt show significantly higher growth rates than those under negative dK/dt. Therefore, significant reduction in crack growth rate would be expected at certain K values that are higher than K_{ISCC}. Consideration of these characteristics will give significant differences in lifetime predictions for cases when a SCC crack propagates into a weld's compressive residual stress field. Similar situations of crack growth under weld residual stress fields can be seen in Core Shroud cracking and recirculation pipe cracking in BWR. A brief analysis will be made on these issues based upon the numerical analysis.

In order to better predict the lifetime of welded components subjected to SCC, experimental verification of such crack growth behavior would be highly recommended.

1. Introduction

Nickel-based alloys are widely used as structural materials in nuclear power plants. Environmentally assisted cracking (EAC) of these materials is one of the limiting factors of the life time of water-coolant nuclear reactors. IGSCC of steam generator (SG) tubes occurred in the mid-1970s and became a main cause of failure of SG tubes in the 1980s in Pressurized Water Reactors (PWR). Primary water stress corrosion cracking (PWSCC) of Vessel Head Penetrations (VHP) fabricated from alloy 600 materials was first observed in the early 1990s in French PWRs and has since then become a generic problem for alloy 600 components in PWR plants. In recent years PWSCC of VHP of alloy 600 has also occurred in other countries.[1-2] SCC of compatible nickel-based weld metals such as alloy 182 has also occurred in recent years. In order to evaluate the remaining lifetime of vessel head penetrations (VHP) in PWR, it is critical to fully understand the crack growth behavior of Ni-based alloys such as alloy 600 and alloy 182, taking into account the effects of material variability, temperature, degree of cold work or warm work, and stress intensity factor, K. Also, in order to predict the crack growth behavior of those alloys near a HAZ or of weld metal subjected to weld residual stress, the effects of the variation of K with crack growth, in other words, the effects of changes of K with time, dK/dt, on crack growth rates should be carefully examined.

Since multiple factors, such as material, environmental, and mechanical factors, are involved in EAC processes, and their interactions are complex, the PWSCC mechanism is still a controversy, even though progress has been made every year. Although much CGR data have been generated in the laboratory, there is still much demand for prediction of PWSCC failures of nickel base alloy components in PWR plants based on a definite mechanism and on deterministic CGR models, because of testing ability, data quality, enormous combinations of real plant conditions, etc. Elucidating the EAC mechanism and developing practical life prediction technologies based on CGR formulation are top priorities. Several CGR models have been proposed, although there are some ambiguities in the quantitative formulation of crack tip mechanics represented by the crack tip strain rate and its synegism with different modes of crack tip oxidation.

A generalized CGR formulation, based on a deformation/ oxidation mechanism and on a theoretical crack tip strain rate equation derived by T. Shoji et al [3], is proposed in this paper. The formulation is used to quantify the crack growth behavior of austenitic alloys in both BWR and PWR environments, emphasizing the interaction between crack tip oxidation and crack tip

mechanics. This paper will mainly discuss the effects of K, YS, and dK/dt at different temperatures, emphasizing the deformation/oxidation interaction at the crack tip.

2. Literature Survey - Existing Crack Growth Data and Significant Parameters for Alloy 600 in PWR Primary Water

Laboratory results showed that many factors affect PWSCC of alloy 600. Material chemistry and microstructure, such as the fraction of Coincidence Site Lattice Boundaries (CSLB), coverage fraction and distribution of grain boundary carbides, temperature, stress intensity factor (K), yield strength (YS), loading pattern and dK/dt, are found to have significant effects on the PWSCC CGR of alloy 600. Crack growth rates of alloy 600 thick-plate materials from tests with fracture mechanics specimens in simulated PWR environments from several reference papers [4-11] are summarized in Figure 1. The CGR data from real PWR plants, EDF data[11] and Cook 2 data, [12] are shown in Figure 1, along with experimental data. The da/dt data are plotted against the stress intensity factor, K.

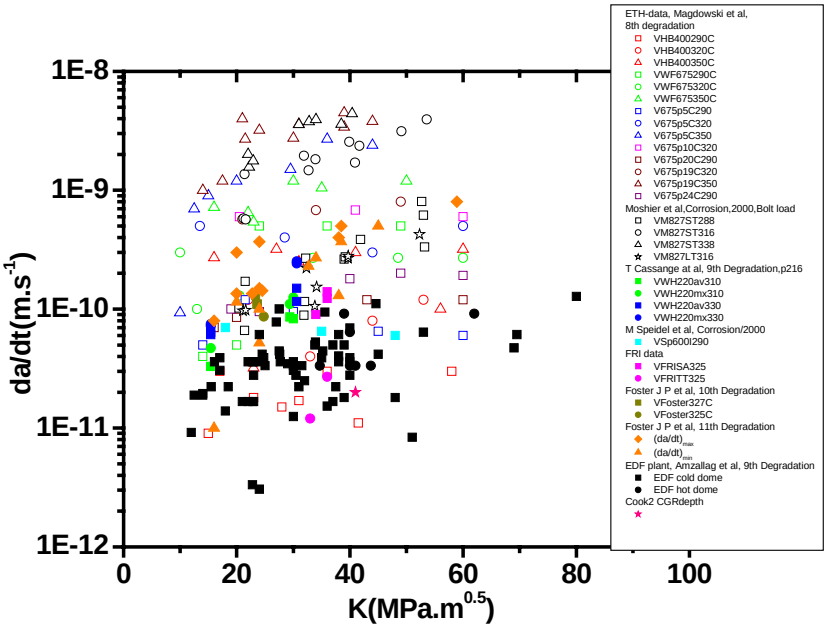

Figure 1 Crack growth rates of alloy 600 thick-plate materials in simulated PWR primary water environments [4-12].

Figure 1 shows that CGR data show much scatter at similar temperatures and K values. The wide spectrum of CGRs may be caused by factors other than K and temperature, such as variability in materials, mechanical properties, loading patterns, and test environments.

It has long been recognized that material variability originating from different material chemistry and heat treatments, such as carbide content and distribution or fraction of Coincidence Site Lattice Boundaries (CSLB) has an enormous effect on the PWSCC CGR of alloy 600. [1,2,13,14] French PWR operating experience showed a maximum change in CGR by a factor of 20 due to material variability.[1-2] It has been found that grain boundary carbides improve PWSCC resistance while intragranular carbides reduce PWSCC resistance. [1,13] Increasing the fraction of CSLB and low angle boundaries reduces the susceptibility of alloy 600 to IGSCC in simulated PWR primary water. [14] Laboratory results also show that increasing the yield strength (YS) by cold working significantly enhances crack growth. [4,8,9] The effect of cold work is introduced in some CGR calculations by a multiplying factor, but the mechanism for enhanced CGR at high yield strengths is not quite clear and is not consecutively quantified for different yield strengths. The orientation of the material contributes significantly to CGRs for deformed materials [9].

The effect of temperature on crack growth rate for alloy 600 has been determined by CGR results in different laboratories. It is known that SCC of alloy 600 is a thermal activation process with a statistical activation energy of ~ 130kJ/mol for crack growth [1] with actual experimental values ranging from 100-180 kJ/mol. Besides temperature, dissolved hydrogen (DH) content has been shown to be a significant parameter on CGR of alloy 600. [15] Maximum CGR was found to occur at a specific level of DH in proximity to the Ni/NiO oxide phase transition. Contact Electric Resistance (CER) measurements supported such theoretical analysis [16].

Much experimental data have been generated on the effects of K on CGR. This topic is of utmost importance because K is the key parameter in most of the existing models for predicting CGR, such as the P. Scott model, [1] EPRI MRP model, [12] and other empirical CGR equations. Several kinds of dependencies of CGR on K were reported by different investigators with different materials. T. Cassagne et al[10] reported a slight slope on the CGR plateau of alloy 600, WF 675 heat with K in the range of 16-40MPa.$m^{0.5}$. In the same paper he also reported a strong dependence of CGR on K for HB 220 heat at 15MPa.$m^{0.5}$ and 30MPa.$m^{0.5}$. R. Magdowski et al[4] reported that CGR-K curves exhibit CGR plateau regions for WF675 heat with different percentages of cold work. CGRs were obtained for 100mm thick double cantilever beam specimens.

A significant dependence of CGR on K for alloy 600, heat 69, was reported by J. P. Foster et al, using CT specimens and active loading. [7] W. C. Moshier et al also reported a strong dependency of CGR on K for alloy 600 materials with different processing orientations after cold working [9].

Clarifying the underlying mechanism for the different CGR-K relationships is important for the quantification of CGR.

Cold worked layers and resultant residual stresses may have significant effects on cracking. Residual stresses in PWR VHPs have been estimated by C. Amzallag et al. [11] Changes in YS and changes in K due to residual stress gradients near weldments may affect crack growth behavior and should be considered in CGR formulations for weld metals.

Laboratory data in the MRP CGR-K diagram [12] show a variability of up to 2 orders of magnitude at similar K values. EDF plant CGR data show a plateau behavior in the CGR-K diagrams. [10] Data scattering was shown in CGR-K diagrams for both experimental data and plant data, implying that parameters other than K might have significant effects.

3. Description of the FRI Generalized CGR model and Sensitivity Analyses

3.1 General Description of SCC Processes for Materials in High Temperature Water

Several mechanisms have been proposed for SCC crack propagation in high temperature water. [1, 17, 18] Among these mechanisms, the following sub-processes can generally be considered to be common to all kinds of EAC crack propagation in high temperature water:

(a) Degradation of the protective surface film at the crack tip by straining or chemical attack.

(b) Enhanced oxidation reaction of the crack tip material.

(c) Formation or growth (recovery) of the protective film.

A schematic of the general processes for EAC of materials in high temperature water is shown in Figure 2. Where i_0 is bare surface oxidation current density, i_p is passive current density, "t_o" is the time for the onset of current decay, t_p is the time for the onset of steady passivation, and t_f is the period of crack tip film degradation.

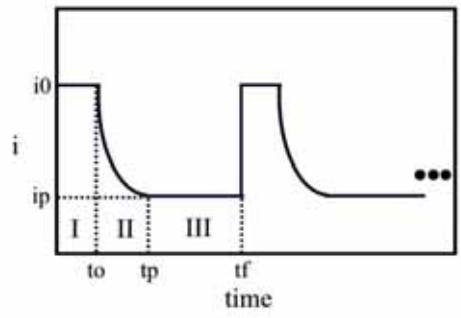

Figure 2. Schematic of the general sub-processes for EAC propagation

Crack growth rate can be expressed by Faraday's equation, Equation (1), as shown as below:

$$V = \frac{da}{dt} = (\frac{M}{\rho z F}) \cdot (\frac{Q_f}{\varepsilon_f}) \cdot \dot{\varepsilon}_{ct} \quad (1)$$

where Qf is the total oxidation charge during a period of film degradation (tf), M is atomic weight, ρ is density, z is change in charge due to the oxidation process, ε_f is the degradation strain of the protective film, and $\dot{\varepsilon}_{ct}$ is the crack tip strain rate. There are,

$$Q_f = \sum_i Q_i \quad (2)$$

$$Q_I = i_0 t_0 \quad (3)$$

$$Q_{II} = \int_{t0}^{tp} i(t)dt \quad (4)$$

$$Q_{III} = i_p (t_f - t_p) \quad (5)$$

where Q_I is the oxidation charge during stage I, the bare surface oxidation period; Q_{II} is the oxidation charge for stage II, the protective film recovery period; and Q_{III} is the oxidation charge in stage III, the passive state. It should be noted that the parameters in Equations (1)-(5) refer to the values at the crack tip that is subject to local stress/and strain. Several types of material/ environment/mechanics interactions at the crack tip can be classified as follows:

(a) $Q_I > Q_I^*$, is a stress/strain enhanced dissolution type interaction,

(b) $Q_{II} > Q_{II}^*$, is a stress/strain retarded repassivation type, through enhanced dissolution or

accelerated oxidation in the presence of a stress/strain field,

(c) $Q_{III}>Q_{III}^*$, is a stress/strain assisted oxidation type,

where superscript * means the condition without stress or strain.

EAC propagation is the result of one interaction or a combination of some of the above interactions. Different modes of EAC can be expressed by Figure 2 through different combinations of time constants and velocity constants (i) in each sub-process. Combinations of crack tip materials, crack tip mechanics, and crack tip chemistry and electrochemistry related to the bulk water chemistry will result in different combinations of time constants and reaction rate parameters in the general EAC processes described in Figure 2.

In simulated BWR normal water chemistry (NWC), high ECP values were observed for austenitic alloys such as stainless steel and nickel base alloys. Although it is postulated that the dissolved oxygen is fully consumed within the crack, it is plausible to assume that the crack tip potential in NWC would be more positive than that in hydrogenated water chemistry (HWC). Different crack tip electrochemical conditions will result in different crack tip oxidation kinetics. It is postulated that the bare surface current density after degradation of the protective film in NWC would be higher than that in de-aerated environments.

In PWR primary water, ECP is rather low and is not far from the equilibrium lines of H_2/H_2O or Ni/NiO reactions. The crack tip potential should be close to this value. It is expected that the bare surface current density would not be as high as that in NWC. The resultant cracking behavior and related controlling factors would be different, although the basic mechanism might be similar.

Assuming the protective film recovery transient process (sub-process II) contributes mainly to Q_f and proceeds through solid state diffusion, Wagner's theory of oxidation, Equation (6), can be used to delineate the transient oxidation rate in terms of oxidation current density i(t)[19],

$$i(t) = k_p \cdot t^{-0.5} \qquad (6)$$

where k_p is the parabolic rate constant.

The deviation from Wagner's law for some metal/and environment combinations can be explained by a change of film composition with time as well as by a decrease in the number of preferential diffusion paths (ex. grain boundaries) occurring with grain growth at high temperature. [20] The deviation of m from the value of 0.5 in Equation (6) can also be explained by the diffusion coefficient's being time-dependent due to relaxation of vacancy concentration. [21] Two reasons for

this time dependency were assumed: formation of divacancies and annihilation of vacancies at structural defects. If these processes are very fast or if vacancies are not injected, the rate constant determined by the diffusion coefficient is independent of the electrode potential, and m=0.5. Instead, during dissolution of alloys the rate constant is often found to change with the electrode potential. The case 0.5<m<1 corresponding to a time-dependent vacancy concentration was observed.

Then, a general equation for oxidation rate can be as follows:

$$i(t) = k_m \cdot t^{-m} \qquad (7)$$

where k_m is an oxidation rate constant, and m is the slope of the oxidation rate decay curve.

Equation (7) is similar to the equation proposed by Heusler, Equation (8), for anodic dissolution governed by a solid state diffusion process [7],

$$i(t) = k_d \cdot t^{-m} \qquad (8)$$

where k_d is an anodic dissolution rate constant.

Kinetic Equations (7) or (8) can be used to describe both the dissolution transient process and the oxidation transient process after degradation of the protective film.

For example, if,

$$k_m = i_0 \cdot t_0^{-m} \qquad (9)$$

Equation (8) becomes the familiar form, Equation (10):

$$i(t) = i_0 \left(\frac{t}{t_0}\right)^{-m} \qquad (10)$$

Equation (10) has been used in some CGR calculations. [3,4]

3.2 Theoretical Formulation of Crack Tip Strain Rate (CTSR) and Validation by 3D-FEM

The importance of dynamic deformation in SCC is widely recognized [4]. The theoretical plastic strain distribution at a crack tip along the crack line for a growing crack in an elastic plastic strain hardening material was given by Gao et al [22] and confirmed experimentally by Gerberich [23] et al.

$$\varepsilon_{ct} = \left(\frac{\sigma_y}{E}\right)\left[\ln\left(\frac{A}{r}\right)\right]^{\frac{n}{n-1}} \qquad (11)$$

where ε_{ct} is the plastic strain at the crack tip□A is generally assumed to be equivalent to the

plastic zone ($R_p=\lambda(K/\sigma_y)^2$), β and λ are dimensionless constants, σ_y and E are yield strength and elastic modulus, respectively, 'r' is the distance from a growing crack-tip (not a stationary crack-tip), and n is the strain hardening exponent as defined by Gao et al in Equation (12).

$$\varepsilon = \begin{cases} (\frac{\sigma}{E}) & for \quad \sigma \le \sigma_y \\ (\frac{\sigma}{E}) + c\cdot(\sigma - \sigma_y)^n & for \quad \sigma > \sigma_y \end{cases} \tag{12}$$

$$\varepsilon_{ct} = \beta(\frac{\sigma_y}{E})\left\{\ln[(\frac{\lambda}{r})(\frac{K}{\sigma_y})^2]\right\}^{\frac{n}{n-1}} \tag{13}$$

Gao's equation, Equation (13), was derived under the assumption of constant crack growth and constant K for plane strain conditions.

Results of 3D FEM analysis on a compact tension (CT) specimen, as shown in Figure 3, show that the calculated crack-tip strain distribution at a growing crack tip has good agreement with the theoretical logarithmic singularity. [24] This confirmation by 3D-FEM of the appropriate strain distribution can provide a general basis for the analysis of stress and strain beyond small scale yielding conditions, where crack-tip strain and strain rate at the crack tip can be evaluated under conditions of small crack size, small ligament, and thin tubing. Work hardening can maintain a crack tip strain field under conditions beyond small scale yielding for ASTM criteria similar to small scale yielding conditions. Therefore, K can be used at higher levels than that for small scale yielding conditions. Although Gao's equation was derived for steady crack growth under quasi-static loading (constant K), the results of 3D-FEM analysis indicate that Gao's equation may still be applicable even under the loading conditions without constant crack growth rate /or constant K.

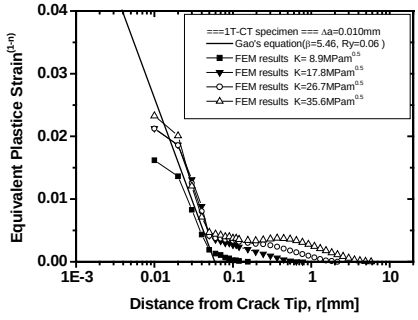

Figure 3 Equivalent strain gradient near the crack tip under constant load conditions, n=5[24]

Based on the strain distribution ahead of a growing crack, a theoretical CTSR formulation, Equation (14), was derived by T. Shoji [3] et al by considering the incremental increase in strain due to a change in distance 'r' from the crack tip and the increase in K caused by crack growth,

$$\dot{\varepsilon}_{ct} = \beta \cdot (\frac{\sigma_y}{E}) \cdot (\frac{n}{n-1}) \cdot [(2 \cdot \frac{\dot{K}}{K} + \frac{\dot{a}}{r}] \cdot \left\{ \ln[\lambda \cdot \frac{(\frac{K}{\sigma_y})^2}{r}] \right\}^{\frac{1}{n-1}} \quad (14)$$

3.3 FRI Generalized Theoretical Formulation of Crack Growth Rate

By substituting $k_m = i_0(t_0)^{-m}$, the general oxidation rate equation takes the form of the CGR equation based on the Slip-Oxidation mechanism[17] by F.P. Ford et al, Equation (15),

$$\frac{da}{dt} = (\frac{M}{\rho z F}) \frac{i_0 t_0^m}{(1-m)\varepsilon_f^m} (\dot{\varepsilon}_{ct})^m \quad (15)$$

Based on the crack tip reaction kinetics and the crack tip strain rate equations, the theoretical crack growth rate can be derived as Equation (16)[3]. This equation is a unique expression for CGR as a function of stress intensity factor created by combining a mechanism of crack growth with the mechanics of a crack tip stress/strain field. This equation also clearly shows the synergistic terms among the material parameters, mechanical properties, electrochemical properties and crack tip mechanics in terms of K and dK/dt[3, 18].

$$\frac{da}{dt} = [\frac{M \cdot i_0}{z \cdot \rho \cdot F \cdot (1-m)}](\frac{t_0}{\varepsilon_f})^m \left\{ \beta \cdot (\frac{\sigma_y}{E}) \cdot (\frac{n}{n-1}) \cdot [2 \cdot \frac{\dot{K}}{K} + \frac{\dot{a}}{r}] \cdot \left\{ \ln[\lambda \cdot \frac{(\frac{K}{\sigma_y})^2}{r}] \right\}^{\frac{1}{n-1}} \right\}^m \quad (16)$$

The generalized FRI CGR formulation, Equation (17), can be obtained by combining Equations (1), (4) and (16):

$$\frac{da}{dt} = \kappa_a \left\{ \beta \cdot (\frac{\sigma_y}{E}) \cdot (\frac{n}{n-1}) \cdot [2 \cdot \frac{\dot{K}}{K} + \frac{\dot{a}}{r}] \cdot \left\{ \ln[\lambda \cdot \frac{(\frac{K}{\sigma_y})^2}{r}] \right\}^{\frac{1}{n-1}} \right\}^m \quad (17)$$

where κ_a is an oxidation rate constant that is a function of local material chemistry, local environmental chemistry, transient interfacial rate kinetic law, and the stress/strain state. The general CGR formulation, Equation (17), will be used for further quantification of crack growth behavior in high temperature water in this paper.

3.4 Sensitivity Analysis of the FRI Generalized CGR Model

Theoretically, the oxidation rate constant $\boldsymbol{\kappa_a}$ in Equation (17) can be calculated based on electrochemical kinetics or on the oxidation rate law, if all the involved parameters are known. Practically, it is difficult to know the values of all the parameters for various material/environment/mechanics combinations, especially in cases where the applied stress/strain might also significantly affect the oxidation rate constant, i.e., $\boldsymbol{\kappa_a}$ may also be stress/strain dependent. Such data are often not available. One effective way is to use Equation (17) to calculate $\boldsymbol{\kappa_a}$ values for different material/environment/load combinations with known crack growth rates, then correlate $\boldsymbol{\kappa_a}$ values to the dominant influencing factors. In such a way, it is possible to find the general form of $\boldsymbol{\kappa_a}$ for specific SCC systems. Then the general form can again be used for further CGR prediction. In this paper, the deformation/oxidation interaction and its effect on CGR are quantified with Equation (17) and the available CGR data base, emphasizing the role of yield strength. The importance of yield strength has been realized recently from both experimental data and field failure experiences in PWR and BWR plants. [2-4,9,11,25] Sensitivity analyses with Equation (17) were performed to delineate intuitively the role of yield strength and K on crack growth under some typical combinations of other factors. By using appropriate parameters, CGR values for different YS levels can be formulated using Equation (17), assuming a constant K condition. Some examples of the effects of different parameters are listed in Figures (4)-(8).

Enhancement factor, *R*, was proposed to quantify the effects of different factors on CGR. For example, $R(YS)_m$ or $R(YS)\ \boldsymbol{\kappa_a}$ means the ratio of CGR at two yield strength levels (YS2 and YS1) for a given *m* or $\boldsymbol{\kappa_a}$ value, respectively.

$$R(YS)_m = CGR(YS2)_m / CGR(YS1)_m \qquad (18)$$

$$R(YS)\ \boldsymbol{\kappa_a} = CGR(YS2)\ \boldsymbol{\kappa_a} / CGR(YS1)\ \boldsymbol{\kappa_a} \qquad (19)$$

Figure 4 shows the calculated CGR-$\boldsymbol{\kappa_a}$ curves for materials with three YS levels, assuming m is constant in all cases. YS of 230MPa was set for as-is solution annealed materials, and YSs of 450MPa and 600MPa were set for deformed materials due to weld-shrink, fabrication cold work,

etc. At each YS level, CGR increases with increasing values of κ_a. This phenomenon is well known for many material/environment/load combinations in high temperature water. Generally higher oxidation rates, corresponding to more oxidative environments, such as BWR NWC with high dissolved oxygen (DO) levels and noble electrochemical potentials (ECP), will result in higher crack growth rates.

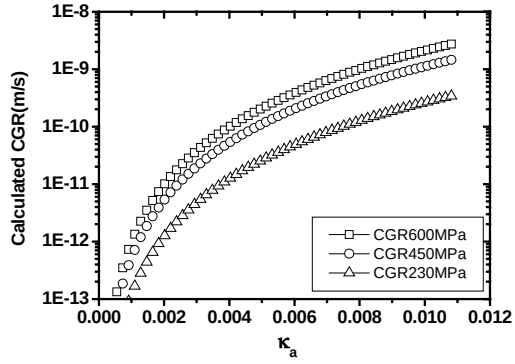

Figure 4 Sensitivity analysis of the effect of YS at different κ_a levels (m= constant) using Equation (17)

Figure 4 shows that CGR is not proportional to κ_a, i.e., a non-linear relationship exists between crack propagation and crack tip oxidation rate due to the deformation/oxidation interaction, as has been described in Equation (17). Such a non-linear relationship shows that, even crack growth is strongly dependent on interfacial reactions, its characteristic kinetics may differ from pure oxidation kinetics. Using only the purely interfacial reaction parameters to deduce the kinetics factors that control CGR may lead to erroneous conclusions.

Figure 4 shows that CGR is higher for higher YS at the same κ_a value. This implies that, even if the pure oxidation rate constant remains constant, CGR can change significantly from the effects of YS on crack tip mechanics. Figure 4 also shows that the effect of YS on CGR is independent of κ_a, i.e., the YS enhancement factor may be the same at different values of κ_a. However, this result is based on the assumption that different YS would not change the values of *m* and κ_a. If m and κ_a also change with YS, then the dependency of m and κ_a on YS should also be considered in the CGR formulation.

Figure 5 shows the calculated CGR-m curves for different values of YS, assuming that κ_a is a constant. For a given YS, CGR decreases with an increase of m. This result is reasonable because a high value of m indicates a high film recovery (or repassivation) rate, which will result in a lower CGR if all other parameters are held constant. Figure 5 also shows that the enhancement factor (R) for a change in YS is not constant for different values of m. $R(YS)_m$ increases with increasing m. This trend implies that the effect of YS is more pronounced for materials with faster repassivation (or faster film recovery) processes. For high values of *m*, the enhancement factor for YS can be rather high, assuming that κ_a is constant. Generally an increase of m will cause a change in the value of κ_a. In this regard, it is still expected that, for a given m, the enhancement caused by a change in YS would not change much, as suggested in Figure 4.

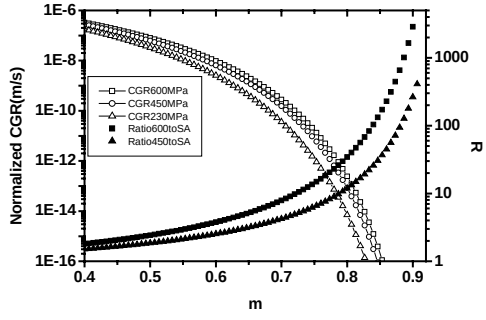

Figure 5. Sensitivity analysis of the effect of YS on CGR for different values of **m** (κ_a =constant) using Equation (17)

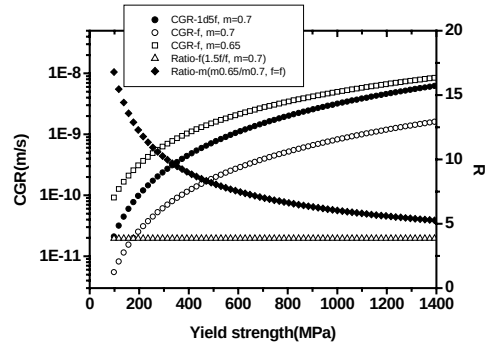

Figure 6. Sensitivity analysis of the effects of κ_a or **m** on CGR for different values of YS using Equation (17)

The combined effects of YS, **m** and κ_a on CGR can be seen in Figure 6. For certain combinations of m and κ_a, CGR increases with YS. The enhancement factor of CGR caused by a change in κ_a is constant at all levels of YS, while the enhancement factor for m is less for an increase in YS. This result shows that CGR enhancement by decreasing *m* (slower film recovery process) could be more significant for materials of lower YS.

Figure 7 shows two CGR curves in terms of K. CGR plateau regions appear at high values of K. At low values of K, CGR increases with K, and more significant effects of K are found for materials with high YS and low n than for materials with low YS and high n. A lower K threshold is found for the latter materials, as shown in Figure 7. This phenomenon may partly account for the

two separate types of CGR-K relationships that were observed in the laboratory results. Lower thresholds and stronger effects of K might be obtained for materials with lower yield strength and higher strain hardening ability. This is consistent with the experimental results in Ref. [10], where a stronger K-dependency was observed for materials with lower yield strength. While in another paper, significant effects of K were also observed for highly cold worked materials with high yield strength, implying that there might be other contributing factors. A threshold K, K_{th} of ca. 9MPa.m$^{0.5}$, observed in the experimental results and used in some CGR formulations, is consistent with the estimated values of K for a given characteristic distance 'r' in the theoretical FRI CTSR formulation.

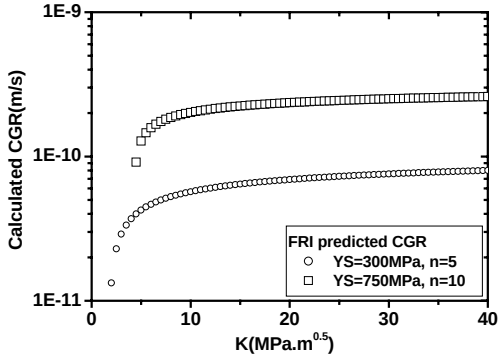

Figure 7. Calculated values of CGR as a function of K for two materials with different values of YS and strain hardening exponent n (Gao's definition).

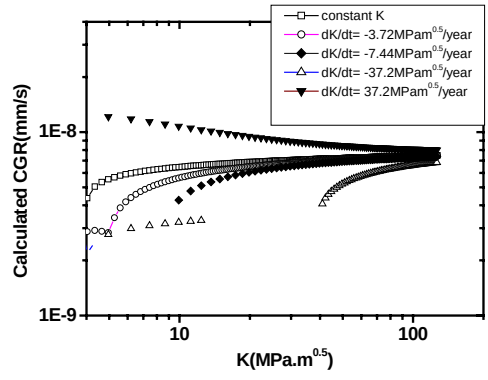

Figure 8. Calculated CGR values with the FRI generalized CGR formulation, under conditions of dK/dt>0, dK/dt=0, and dK/dt<0.

Sensitivity analysis was used to examine the effects of dK/dt on CGR. The change of K over time can be from the crack growth itself, from residual stress at or near weldments, etc. CGR-K diagrams for the conditions of dK/dt>0, dK/dt=0, and dK/dt <0 were obtained using the FRI generalized CGR model. The results are shown in Figure 8. The calculated values of CGR were found to be scattered in specific regions for negative values of dK/dt, which may have been caused by the characteristic resistance 'r' of the selected values and the real size of crack tip plastic zone. The general trend in Figure 8 shows that dK/dt has a significant effect on CGR in low K regions. A

positive dK/dt results in a higher CGR, while a negative dK/dt results in a lower CGR, compared to the CGR under constant K. For high values of K, all the curves are close to those under constant K. This can be seen from the theoretical CTSR and CGR formulations, Equations (14) and (17).

4. Numerical Analysis of Experimental CGR data

In this paper, the crack growth rates of alloy 600 in simulated PWR primary or in plants will be analyzed with the proposed FRI generalized CGR formulation and compare to some existing CGR models, such as the Scott model, modified Scott model and EPRI MRP model.

4.1 Some K-centered CGR equations

P.M. Scott developed a CGR model, equation (20), for PWSCC CGR of alloy 600 as a function of the stress intensity factor. [1] This model was derived from published laboratory data for rather heavily cold worked (CW) specimens of flattened steam generator tubing tested in simulated PWR primary water at 330^0C. The value of 9MPa.m$^{0.5}$ for the effective value of the crack growth threshold for long cracks was based on the evidence at that time and new data tend to reinforce this value. da/dt is used in the following equations to represent CGR. The Scott model, for CW alloy 600 at 330^0C, is shown as Equation (20),

$$\frac{da}{dt} = 2.8 \cdot 10^{-11} (K - 9)^{1.16} \qquad (20)$$

It was also observed that the maximum CGRs at 323^0C in the plants were about one tenth as fast as those measured in the above mentioned laboratory tests. This difference may have originated from the effects of cold work on crack growth rate and from the small temperature difference. A coefficient of 0.1 was introduced to produce a modified Scott model. The modified Scott model, for non-CW alloy 600 at 330^0C, is shown as Equation (21).

$$\frac{da}{dt} = 2.8 \cdot 10^{-12} (K - 9)^{1.16} \qquad (21)$$

EPRI MRP[12] developed a screened PWSCC CGR data base of alloy 600 thick-plate materials with 158 CGR data points from tests performed by Westinghouse, Studsvik, EDF, CEA, and CIEMAT. The data were plotted in the form of log(CGR)-K, with CGRs adjusted to 325^0C using an activation energy of 130kJ/mol. The MPR model was based on this CGR data base and is shown as Equation (22),

$$\frac{da}{dt} = \exp[-\frac{Q_g}{R}(\frac{1}{T} - \frac{1}{T_{ref}})]\alpha(K - K_{th})^{\beta} \qquad (22)$$

In the above equations, K is in MPa.m$^{0.5}$, T is in ^{0}K, and da/dt is in m/s. At 325^{0}C, α=2.67x10^{-12}, K_{th}=9MPam$^{0.5}$, Q_g=130kJ/mol, and β=1.16.

The effect of temperature is added to the formulations by using an activation energy of 130kJ/mol in Equations (20)-(22), then,

$$(\frac{da}{dt})_{mScott}(T,K) = 2.80 \cdot 10^{-12} \cdot (K-9)^{1.16} \cdot e^{[\frac{130000}{8.314}(\frac{1}{603.12} - \frac{1}{T})]} \qquad (23)$$

$$(\frac{da}{dt})_{Scott}(T,K) = 2.80 \cdot 10^{-11} \cdot (K-9)^{1.16} \cdot e^{[\frac{130000}{8.314}(\frac{1}{603.12} - \frac{1}{T})]} \qquad (24)$$

$$(\frac{da}{dt})_{MRP}(T,K) = 2.67 \cdot 10^{-12} \cdot (K-9)^{1.16} \cdot e^{[\frac{130000}{8.314}(\frac{1}{598.12} - \frac{1}{T})]} \qquad (25)$$

4.2 Numerical Analysis of the K-effect

Two sets of PWSCC CGR data for alloy 600 tested in different laboratories were analyzed with the FRI generalized formulation, emphasizing the effect of K. Due to the match the size of crack tip plastic region and the value of 'r' used in the formulation, effective K values, (K-9), were used in the calculation.

One set of CGR data for alloy 600 material, heat 69 with yield strength of 274 MPa, were reported by J. P. Foster et al, [7] as shown in Figure 9. The results show a significant effect of K on CGR. In this case, the experimental values are ca. 5 times greater than the CGR values calculated from the modified Scot model and MRP model. Another set of data for heavily cold worked alloy 600 with high YS of 827MPa was reported by W.C. Moshier et al, [9] and shown in Figure 10. Values of CGR for this material having high YS are ca. 3.5 times greater than the values calculated by the Scott model, and much higher than the values predicted by the modified Scott model and the MRP model. CGR values predicted by the FRI generalized model for each material show a proximity to the experimental values. Differences in the values of CGR between the two materials can be partly explained by the effect of YS embedded in the FRI generalized formulation.

There are other cases where experimental CGR-K curves show rather wide plateau regions at high values of K. [4] This is consistent with the CGR-K behavior predicted by the FRI generalized formulation.

It has already been pointed out that determining the CGR-K relationship is vitally important for the CGR formulation. Material properties, such as YS and strain hardening ability may contribute to the observation of different types of CGR-K curves. More theoretical and experimental work is needed to clarify this phenomenon.

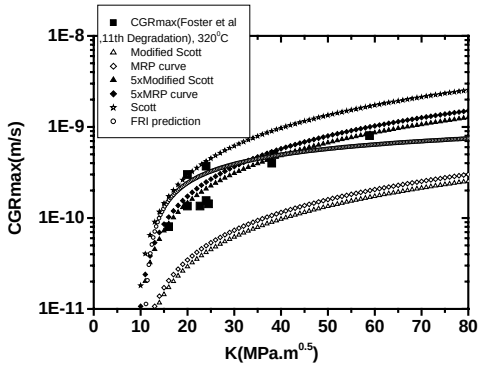

Figure 9 Maximum PWR SCC CGR data for alloy 600, heat 69 (YS of 274 MPa), as a function of K at 320^0C [7] and prediction of CGR by several models.

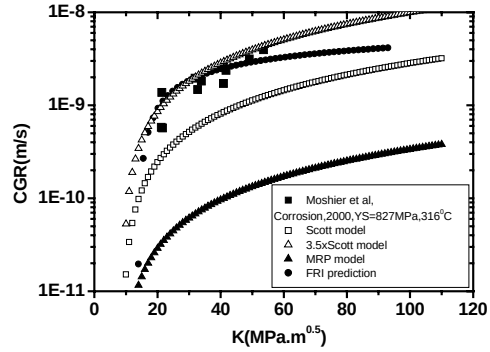

Figure 10 PWR SCC CGR data for cold worked alloy 600 (YS of 827MPa) as a function of K at 316^0C [9] and predicted values of CGR by several models.

4.3 Numerical Analysis of the Effects of YS and of Temperature

Experimental [4] and predicted PWSCC CGRs for alloy 600 in simulated PWR primary water at 290, 320, and 350^0C are shown in Figure 11. CGR increases significantly with increasing YS at all temperatures. Increasing temperature significantly increases CGRs for materials of the same YS. The apparent activation energy for crack growth ($E_{a,CGR}$) can be obtained with Equation (26) from the experimental CGR data in Figure 11. The calculated values of $E_{a,CGR}$ are ca. 151-159 kJ/mol, relatively independent of the yield strength.

$$CGR = A * e^{(\frac{-E_{a,CGR}}{RT})} \qquad (26)$$

where A is a constant at a specific temperature.

The CGR values at each temperature were formulated using Equation (17), assuming *m* is a constant. Figure 11 shows that the CGR values predicted in such a way are quite close to the experimental data. These results imply the possibility that the values of *m* are similar at these temperatures.

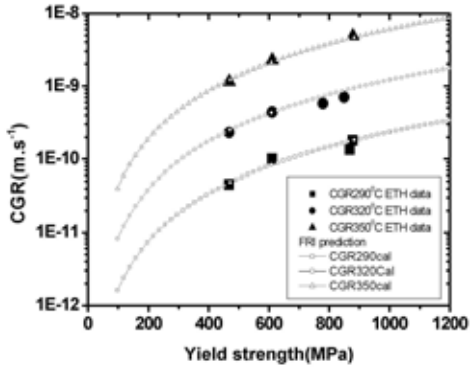

Figure 11. Experimental [4] and predicted CGR for alloy 600 in simulated PWR environments at different temperatures.

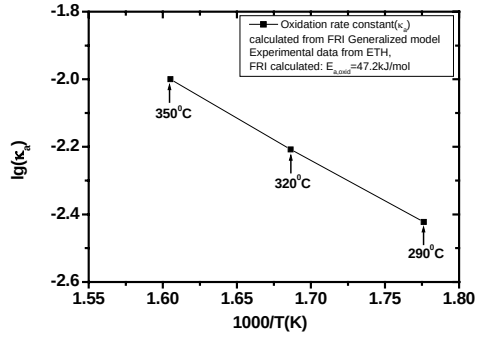

Figure 12 κ_a values at different temperatures calculated with the data from Figures 11 using equation (14).

Assuming a constant K, the following relationship between the apparent activation energy for crack growth and for the crack tip oxidation can be derived from Equation (27),

$$E_{a,oxd} = (1-m)\, E_{a,CGR} \qquad (27)$$

The calculated values of oxidation rate constants (κ_a) at different temperatures are shown in Fig. 9. There is an apparent linear relationship between lg(CGR) and (1/T). So, the activation energy for pure oxidation, $E_{a,oxid}$, can be calculated with Equation (28) through linear regression of the data in Figure 12.

$$\kappa_a = \kappa_a^0 * e^{(-\frac{E_{a,oxid}}{RT})} \qquad (28)$$

where κ_a^0 is a constant at a specific temperature.

The calculated value of $E_{a,oxid}$ is 47.2 kJ/mol, which is close to the value obtained with Equation (27) using the activation energy for crack growth.

The results show that, the activation energy for crack growth can be several times higher than that for a pure oxidation reaction at the crack tip. This implies that, when probing into CGR

mechanisms by comparing the activation energy of CGR with the activation energy of candidate interfacial reactions, care should be taken to consider this difference.

As shown in Figure 13, another set of CGR data for alloy 600 for various values of yield strength [9] can be modeled with the FRI generalized CGR formulation. The predicted results again confirm the applicability of the new model to PWSCC CGR formulation.

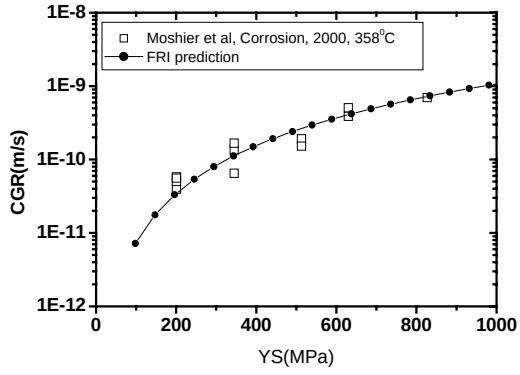

Figure 13. Experimental CGR[9] and CGR values predicted by the FRI generalized CGR formulation for alloy 600 in simulated PWR primary water

4.4 Numerical Analysis of the Effect of dK/dt

As stated in the sensitivity analysis, dK/dt may have a significant effect on CGR. Experimental results related to controlling dK/dt during EAC are rarely seen. Comparing the results from active loading tests with those from constant displacement tests may give clues to the effects of dK/dt. In active loading tests, it is supposed that K is kept constant or increases slightly. In constant displacement tests, K should decrease due to stress relaxation during crack propagation in cases when crack growth rate is not high. Figure 14 shows the CGRs obtained at similar K levels using different loading modes. CGR values obtained under active loading are higher than those under constant displacement loading tests. The CGR ratios, defined in Equation (29), are higher than 1.0 and can be as high as 4.8. Thus, the effects of dK/dt predicted by the FRI generalized CGR formulation are partly demonstrated by these results. More precisely controlled tests on the effects of dK/dt are highly required to further validate the FRI prediction and to give more relevant data for lifetime predictions of weldments where dK/dt might be a significant factor on the crack growth.

$$\text{CGR ratio}=\text{CGR(active loading)}/\text{CGR(contant displacement)} \qquad (29)$$

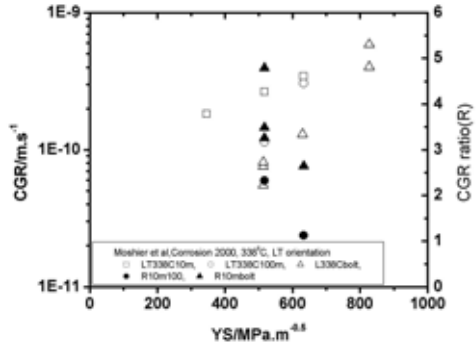

Figure 14. CGR data from Ref. [9] for alloy 600 in simulated PWR primary water under different loading methods. There are two kinds of active loading. Symbol '10m' means active loading with a holding time of 10 min, and symbol '100m' means active loading with a holding time of 100min.

4.5 Numerical Analysis of Other Material/Environment Combinations

The primary water SCC (PWSCC) CGR data for deformed simulated grain boundary (SGB) materials and deformed solution-annealed 304L and 316L stainless steels in simulated PWR primary water are shown in Figure 15. [26] SGB materials, with low Cr contents, and high Ni and/or high Si contents, are designed to simulate grain boundaries of irradiated 304L stainless steels. The crack growth rates of all materials increased with increasing YS. The line predicted by the FRI generalized formulation shows a promising approximation to the experimental data. This result means that this new model can be applied to calculate SCC CGR for both BWR environments and PWR environments.

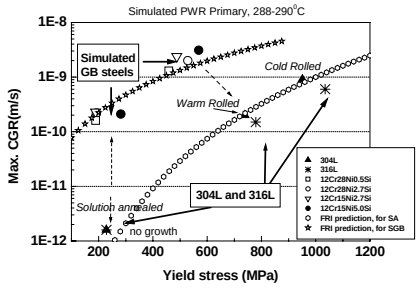

Figure 15 Experimental and predicted CGRs for SGB materials and stainless steels of various YS values in simulated PWR water at 290^0C[26]

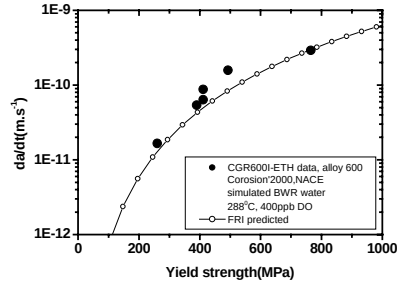

Figure 16 Experimental da/dt-YS curve (ETH data)[25] and FRI prediction line for alloy 600 in simulated BWR water.

The FRI generalized CGR formulation was also used to calculate the CGR values of alloy 600 in simulated BWR oxygenated water. [3] The predicted enhancing effects of YS on CGR are quite close to the experimental data, Figure 16. This gives another example for the applicability of the FRI generalized CGR formulation.

5. Prediction of CGR in Weld Residual Stress Fields

5.1 Core Shroud Cracking in BWR plants

Recently many cracking incidences in core internals and primary loop recirculation pipes in BWR plants were found by NDI [27-29], where TGSCC and IGSCC cracking occurred in base metals and also in weld metals of 316L stainless steels without apparent sensitization. Figure 17 shows one example of the distribution of the axial residual stress distribution through the depth of H6a in a BWR core shroud. [27] The maximum residual tensile stress exists at the surface and can be as high as 300MPa, which is close to the yield strength of solution annealed stainless steels. At first residual stress decreases for increasing depth, then increases after reaching a minimum value. At certain depths, the residual stress is compressive. The corresponding K values calculated according to API 579 are shown in Figure 18. [27] K at first increases then decreases after reaching a maximum value at a depth of ca.10mm. Crack growth rates were calculated using the disposition curves in JSME S NA1-2002[30], as shown in Figure 19 and Equations (30)-(32). The resultant crack depth versus time relationship is shown in Figure 20[27]. High crack growth rates are expected for a period of 4-9 years. CGR starts to decrease after ca. 9 years. This kind of crack growth behavior can be explained based on the effects of K and dK/dt as demonstrated in the previous analysis. Experimental demonstration of such behavior is highly recommended for more deterministic plant life predictions.

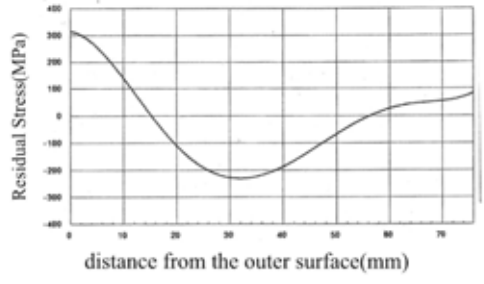

Figure 17 Distribution of the axial residual stress in H6a of a BWR Core shroud [27]

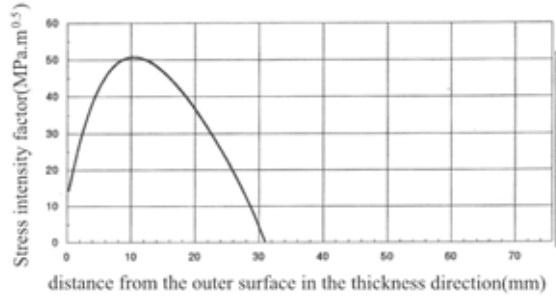

Figure 18 Estimated distribution of K in H6a in a BWR Core Shroud [27]

$$\frac{da}{dt} = 3.33 \cdot 10^{-11} \cdot K^{2.161} \qquad (30) \qquad \text{(da/dt in mm/s, for } 6.7 \leq K \leq 57.9 \text{MPa.m}^{0.5}\text{)}$$

$$\frac{da}{dt} = 2.0 \cdot 10^{-9} \qquad (31) \qquad \text{(da/dt in mm/s, } K < 6.7 \text{ MPa.m}^{0.5}\text{)}$$

$$\frac{da}{dt} = 2.1 \cdot 10^{-7} \qquad (32) \qquad \text{(da/dt in mm/s, } K > 57.9 \text{MPa.m}^{0.5}\text{)}$$

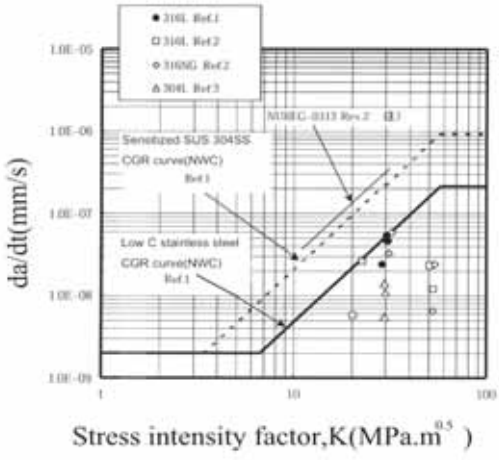

Figure 19 SCC CGR-K diagram for stainless steels in BWR environments [27, 30]

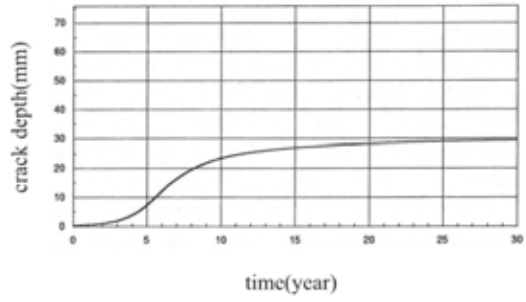

Figure 20 Increase in crack depth over time for a H6a weld in a BWR core shroud [27]

5.2 Vessel Head Penetration Cracking

EDF conducted an extensive in-service inspection program to determine the SCC CGRs in vessel head penetrations fabricated from alloy 600. The results were reported by C. Amzallag et al,[11] Figure 21. CGRs measured in service in plants have been related to the stress intensity factors. A CGR plateau region at high values of K, where CGR is relatively insensitive to K, was observed in the CGR-K diagram obtained for vessel head penetrations. Values of CGR were found to be scattered in the CGR-K diagram, with variations of up to almost one order of magnitude. The calculated values with modified Scott model and MRP model at 290^0C are close to the lower bound of the plant data. The calculated values with modified Scott model and MRP model at 310^0C are near the mean values of the plant data. At the same temperature and K, CGR values calculated by the MRP model are 17% higher than the values calculated by the modified Scott model. The CGR values predicted with the FRI generalized CGR model are also shown in Figure 21. Two yield

strengths, 300 MPa to represent low YS, and 700MPa to represent high YS due to weld strain or residual stress, were used in the calculations. The residual stress distribution estimated by C. Amzallag et al showed that the maximum residual stress in vessel head penetrations can be as high as ca. 500MPa. Results show that, CGRs calculated with higher yield strength (700MPa) meet the upper bound of the plant data, and CGRs calculated with lower yield strength (300MPa) meet the lower bound of the plant data. One CGR from Cook 2[12] is located near the lower bound of the EDF data. These results imply that the uneven distribution of yield strength due to residual stress gradients near the weldments may contribute to the scattered data in the CGR-K diagram, although there might be other contributing factors.

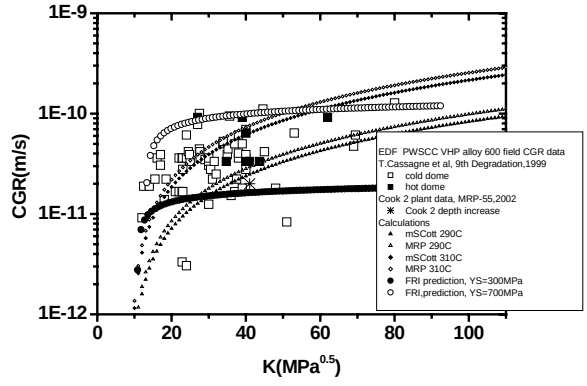

Figure 21 Plant CGR data for vessel head penetrations from EDF and Cook2, along with values predicted by different CGR models

6. Disposition of Flaws

Both experimental and plant CGR data for alloy 600 show scattering in the CGR-K diagrams. These results can be preliminarily quantified by the FRI generalized CGR formulation. Some K-dependent CGR models such as the Scott model and MRP model have been used in CGR calculation. After taking the oxidation mechanism into consideration, the crack growth rate of alloy 600 in simulated PWR primary water can be predicted in a more deterministic way by the FRI generalized crack growth model based upon crack tip strain rate, emphasizing the effects of K, YS, dK/dt, temperature, and strain hardening ability.

The following characteristic features should be taken into consideration for the disposition of flaws:

(a) Several kinds of dependence on K were observed from laboratory and plant CGR data. Variations in mechanical properties, such as strain hardening ability, may contribute to the variations in the types of CGR-K relationships. Clarifying these relationships is necessary for the disposition of flaws.

(b) CGR is highly sensitive to YS, and this effect could be one of the main factors for the scatter in the CGR data base.

(c) The time variation of K, dK/dt, during crack growth can significantly affect the CGR of structural materials in either BWR or PWR, especially for weldments suffering from EAC. Residual stress/stain analysis is necessary for crack growth rate formulation and lifetime prediction of Nuclear Power Plant (NPP) components, especially for weldments.

More CGR data from well designed and controlled conditions simulating real plants are required for the quantification of CGR in power plants, and especially for weldments where complex stress states may have significant effects on crack initiation and growth behavior.

7. Conclusions

The FRI generalized CGR formulation was proposed and was used to predict the PWSCC crack growth rates for alloy 600 from laboratories and from nuclear power plants. The formulation can also be applied to predict CGRs for other material/environment combinations, such as deformed stainless steels in simulated PWR primary water or alloy 600 in simulated BWR high temperature pure water. The contribution of crack tip oxidation and crack tip mechanics, and their synergism to crack growth can be quantified with this model. The significance of K and yield strength, and dK/dt on CGR was demonstrated by numerical analysis. The results were compared to those calculated by other CGR models, such as the Scott model and the EPRI MRP model. Good agreements of experimental and field data with the numerical results are confirmed based on the FRI model. Values for apparent activation energy for PWSCC CGR for alloy 600 were calculated, and the difference from the apparent oxidation activation energy was quantified with the FRI generalized formulation. It was pointed out that care should be taken when using the apparent activation energy as a criterion for judging the rate controlling processes of EAC crack growth. Numerical calculations showed that CGR under positive dK/dt was higher than that under negative dK/dt and

apparent threshold behavior can be seen. The effect of dK/dt on CGR can be significant and rather critical for lifetime predictions of NPP welded components such as VHPs in PWR and core shrouds in BWR. The FRI generalized theoretical CGR model provides a deterministic way to quantify SCC behavior, especially concerning the effects of yield strength, stress intensity factor-K and dK/dt. Experimental verification of crack growth behavior under conditions of positive and negative dK/dt would be highly recommended for better lifetime predictions of NPP welded components.

Acknowledgements

This work has been supported by the Grant-in Aid for COE Research (No. 11CE2003) and also partially supported by PEACE(II) program jointly organized by Tohoku Univ., EPRI, Ski, VTT, TEPCO, KEPCO, ToEPCO, JAPCO, HITACHI Ltd., MHI and TOSHIBA Co. The authors would like to express their appreciation for these supports. Also, two of the authors (Z.P. Lu and Q.J. Peng) would like to thank JSPS for the support through the Postdoctral Research Fellow program. Discussions with Mr. Douglas Shukert are gratefully acknowledged.

References

1. P. Scott, C. Benhamou. An Overview of recent Observations and Interpretations of IGSCC in Nickel Base alloys in PWR Primary Water. Proc. of the 10th. International Symposium on Environmental Degradation of Materials in Nuclear Power Systems - Water Reactors, 2001, NACE.
2. P. Scott, P. Combrade, On the Mechanism of Stress Corrosion Crack Initiation and Growth in Alloy 600 Exposed to PWR Primary Water. 11th International Symposium on Environmental Degradation of Materials in Nuclear Power Systems - Water Reactors, 2003, Skamania, ANS.
3. T. Shoji, S. Suzuki, R. G. Ballinger. Theoretical Prediction of SCC Growth Behavior. Proc. 7th Int. Symp. Environmental Degradation of Materials in Nuclear Power Systems-Water Reactors, 1995, NACE, p881.
4. R. Magdowski. F. Vaillant, C. Amzallag, and M. O. Speidel. Stress Corrosion Crack Growth Rates of Alloy 600 in Simulated PWR Coolant, in Proc. of the 8th International Symposium on Environmental Degradation of Materials in Nuclear Power Systems - Water Reactors, S. M. Bruemmer, ed., American Nuclear Society, La Grange Park, IL, pp.333-338 (1997).

5. C. Amzallag, S. Le Hong, C. Pag6, A. Gelpi, "Stress corrosion life assessment of alloy 600 components", Proceedings of the 9th International Symposium on Environmental Degradation of Materials in Nuclear Power Systems - Water Reactors, Newport Beach, CA: TMS, 1999, p243.
6. J. P. Foster, W. H. Bamford, R. S. Pathania, and A. McIlree. Effects of Loading on Alloy 600 Crack Growth Rate Behavior. Proc. 10th International Symposium on Environmental Degradation of Materials in Nuclear Power Systems - Water Reactors, 2001.
7. J. P. Foster, W. H. Bamford, R. S. Pathania. Alloy 600 Crack Growth Rate Stress Intensity Dependence. 11th International Symposium on Environmental Degradation of Materials in Nuclear Power Systems - Water Reactors, 2003, Skamania, ANS.
8. M. O. Speidel. Stress Corrosion Crack Growth in Alloy 600 Exposed to PWR and BWR Environments. Corrosion/2000, NACE. Paper No.222.
9. W. C. Moshier and C. M. Brown. Corrosion, 56 (3), 307-320(2000).
10. T. Cassagne, D. Caron, J. Daret, and Y. Lefevre. Stress Corrosion Crack Growth Measurements in Alloys 600 and 182. Proceedings of the 9th International Symposium on Environmental Degradation of Materials in Nuclear Power Systems - Water Reactors, (Newport Beach, CA: TMS, 1999), p217.
11. C. Amzallag, F. Vaillant, "Stress Corrosion Crack Propagation Rates in Reactor Vessel Head Penetrations in Alloy 600", Proceedings of the 9th International Symposium on Environmental Degradation of Materials in Nuclear Power Systems - Water Reactors, (Newport Beach, CA: TMS, 1999), p.235.
12. Materials Reliability Program (MRP)-Crack Growth Rates for Evaluating Primary Water Stress Corrosion Cracking (PWSCC) of Thick-wall Alloy 600 Material (MRP-55). July, 2002. By PWR Materials Reliability Program Alloy 600 Issues Task Group.
13. G. S. Was, K. Lian. 54 (9), 675-688(1998)
14. B. Alexandreanu, B. Capell, G. S.Was. Mat Sci. Eng. A-Struct., 300 (1-2), 94-104 (2001).
15. D.S. Morton, S. A. Attanasio, and G. A. Young. Primary Water SCC Understanding and Characterization Through Fundmental Testing in the Vicinity of the Nickel-Nickel Oxide Phase Transition. Proceedings of the 10th International Symposium on Environmental Degradation of Materials in Nuclear Power Systems - Water Reactors, NACE, 2001.
16. S.A. Attanasio, D. S. Morton, M. A. Ando, N. F. Panayotou and C. D. Thompson. Measurement of the Nickel/Nickel Oxide Phase Transition in High Temperature Hydrogenated Water Using

Contact Electric Resistance (CER) Technique. Proceedings of the 10th International Symposium on Environmental Degradation of Materials in Nuclear Power Systems - Water Reactors, NACE, 2001.

17. F. P. Ford, *Corrosion*, 52(5), 375-395 (1996).
18. T. Shoji. Progress in the Mechanistic Understanding of BWR SCC and Its Implication to the Prediction of SCC Growth Behavior in Plants. 11th lnt. Symp. on Environmental Degradation of Materials in Nuclear Power Systems-Water Reactors, ANS, Skamania, 2003.
19. N. Birks and G. H. Meier. Introduction to High Temperature Oxidation of Metals. Edward Arnold, 1983. p42.
20. C. Badini, F Laurella. Surface and Coating Technology. 135, 291-298(2001).
21. K. E. Heusler. Corrosion Science. 39(7), 1177-1191(1997).
22. Y. C. Gao, K. C. Kwang. Elastic-Plastic Fields in Steady Crack Growth in a Strain-Hardening Material. 5th Int. Conf. on Fracture, France. Vol.2, pp669-682. 1981.
23. W. W. Gerberich, D. L. Davidson, and M. Kaczorowski. J. Mechanics and Physics of Solids. 38, p87 (1990)
24. T. Shoji, T. Yamamoto, K. Watanabe and Z. P. Lu. 3D-FEM Simulation of EAC Crack Growth Based on the Deformation/Oxidation Mechanism. 11th lnt. Symp. on Environmental Degradation of Materials in Nuclear Power Systems-Water Reactors, ANS, Skamania, 2003.
25. M. O. Speidel and R. Magdowski. Stress Corrosion Crack Growth in Alloy 600 Exposed to PWR and BWR Environments. Corrosion/2000, NACE, Paper 222.
26. T. Shoji, G. F. Li, J. H.Kwon, S. Matsushima and Z.P. Lu. Quantification of Yield Strength Effects on IGSCC of Austenitic Stainless Steels in High Temperature Waters. 11th Int. Symp. on Environmental Degradation of Materials in Nuclear Power Systems-Water Reactors, ANS, Skamania, 2003.
27. Documents presented at 5th Structural Integrity Evaluation Committee, NISA, February 18, 2003.
28. Documents presented at 6th Structural Integrity Evaluation Committee, NISA, February 26, 2003.
29. Documents presented at 7th Structural Integrity Evaluation Committee, NISA, March 10, 2003.
30. Codes for Nuclear Power generation Facilities-Rules on Fitness-for Service for Nuclear Power Plants. JSME S AN1-2002, Oct.10, 2002, JSME.

HACF Model Predictions for Alloy 600 Low Potential Stress Corrosion Cracking

Interacting Sensitivities of Crack Growth Rate to Stress Intensity Factor, Yield Stress, Temperature, Carbon Concentration, and Crack Growth Orientation

M. M. Hall, Jr., W. C. Moshier and D. J. Paraventi

Bechtel Bettis, Inc.

Abstract

A hydrogen-assisted creep-fracture (HACF) model is being developed for the intergranular stress corrosion cracking (SCC) of Ni-Cr-Fe Alloy 600 in the hydrogen-reducing, low-potential primary side environment of a Pressurized Water Reactor (PWR). Development of the model includes considerations of mechanical and physical phenomena related to applied stress intensity factor, yield stress (cold work), temperature, carbon concentration, and crack growth orientation. Also considered are corrosion phenomena responsible for hydrogen embrittlement of the crack tip; hydrogen evolution, absorption, permeation and trapping within the crack tip zone. HACF model predictions are found to be consistent with Alloy 600 crack growth rate (CGR) data trends reported here and elsewhere in the SCC literature. The stress intensity factor (SIF) exponent either increases or decreases with increasing temperature, depending on crack growth orientation relative to deformation textures introduced by cold work. The SIF exponent decreases with increasing yield stress; the apparent activation energy decreases with increasing applied SIF and increasing yield stress, the magnitude of these sensitivities depending on level of cold work and crack growth orientation. Carbon increases the yield stress, decreases the strain hardening and increases the apparent activation energy. The effect of crack growth orientation is modeled as an orientation-dependent effect of carbon on the mechanical component of the apparent activation energy. The observation that there is a local maximum in Alloy 600 SCC CGR for coolant-borne hydrogen concentrations in vicinity of the Ni – NiO phase equilibrium is not treated quantitatively here but is discussed within context of the HACF model.

Introduction

Crack growth rate (CGR) algorithms are needed for the disposition of crack-like indications found during inspections of reactor components. Development of high-confidence CGR disposition curves requires high quality data that are capable of revealing SCC CGR sensitivity to engineering variables such as temperature, applied stress intensity factor, coolant water chemistry and materials conditions. Physically based CGR models are preferred for development of engineering data correlations as they provide added confidence that the data have been analyzed using the best available fundamental understanding of the mechanical, physical and corrosion phenomena contributing to CGR.

During the past decade, Moshier[1] and coworkers and others[2, 3, 4, 5] have been obtaining the Alloy 600 SCC CGR data that are required for quantification of the crack growth phenomenology. During this time, Hall[6] and Hall and Symons[7, 8] have been developing the HACF phenomenological model for low potential SCC. In this paper we provide additional SCC CGR data and data analyses using the HACF model to illustrate the sensitivities of Alloy 600 CGR to applied stress intensity factor, yield stress (cold work), temperature, carbon concentration, and crack growth orientation.

The HACF Model

Past development of the HACF model and a summary of the phenomenological observations that support a hydrogen-assisted creep-fracture crack advance mechanism are provided in a previous publication. The essential features of the HACF model and model equations are illustrated in Figure 1. In the HACF model, crack advance occurs by the creep fracture of hydrogen-embrittled grain boundaries. The model equations are developed assuming a steady crack-growth rate and the quasi-static assumption that, at a fixed distance ahead of the moving crack, all processes have reached their steady or time-averaged values. Within these assumptions, the crack tip strain rate is constant at a distant point that moves with the crack and the crack growth rate can be expressed as in Equations (1.a) and (1.b), Figure 1. Symbols used in equation development are found in Table I.

At the temperatures of PWR normal operation (T > 250 °C), the cathodic reduction of water produces nascent hydrogen with a fugacity f_{cor} that exceeds the usual coolant-borne hydrogen fugacity, f_{DH}. The fugacity of this corrosion-generated hydrogen is dependent on the crack tip pH and the hydrogen overvoltage of the crack tip corrosion-oxidation reaction. The crack tip hydrogen concentration, equation (2), is a function of both the hydrogen permeation rate as well as the crack velocity. When the hydrogen permeation rate is greater than the Alloy 600 SCC crack velocity (for example, for mill annealed Alloy 600 and T > 250 °C), the CGR is independent of the permeability. In this case, the CGR equation can be simplified to obtain a power-law CGR equation, (3.a), which is the form that is commonly assumed for empirical SCC CGR correlations. Note that we have adopted here the logarithmic expression for stress-dependent activation enthalpy discussed by Hall and Symons. This choice is compatible with the available analytic solutions to the crack tip stress-strain rate problem and allows us to obtain the more customary power-law CGR equation in lieu of the exponential-law equation of our previous publication. When the hydrogen permeability does not exceed the crack velocity, equation (2) can be solved to obtain an equation in which CGR is proportional to the hydrogen permeation rate. This low-temperature limiting form of the HACF model is not discussed here.

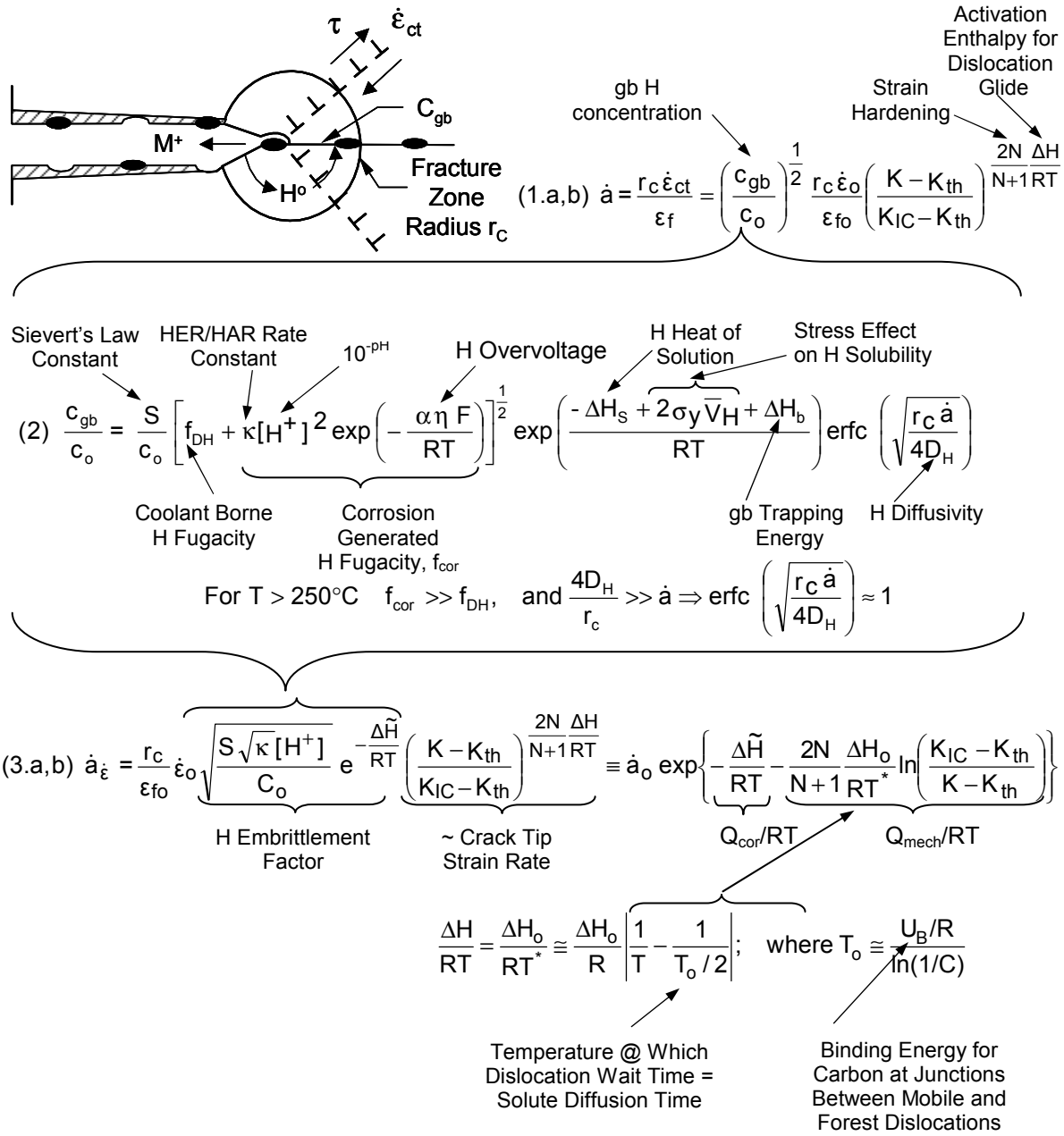

Fig. 1. Essential features of the HACF model with model equations showing corrosion and mechanical contributions to the crack growth rate.

Table I. List of Symbols

$\dot{a}$	crack growth rate	T_o	transition temperature
$\dot{a}_o$	rate constant	F	Faraday's constant
c	hydrogen concentration	U_B	binding energy – carbon to mobile-forest dislocation junctions
c_{gb}	grain boundary carbon concentration	$\overline{V}_H$	hydrogen atomic volume
c_o	reference hydrogen concentration	α	constant having a value, between ½ and 2, characteristic of the hydrogen evolution and absorption reactions
D_H	hydrogen diffusivity	ε_f	strain to fracture crack tip fracture zone
f_{cor}	fugacity of corrosion generated hydrogen	ε_{fo}	strain to fracture crack tip zone with reference hydrogen concentration c_o
f_{DH}	fugacity of coolant borne hydrogen	$\dot{\varepsilon}_o$	crack tip strain rate constant
K_I	applied stress intensity factor	$\dot{\varepsilon}_{ct}$	crack tip strain rate
K_{IC}	critical stress intensity factor (toughness)	$\Delta\tilde{H}$	apparent activation enthalpy for corrosion processes
K_{th}	threshold stress intensity factor	$[H^+]$	10^{-pH}
N	strain hardening exponent	ΔH_B	binding energy – hydrogen to grain boundaries
Q_{cor}	apparent activation energy assignable to corrosion processes	ΔH_o	drag-free activation enthalpy for dislocation glide
Q_{mech}	apparent activation energy assignable to mechanical processes	ΔH_S	hydrogen heat of solution
R	gas constant	κ	ratio of HER/HAR reaction rate constants
r_C	creep fracture zone radius	η	hydrogen overvoltage
S	Sievert's Law constant	σ_Y	room temperature yield stress
T	Temperature		

The CGR is proportional to a hydrogen-embrittlement factor

$$\left(\frac{c_{gb}}{c_o}\right)^{1/2} = \sqrt{\frac{\sqrt{\kappa}\, S[H^+]}{c_o}}\, e^{-\frac{\Delta\tilde{H}}{RT}} \tag{4}$$

where

$$\Delta\tilde{H} = \frac{\alpha\Delta\eta F}{2RT} + \Delta H_s - 2\sigma_y \overline{V}_H - \Delta H_b\,. \tag{5}$$

The stress intensity factor (SIF) exponent is given by

$$m \equiv \left.\frac{\partial \ln \dot{a}}{\partial \ln K_R}\right|_{T,\eta} = \frac{2N}{N+1}\frac{\Delta\tilde{H}}{RT}\ , \tag{6}$$

where K_R is a normalized effective applied SIF given by

$$K_R \equiv \frac{K - K_{th}}{K_c - K_{th}}. \tag{7}$$

According to Equation (6), the SIF exponent is inversely dependent on temperature and decreases with decreasing strain hardening, N, which, for cold worked material, decreases with increasing levels of cold work (increasing yield stress) and increasing carbon concentration, C.

In a recent publication Hall and Symons[8] considered the effects of carbon and dynamic strain aging on the deformation rate behavior of Alloy 600. Results of this work suggests the following phenomenological expression for the activation enthalpy

$$\Delta H = \Delta H_o \left\{ 1 - \exp\left[-\beta \left(\ln\left(\frac{T}{T_o} \right) \right)^2 \right] \right\}. \tag{8}$$

T_o is the temperature for which the mobile dislocation wait time is equal to the carbon diffusion time, a condition that depends on the carbon concentration and crack growth orientation relative to deformation textures introduced by cold work:

$$T_o = \frac{U_B / R}{\ln(1/C)}. \tag{9}$$

U_B is the thermal energy required to de-trap carbon located at the junctions between mobile and forest dislocations. U_B is an increasing function of the orientation-dependent number density of junctions formed between of mobile crack tip dislocations and pre-strain deformation-induced immobile forest dislocations threading the dislocation glide planes. The drag-free activation enthalpy, ΔH_o, also is an increasing function of the carbon.

For temperatures in vicinity of T_o, Equation (6) can be written approximately as

$$\Delta H = \Delta H_o \left| 1 - \frac{T}{T_o} \right|. \tag{10}$$

This linearized expression facilitates data fitting routines. Then ΔH has a minimum value at $T = T_o$ so that the SIF exponent, Equation (4), is expected to decrease with increasing temperature for $T < T_o$ and increase with increasing temperatures for $T > T_o$.

The power-law HACF CGR equation can be rewritten in exponential form to emphasize that the apparent activation energy, Q, is a sum of activation energies due to both corrosion and mechanical processes

$$Q \equiv -R \frac{\partial \ln \dot{a}}{\partial (1/T)_{K_R,\eta}} = Q_{cor} + Q_{mec} = \Delta\tilde{H} + \frac{2N}{N+1} \Delta H \ln (1/K_R) . \quad (11)$$

The mechanical activation energy (Q_{mec}), which is related to the SIF exponent (m, Equation (6)) has the carbon and yield stress dependencies of m plus decreases with increasing applied SIF, K.

The grain boundary hydrogen-trapping energy (ΔH_b) and the electrochemical Gibbs free energy of the hydrogen evolution and absorption reactions ($Q_{EC} = \alpha \eta F$) make significant contributions to $\Delta\tilde{H}$. The trapping energy ΔH_b depends on grain boundary carbide coverage and morphology, which are determined by the carbon concentration and heat treatment condition of the alloy[9]. The hydrogen overvoltage (η) (and therefore, Q_{EC}) depends on the predominant crack-tip corrosion-oxidation reaction, which is a function of the Fe and Cr content of the alloy and the coolant borne hydrogen concentration (DH_2). The composition and structure of the predominate oxide phase are sensitive functions of DH_2 for concentrations near the equilibrium concentration for the Ni/NiO phase transition. Moreover, η increases (negatively) as the Fe and Cr contents of the oxide film increase. The concomitant effects of dissolved hydrogen concentration on both crack tip oxide and CGR have been reported[10].

Experimental

Alloy 600 plate material (Table II), containing 0.063 w/o C, was high temperature annealed (HTA) in an inert atmosphere at 1075 °C for 24 hours and furnace cooled for 24 hours resulting in a grain size of 60 to 70 μm and extensive grain-boundary carbide decoration. The as-heat treated plate was cold rolled to thickness reductions of 0 to 28.5% and room temperature yield stress of 187 MPa to 826 MPa. Crack growth rate tests were conducted using fatigue precracked bolt-loaded 0.4T and 0.8T compact tension specimens having Short Transverse (ST) and Longitudinal Transverse (LT) orientations[11] relative to deformation texture introduced by cold work. ST and LT CGR data are available for a yield stress of 826 MPa over a range of applied SIF factor from about 7.5 MPa Sqr-m to 55 MPa Sqr-m. Only LT CGR data are available for the other yield stress materials and these data were obtained over a narrow range of applied SIF having an average value of about 38.5 MPa Sqr-m. Periodic inspections of specimens using micro-focus X-ray imaging were used to determine the onset of cracking and extent of crack growth. Destructive examinations post-test were used to confirm final crack sizes. Tests were conducted in refreshed autoclaves containing deaerated pure water; dissolved oxygen < 10 ppb, dissolved hydrogen 40-60 STP cc/kg, room temperature pH 10.2 - 10.3 and conductivity of 45 μS. Tests were conducted at 252 °C, 288 °C, 316 °C, 388 °C, and 360 °C.

Table I. Alloy Chemistry, weight percent

Ni	Cr	Fe	C	Ti	P	S
77	15	8	0.063	0.25	<0.005	<0.001

Also reported here are CGR data obtained by Speidel and Magdowski[2,3] on Alloy 600 hot rolled bar containing 0.10 w/o carbon and having a room temperature yield stress of 474 MPa. This material was further cold reduced by approximately 20% and 40% resulting in yield stresses of 981 MPa and 1053 MPa. The starting grain size was 20 μm with predominantly intragranular carbides. Fatigue pre-cracked, wedge-loaded, double-cantilevered beam specimens having the RL orientation were tested in deaerated pure water in static autoclaves and SCC crack sizes were determined destructively post-test.

Results

CGR Sensitivity to Applied Stress Intensity Factor; SIF Exponent m

Figure 2 shows the ST orientation CGR data plotted as log CGR vs. linear stress intensity factor (SIF), where we use the normalized effective SIF, K_R. Curves drawn through the data in these figures and the ones discussed below represent the best-fit correlations obtained using the HACF model equations. While the log-linear plot is customary, a log-log plot, Figure 3, provides a better visualization of the temperature dependence of the SIF exponent, m, that is, the slopes of the curves in Figure 3. Figure 4 shows that for crack growth in the ST orientation, m decreases with increasing temperature from a value of 3.4 at 252 °C to 0.12 at 360 °C. This implies (see Equations 1 and 3) that for the ST crack growth orientation, $T_o > 360$ °C.

Shown in Figures 5, 6 and 7 are similar plots for the LT orientation data. Note that in this case, in contrast to the ST data, m increases with increasing temperature, from 1.6 at 252 °C to 3.8 at 360 °C. This trend with temperature implies that for the LT crack growth orientation, $T_o < 252$ °C. Figure 8 shows the effect of carbon concentration and crack growth orientation on T_o. Figures 9, 10 and 11 show these plots for crack growth in the RL orientation for specimens taken from cold worked bar[2,3]. Note that for crack growth in the RL orientation, m increases with temperature in a manner similar to the ST data trend. The RL data show that m also decreases with increasing yield stress. This is consistent with the HACF model prediction that m decreases with decreasing N, which decreases with increasing yield stress, as shown in Figure 12.

CGR Sensitivity to Temperature; Apparent Activation Energy Q

Figure 13 shows an Arrhenius plot of the ST orientation CGR data for a range of increasing applied SIF. Figure 14 shows that the apparent activation energy, Q, derived from the curves in Figure 13, decreases rapidly with increasing SIF, consistent with the HACF model Equation 6. Figure 15 is an Arrhenius plot of the LT orientation CGR data for increasing room temperature yield stress. Figure 16 shows that for the LT orientation, there is a smaller decrease in the apparent activation energy with increasing yield stress. This figure also shows that the effect of yield stress on Q is larger for crack growth in the RL orientation. Decreasing Q with increasing yield stress (decreasing strain hardening) is consistent with the HACF model, equation (11). The lower sensitivity of Q to yield stress for the LT orientation data, compared to the ST CGR data, is due to the smaller contribution of Q_{mech} to Q for the LT crack growth orientation. Figure 17 shows that the drag-free activation enthalpy, ΔH_o, increases with increasing carbon concentration.

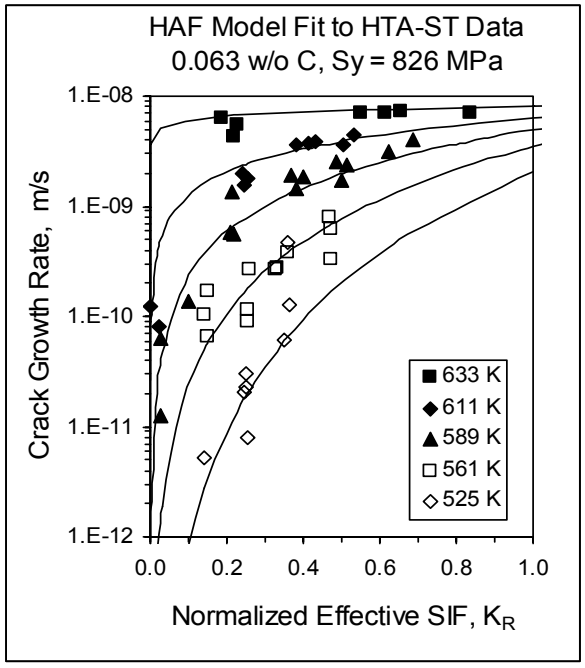

Figure 2. HACF Model Fit to HTA-ST CGR Data. Conventional log-linear plot emphasizes near threshold behavior.

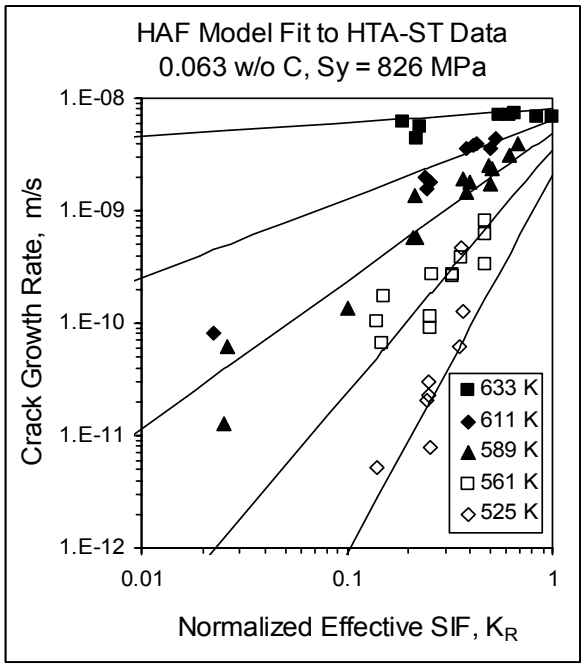

Figure 3. HACF Model Fit to HTA-ST CGR Data. Log-log plot emphasizes temperature dependence of the SIF exponent.

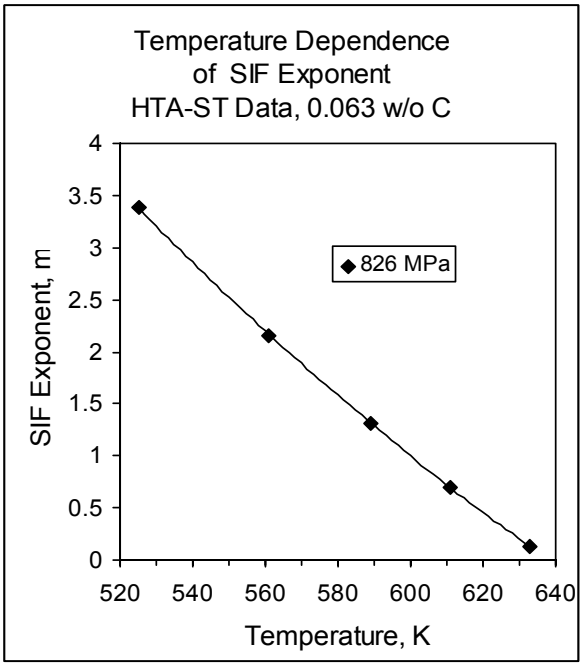

Figure 4. Temperature Dependence of the SIF Exponent for HTA-ST CGR Data.

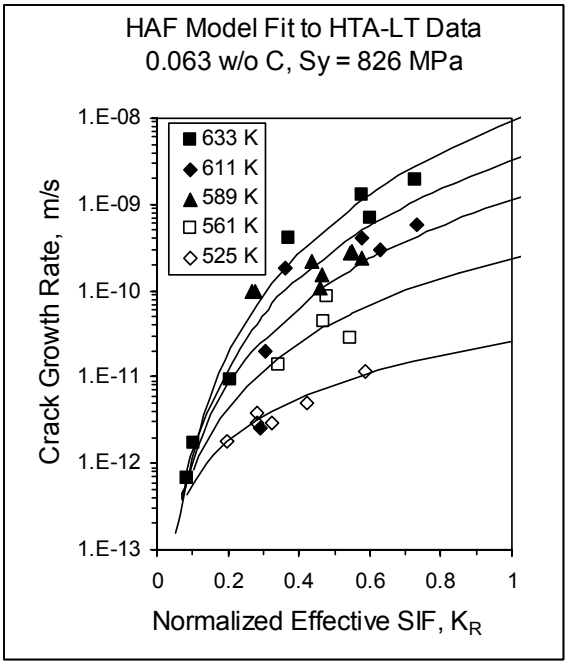

Figure 5. HACF Model Fit to HTA-LT CGR Data. Significant differences exist between LT and ST sensitivities to applied SIF.

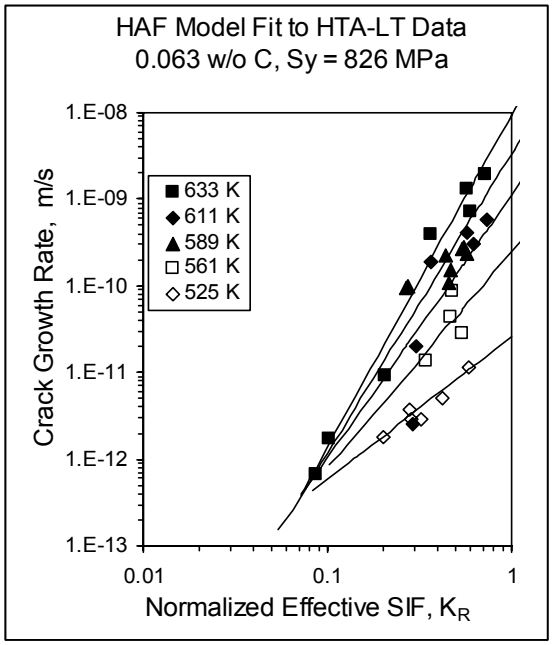

Figure 6. HACF Model Fit to HTA-LT CGR Data.

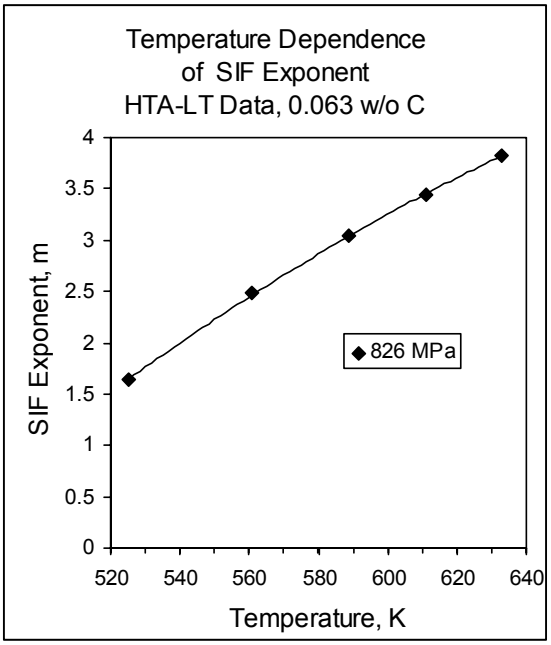

Figure 7. Temperature Dependence of the SIF Exponent for HTA-LT CGR Data.

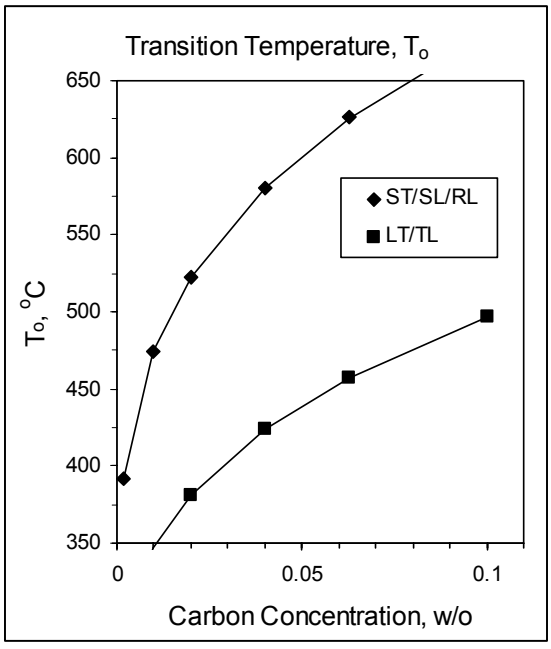

Figure 8. Carbon and Crack Growth Orientation Dependence of the Transition Temperature.

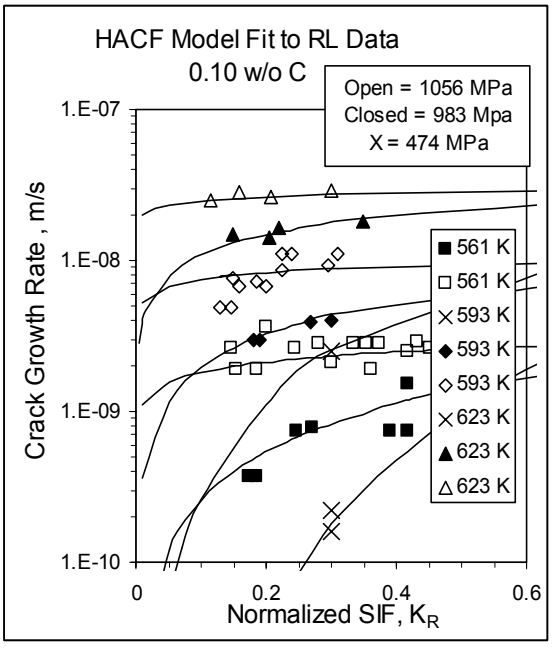

Figure 9. HACF Model Fit to RL CGR Data. Both temperature and yield stress (cold work) effects on CGR are shown.

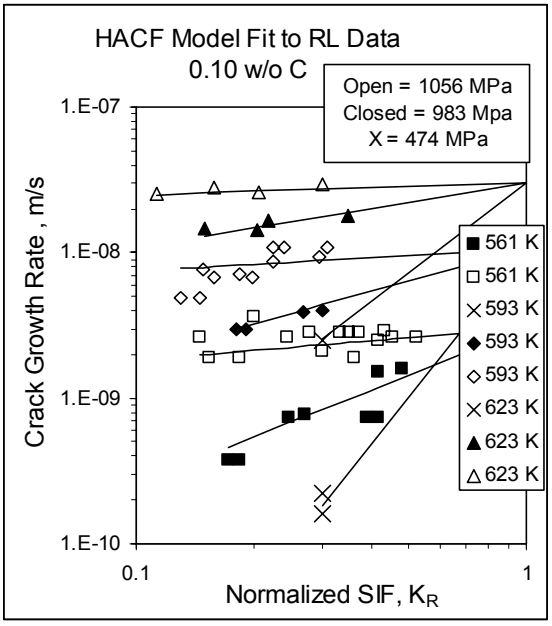

Figure 10. HACF Model Fit to RL CGR Data. Temperature dependence of the SIF exponent is similar to that of HTA-ST data.

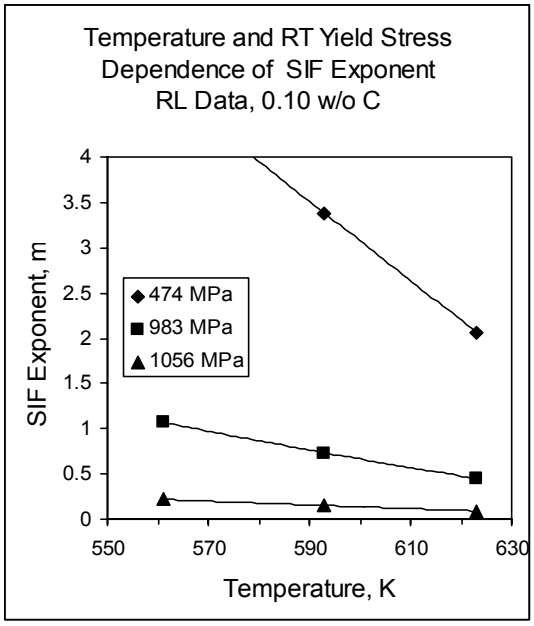

Figure 11. Temperature and Yield Stress Dependence of the SIF Exponent for RL CGR Data.

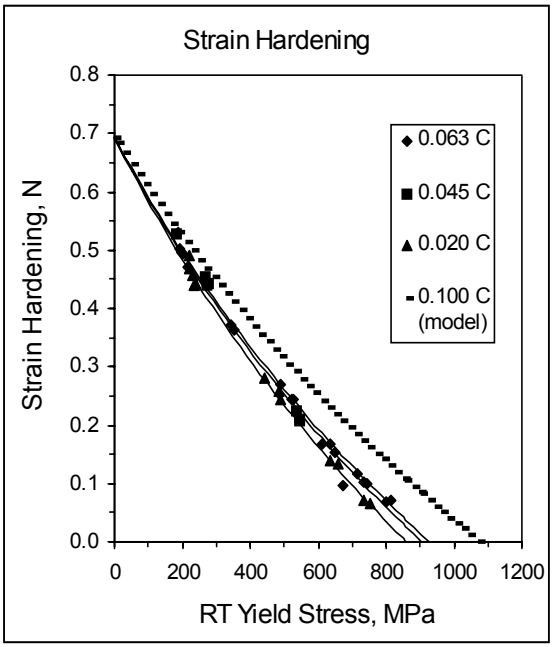

Figure 12. Strain Hardening Exponent as a Function of Yield Stress for Cold Worked Alloy 600.

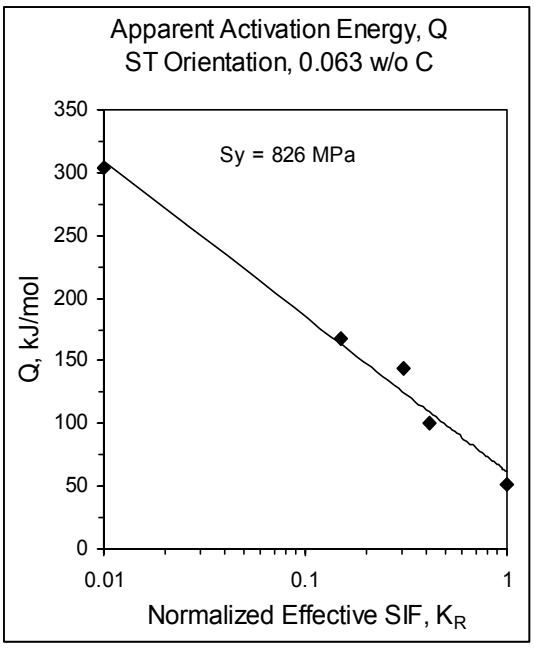

Figure 13. HACF Model Fit to HTA-ST CGR Data. Temperature dependence is an apparent function of the applied SIF.

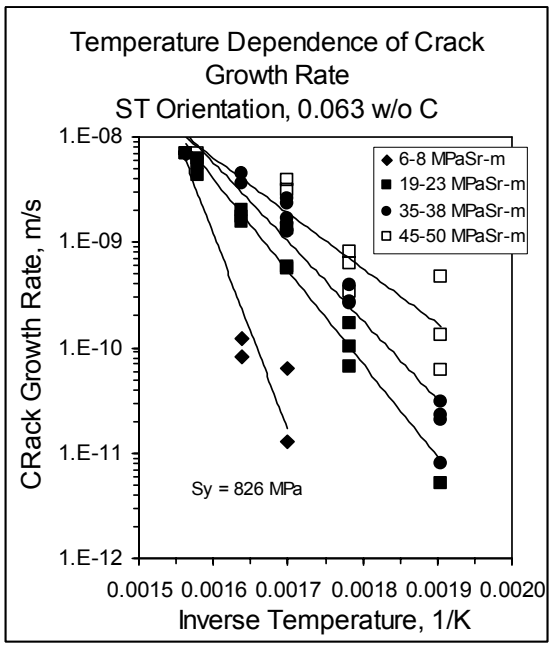

Figure 14. Temperature Dependence of HTA-ST CGR Data. The apparent activation energy decreases with increasing SIF.

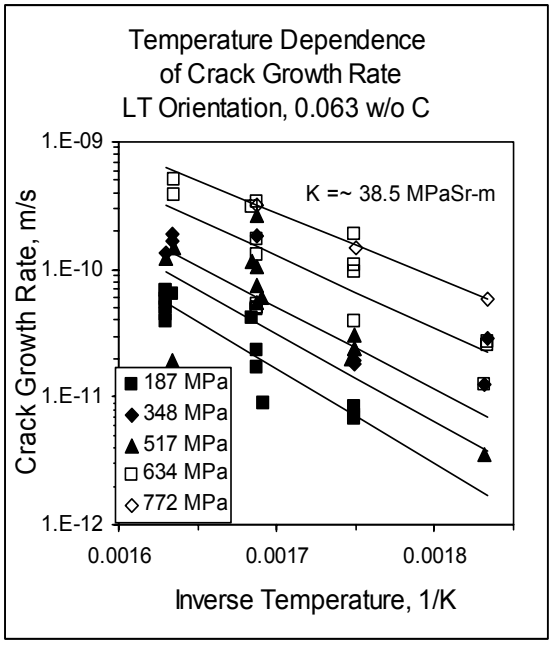

Figure 15. HACF Model Fit to HTA-LT CGR Data. Temperature dependence is an apparent function of yield stress.

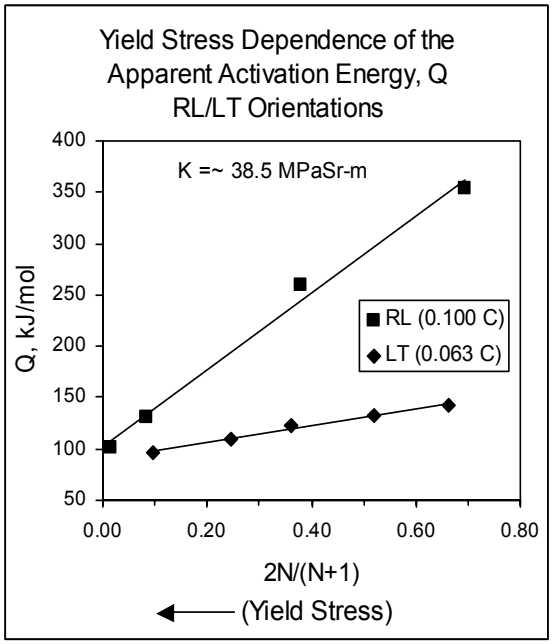

Figure 16. Dependence of the Apparent Activation Energy on Strain Hardening Exponent (Yield Stress) for RL and LT Data.

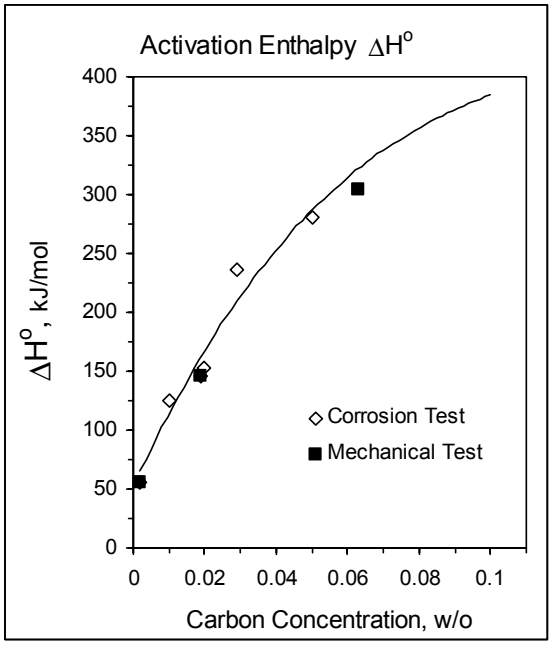

Figure 17. Dependence of the Drag-Free Activation Enthalpy for Dislocation Glide on Carbon Concentration.

DISCUSSION

Aqueous stress corrosion cracking is a complex phenomenon that has been under investigation for over 100 years. Progress in modeling SCC has been slow due to the large number and complexity of the processes that contribute to SCC crack advance. Thermally activated chemical and electrochemical processes take place within the aqueous environments established in the bulk water, the crack enclave and within the water-oxide-metal interface. As engineering materials possess included phases of varying and interacting corrosion characteristics, and given the possibility of a sequestered crack tip environment, the crack tip corrosion processes are the more complex. These aqueous environments and products of the corrosion processes interact with a structurally inhomogeneous material that is subject to complex, thermally activated mechanical and physical processes that operate within the stress field of the crack tip zone. These interacting processes cause embrittlement of the crack tip leading to local fracture and crack advance.

Phenomenological SCC modeling provides one means for making more rapid progress than may be possible by development of purely fundamental models. The significant advantage provided by phenomenological modeling is that not all process are included; only those that are *judged* to contribute most significantly to crack advance. Phenomenological SCC models are developed from observations, as opposed to being derived from a priori arguments, and mathematically describe the observed sensitivities of the phenomenon of SCC crack growth to mechanical stress, temperature and electrochemical potential. These sensitivities are modeled using mathematical descriptions of the sub-processes that are judged to make greatest contribution to crack advance. Phenomenological SCC models may reflect a significant level of fundamental and mechanistic understanding and, by adjustment of the model fitting parameters, often can be applied more generally to other materials undergoing SCC in different environments by the same mechanisms. The level of confidence that can be developed in phenomenological models increases with the number and complexity of the observable phenomena that can be explained and simultaneously correlated. The approach strives to minimize complexity of expression but allows for increasing complexity as added data and observations not predicted by the model become available. Model development typically continues as long as added data expand coverage of the model variables.

The HACF model appears to describe adequately the SIF and temperature sensitivities of the Alloy 600 SCC data presented here. There are other CGR data in the literature[4,5] that demonstrate many of these stress and temperature dependencies but have ambiguous specimen processing histories and are thus not included in this study. Much of the remaining literature data have been obtained using specimen geometries that do not meet the requirements for obtaining ASTM valid SCC CGR data[12] and are not included here.

The higher temperature, limiting form of the HACF model attributes the observed temperature, yield stress, carbon concentration and crack growth orientation dependencies of the SIF exponent and apparent activation energy to mechanical and physical processes. Although stress-dependent corrosion processes have been proposed, the full range of observed apparent activation energies for PWR SCC of Ni base alloys cannot be reconciled with those observed for corrosion processes. Moreover, the observed dependence of the apparent activation energy on applied SIF and yield stress implies a mechanical rather than an electrochemical process as the rate-determining step. The HACF model predicts that stress-independent corrosion processes will have a major influence on the CGR rate through the rate constant, $\dot{a}_o$.

Morton et al.[13] have pointed out that activation energies are properly obtained by conducting CGR experiments over a range of temperatures while holding the electrochemical potential (ECP) fixed. This requirement is consistent with Equations (6) and (11) and the discussion of these equations, above. The data reported here do not meet this requirement in that the coolant-borne hydrogen, not the ECP was held constant. Therefore, both the SIF exponent, m, and the apparent activation energy, Q, derived here by application of the HACF model to these data, are expected to differ from the values obtained with ECP held constant. However, as a practical manner, constant coolant-borne hydrogen is more representative of PWR plant operations so that the values obtained here are more appropriate to the intended application.

Conclusions

The Alloy 600 SCC crack growth rate data presented and discussed above clearly show interacting effects of stress and temperature on the CGR. Sensitivity to applied stress intensity factor is dependent on temperature and yield stress and the sensitivity to temperature is dependent on the applied stress intensity factor and yield stress. The yield stress is dependent on the alloy carbon concentration and the amount of cold work. The magnitudes of these sensitivities are dependent on crack growth orientation relative to deformation textures introduced by cold work. Data showing these phenomenological behaviors are well correlated using the HACF model equations. Physically based phenomenological models such as the HACF model provide increased confidence that engineering data correlations used in the disposition of defect indications have been derived based on an understanding of the mechanical, physical and corrosion phenomena contributing to SCC crack growth.

References

[1] W. C. Moshier and C. M. Brown, "Effect of Cold Work and Processing Orientation on Stress Corrosion Cracking of Alloy 600", Corrosion, 56, (2000) 307 – 320.

[2] M. O. Speidel and R. Magdowski, "Stress Corrosion Crack Growth of Cold Worked Nickel Base Alloy 600," Corrosion-Deformation Interactions CDI 92, ed. T. Magnin and J.M. Gras (Les Editions de Physique Les Ulis, 1993), 107-115.

[3] M. O. Speidel and R. Magdowski, "Stress Corrosion Cracking of Nickel Base Alloys in High Temperature Water," Sixth International Symposium on Environmental Degradation of Materials in Nuclear Power Systems – Water Reactors, ed. R. E. Gold and E. P. Simonen, (Warrendale, PA, The Minerals, Metals and Materials Society, 1993), 361-371.

[4] R. Magdowski, F. Vaillant, C. Amzallag and M. Speidel, "Stress Corrosion Crack Growth Rates of Alloy 600 in Simulated PWR Coolant," Eigth International Symposium on Environmental Degradation of Materials in Nuclear Power Systems – Water Reactors, ed. A. R. McIlree and S. M. Bruemmer, (La Grange Park, Il, USA, The American Nuclear Society, 1997), 333-339.

[5] F. Vaillant, C. Amzallag and J. Champredonte, "Crack Growth Rate Measurements of Alloy 600 Vessel Head Penetrations," Eigth International Symposium on Environmental Degradation of Materials in Nuclear Power Systems – Water Reactors, ed. A. R. McIlree and S. M. Bruemmer, (La Grange Park, Il, USA, The American Nuclear Society, 1997), 357-365.

[6] M. M. Hall, Jr., "Thermally Activated Dislocation Creep Model for Primary Water Stress Corrosion Cracking of Ni-Cr-Fe Alloys," Proceedings of International Symposium on Plant Aging and Life Prediction of Corrodible Structures, ed. T. Shoji and I. Shibata, NACE, (1997), 107-116.

[7] M. M. Hall, Jr. and D. M. Symons, "Hydrogen Assisted Creep Fracture Model for Low Potential Stress Corrosion Cracking of Ni-Cr-Fe Alloys", Symposium on Chemistry and Electrochemistry of Corrosion and Stress Corrosion Cracking: A Symposium Honoring the Contributions of R. W. Staehle, New Orleans, LA: TMS, (2001), 447-466.

[8] M. M. Hall, Jr. and D. M. Symons, "Constitutive Deformation Model for Analysis of Stress Corrosion Crack Tip Strain-Rates In Ni-Cr-Fe Alloy 600", Proceedings of the International Conference on Hydrogen Effects on Material Behavior and Corrosion-Deformation Interaction, Moran, WY, TMS/ASM, 2002.

[9] G. A. Young and J. R. Scully, "Evidence that Carbide Precipitation Produces Hydrogen Traps in Ni-17Cr-8Fe Alloys," Scripta Materialia, 36 (1997), 713-719.

[10] D. Caron, "A Study of the Correlation Between the Crack Growth Rate Susceptibility of Alloy 600 and the Nature of the Surface Film Formed in Primary Water", PhD Thesis, Direction de l'Energie Nucleaire, October 4, 2000.

[11] ASTM Standards, Vol. 3.1, E399-90, American Society for Testing and Materials, West Conshohocken, PA, (1999) 410.

[12] T. Cassagne and A. Gelphi, "Crack Growth Rate Measurements on Alloy 600 Steam Generator Tubing in Primary and Hydrogenated AVT Water," Sixth International Symposium on Environmental Degradation of Materials in Nuclear Power Systems – Water Reactors, ed. R. E. Gold and E. P. Simonen, (Warrendale, PA, The Minerals, Metals and Materials Society, 1993), 679-686.

[13] D. S. Morton, S. A. Attanasio, J. S Fish and M. K. Schurman, "Influence of Dissolved Hydrogen on Nickel Alloy SCC in High Temperature Water", Corrosion 99, NACE, 1999.

SCC Growth Rate of Nickel Based Alloy 132 in PWR Primary Water

T. Yonezawa*, K. Tsutsumi, H. Kanasaki*, K. Yoshimoto*, Y. Nomura*, S. Asada****

* *: Takasago R & D Center, Mitsubishi Heavy Industries, LTD.*
2-1-1 Shinhama Arai-cho Takasago Hyogo 676-8686 Japan

** *: Kobe Shipyard & Machinery Works, Mitsubishi Heavy Industries, LTD.*
1-1 Wadasaki- 1 Hyogo-ku Kobe 652-8585 Japan

ABSTRACT

To investigate the primary water stress corrosion cracking (PWSCC) crack growth rate (CGR) of nickel based alloy weld metal, many studies have been carried out on Alloy 182 and evaluation curves have been proposed. In Japan, Alloy 132 has been used instead of Alloy 182 from the viewpoint of hot cracking resistance. However, no PWSCC CGR data on Alloy 132 has been reported. In this study, we investigated the PWSCC CGR of Alloy 132 in comparison with the literature data on Alloy 182, and evaluated the effect of loading condition on the PWSCC CGR of Alloy 132.

We conducted SCC growth measurement tests on Alloys 132 and 82 weld metals at 325 ^{o}C in simulated primary water. Then we examined the effects of K value, periodic unloading interval and orientation of CT specimen on CGR. Based on the results obtained, we consider an evaluation curve for the CGR of Alloy 132 weld metal and recommended a test procedure of CGR.

Conclusions.

1) PWSCC CGR for Alloy 132 weld metal was remarkably affected by K value, from 20 to 35 MPa√m.
2) The PWSCC CGR of Alloy 132 in this study was not larger than that of Alloy 182 in the literature data.
3) The PWSCC CGR propagated along the dendrite was about 3 times faster than that perpendicular to the dendrite.
4) The periodic unloading method is not applicable for the PWSCC CGR measurement of nickel based alloy weld metals, to maintain a straight crack front.
5) The effect of periodic unloading on PWSCC CGR was observed. Periodic unloading is recommended to produce the inter-dendritic pre-crack, but constant loading is recommend for CGR measurement test with significant long holding time to eliminate the influence of fatigue.

I. INTRODUCTION

In Japan, maintenance guide rule as ASME Sec.XI for allowable stress corrosion cracking (SCC) flaw size is not established except austenitic stainless steels for BWRs. In order to complete data base for the maintenance guide rule for allowable SCC flaw size, the Japanese national project on SCC crack growth rate (CGR) measurement test program on the Alloy 600 and its weld metals of Ni based alloys for PWRs and BWRs has been started from April 2000. Before starting this project, authors have checked the propriety and applicability of periodic unloading method for the primary water stress corrosion cracking (PWSCC) CGR measurement test.

In western PWR plants, Alloy 182 is used for shielded metal arc welding (SMAW) method to Alloy 600 at the boundary of the reactor pressure vessel. In Japanese PWR plants, NIC 70A (trade name) was used for different welding method as the SMAW and consideration of resistance of hot cracking. The difference welding method means the difference of welding electric current as direct current for Alloy 182 or alternating current for NIC 70A. This welding material is nearly the same as Alloy 132 in AWS.

Alloy 82 is used for tungsten inert gas (TIG) or metal inert gas (MIG) or metal active gas (MAG) welding method.

Chemical compositions of Alloys 182, 132 and 82 are 67%Ni-15Cr%-8%Fe-7%Mn-1.8%Nb-0.5%Ti, 70%Ni-15%Cr-9%Fe-1%Mn-2.5%Nb, and 71%Ni-20%Cr-2%Fe-3%Mn-2.5%Nb-0.5%Ti, respectively. The chromium content of Alloy 82 is about 5% higher than that of Alloys 182 and 132. But, efficiency about the stabilization of solute carbon based upon niobium and titanium content is higher than that of Alloys 182 and 132.

The effect of chemical composition on the PWSCC susceptibility for Ni-Cr-Fe alloy as Alloy 600 is reported as follows;

The PWSCC susceptibility decreases with an increase of chromium content for Ni-Cr-Fe alloy, as shown in Figure 1[(1)] This reason is thought that the anodic dissolution of Ni-Cr-Fe alloy shall be restrained and also grain boundary chromium carbide as $M_{23}C_6$ must be dominant, with increasing of chromium content.[(1)] The PWSCC susceptibility increases by the addition of niobium for Alloy 600, as shown in Figure 2[(2)] This reason is thought that the chromium carbide as $M_{23}C_6$ hardly precipitate due to the niobium addition for the Alloy 600, because the niobium stabilizes the solute carbon as the NbC carbides.[(2)] The effect of titanium addition on the PWSCC susceptibility for Alloy 600 is not reported, but the stabilizing effect of titanium addition is basically same as niobium addition for Alloy 600. So, it can be easily estimated that the PWSCC susceptibility increases by the addition of titanium for Alloy 600. From the view point of efficiency about the stabilization of solute carbon, weight percentages of niobium has the same efficiency as the twice of the weight percentages of titanium, because the mass of niobium is about twice of that of titanium.

Therefore, the PWSCC susceptibility of Alloy 82 may be not so low.

The chromium content and efficiency about the stabilization of solute carbon based upon niobium and titanium content of Alloy 132 are basically same as them of Alloy 182. Therefore, the PWSCC susceptibility of Alloy 132 shall be same as that of Alloy 182.

In this study, we compared the PWSCC crack growth rate (PWSCC CGR) of Alloy 132 with the PWSCC CGR literature data on Alloy 182.[(3, 4, 5, 6, 7, 8)] We summarize this test and recommend PWSCC CGR measurement test techniques.

II. TEST METHODS

II. A. Material

A dissimilar metal welding model for the first stage of Japanese domestic PWR pressure vessels (PV) was manufactured by the shielded metal arc welding rod Alloy 132, as shown in Figure 3. That is, the dissimilar metal welding between type 316 austenitic stainless steel and SA508 cl.2 steel was performed by the shielded metal arc welding rod of Alloy 132 after the buttering of Alloy 82 on the SA 508 cl.2 steel.

The welding direction of the shielded metal arc welding by Alloy 132 is perpendicular to the cross section in Figure 3.

The specimens of Alloy 82 welded metal for PWSCC CGR measurement test were taken from the deposited metal coupon, as shown in Figure 4.

The post weld heat treatment was not conducted after the shielded metal arc welding in this model. All the specimens for PWSCC CGR measurement test were taken from Alloys 132 and 82 welded metals of this model.

The chemical composition and tensile properties of the Alloy 132 welded metal of this model are shown in Tables 1 and 2, respectively. The specification of the chemical compositions for Alloys 132 and 182 are also shown in Table 1. Alloy 182 contains titanium and niobium, but Alloy 132 does not contain titanium.

II. B Test specimen

1/2 TCT specimens were machined from the above Alloy 132 weld metal in accordance with ASTM standards E 399 as shown in Figure 5.

The specimen orientations are LS and TS when SCC propagation direction is along the dendrite, and LT when SCC propagation direction is perpendicular to the dendrite as shown in Figure 6. The specimen LS and LT orientations share a common crack plate, although the crack directions relative to the dendrite are different.

These specimens were slit by electro-discharge machining (EDM) and pre-cracked by fatigue in air, prior to SCC testing. The fatigue pre-crack was generated at a stress intensity factor range (delta K) of about 15 MPa$\sqrt{m}$, which is below 80% of K level at SCC test condition, 20 MPa$\sqrt{m}$. The pre-crack length was controlled to about 1 mm. After introducing of fatigue pre-crack, the specimens were 10% side grooved and washed with ultra-sonic wave cleaning system over 30 minutes in acetaldehyde to eliminate impurities.

II. C PWSCC test methods

The schematic of the SCC test equipment is shown in Figure 7. Water chemistry was controlled in the controlling tank. The water was pressurized by the high-pressure pump and then heated up to the test temperature by heater. The heated water was flowed into the autoclave for the SCC tests. The water was cooled by cooler and passed through the filter to remove contamination. The flow rate of the test water was about 20 liters per hour. The specimens were tested in refreshed autoclaves with simulated reactor coolant system (RCS) water chemistry of 1800ppm as boron, 3.5ppm as lithium and 30cc/STP·kg H_20

hydrogen. Dissolved oxygen was kept less than 5 ppb to meet the water chemistry at the beginning of the fuel cycle in typical Japanese PWRs. The water in the controlling tank was adjusted once per two weeks to meet target water chemistry. The test temperature near the specimen was measured by thermocouples in the auto-claves. The test temperature was controlled by the heaters located at the outside of autoclaves, to meet within ± 1 °C of the target temperature. The SCC tests were performed at 325 °C to meet the upper boundary of the target components in Japanese PWR plants.

SCC CGR measurement tests were conducted in active loading condition with K_I values of 20, 35 and 60 MPa√m based on the test data using 1/2 T CT specimens.[4] The K_I values of specimens for SCC CGR measurement were calculated using the formulations in ASTM standards E 399 and E 813.

The autoclave facility loaded the specimens and measured the SCC length using the reverse direct current (DC) potential difference technique. Figure 8 shows a schematic of the direct current potential drop method (DC PDM) system. The system consisted of a DC power supply, DC solid-state switch, voltmeter and computer. The specimen was electrically isolated from the auto-clave, DC current was 5 ampere and the interval of measurement was 3 minutes. Platinum wires, which had high corrosion resistance and small electric resistance, were used for current and voltage lead wires. It is difficult to measure accurate voltage of DCPDM in high temperature water due to the pseudo signal of thermo-electromotive force. So, reversed DCPDM was signal of thermo-electromotive force. So, reversed DCPDM was used to eliminate the effect of the pseudo signal.

The SCC length was estimated from the DC potential data using the master curve. The curve, which shows the relation between the DC potential and crack length, was obtained in air. However, the accuracy of the DCPDM for weld metal specimens is not always good because of the non-uniform crack front. So, the calculated crack lengths using reverse DCPDM were compared with SCC length measured by scanning electron microscopy (SEM). The average crack depth, which was obtained with dividing the area of SCC by the integrated length of PWSCC initiation grown from the fatigue pre-crack, was used for CGR calculation.

The loading conditions involve maintaining a constant load during the test with an unloading and reloading cycle of R = 0.7 (R ratio = minimum load / maximum load). The load increasing duration for starting up was 3 minutes and the unloading / reloading as periodic unloading was accomplished during 5 seconds, after each holding time of constant loading.

III. TEST RESULTS

The results of CGR measurement test are summarized in Table 3. Figure 9 shows the correlation between the K value and PWSCC CGR for Alloys 132, 82 and 182 weld metals. The testing parameters are the K value and orientation of the specimens, as TS and LS.

III. A The effect of K value on the PWSCC CGR

In the PWSCC CGR measurement test for the initial K value of 20 MPa√m, the PWSCC did not grow from the fatigue pre-crack in the specimens, during 1000 hours of SCC tests. Figure 10 shows the results

of crack length estimated from PDM signal versus testing time for the TS specimen. Vertical axis shows the crack length estimated from PDM signal. Constant loading was applied to these specimens from the starting point to 200 hours. But, the PDM signal was not changed during 200 hours testing. So, the periodic unloading technique, which R was 0.7 and holding time was 9000 sec, was applied to these specimens after constant load testing during 200 hours. However, the changing of PDM signal as growth of PWSCC was not observed during 1000 hours. Also, no IGSCC was observed at post-test destructive examination. The estimated CGRs of these specimens were evaluated less than 5.6×10^{-12} (m / s), based on 0.02 mm as the detection limit of SCC growth by PDM.

In the PWSCC CGR measurement test for the initial K value of 35 MPa√m, the PWSCC was grown from the fatigue pre-crack in the specimens under the periodic unloading condition. Figures 11 and 12 show the results of crack length estimated from PDM signal vs. testing time for the TS and LS specimens respectively. The vertical axis shows the crack length estimated from the PDM signal corrected based on SEM measurements of the crack depth. The PDM signal changed as the growth of PWSCC was observed after the initial K value of 35 MPa√m for the TS and LS specimens. The estimated CGRs of these specimens were scattered in a two-digit range according to material conditions.

In the PWSCC CGR measurement test for the initial K value of 60 MPa√m, the PWSCC was grown from the fatigue pre-crack in the specimens under the periodic unloading condition. The estimated CGRs of 60 MPa√m are nearly equal to those of 35 MPa√m in the LS specimen.

III. B The effect of the kind of material on the PWSCC CGR

Within the data in this study, the CGRs of Alloy 132 were revealed to be higher than the CGRs of Alloy 82 as shown in Figure 9. Compared with the same oriented specimen along the dendrite direction (LS direction), the CGRs of Alloy 132 (□) were accelerated by a factor larger than 2 to 8 from the CGRs of Alloy 82 (○).

III. C The effect of the dendrite direction on the PWSCC CGR

The CGR along the dendrite direction (LS, TS) was about 3 to 10 times larger than that perpendicular to the dendrite direction (LT). However, no significant difference observed between the CGR along to the same parallel to the dendrite direction (LS, TS).

III. D Comparison of the CGRs between Alloys 182 and 600

In this study, the CGRs of Alloy 132 were basically same as the evaluated CGR curve of Alloy 182 [2] ($da/dt=1.40 \times 10^{-11}$ $(K\text{-}9)^{1.16}$) and larger than that of Alloy 600 ($da/dt=2.23 \times 10^{-12}$ $(K\text{-}9)^{1.16}$) That is, the evaluated CGR curve for Alloy 182 can be used to estimate CGRs for Alloy 132 and Alloy 82 welds.

III. E Fractography

Figures 13, 14 and 15 show typical results of fractography by SEM on the fracture surface of LS and TS specimens after testing, respectively.

On these fracture surfaces, the PWSCC was grown from the fatigue pre-crack, and the cracks were grown along the inter-dendrite boundary. But the crack front of these inter-dendritic PWSCC (ID PWSCC) was not uniform and the area of no ID PWSCC initiation zone was also observed at the fatigue pre-crack tip. Figure 15 shows that the crack propagation path was inter-dendrite and parallel direction for dendrite.

The average crack depth of ID PWSCC was obtained by dividing the area of SCC by specimen thickness, as described above. The average crack depths of ID PWSCC for TS and LS specimens were 0.7 mm and 1.3 mm, respectively. D.C. potential crack growth rates for these specimens were corrected based on these values.

Figures 16 and 17 show the fractographic features for LT specimen of Alloy 132. The PWSCC was also observed to have grown from the fatigue pre-crack in this specimen, but the propagation path of the cracks was complicated SCC propagated perpendicular to dendrite direction and its front was not uniform We will continue the study regarding to the relation between SCC growth mechanism and orientation of test specimen.

IV. DISCUSSION

The effect of periodic unloading on the PWSCC CGR of nickel based Alloy 132 weld metal in simulated PWR primary water was evaluated based upon the above results, from the viewpoints of maintaining a straight crack front, effect of the holding time on accelerating the SCC CGR, and reducing the SCC incubation time.

IV. A The maintaining of the straight crack front

A straight crack front was not gained for all tested specimens of the Alloys 132 and 82 in spite of periodic unloading. The same tendency was reported by Brown for Alloy 82.[6]

In the PWSCC CGR measurement test with the periodic unloading technique for mother metal Alloy 600 in simulated PWR primary water, a straight crack front was reported by Andresen and Foster et al.,[9,10] but in this study, a straight crack front was not obtained for weld metal Alloys 132 and 82 in simulated PWR primary water in spite of periodic unloading. The reason for this difference seems to be the affect of the grain size and the residual stress. That is, PWSCC susceptibility is influenced by the metallurgical state of the grain boundaries, such as crystal direction and segregation.[11] In the weld metal, the metallurgical state of the grain boundaries is complicated and residual stress remains in the weld metal after cutting the specimens.

Future research on the effect of grain size and residual stress on the shape of PWSCC front for weld metal is required to maintain straightening of the PWSCC crack.

IV. B The effect of the holding time on acceleration of the SCC CGR

The relation between the holding time and PWSCC CGR for the Alloy 132 is shown in Figure 18. In the LT orientation, CGRs at 360 and 1080 sec. holding times are about three times greater than at 9000 sec. But CGRs at 9000 sec. holding times are comparable with those obtained under constant load. In the LS and TS orientations, CGRs at 9000 sec. holding times is about twice greater than the constant load. The holding time effects for LS and TS orientations are greater than LT orientation. Vaillant et al also reported that CGRs under periodic unloading condition were greater than that under constant loading condition.[12,13,14] In this study, it is also estimated that the CGRs decrease with an increase of holding time, in this range as shown in Fig. 18.

The CGR of Alloy 82 under periodic unloading condition was nearly equal under constant loading condition, compared with that of Alloy 132. However, the CGR data of Alloy 82 is limited. Further data is required to perform quantitative analysis on the CGR of Alloy 82.

IV. C Reducing SCC incubation time

In this study, the PWSCC CGR measurement test was performed under constant loading, and then due to no change of the PDM signal, under periodic unloading. As a result, the PDM signal was immediately changed after converting to periodic unloading from constant loading. The ID PWSCC pre-crack under the periodic unloading technique is useful for shortening the incubation time for PWSCC initiation.

On the other hand, the PWSCC CGR measurement test was performed by constant loading after being converted to periodic unloading due to no change of the PDM signal by constant loading. The PDM signal was immediately changed after converting to periodic unloading from without periodic unloading.

EdF/CEA reported that the use of cyclic loading as a periodic unloading technique significantly increases the CGRs.[12] They indicated that the CGRs depend on the yield strength level of the materials [12] and the CGRs for low susceptible materials under periodic unloading technique were three times larger than that by constant loading, but the CGRs for the high susceptible materials under periodic unloading technique were the same as that under constant loading.[12]

It is necessary to consider not only the influence of periodic unloading but also the influence of yield strength at PWSCC CGR.

It is suggested by these results that recommended holding times will vary for different materials and specimen orientations. In figure 16, Alloy132 (LT orientation) and 82 are small influence of fatigue in 9000sec holding time. But Alloy132 (LS and TS orientations), SCC CGRs in 9000 sec holding time are greater than CGRs of constant load.

Periodic unloading is recommended for producing the ID pre-crack for the PWSCC CGR measurement test. But, the effect of periodic unloading on the real PWSCC CGR is not always well known. So, it seems that the ID PWSCC CGR measurement test should be conducted under constant loading or trapezoidal wave with a sufficiently long holding time to eliminate the influence of fatigue.

V. CONCLUSIONS

This study conducted CGR measurement tests on Alloys 132 and 82 under several conditions of periodic unloading. The main conclusions are as follows:

(1) PWSCC CGR for Alloy 132 welded metal was remarkably affected by K value. The PWSCC was grown at 35 and 60 MPa√m of K value, but not grown at 20MPa√m of K value at 325 °C.

(2) The PWSCC CGR of Alloy 132 in this study was basically same as that of Alloy 182 reported in the literature.

(3) The PWSCC was propagated along the dendrite, CGRs of the TS and LS specimens were about 3 to 10 times larger than that of the perpendicular direction LT specimen.

(4) The crack front of PWSCC on the fracture surface of specimens was not uniform, even under periodic unloading.

(5) Periodic unloading is recommended for producing the ID pre-crack for the PWSCC CGR measurement test. But, the effect of periodic unloading on the real PWSCC CGR is not always well known. So, it seems that the ID PWSCC CGR measurement test should be conducted under constant loading or trapezoidal wave with sufficiently long holding time to eliminate the influence of fatigue.

REFERENCES

1) T.Yonezawa,N.Sasaguri,K.Onimura: "Effects of Metallurgical Factors on Stress Corrosion Cracking of Ni-base Alloys in High Temperature Water", Proceedings of the 1988 JAIF International Conference on Water Chemistry in Nuclear Power Plants, (1988), P.490
2) T.Yonezawa, K.Onimura: "Effect of Chemical Compositions and Microstructure on the Stress Corrosion Cracking Resistance of Nickel Base Alloys in High Temperature Water", Proceedings of EVALMAT 89 Vol.1, (1989), P.235
3) M. ITOW, Y. ABE, A. SUDO and T. TAKENO: "Crack Growth Rates of Alloy 182 in High Temperature Water ", Proceedings of the 7th Degradation Conf. 1995
4) W. BAMFORD, JOHN FOSTER and RAJ PATHANIA: "An Investigation of Alloy 182 Stress Corrosion Cracking in Simulated PWR Environment ", Proceedings of the 9th Degradation Conf. 1999
5) THIERRY CASSAGNE, DIDIER CARON, JACQUES DARET and YVES LEFEVRE "Stress Corrosion Crack Growth Rate Measurements in Alloy 600 and 182 in Primary Water Loops Under Constant Load ", Proceedings of the 9th Degradation Conf. 1999
6) C.M.BROWN and W.J.MILLS: "Effect of Water on Mechanical Properties and Stress Corrosion Behavior of Alloy 600, Alloy 690, EN82H Welds, and EN52 Welds", Corrosion Vol.55, p.173, 1999
7) W. BAMFORD, L. TUNON-SANJUR, K. HSU, J. FOSTER and A. MCLLREE: "Alloy 182 Weld Crack Growth, and Its Impact on Service-Induced Cracking in Operating PWR Plant Piping ", Proceedings of the 10th Degradation Conf. 2001
8) C. AMZALLAG: "Measurements of Stress Corrosion Cracking Propagation Rates in Weld Alloys 182 in Primary Water of PWR " Proceedings of the 10th Degradation Conf. 2001
9) P. ANDRESEN "Experimental Quality Guidelines for SCC Testing",

10) J. FOSTER, W. BAMFORD and RAJ. PATHANIA: "Effect of Materials Variables on Alloy 600 Crack Growth Rates", Proceedings of the 8th Degradation Conf. (1997)
11) T.YONEZAWA "Alloy 600 Round Robin Test", ICG-EAC/IASCC Meeting 2001
12) F.VAILLANT, S.LE HONG: "Evaluation des Vitesses de Propagation en Milieu Primaire de Materiaux de Traversees de Cuve en Alliage 600 et de Metaux Deposes en Alliage 182", EdF Proprietary Report, HT-44/96/024/A, 1997
13) F. VAILLANT, C. AMZALLAG, and J. CHAMPREDONDE: "Crack Growth Rate Measurements of Alloy 600 Vessel Head Penetrations", Proceedings of the 8th Degradation Conf. 1997
14) F. VAILLANT and C. AMZALLAG: "Crack Growth Rates on Alloy 600 in Primary Water in Laboratory Conditions ", ICG-EAC/IASCC Meeting, 1999

Table 1 Chemical compositions of Alloy 132 and 82 weld metal

	Chemical Composition (%)										
	C	Si	Mn	P	S	Ni	Cr	Ti	Nb	Cu	Fe
Alloy 132 Specification	<0.08	<0.5	2.0-3.5	<0.015	<0.015	>68.0	13 –17	-	1.5-4.0	<0.5	<11
Alloy 132 Check	0.04	0.22	2.9	0.003	0.001	71.0	14.5	-	1.85	0.02	9.49
Alloy 182 Specification	<0.10	<1.0	5.0-9.5	<0.03	<0.015	59.0 min.	13 – 17	<1.0	1.0-2.5	<0.50	<10
Alloy 82 Specification	<0.10	<0.5	2.5-3.5	<0.03	<0.015	67.0 min.	18- 22	<0.75	2.0-3.0	<0.50	<10
Alloy82 Check	0.04	0.25	2.86	0.005	0.001	72.87	19.03	0.40	2.44	0.03	Bal.

Table 2 Tensile properties of Alloy 132 and 82 weld metal

	UTS (MPa)	0.2% YS (MPa)	Elongation
Alloy 132	>551	>241	>30
Test Results	608	379	45
Alloy 82 Specification	>550	–	>30
Test Results	678	422	46

Table 3 Summary of Alloy 132 and 82 crack growth rate measurement test

Material	Environ-ment	Speci-men	Orienta-tion	K (MPa√m)	Periodic Unloading	Testing Time (hrs)	IGSCC area /thickness (%)	CGR da/dt (m/s)	Modified CGR da/dt (m/s)	T.P. No.
Alloy132	Simulated PWR Primary Water DO<5ppb DH=30cc/kg B:1800ppm Li:3.5ppm 325°C	1/2TCT	TS	20	R=0.7, Holding Time 9000s.	1000	-	<5.6E-12	<5.6E-12	MG7-1
					Constant Load	200		Not grown	Not grown	
		1/2TCT		35	R=0.7, Holding Time 9000sec.	950	75.6	2.4E-10	3.2E-10	MG7-2
					Constant Load	200		Not grown	Not grown	
		1/2TCT	LS	20	R=0.7, Holding Time 9000s.	1000	-	<5.6E-12	<5.6E-12	MG7T-1
					Constant Load	200		Not grown	Not grown	
		1/2TCT		35	R=0.7, Holding Time 9000s.	800	61.8	5.5E-10	8.9E-10	MG7T-2
					Constant Load	200		Not grown	Not grown	
		1/2TCT	LS	35	R=0.7, Holding Time 1080s.	200	50.0	1.67E-10	3.3E-10	132-2
					R=0.7, Holding Time 9000s.	200		5.6E-11	1.1E-10	
		1/2TCT		60	R=0.7, Holding Time 9000s.	439	67.6	4.0E-10	5.9E-10	132LS-1
		1/2TCT	TS	35	R=0.7, Holding Time 9000s.	800	65.0	2.5E-10	3.9E-10	MG7-5
					Constant Load	650	65.0	1.1E-10	1.7E-10	
		1/2TCT	LT	35	R=0.7, Holding Time 1080s.	350	50.6	8.3E-11	1.6E-9	MG7L-1
					R=0.7, Holding Time 9000s.	950	50.6	2.2E-11	4.4E-10	
					Constant Load	600	50.6	2.5E-11	4.9E-10	
		1/2TCT		35	R=0.7, Holding Time 360s.	800	100	8.3E-11	8.3E-11	132-LT2
					R=0.7, Holding Time 9000s.	300		2.8E-11	2.8E-11	
Alloy82		1/2TCT	LS	35	R=0.7, Holding Time 9000s.	349	4.5	4.9E-12	1.1E-10	82-3
		1/2TCT		35	R=0.7, Holding Time 9000s.	400	10.7	3.3E-11	3.1E-10	82-2
					Constant Load	100		3.3E-11	3.1E-10	

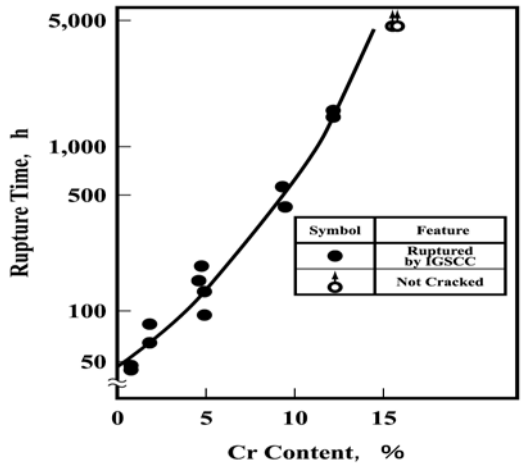

Fig 1 Effect of Cr content on the stress corrosion cracking resistance of solution annealed Ni base-Cr-Fe alloys in 360℃ high temperature water using by constant load stress corrosion cracking test (applied stress is 2.4 × 0.2% Proof stress)

Alloy	Annealing Temp. (℃)	Exposure Time (h) 1,000 5,000 10,000
Nb Add. Alloy 600	950	
LT.Ann. Alloy 600	900	

No Crack Crack

Fig 2 Effect of Nb addition on the sress corrosion cracking resistance of annealed Alloy 600 in 360℃ high temperature water, using by prestrained U bent specimen.

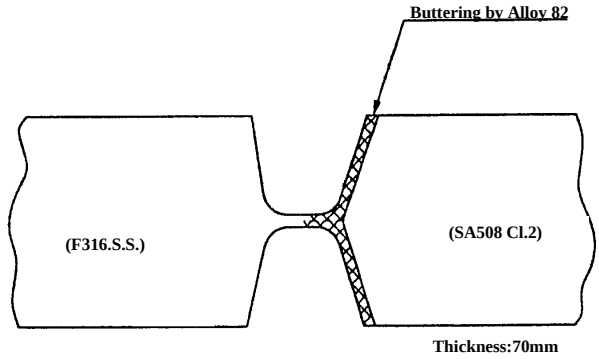

Figure 3 Welding joint configuration of dissimilar metal arc welding model by Alloy 132

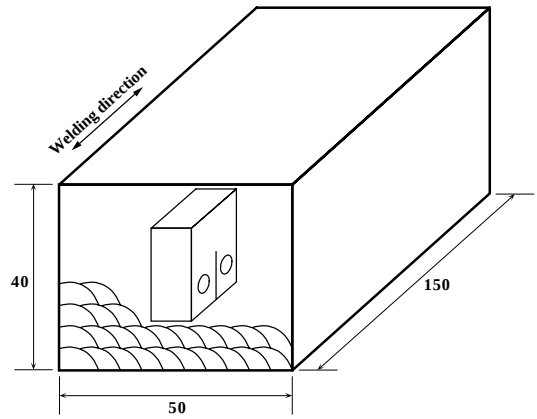

Figure 4 Machining orientations of CT specimens from deposited metal model of TIG welding by Alloy 82

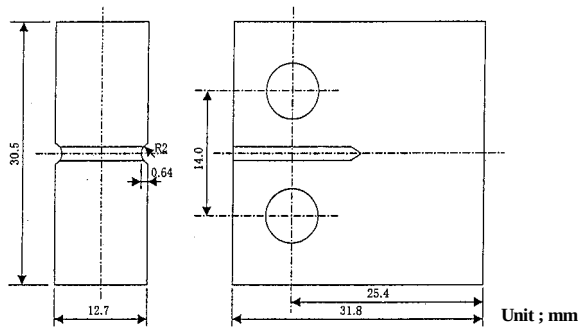

Figure 5 Configuration of 1/2 CT specimen

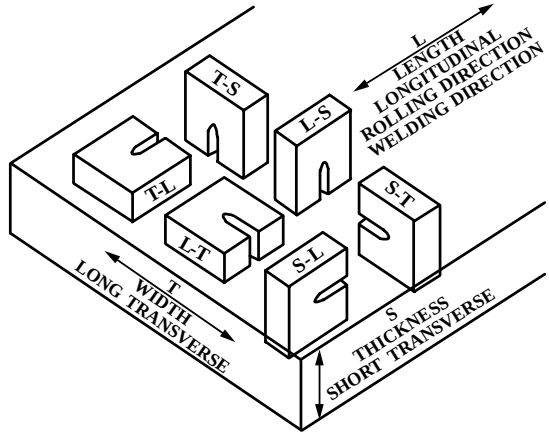

Figure 6 Terminology used for orientation of cracks in the test specimens with respect to the weld

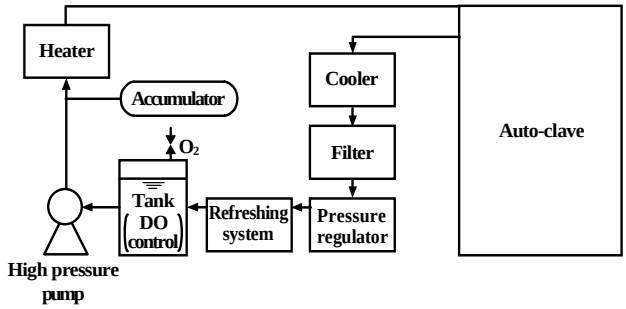

Figure 7 Schematic of the SCC test equipment

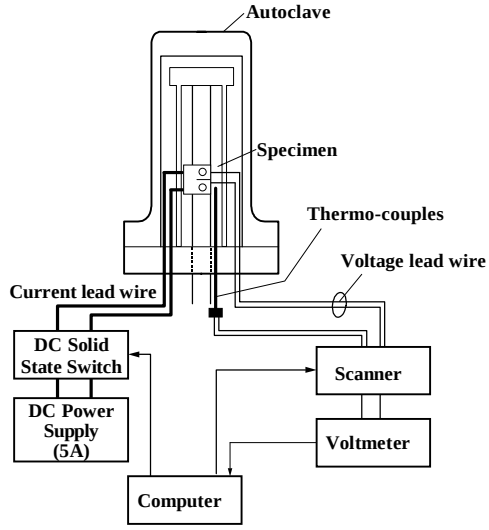

Figure 8 Schematic of the CGR on-line monitoring system

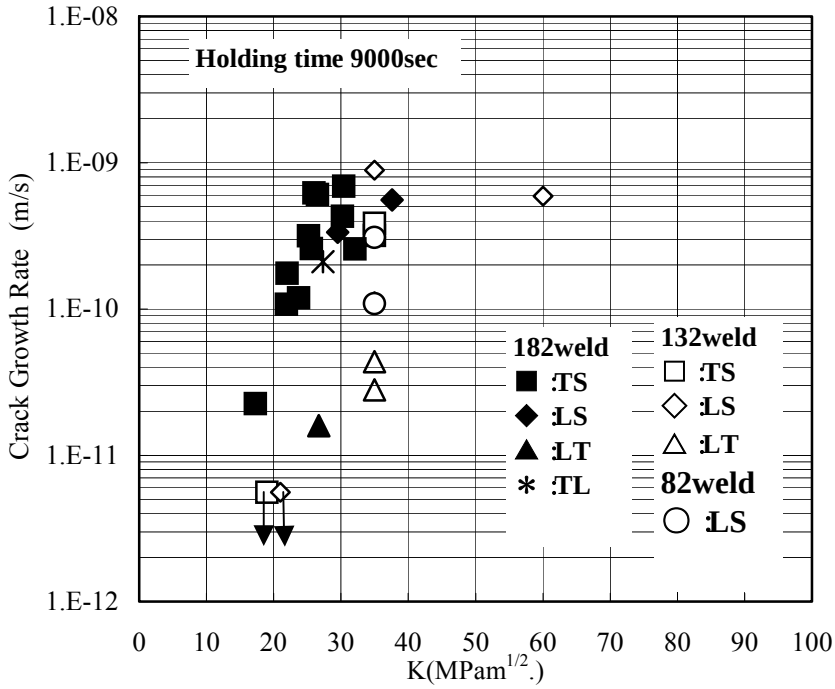

Figure 9 Comparison between CGR of Alloy 132 ,82 and 182 welds

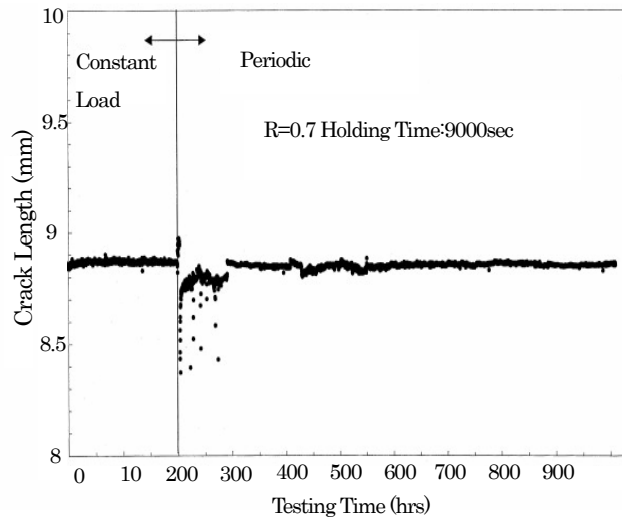

Figure 10 CGR on-line monitoring results (K=20MPa√m, TP. No. MG7-1)

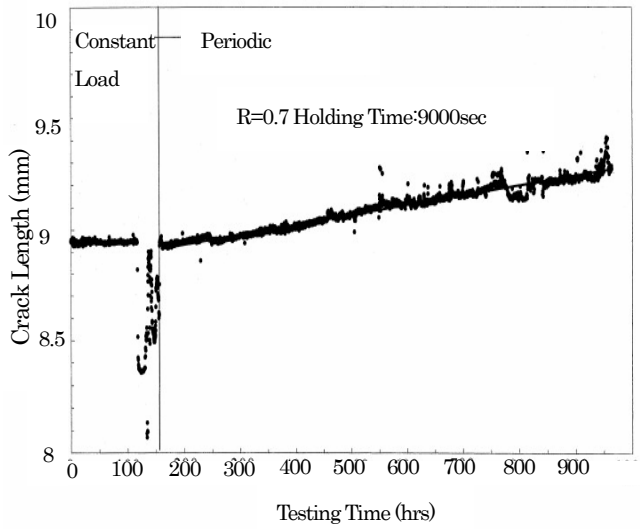

Figure 11 CGR on -line monitoring results (K=35MPa√m, TP. No. MG7-2)

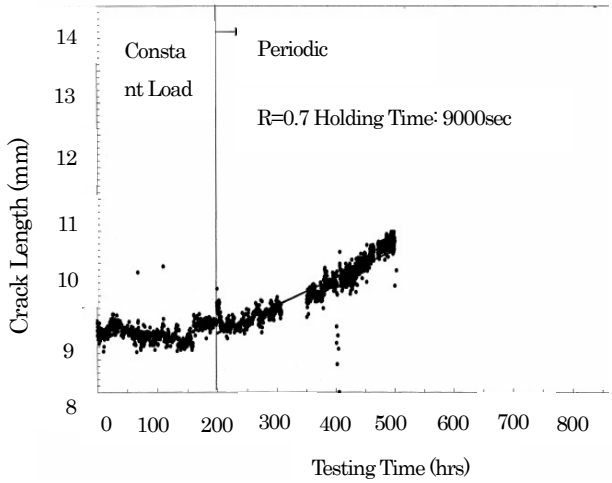

Figure 12 CGR on line monitoring results (K=35MPa√m, TP. No. MG7T-2)

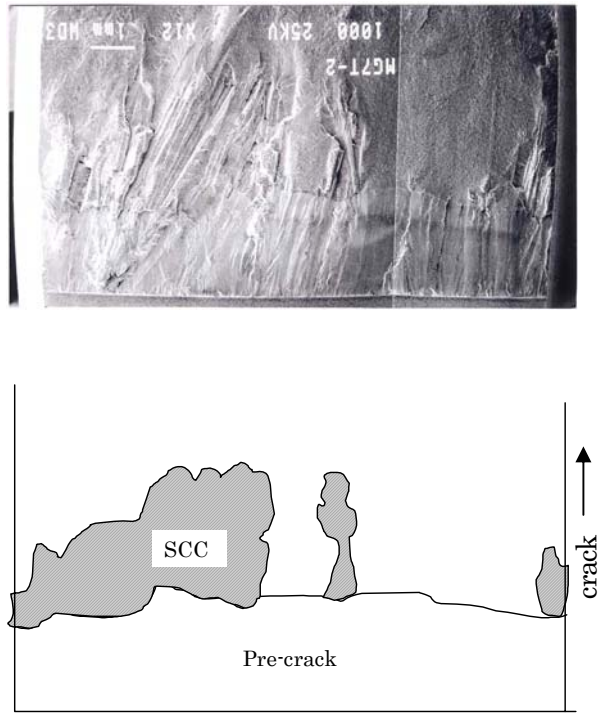

Figure 13 Fractography of LS specimen (K=35MPa√m, TP.No.MG7T-2)

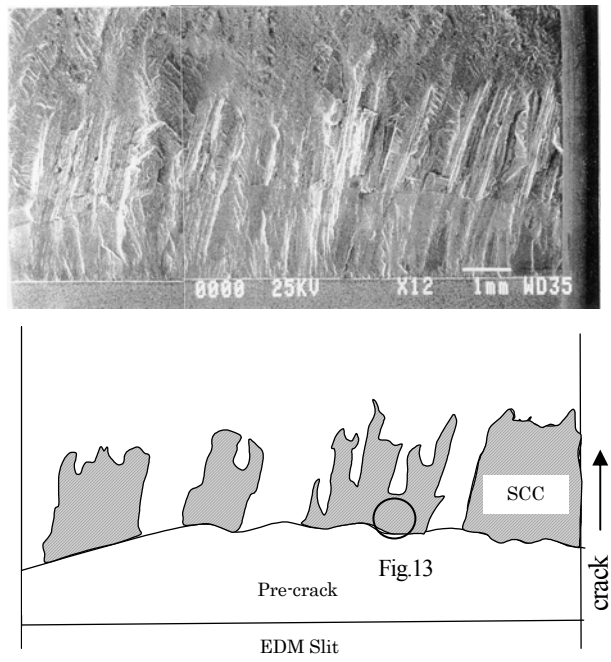

Figure 14 Fractography of TS specimen(K=35MPa√m, TP.No.MG7-5)

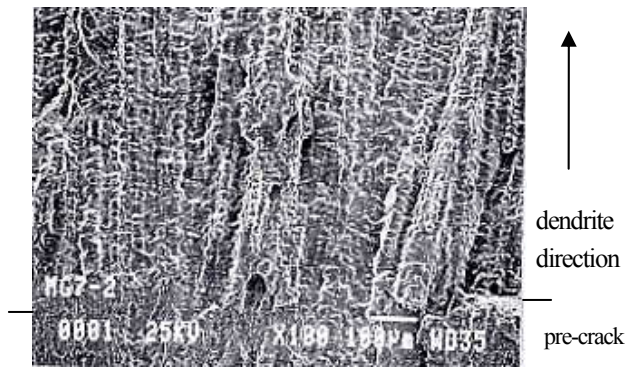

Figure15 Magnification of TP. No. MG7-5 (Parallel to dendrite)

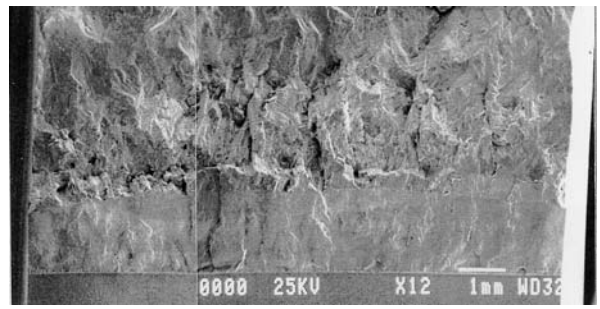

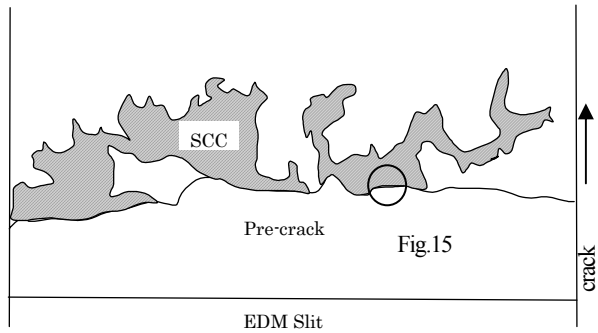

Figure 16 Fractography of LT specimen (K=35MPa√m, TP. No. 132-LT2)

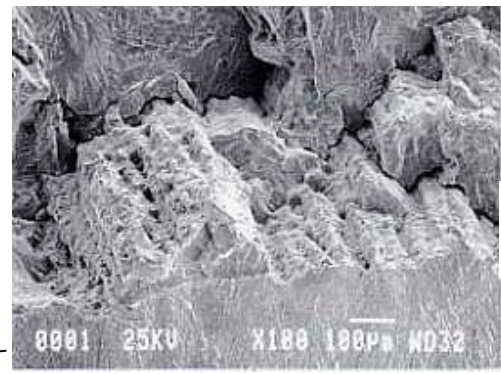

dendrite direction

pre-crack

Figure17 Magnification of TP. No. 132-LT2 (Perpendicular to dendrite)

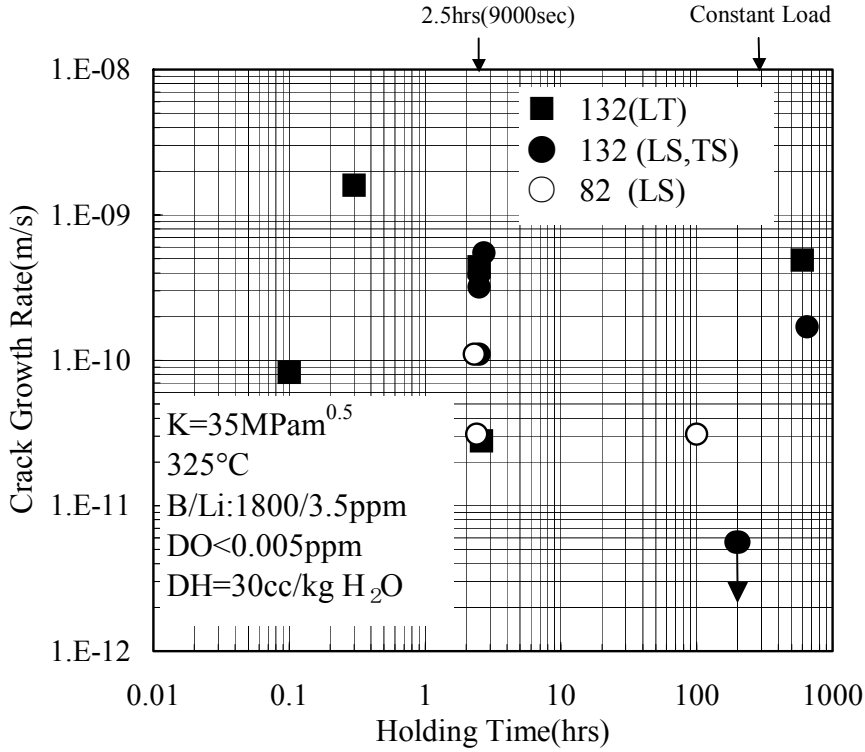

Figure 18 The effect of holding time for cyclic loading on CGRs

The Stress Corrosion Crack Growth Rate of Alloy 600 Heat Affected Zones Exposed to High Purity Water

George A. Young, Nathan Lewis, and David S. Morton
Lockheed Martin Corporation
Schenectady, NY 12301-1072

Abstract

Grain boundary chromium carbides improve the resistance of nickel based alloys to primary water stress corrosion cracking (PWSCC). However, thermal cycles from fusion welding can solutionize beneficial grain boundary carbides, produce locally high residual stresses and strains, and promote PWSCC in the heat affected zone (HAZ). The present research investigates the crack growth rate of an A600 HAZ as a function of test temperature and of electrochemical potential. The A600 HAZ was fabricated by depositing EN82H filler metal onto a mill-annealed A600 plate via gas tungsten arc welding. Fracture mechanics based, stress corrosion crack growth rate testing was performed in high purity water between 600°F and 680°F at an initial stress intensity factor of 40 ksi√in. The HAZ samples exhibited significant SCC, entirely within the HAZ at all temperatures tested. While the HAZ samples showed the same temperature dependence for SCC as typical A600 base material (HAZ: 29.8 ± 11.2 $|_{95\%}$ kcal/mol vs. A600 Base: 34.7 ± 4.21 $|_{95\%}$ kcal/mol), the crack growth rates were ~30X faster than the A600 base material tested at the same conditions. Similar to A600 base metal, the A600 HAZ exhibited a maximum crack growth rate when tested near the Ni/NiO phase transition. The increased crack growth rate of the A600 HAZ relative to the base metal is attributed to fewer intergranular chromium rich carbides and to increased plastic strain in the HAZ.

Background

Nickel-chromium-iron alloys such as Alloy 600 (A600) and Alloy 690 (A690) are often used in nuclear environments due to their resistance to general corrosion, localized corrosion, and to stress corrosion cracking (SCC). When used in deaerated primary water environments, A600 and A690 are heat treated to precipitate chromium rich carbides on the grain boundaries to maximize the resistance of these alloys to primary water stress corrosion cracking (PWSCC). In A600, the carbide can be Cr_7C_3 or $Cr_{23}C_6$, while in A690, the $Cr_{23}C_6$ precipitate is most common. However, fusion welding can solutionize grain boundary carbides and produce increased residual tensile stresses in the HAZ [1] that may render the heat affected zone (HAZ) more susceptible to primary water stress corrosion cracking (PWSCC) than the unaffected base metal.

Primary water SCC has been reported in commercial A600 control rod drive mechanism (CRDM) head penetrations near the A600 / E-182 weld interface [2-6]. In the commercial CRDM cracking, an as welded, partial penetration shielded-manual-arc-weld produces locally high residual tensile stresses on the order of 100 ksi [1] and may solutionize intergranular chromium carbides adjacent to the weld deposit [2]. The CRDM cracking appears to exhibit three distinct locations of cracking: (1) from the A600 head penetration ID toward the OD [2, 3], (2) in the E-182 J-groove weld [3, 7], and (3) near the interface of the A600 penetration OD and the E-182 J-groove weld (*i.e.* near or possibly in the A600 heat affected zone) [4, 5, 8].

In spite of concerns with HAZ SCC, limited data exist for the crack growth rates of heat affected zones. In part, this is due to the small scale of material affected, typically on the order of ~1 mm in width for gas-tungsten-arc-welding (GTAW). Furthermore, a HAZ is not uniform in its structure or composition since there is a temperature gradient from the edge of the fusion zone into the base metal. Near the fusion zone, welding temperatures can solutionize precipitates, cause local melting via constitutional liquation, induce recrystallization, and promote diffusional segregation of alloying elements or environmental contaminants (*e.g.* hydrogen). Similarly, thermal cycles from multi-pass welds or from post-weld heat treatments may cause precipitation or elemental segregation to grain boundaries.

Given the complex thermal history of a multi-pass weldment, fabrication of a bulk HAZ sample (typically via Gleeble methods) is a difficult task. The distance away from the fusion zone that is of interest must be defined, since this will dictate the relevant thermal cycles. Once the distance from the fusion zone is selected, parameters that must be defined include: (1) the peak temperature, (2) the hold time at the peak temperature, (3) the appropriate mechanical conditions during thermal cycles, (4) the cooling rate, (5) the thermo-mechanical effects of subsequent weld beads and (6) the appropriate post weld heat treatment. Since there is no *a priori* way of determining the precise distance away from the fusion zone that is most susceptible to SCC, testing of simulated HAZ's likely involves multiple samples with a range of thermal histories.

Instead of testing a simulated HAZ, the present research elected to test samples machined from an actual weldment. The challenge of this method is to (1) precisely machine the notch of the compact tension specimen in the HAZ and (2) to ensure that the fatigue precrack remains in the HAZ. Once the end of the fatigue precrack is in the HAZ, it is believed that SCC will seek the most susceptible path in terms of microstructure, microchemistry, and residual stresses and strains. In this manner, reliable data can be obtained to characterize the growth rate of PWSCC in HAZ's [9, 10].

Experimental Procedure

Materials

The compositions of the A600 and EN82H weld wire used in this study are given in Table 1. The HAZ specimens were machined from the interface between the 3" thick A600 plate and a 3" thick multi-pass, automatic gas-tungsten-arc-weld (GTAW). The GTAW was deposited with the parameters given in Table 2. The weld deposit was approximately 3" high x 3.25" wide x 15" long while the base plate was nominally 3" thick x 12" wide x 24" long. No post weld heat treatment was employed.

Table 1. *Chemical Compositions of Alloy 600 and EN82H Filler Metal*

Alloy	Heat	Ni	Cr	Fe	C	Mn	Si	Cu	Nb+Ta	Ti
A600	*44639*	76.37	14.74	7.35	0.071	0.350	0.31	0.020	---	---
EN82H	YM7553	71.5	20.1	2.39	0.04	2.88	0.08	0.010	2.3	0.47

Table 2. *Summary of Welding Parameters Used to Make the EN82H Weld Deposit*

Filler Metal	Polarity	Shielding Gas	Current (Amps)	Voltage (Volts)	Travel Speed (in./min.)	Wire Feed (in./min.)
0.045" dia. EN82H	DCSP	95%Ar/5%H_2	310	12.5	6.5	180

Stress Corrosion Testing

Compact tension (CT) specimens (1.0T) were machined from the base material and the heat affected zone in the S-L orientation. In the HAZ samples, the notch root of the CT specimen was in the HAZ as shown schematically in Figure 1. In order to facilitate precise location of the notch, oversized machining blanks were polished and etched prior to machining. After machining, the specimens were fatigue precracked approximately 100 mils beyond the machined notch and tested in hydrogen deaerated water under constant load to determine their SCC growth rate. The nominal conditions of the SCC testing are given in Table 3. The dissolved hydrogen concentrations were chosen to be at an approximately constant electrochemical potential (~0 to +10mV) relative to the Ni/NiO phase stability line. Additional details of the Ni/NiO phase stability can be found in References [11, 12].

Table 3. *Parameters Used in the High Purity Water Stress Corrosion Tests*

Temperature (^oF / ^oC)	Hydrogen (scc/kg)	Approximate ΔECP from Ni/NiO (mV)	Initial Stress Intensity Factor (ksi $\sqrt{in}$)
600 / 316	9	+2	40
640 / 338	1	-41	40
	18	+6	40
	120	+56	40
680 / 360	30	+6	40

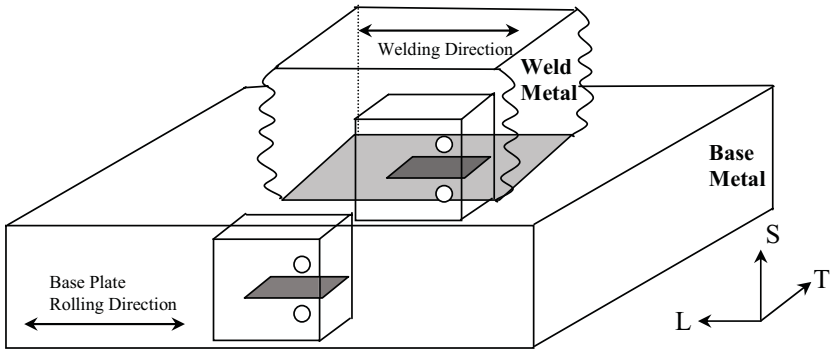

Figure 1. *Schematic of the HAZ specimen and base metal specimen orientation relative to the weld deposit. For the HAZ specimens, the notch tip lies in the HAZ. The sketch is not to scale.*

Results and Discussion

Specimen Fabrication

For the HAZ samples, post-test inspection revealed that all of the machined notches, fatigue precracks, and subsequent SCC were located within the HAZ. The location of a typical notch and precrack is shown in Figure 2. For some specimens, the notch and precrack were located closer to the EN82H weld metal. As will be shown below, it appears that in the weld investigated, the preferred SCC plane is approximately 20 mils (~0.5 mm) from the EN82H / A600 interface.

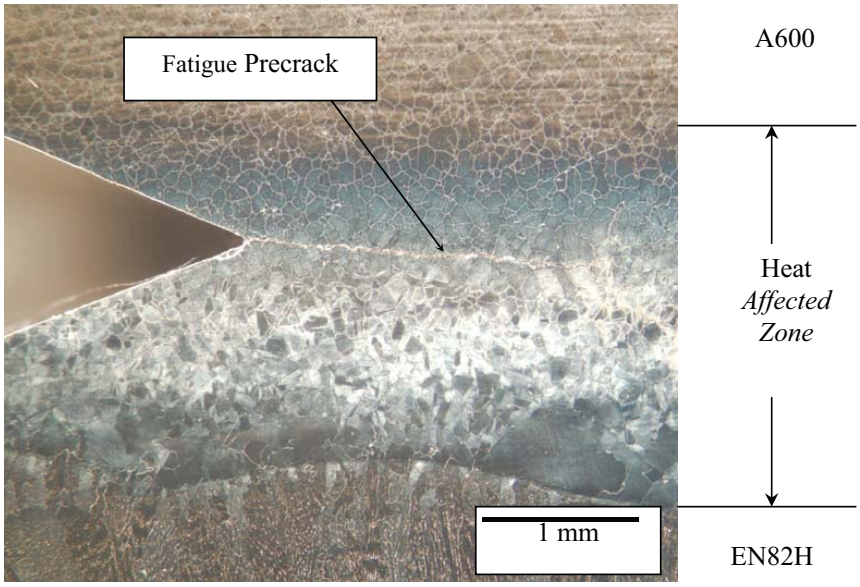

Figure 2. *Light macrograph of the CT specimen notch and fatigue precrack. Note that the precrack is entirely within the A600 HAZ. 8:1 Phosphoric Acid, Electrolytic Etch.*

A600 Base and A600 HAZ Crack Growth Rates

In-situ instrumentation of the crack mouth opening displacement was conducted with linear variable displacement transducers (LVDT's). The LVDT instrumentation was used to define the start of crack growth. However, instrumentation was not used to determine the crack growth rates. Since out of plane cracking and extensive crack branching were observed with the HAZ samples (and likely bias the instrumentation) crack growth rates were calculated from visual measurements of the crack lengths. To facilitate crack measurement, the samples were heat tinted prior to measurement and thirty separate measurements across the CT specimen width were used to determine the average and maximum crack lengths. The SCC test results are summarized in Figure 3 and show that the crack growth rates for HAZ samples range between ~0.5 mils/day at 600°F to ~3.6 mils/day at 680°F. Relative to the A600 base plate (squares) the HAZ samples (circles) crack approximately 30X faster.

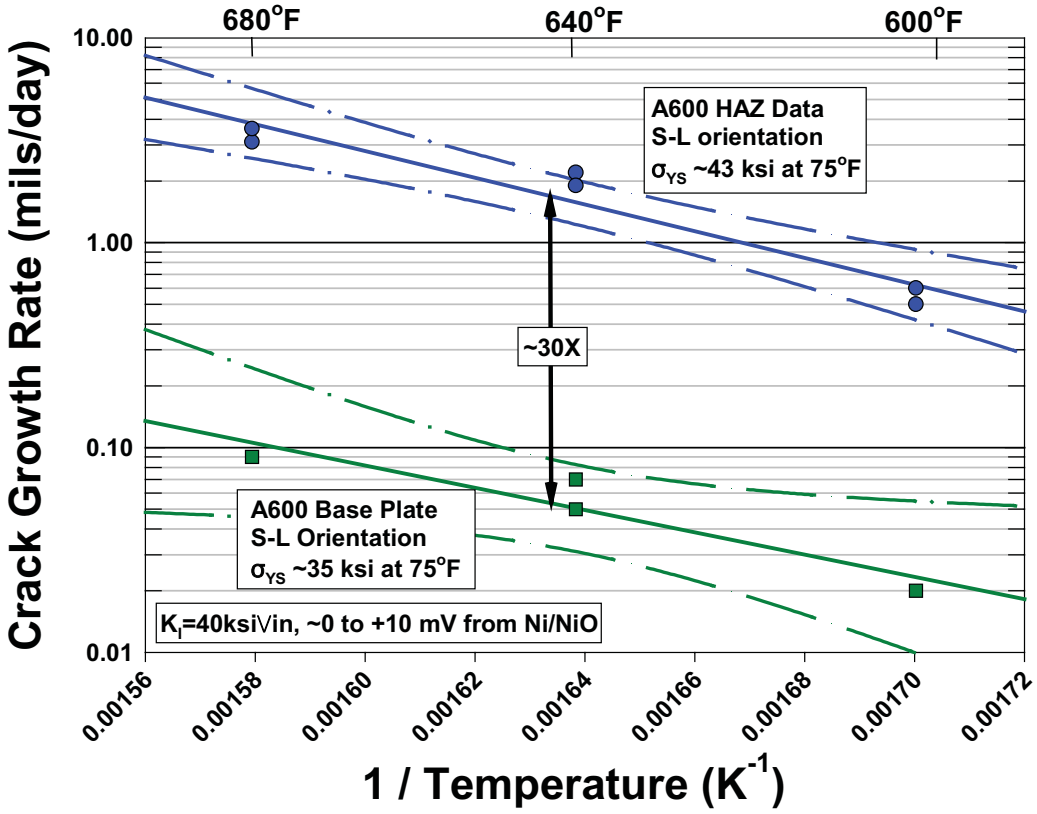

Figure 3. *Comparison of the A600 HAZ data (blue points) with a prediction for typical high temperature annealed A600 (i.e. the unaffected base material).*

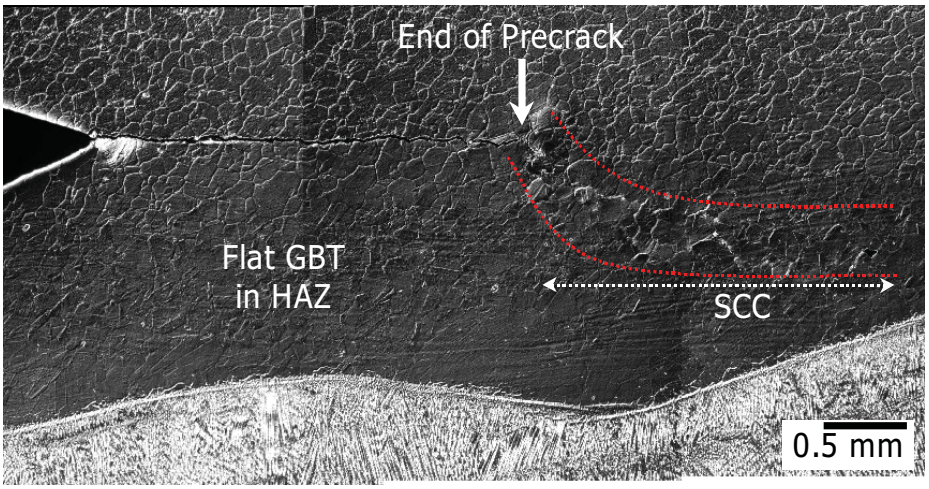

Figure 4. *Cross section of the fatigue precrack and SCC crack plane from an A600 HAZ sample at 680°F. GBT refers to the grain boundary topography.*

Activation Energy Analysis

Primary water stress corrosion cracking often follows Arrhenius-type temperature dependence. The slopes of the trend lines in Figure 3 are proportional to the apparent activation energy for crack growth. Table 4 and Figure 5 summarize the apparent activation energy ($Q_{Apparent}$) for crack growth between the A600 base metal and the A600 HAZ. For comparison, the A600 base metal Q was calculated at both constant dissolved hydrogen concentration in the water ($40\ scc_{H_2}/kg_{H_2O}$) using the data of Morton *et al.* [11]. Comparing the data at constant potential, the A600 HAZ material exhibits an activation energy of 29.8 ± 11.2 kcal/mol, which is in good agreement (95% confidence) of the $Q_{Apparent}$ for SCC in low temperature annealed (LTA) A600 base metal (34.7 ± 4.21 kcal/mol). Note that the HAZ data are not compared to the apparent activation energy for the A600 base metal tested in the present study due to the limited data available. Instead, comparison is made to a much larger dataset.

If the apparent activation energy were calculated at constant dissolved hydrogen, instead of constant potential, the Q value may be biased high. The effect of the dissolved hydrogen level on SCC has been discussed previously by Morton *et al.* [11] and is shown schematically in Figure 6. Since the crack growth rate is influenced by the proximity to the Ni/NiO phase transition, testing to determine the "true" activation energy for crack growth should be conducted either at constant electrochemical potential or far into the Ni metal or NiO stability regimes. As shown by the schematic in Figure 6 at a constant hydrogen level of 40 scc/kg, crack growth rate data above ~580°F will be biased toward faster crack growth rates relative to tests done farther into the nickel metal stability regime. It should be stressed that Figure 6 is a schematic and the precise location, width, and magnitude of the peak can vary with different alloys.

Table 4. ***Summary*** *of Apparent Activation Energies:* $\dot{a} = A_0 \exp\left(-Q_{Apparent} / RT\right)$

Material	Apparent Activation Energy, $Q_{Apparent}$ (kcal/mol) / (kJ/mol)	$Q_{Apparent}$ 95% Confidence (kcal/mol) / (kJ/mol)	R^2
HAZ	29.8 / 125	± 11.2 / ± 47.0	0.93148
LTA* A600 Base Material at Constant Electrochemical Potential	34.7 / 145	± 4.21 / ± 17.6	0.86363
LTA* A600 Base Material at Constant Dissolved Hydrogen ($40\ scc_{H_2} / kg_{H_2O}$ **)**	42.1 / 176	± 4.25 / ± 17.8	0.88860

***LTA** = Low temperature annealed (*i.e.* <1850°F)

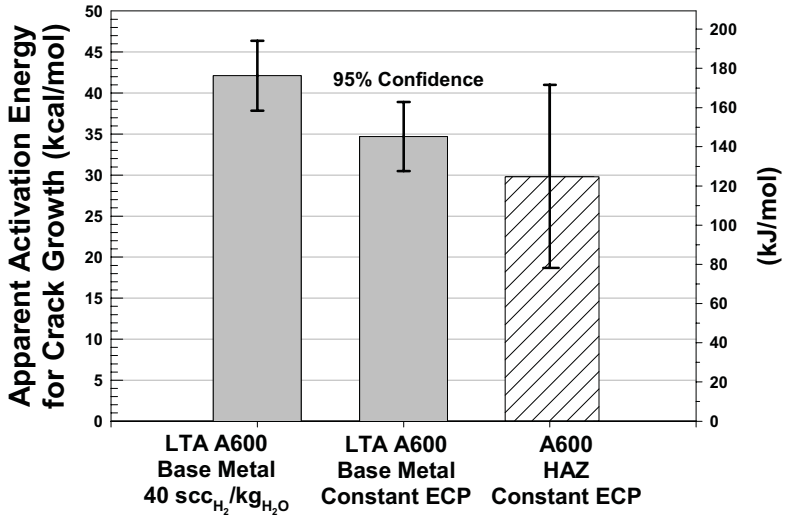

Figure 5. *Comparison of the apparent activation energies for primary water SCC between typical low temperature annealed (LTA) A600 base metal (gray) and the A600 HAZ (striped). Note the good agreement between base metal and HAZ Q calculated at constant electrochemical potential, while the Q from constant hydrogen concentration (40 scc/kg) is biased high.*

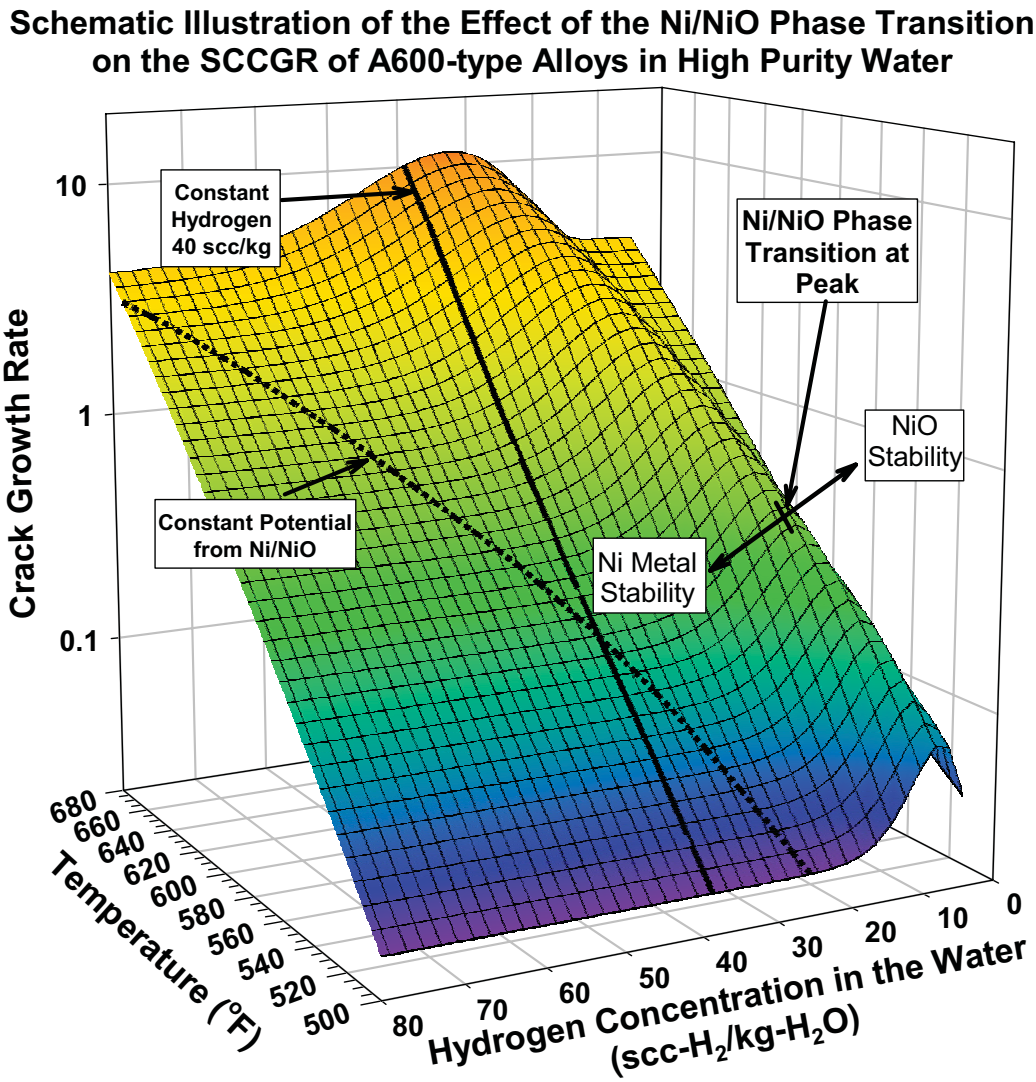

Figure 6. *Schematic illustration of the effect of the Ni/NiO phase transition on the stress corrosion crack growth rate of A600-type alloys in high purity water. When determining the activation energy for crack growth, testing should be done at constant potential (dashed line) or far into the Ni metal stability regime to avoid biasing some of the data to faster crack growth rates and larger apparent activation energies.*

HAZ Microstructure

A typical HAZ microstructure is shown in Figure 7 where the edge of the EN82H weld is on the right and unaffected base metal is toward the left. When viewed with Nomarski differential interference contrast illumination, the grain boundary topography is flat, indicative of little intergranular chromium carbide precipitation. Near the SCC crack, the ASTM grain size is approximately 3.6 or ~100 μm diameter grains. While extensive secondary cracking was observed in the HAZ, no cracking was observed in either the unaffected base metal or in the EN82H weld metal.

The HAZ region was also investigated via transmission electron microscopy (TEM), as shown in Figures 8, 9, and 10. In Figure 8, TEM shows that there are fine, discontinuous M_7C_3 and $M_{23}C_6$-type carbides on many of the HAZ grain boundaries. In contrast, the unaffected A600 base metal shows extensive inter- and intra-granular M_7C_3-type carbide precipitation. One likely scenario is that the first welding pass solutionized (or partially solutionized) the M_7C_3 carbides while subsequent welding passes acted to precipitate the $M_{23}C_6$ carbides.

HAZ Microchemistry

Compositional profiles of unaffected base metal and HAZ grain boundaries show the effect of the difference in chromium carbide structure on the near grain boundary composition (Figure 9). The HAZ shows a much narrower Cr depleted zone, consistent with the fewer, finer $Cr_{23}C_6$-type carbides relative to the extensive Cr_7C_3 carbide precipitation in the base metal. The near grain boundary chromium concentration is likely important to crack tip corrosion processes and to the fugacity of hydrogen produced via corrosion. For example, the higher average chromium concentration near the HAZ grain boundaries likely increases the fugacity of hydrogen produced during the corrosion reaction $A600 + H_2O(l) \rightarrow (Ni, Cr, Fe)O(s) + H_2(g)$, where Cr can substitute into the NiO-type oxide. The types of crack tip oxides and the resultant hydrogen fugacities are discussed elsewhere [13].

HAZ Deformation

In addition to the difference in carbide structure, TEM examination also showed that the HAZ contained significantly more plastic strain than the unaffected base metal. Figure 10 shows TEM micrographs between the HAZ (left) and the base metal (right). The HAZ micrographs show both increased dislocation density and the accumulation of low angle boundaries relative to the unaffected A600 base material. Plastic strains in the HAZ were further characterized via microhardness and electron backscatter diffraction. A microhardness traverse (Figure 11) shows that the hardness trend is EN82H (KHN=255) > A600 HAZ (KHN=242) > A600 Base Metal (KHN=228).

Figure 12 shows a map of the intra-grain, plastic strains for the A600 base metal, HAZ, and the EN82H weld adjacent to the HAZ. The base metal shows very low strains (blue) while the HAZ and weld show significant plastic strain (green through red), in agreement with the TEM findings. The increased strain in the HAZ is also consistent with its SCC susceptibility and its higher strength and decreased ductility as discussed below. In Figure 12, the white points are areas where no diffraction pattern could be determined.

The EBSD data can also be used to quantify the amount of residual plastic strain in the HAZ [14-18]. However, strain quantification requires a suitable calibration curve that relates the average intra-grain misorientation or "amis" parameter to the plastic strain. Calibration curves for annealed A600, annealed EN82H weld filler metal, and for high purity nickel are given in Figure 13. The amis parameter measurements for the unaffected base metal, the HAZ, and the EN82H weld metal adjacent to the HAZ are 0.3^{o}, 1.5^{o}, and 1.4^{o} respectively. These amis values correspond to ~0% plastic strain in the base metal, ~6% in the HAZ and ~4% in the weld metal adjacent to the HAZ.

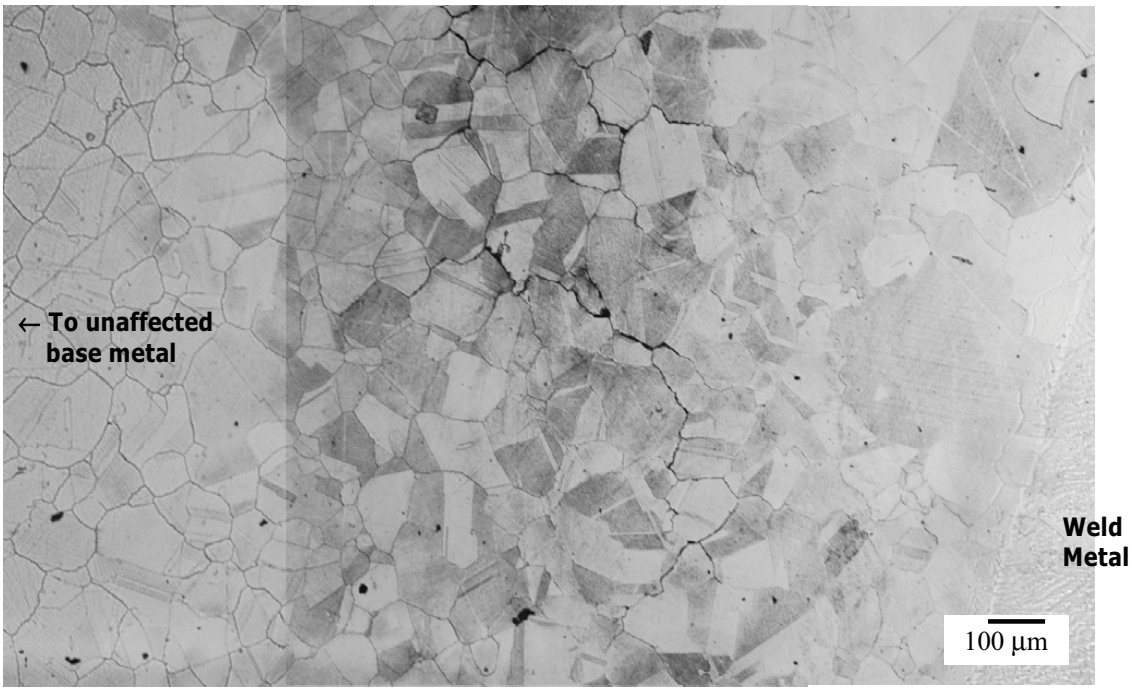

Figure 7. *Light micrograph of a HAZ SCC crack. Note the intergranular crack path and crack branching. 8:1 phosphoric acid, Nomarski, DIC.*

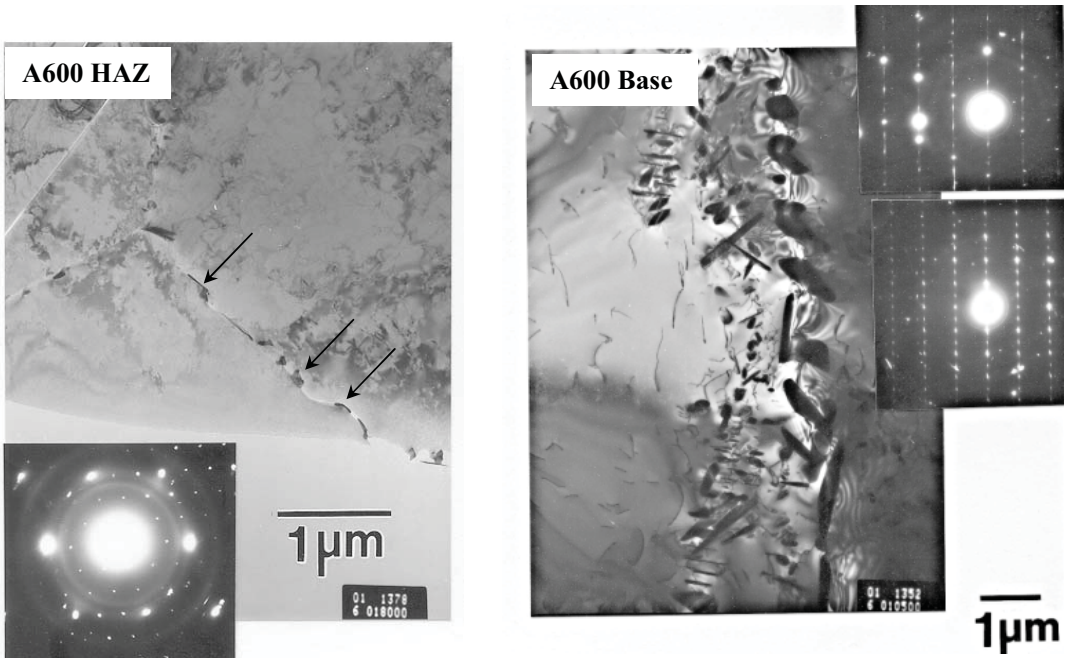

Figure 8. *Transmission electron microscopy of the A600 HAZ (left) and the A600 base material (right). Note the few $M_{23}C_6$-type carbides in the HAZ (arrows) while the unaffected base material displays extensive inter- and intra-granular M_7C_3-type carbides.*

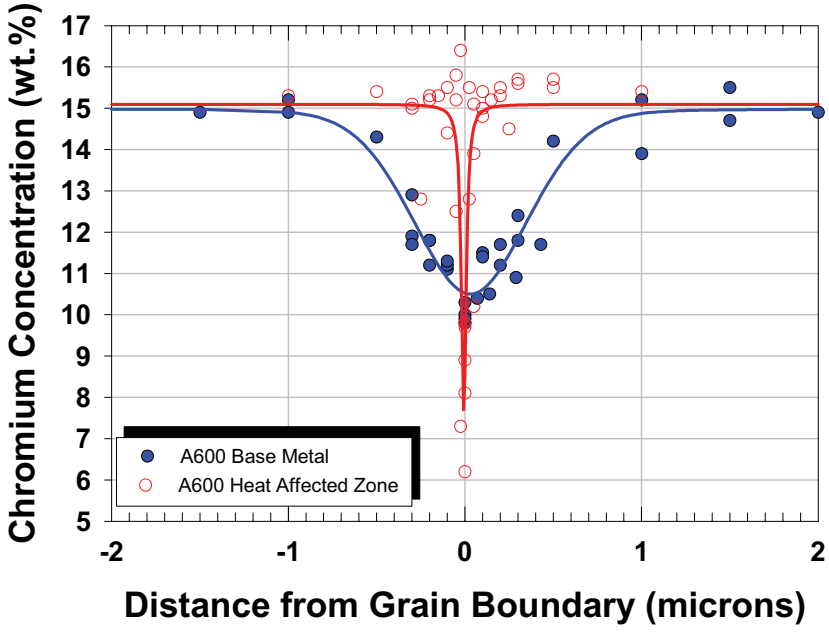

Figure 9. *Comparison of chromium depletion near unaffected base metal (solid blue points) and the heat affected zone (open red points). The HAZ shows a much sharper Cr depleted zone, consistent with the fewer, finer $Cr_{23}C_6$-type carbides relative to the extensive Cr_7C_3 carbide precipitation in the base metal.*

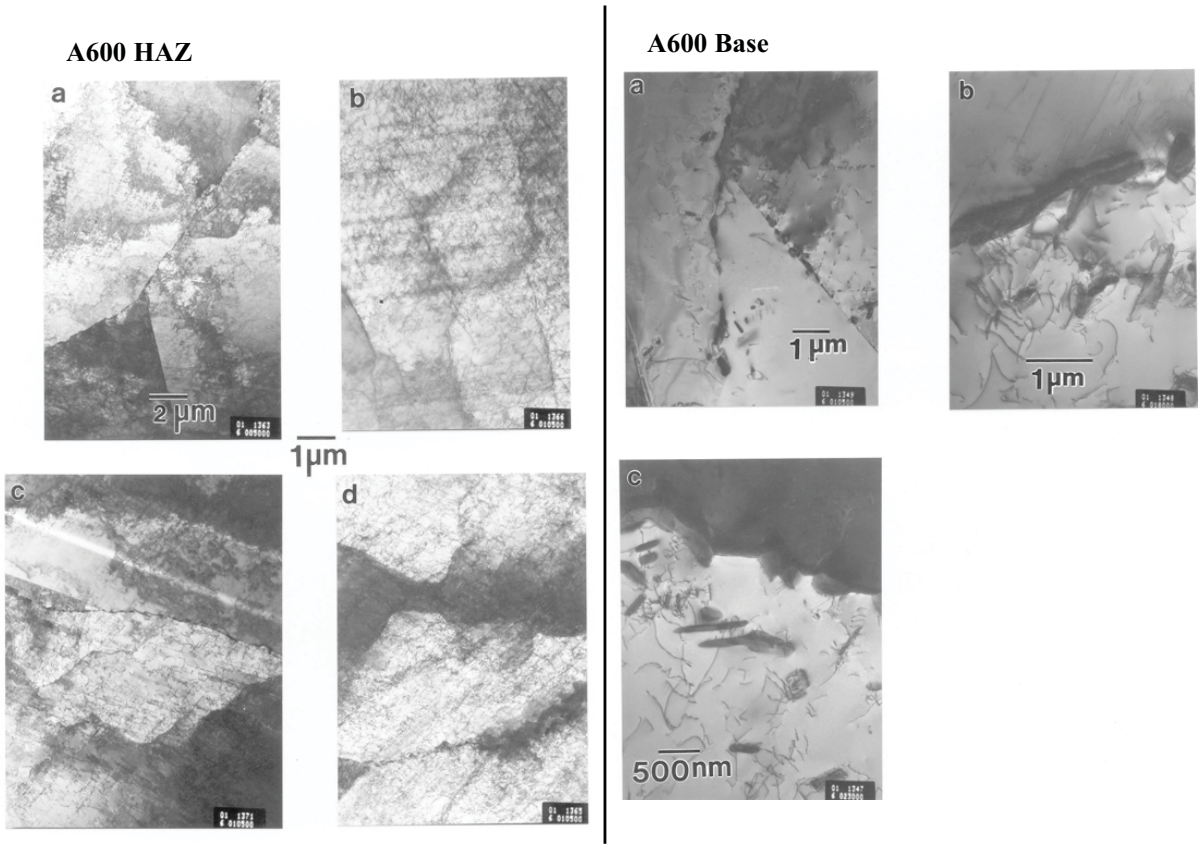

Figure 10. *Transmission electron microscopy of the A600 HAZ (left) and the A600 base material (right). Note the increased dislocation density and the bend contours in the HAZ while the A600 base material is relatively strain free.*

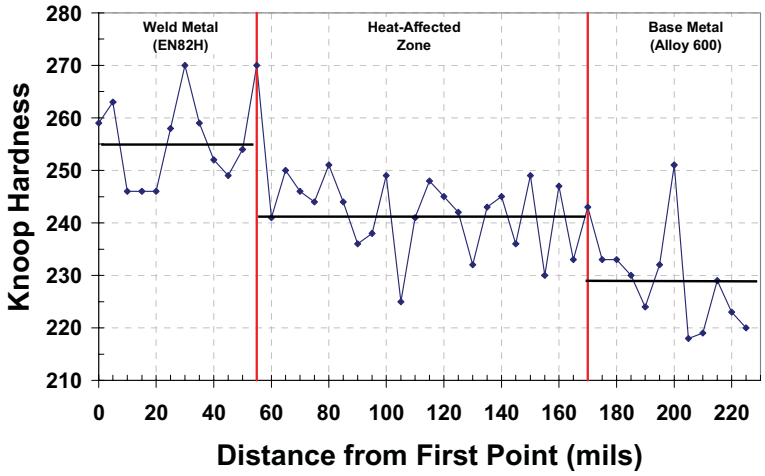

Figure 11. *Microhardness traverse across the EN82H weld, A600 HAZ and A600 base metal. Knoop hardness, 500 gf.*

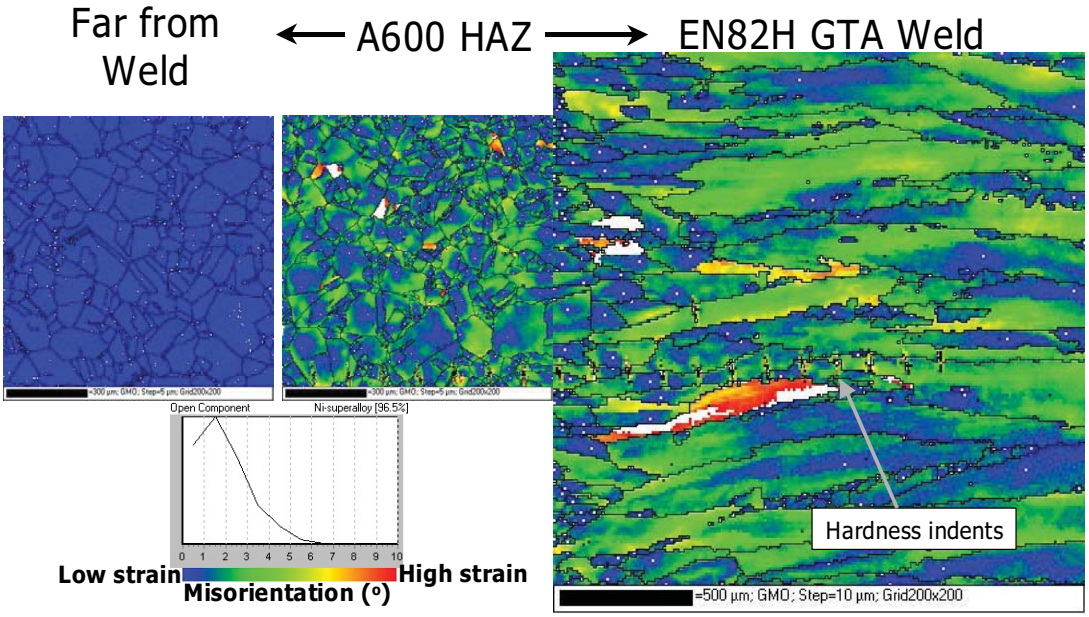

Figure 12. *Electron backscatter diffraction maps of the intra-grain strains. The A600 base metal (left) shows very little strain while the HAZ and the near HAZ weld show significant strains.*

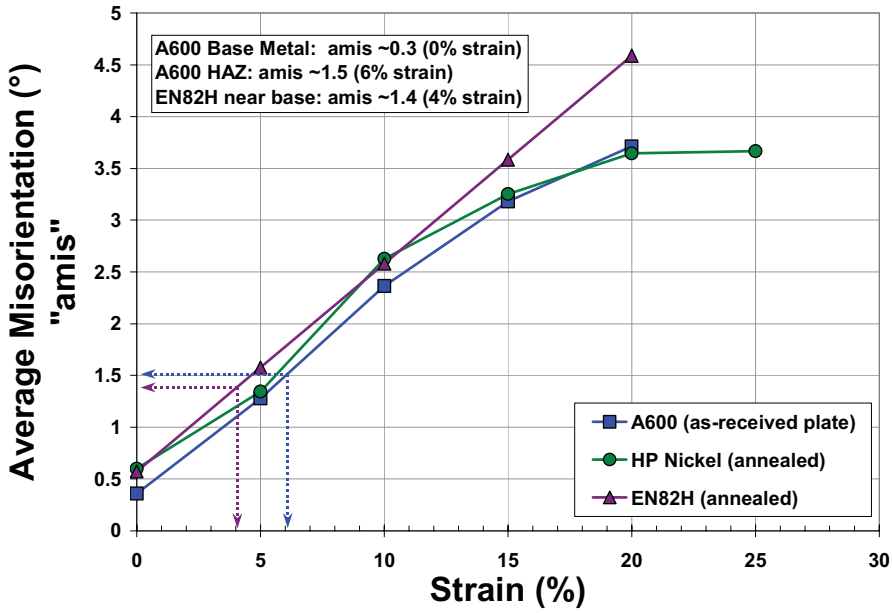

Figure 13. *Calibration curves relating the applied tensile strain at room temperature to the average intra-grain misorientation (amis) parameter. The HAZ samples exhibited ~6% plastic strain.*

Effect of Coolant Hydrogen

As discussed previously, many nickel-base alloys exhibit a maximum in SCCGR in primary water near the Ni/NiO phase transition [11]. For wrought A600 with significant precipitation of intergranular chromium rich carbides (typical of mill annealed A600 base metal), the SCC crack growth rate exhibits a maximum approximately 2.8X faster than rates measured far into the nickel metal regime as shown in Figure 14 [11]. Other nickel base alloys (X-750 Condition AH and EN82H weld metal) show a larger effect of coolant hydrogen on the SCCGR, on the order of 8X and the maximum crack growth rate is shifted into the NiO stability regime [11]. The available data for A600 HAZ material (circles in Figure 14) indicate that the HAZ behaves similarly to the A600 base material with the maximum crack growth rate occurring approximately at the Ni/NiO phase transition and with a magnitude of ~2.8X.

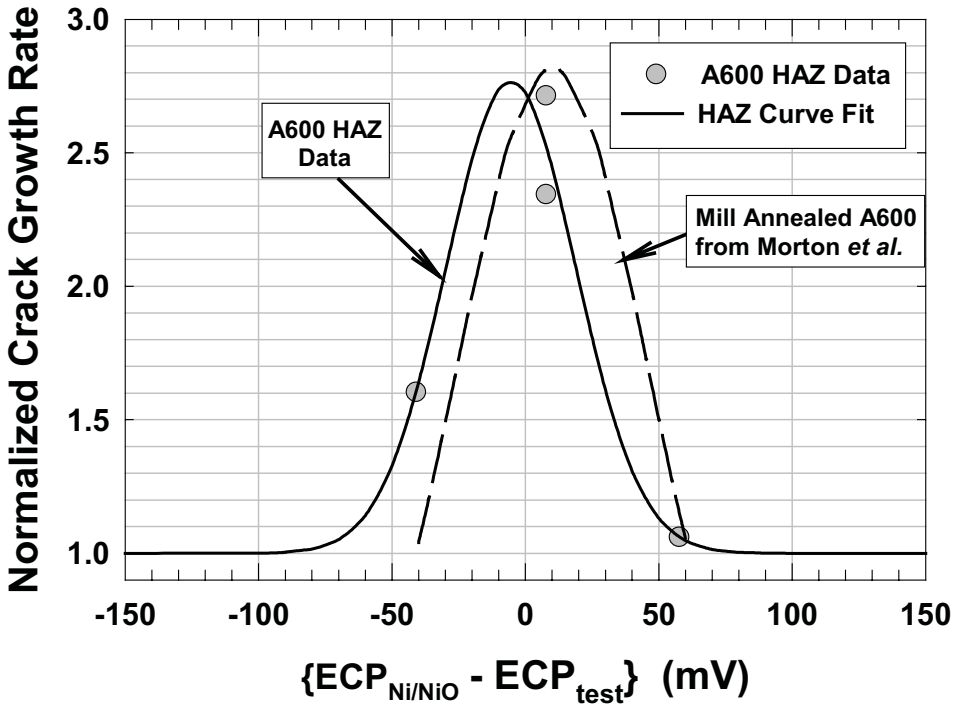

Figure 14. *Comparison of the effect of electrochemical potential on the crack growth rate of A600 base material and on the A600 heat affected zone, showing almost identical response. See reference [11] for additional information.*

Conclusions

- Relative to high temperature annealed base material, A600 HAZ's are highly susceptible stress corrosion cracking in high purity, high temperature water. The increased susceptibility of the HAZ is attributed to their microstructure (fewer, finer intergranular chromium carbides) and to increased levels of plastic strain (~6% for the HAZ tested).
- The apparent activation energy for SCCGR of A600 HAZ material in primary water 29.8 ± 11.2 $\big|_{95\%}$ kcal/mol, which is within experimental error of the value for typical low temperature annealed A600 base metal (34.7 ± 4.21 $\big|_{95\%}$ kcal/mol).
- Similar to A600 base metal, the A600 HAZ exhibits a maximum in crack growth rate near the Ni/NiO phase transition. The maximum magnitude of the effect of electrochemical potential on the SCC rate is estimated to be 2.8X.
- When stress corrosion cracking of A600 heat affected zones is a concern, welding heat input, inter-pass temperatures, and post weld heat treatments should be engineered to promote intergranular chromium carbide precipitation and to minimize residual plastic strains.

Acknowledgements

The Authors wish to thank Dr. Steve Attanasio, Mr. John Mullen, Ms. Debbie Perry, Mr. Nelson Schwarting, Mr. Stanley Watroba, Dr. Weldon Wilkening, Mr. Horace Williams, and Mr. John Wuthrich who provided critical input to the test procedure and data analysis. Ms. Michelle Othon and Dr. Luke Brewer of the General Electric Global Research and Development Center performed the orientation imaging microscopy. Mr. Glenn White and Dr. Jeff Gorman of Dominion Engineering provided helpful background information.

References

1. Hall, J.F.*, et al. Measurement of Residual Stresses in Alloy 600 Pressurizer Penetrations*. in *Conference on the Contribution of Materials Investigation to the Resolution of Problems Encountered in Pressurized Water Reactors*. 1994. Paris: Societe Francaise d'Energie Nucleare.
2. Buisine, D.*, et al.*, *Stress Corrosion Cracking in the Vessel Closure Head Penetrations of French PWR's*, in *Sixth International Symposium on Environmental Degradation of Materials in Nuclear Power Systems-Water Reactors*, R.E. Gold and E.P. Simonen, Editors. 1993, TMS: San Diego, CA. p. 845-853.
3. NRC, *Circumferential Cracking of Reactor Pressure Vessel Head Penetration Nozzles*, NRC Bulletin, 2002-01, United States Nuclear Regulatory Commission, Washington, D.C., 3 August, 2001.
4. Strosnider, J.R., *Staff Preliminary Technical Assessment of Reactor Pressure Vessel Head Penetration Nozzle Cracking*, Preliminary Technical Assessment, Unites States Nuclear Regulatory Commission, Washington, D.C., 4 December 2001.
5. Anderson, C., *30 Day Response to NRC Bulletin 2001-01 for ANO-1; Circumferential Cracking of VHP Nozzles*, 1CAN090102, NRC, September 4, 2001.

6. NRC, *Davis-Besse Reactor Vessel Head Damage*, NRC Update, U.S. Nuclear Regulatory Commission, Washington, D.C., November, 2002.
7. Lang, T., *Crack Indication in J-Groove Weld of Old CRDM Nozzle 3*, Condition Report, 02-05536, September 7, 2002.
8. Alexion, T.W., *Arkansas Nuclear One, Unit 1, Reactor Pressure Vessel Head Weld Repairs*. 2002, NRC: Rockville, MD.
9. Andresen, P.L.*, et al. Mechanisms and Kinetics of SCC in Stainless Steels*. in *10th International Conference on Environmental Degradation of Materials in Nuclear Power Systems - Water Reactors*. 2001. Lake Tahoe, NV: NACE.
10. Kilian, R.*, et al. Intergranular Stress Corrosion Cracking of Stainless Steel Piping Materials in BWR Environments*. in *10th International Conference on Environmental Degradation of Materials in Nuclear Power Systems - Water Reactors*. 2001. Lake Tahoe, NV: NACE.
11. Morton, D.S., *Primary Water SCC Understanding and Characterization Through Fundamental Testing in the Vicinity of the Nickel/Nickel Oxide Phase Transition*. in *10th International Conference on Environmental Degradation of Materials in Nuclear Power Systems - Water Reactors*. 2001. Lake Tahoe, NV: NACE.
12. Attanasio, S.A.*, et al. Measurement of the Nickel/Nickel Oxide Phase Transition in High Temperature Hydrogenated Water Using the Contact Electric Resistance Technique*. in *Tenth International Conference on Environmental Degradation of Materials in Nuclear Power Systems - Water Reactors*. 2001. Lake Tahoe, NV: NACE.
13. Lewis, N.*, et al. Stress Corrosion Crack Growth Rate Testing and Analytical Electron Microscopy of Alloy 600 as a Function of Pourbaix Space and Microstructure*. in *Chemistry and Electrochemistry of Corrosion and Stress Corrosion Cracking*. 2001. New Orleans, LA: TMS.
14. Young, G.A. *Quantification of Residual Plastic Strains in Nr-Cr-Mn-Nb GTAW Welds via Electron Backscatter Diffraction*. in *Trends in Welding Research*. 2002. Pine Mt., GA: ASM.
15. Young, G.A. *Factors Affecting the Hydrogen Embrittlement Resistance of Ni-Cr-Mn-Nb Welds*. in *Trends in Welding Research*. 2002. Pine Mt., GA: ASM.
16. Sutliff, J.A., Microscopy and Microanalysis Proceedings, 1999: p. 236.
17. Angeliu, T.M. *Microstructural Characterization of L-Grade Stainless Steels Relative to the IGSCC Behavior in BWR Environments*. in *Corrosion 2001*. 2001: NACE.
18. Lehockey, E.M. and A.M. Brennenstuhl. *Characterization of Plastic Strains and Crystallographic Properties Surrounding Defects in Steam Generator Tubes by Orientation Imaging Microscopy*. in *4th CNS International Steam Generator Conference*. 2002. Toronto, Ontario, Canada.

In-situ Raman Spectroscopic Study on Alloy 600 CRDM Nozzle Materials in PWR and Its Implications to PWSCC

Ji Hyun Kim[1], Il Soon Hwang[1] and Tae Ryong Kim[2]

[1] *Department of Nuclear Engineering, Seoul National University, Seoul, Republic of Korea*
[2] *Korea Electric Power Research Institute, Daejon, Republic of Korea*

ABSTRACT

Although there has been no general agreement on the mechanism of primary water stress corrosion cracking (PWSCC) as one of major degradation modes of Ni-base alloys in pressurized water reactors (PWR's), common postulation derived from previous studies is that the damage to the alloy substrate can be related to mass transport characteristics and/or repair properties of overlaid oxide film. Recently, it was shown that the oxide film structure and PWSCC initiation time as well as crack growth rate were systematically varied as a function of hydrogen partial pressure in high temperature water, supporting the postulation. In order to understand how the oxide film composition can vary with water chemistry, this study was conducted to characterize oxide films on Alloy 600 by an in-situ Raman spectroscopy. Based on both experimental and thermodynamic prediction results, Ni/NiO equilibrium condition was defined as a function of electrochemical potential and temperature. The results agree well with Attanasio et al.'s data by contact electrical resistance measurements. The anomalously high PWSCC growth rate consistently observed in the vicinity of Ni/NiO equilibrium is then attributed to weak thermodynamic stability of NiO. Redox-induced phase transition between Ni metal and NiO may undermine the integrity of NiO and enhance presumably the percolation of oxidizing environment through the oxide film, especially along grain boundaries. The redox-induced grain boundary oxide degradation mechanism has been postulated and will be tested by using the in-situ Raman facility.

INTRODUCTION

Primary water stress corrosion cracking (PWSCC) is one of major degradation modes that have been observed to occur predominantly along grain boundaries in a Ni-base Alloy 600 for steam generator (SG) tubes and penetration nozzles in the primary circuit of PWR's. Such an intergranular stress corrosion cracking (IGSCC) has been observed under specific combinations of materials and environmental conditions.[1] The PWSCC of Alloy 600 components is directly related with safety concerns as the root cause of potential rupture of SG tubes or nozzle ejection despite the fact that they have relatively large safety margins. With increasing number of plants operating beyond their design lives, rapidly growing numbers of PWSCC are observed in Ni-base components that are critical to the plant reliability.

The PWSCC phenomenon of Alloy 600 has been extensively studied primarily to establish empirical models for predicting the crack initiation time and crack growth rates for field components.[2-7] In order to formulate more fundamental solutions, it is necessary to understand PWSCC mechanism. Mechanistic models proposed to date are based on slip-dissolution/oxidation[2], corrosion-enhanced plasticity[3], internal oxidation[4,5] and creep[6,7]. Even though there is no satisfactory agreement as to the mechanism of PWSCC, one common postulation is that the damage to the alloy substrate can be related to mass transport characteristics, rupture and/or repair properties of overlaid oxide film.

Earlier studies have shown that dissolved hydrogen concentration in high temperature water affects the PWSCC susceptibility of nickel base alloys.[3,8-11] These results have highlighted that the crack growth rate at a given stress intensity factor and temperature displays a bell-shape peak in the vicinity of dissolved hydrogen concentration that corresponds to thermodynamic equilibrium between nickel metal (Ni) and nickel oxide (NiO), as shown in Figure 1.[10] More recently, it was also shown that the oxide film structure, PWSCC initiation time and crack growth rate were systematically varied as a function of hydrogen partial pressure in high temperature water.[10-12] These observations are believed to constitute strong evidences that the nature of oxide film on the surface of Alloy 600 plays a key role in the process of PWSCC.

To date, oxide film characterizations for Alloy 600 exposed to PWR water have been made only by ex-situ methods. [10,12,32] Since domains of oxide stability changes significantly with temperature and water chemistry, as evidenced in the case of Ni/NiO, an in-situ examination is highly desired. The present study is aimed at a direct characterization of the chemistry and structure of oxide film by in-situ Raman spectroscopy under PWR primary water conditions in order to verify earlier results and obtain basic information conducive to mechanistic understanding. In-situ Raman spectroscopy can be conducted by analyzing oxide film properties using reflected laser beam through a hermetically sealed window in various conditions exhibiting different PWSCC susceptibilities The Raman system developed in this study is capable of examining the effect of temperature, dissolved hydrogen concentration, strain and impurity concentration on oxide film behavior at temperature of up to 350℃ and pressure of up to 18 MPa. Observed results were compared with thermodynamic

calculations for the thermodynamically stable oxide phases so that meaningful conclusions can be drawn.

EXPERIMENTAL

A. Materials for Raman Spectroscopy

The Alloy 600 used in this work for analysis of the oxide films have been produced by Sumitomo Metals, Inc. following typical specification of a reactor pressure vessel (RPV) head penetration nozzles in PWRs, for the EAC-J round robin test under the auspice of the International Cooperative Group on Environmentally Assisted Cracking (ICG-EAC). Chemical composition of Alloy 600 used in this study is given in Table 1. The material was supplied in the condition of solution-annealed at 1050℃ for 2 hours followed by water-cooling. Its microstructure showed partially solutionized carbides with an average grain size of about 50 μm. Alloy 600 specimens for the in-situ Raman spectroscopy was machined by electro-discharge machining (EDM) in the form of a disk with 7 mm diameter and 1 mm thickness. All the machined specimens were mechanically polished down to 1μm Al_2O_3 powder, then rinsed with ethanol, and finally with deionized water prior to installation in the high pressure cell.

To obtain reference Raman spectra, the commercial high purity powders of NiO (99.998%), $NiFe_2O_4$ (99%), Cr_2O_3 (99.998%), and $NiCr_2O_4$ (90%) were loaded on the developed Raman system and measurements were made in room temperature and air condition. Average particle size of high purity powder was 44μm for NiO, 200 μm for $NiFe_2O_4$, 800μm for Cr_2O_3, and 150μm for $NiCr_2O_4$. Powder color was dark green for NiO, brown for $NiFe_2O_4$, and green for Cr_2O_3 and $NiCr_2O_4$. Powder samples were mixed with deionized water, placed in the recess of sample holder, and finally dried to obtain aggregate deposition on the sample holder.

B. Test Conditions

For the surface oxide formation, the Alloy 600 specimens were exposed to simulated PWR primary water environments inside the high-pressure cell. The cell for the in-situ observation at high temperature and pressure condition was constructed with a custom-designed 1 liter-capacity autoclave. The cell was made of Alloy 690 and a water-mixing tank was made of titanium. The head of a water-charging pump was made of titanium and balls of check valves were made of sapphire. All other components exposed to high temperature water including compression fittings and tubings were made of Alloy 600. The nominal flow rate to the cell was maintained at 4 liters per hour during experiments.

The cylindrical cell was machined with two penetrations in the sidewall to accommodate optical windows for the Raman spectroscopy. The initial window assembly, composed of 4.5 mm thick sapphire with gaskets to seal high-pressure water,

was designed after Hurst et al.'s work.[14] In this work, gaskets were made of gold-plated Ni-base Alloy 718. Because the optical surface of the sapphire was degraded by pitting corrosion in high temperature water during the study, a 0.25 mm thick CVD diamond disk was placed on the water side of the sapphire window and this has greatly reduced surface attack on the sapphire window. The Alloy 600 specimen was held in the recess of an oxidized zirconium metal by an Alloy 718 washer with the gasket of an oxidized zirconium sheet in order to electrically insulate the specimen for the cell.
The Raman spectroscopy system is consisted of an excitation laser source, a spectrometer and optical components including mirrors and filters. Figure 2 shows the layout drawing of optical system with near backscattering geometry including optical cell and water chemistry loop used in this work. A more detailed description for the developed Raman system is given elsewhere.[15]

The chemical condition of a typical PWR primary water was used. Water with a resistivity of 18 MΩ-cm was mixed with chemicals to produce 1,000 ppm boron in the form of boric acid (H_3BO_3) and 2 ppm lithium in the form of lithium hydroxide (LiOH). Two different levels of hydrogen concentration were prepared with corresponding dissolved hydrogen concentrations of 2.68 ppm and 0.089 ppm (30 cm^3(STP)/kg or 1 cm^3(STP)/kg) at 25℃, respectively, according to the solubility data.[13] The operating pressure was about 18 MPa and the temperature was increased from room temperature to 350℃. Measurements were after stabilizing temperature at 250, 290, 320 and 350 C, respectively. At the conclusion of experiment the cell was cooled and a specimen was analyzed by the Raman system in room temperature air.

C. Morphology of Oxide Film on Alloy 600

Upon the completion of in-situ Raman spectroscopic measurements, the Alloy 600 specimens was removed from the cell for microstructural examinations. Figure 3 shows the morphology of the surface oxide film observed by a field emission scanning electron microscope (FE-SEM) after series of exposures that ended at 350℃ PWR water for 110 hours. The surface oxide film is composed of a compact layer by small crystallites of few tens of nm in diameter. Scattered crystallites of about 200 nm in diameter are present on the compact layer.

Figure 4 shows the transmission electron micrographs on a cross-section of Alloy 600 specimen oxidized in simulated PWR water with 30 cm^3(STP)/kg of dissolved hydrogen concentration for 71 hours. The thickness of oxide film on Alloy 600 was observed to be in the range of 12 ~ 180 nm. Compact layers and other crystalline phases on Alloy 600 observed by TEM have the same morphology as those in the FE-SEM micrographs of Figure 3.

RESULTS

A. Reference Raman Spectra for High Purity Oxide Powders

The first series of experiments were conducted to obtain reference Raman spectra on pure oxides using powder samples. Results were compared with literature data in order to verify the developed system. The results of experiments with nickel and chromium oxides and spinels in room temperature air environment are summarized in Table 2. As shown in Table 2, the Raman features of the reference spectra for high purity powders show good agreements between the measurement in this work and literature data [16-19]. Further details of results in this study are given elsewhere [15].

B. In-situ Raman observation in PWR Water with 30 cm^3(STP)/kg of Dissolved Hydrogen Concentration

To maintain the dissolved hydrogen concentration (DH_2) of 30 cm^3(STP)/kg in the simulated PWR water, pure hydrogen gas was injected into the water storage tank with the cover gas pressure of 170 kPa. Based on Henry's law, a dissolved hydrogen concentration of 2.68 ppm is expected.[13] The operating pressure was about 18 MPa and the temperature was gradually increased from room temperature to 350℃ at an average rate of 40℃/hour. Temperatures at which Raman spectra were collected with the remained time length are summarized in Table 3.

Figure 5 shows the in-situ Raman spectra of Alloy 600 specimen obtained by holding temperatures at 250, 290, 320, and 350℃, respectively, while temperature increased. Peaks observed at ca. 417 cm^{-1}, 743 cm^{-1} in the in-situ Raman spectra were originated from the sapphire window. A feature in the range of ca. 546-587 cm^{-1} in the spectrum acquired at 250℃ was known to be attributed to α-CrOOH based on Maslar et al.'s work.[19] According to the explanation described in Ref. 19, [$Cr^{III}O_6$] octahedral are common structure to both Cr_2O_3 and α-CrOOH [21]. Therefore, one might reasonably expect the Raman wavenumbers of α-CrOOH to be observed in approximately the same wavenumber range as those of Cr_2O_3, i.e., ca. 300-613 cm^{-1}.

The crystallographic structure of the Cr_2O_3•nH_2O powder is yet unknown. The Cr_2O_3•nH_2O XRD pattern does not match any chromium hydrate/hydroxide reference patterns.[19] The broad XRD peaks are typical of a hydrate consisting of a mixture of different metastable hydrates/hydroxides. This result is consistent with a report on the Cr_2O_3•nH_2O possessing variable water content.[22] While the observed Raman peaks for Cr_2O_3•nH_2O cannot be attributed to a particular structural characteristic, the Cr_2O_3•nH_2O Raman spectrum illustrates that the Raman peaks of some hydrated Cr^{III} oxide are observed in approximately the same wavenumber range as those of Cr_2O_3. Additionally, the infrared (IR) spectrum of α-CrOOH exhibits features in this wave number range, i.e., peaks at 525 and 610 cm^{-1}.[23] Therefore, the shared structural features of Cr_2O_3 and α-CrOOH and the wavenumber range of the Raman features in the Cr_2O_3

and Cr_2O_3•nH_2O reference spectra are consistent with the assignment of the measured Raman features to α-CrOOH.

Several intense peaks are also observed in the 840-880 cm^{-1} range of spectra in Figure 5. According to the extensive discussion by Maslar et al.[19], this feature would be attributed to Cr^{VI} or crystalline Cr^{III}/Cr^{VI} species assuming a chromium species is responsible for this feature. This explanation can account for the weak signature observed in the 340-350 cm^{-1} range in the spectra of the specimen at 250℃. Chromium oxide features in this wavenumber range are generally attributed to Cr^{VI}–oxygen terminal stretching modes or mixed Cr^{III}/Cr^{VI} oxide vibrational modes.[24] Hydrated surface chromate species have been reported to exhibit a vibrational mode at ca. 865 cm^{-1}.[25] The most intense peak in the aqueous $HCrO_4^-$ Raman spectrum was reported from ca. 880 to 899 cm^{-1}.[26,27] A number of mixed Cr^{III}/Cr^{VI} oxides have been identified during the thermal decomposition of various chromium-containing materials. Crystalline chromium oxide compounds such as Cr_3O_8, Cr_2O_5, and XCr_3O_8 (X = Na, K, Rb) exhibit their most intense Raman spectral features in the ca. 820-904 cm^{-1} range at room temperature. The most intense Raman spectral feature of an amorphous Cr^{III}/Cr^{VI} compound has been observed at 859 cm^{-1}. In the spectra obtained at 250 ℃ and 290 ℃, weak features appeared at 704 cm^{-1} that were attributed to nickel ferrite spinel ($NiFe_2O_4$) features.

In the spectra obtained at 320 ℃, features of pure chromium oxide including α-CrOOH, Cr^{VI} and crystalline Cr^{III}/Cr^{VI} compounds become weaker, while nickel oxide features are firstly observed and become more apparent in subsequent spectra up to 350℃. The features at 550 cm^{-1} and 910 cm^{-1} were attributed to NiO phase. Also, features of nickel chromium spinel ($NiCr_2O_4$) were detected in this temperature range. The features at ca. 682 cm^{-1} and 430 cm^{-1} were attributed to $NiCr_2O_4$ phase.[17,18] Also, nickel oxide and nickel chromite phase were still detected on the specimen surface as exposure time increases at 350 . The $NiCr_2O_4$ is one of thermodynamically stable phases in a reducing aqueous environment with the range of hydrogen overpressure at about 300℃. A more detail study that was performed to identify thermodynamically stable phase of nickel base alloy in high temperature water was described in ref. 28.

C. In-situ Raman observation in PWR Water with 1 cm^3(STP)/kg of Dissolved Hydrogen Concentration

To maintain the dissolved hydrogen concentration of 1 cm^3(STP)/kg in water, 5% hydrogen gas balanced with 95% helium gas was injected into the water with the overpressure of 0.7 atm and it made a dissolved hydrogen concentration of 0.089 ppm in this study.[13] Temperatures at which Raman spectra were collected with the remained time length are summarized in Table 3.

Figure 6 shows the in-situ Raman spectra of Alloy 600 specimen obtained at the lower hydrogen concentration while temperature increased. A feature in ca. 546-587 cm^{-1} range in the spectrum acquired at 250℃ was attributed to α-CrOOH from the same rationale as that described earlier in the result with DH_2=30 cc/kg. Also, the intense peaks feature that would be attributed to Cr^{VI} or crystalline Cr^{III}/Cr^{VI} species was

observed in the 840-880 cm^{-1} range.

As temperature increased, clear features in 550 and 910 cm^{-1} which were attributed to nickel oxide (NiO) were firstly appeared and became weaker in subsequent spectra up to 350℃. After 23 hours at 350℃ in this condition, the features of nickel oxide phase were still detected on the Alloy 600 specimen surface at 350 .

D. Effect of Dissolved Hydrogen Concentration Change in PWR Water

To investigate the effect of dissolved hydrogen concentration on the formation of oxide film of Alloy 600 in high temperature water, dissolved hydrogen concentration was increased from 1 to 30 cc/kg, immediately following the measurement at 1 cc/kg. In-situ Raman spectroscopic measurement of Alloy 600 surfaces was made both before and after the change of hydrogen concentration.

Figure 7 shows the change of Raman spectra with the increase of dissolved hydrogen concentration in water at 350℃. In high temperature water with 1 cc/kg of hydrogen concentration, features of pure chromium oxide including α-CrOOH, Cr^{VI} and crystalline Cr^{III}/Cr^{VI} compounds and nickel oxide (NiO) features were observed at the oxide film of Alloy 600 specimen. With the increase of dissolved hydrogen concentration, nickel chromium spinel ($NiCr_2O_4$) features were appeared in the observed Raman spectrum.

E. Comparison between in-situ and ex-situ Raman spectra

Figure 8 represents the ex-situ Raman spectrum for the surface film on Alloy 600 specimen obtain in room temperature air after it was cooled down from high temperature observations. Results are compared with the in-situ Raman spectrum oxide film of Alloy 600 in 350℃ water with DH_2=30 cc/kg. As shown in Fig. 8, it can be seen that only the intensity of a peak at ca. 870 cm^{-1} in the ex-situ spectra was weakened comparing with that in the in-situ spectra.

According to earlier work by Gui and Devine[29] and Melendres et al.[30], the feature appeared at ca. 870 cm^{-1} was known to be attributed to the total symmetric stretch vibration of borate ions located in the water. Also, the feature appeared at this range of wave number was known to be originated from chromium oxides, as previously explained at the part of in-situ experimental results in this study, following the extensive discussion in Maslar et al.'s work[19]. Consequently, it can be concluded that Cr-oxide peak and borate peak coincided with each other at ~870cm^{-1} and the intensity of the Raman peak at ca. 870 cm^{-1} in the ex-situ spectra was weakened by the absence of borate ion.

DISCUSSION

A. Observation vs. Prediction of Oxide Film Composition

Table 4 summarizes the experimental observations of surface oxide phases of Alloy 600 in 350℃ water in comparison with literature data[10,12,33] at each dissolved hydrogen concentration. At higher dissolved concentration, $NiFe_2O_4$ precipitates reported in ref. 10 and 30 could be made by Fe ion dissolution from high temperature flowing system including autoclave, tubes and fitting for longer exposure time than this work. At lower dissolved concentration, the observed oxide phases agree well with those reported in literature.

From the viewpoint that electrochemical potential-pH diagrams can be useful in predicting thermodynamically stable phases, thermochemical calculations can provide very much meaningful information to explain the corrosion behavior of Alloy 600 in high temperature water. Although the pH was not measured at high temperature and pressure during this investigation, this value can be estimated using aqueous thermochemical calculation softwares. In this work, pH values of primary water in PWR were calculated as a function of temperature using MULTEQ®.[32] Electrochemical potential value was calculated by using the Nernst equation assuming that the surface of Alloy 600 behaves as a hydrogen electrode in the hydrogen-containing water environment. The potential of hydrogen electrode is given as below;

$$E_{H^+/H_2}(T) = E^{o}_{H^+/H_2}(T) - 2.303\frac{RT}{2F}\left[\log f_{H_2} + 2pH\right]$$

$$= -2.303\frac{RT}{2F}\left[\log f_{H_2} + 2pH\right] \quad vs.\,SHE\,(T)$$

Table 5 summarizes the comparison between experimental observations and thermochemical prediction of oxide phases of Alloy 600 at each condition of temperature and hydrogen concentration. It can be known that the consideration of formation of chromium oxide hydroxide (CrOOH) and nickel spinels can make differences in the thermochemical prediction results, regardless of dissolved hydrogen concentration in 350℃ water. At both conditions of dissolved hydrogen concentration, nickel ferrite ($NiFe_2O_4$) phases that were predicted to be thermodynamically stable assuming that nickel spinels can be formed in this system were not experimentally detected. When the observed oxide phases are compared with the predicted stable phases of Alloy 600 at 350℃, all the observed oxide phases but Cr-oxides are included in predicted stable phases. But the thermochemical predictions with CrOOH and Ni spinels do not agree with the observed results at both hydrogen concentrations in 350℃ water. In contrast, the predicted Ni/NiO equilibrium line is in good agreement with the observed results. This suggests that relatively simple oxide phases identified by in-situ Raman spectroscopic investigation can be used to verify thermodynamically stable phases.

In-situ Raman spectroscopy is shown to be a very useful experimental tool that can provide valuable information about oxide films and the SCC behavior of Alloy 600 in

high temperature aqueous environments. In this work, dissolved hydrogen concentration was experimentally known to play an important role on the formation of oxide films on the Alloy 600 in high temperature water. Different compositions of oxides were produced at different conditions of dissolved hydrogen concentration in high temperature water.

B. Ni/NiO Equilibrium

From the results of in-situ Raman spectra measurements of Alloy 600 with the increase of temperature, dissolved hydrogen concentration is one of the most important experimental parameters in this study. While nickel oxide was observed at 320℃ or higher at the higher hydrogen concentration, nickel oxide was observed at 290℃ or higher at the lower hydrogen concentration. To compare experimental results with calculations, thermochemical calculations for Alloy 600 were made as a function of temperature, as described in ref. 28. In this calculation, for simplicity, it was assumed that nickel oxide could be produced whereas spinel oxide could not form. Figure 9 summarizes both the experimental results of in-situ Raman observation with two different levels of dissolved hydrogen concentration and the thermochemical calculation of Ni/NiO equilibrium as a function of temperature. In Figure 9, dashed line represents a previous experimental result of nickel/nickel oxide transition using a contact electric resistance (CER) instrument by Attanasio et al.[33] By comparison between this and previous results, it can be seen that a good agreement was found between in-situ Raman results and those from contact electrical resistance (CER) measurements on Ni/NiO equilibrium

C. Implication to PWSCC Mechanism

Previous studies[10,11] showed that there exists a critical dissolved hydrogen concentration at high temperature corresponding the maximum susceptibility of Alloy 600 to PWSCC. The present in-situ Raman spectroscopic study showed that the phase changes between nickel metal (Ni) and nickel oxide (NiO) and the thermodynamic equilibrium of Ni/NiO were clearly observed over relatively narrow range of dissolved hydrogen concentration in high temperature water. Under experimental conditions in the vicinity of Ni/NiO, it is likely ECP can fluctuate due to uncontrollable variations in temperature, hydrogen concentration, and water pH. Similar variation can be expected during actual PWR operations. Therefore it is conceivable that electrochemical condition of PWR water can cross Ni/NiO equilibrium repeatedly.

It was previously reported that oxide phase change from one to another can cause stress-induced degradation of oxide integrity and hence is responsible for an accelerated corrosion in zirconium alloys[34] and Cu[35] in nuclear power plants. Recently, it was clearly demonstrated that the PWSCC sensitivity of Alloy 600 was increased in high temperature water with dissolved hydrogen concentration corresponding to Ni/NiO equilibrium condition.[36] Considering large difference in their molar volumes, alteration of water chemistry cross Ni/NiO can severely undermine oxide integrity due to high

stresses involved.

From the observed PWSCC behavior, it can be postulated that repeated phase changes between Ni metal and NiO occurs more rapidly along grain boundaries due to faster diffusion. Consequently, degradation of oxide integrity can enhance the percolation of oxidant preferentially along grain boundaries to accelerate PWSCC. The redox-induced grain boundary oxide degradation mechanism is depicted in Figure 10. To verify this postulation, a series of PWSCC testing can be performed with cycling of dissolved hydrogen concentration from lower (higher) DH_2 via DH_2 corresponding to Ni/NiO equilibrium to higher (lower) DH_2 in high temperature water. From the mitigation standpoint based on redox-induced oxide degradation and percolation, it may be suggested that the dissolved hydrogen concentration in water should be controlled more precisely and/or should be maintained at relatively lower contents far away from Ni/NiO equilibrium condition in order to reduce PWSCC sensitivity of Alloy 600 in nuclear power plants.

CONCLUSIONS

In-situ Raman spectroscopic investigation has been conducted for surface oxide films on a nickel-base Alloy 600 exposed to simulated PWR primary water with 1,000 ppm boron and 2 ppm lithium at a pressure of 18 MPa, for temperatures ranging up to 350℃ and dissolved hydrogen concentrations ranging from 1 to 30 cc/kg in an optically accessible high-pressure cell. From this study, following conclusions are made:

1. An in-situ Raman spectroscopic system was developed successfully to provide valuable information for the oxide film in PWR water conditions.
2. At the lower dissolved hydrogen concentration (1 cm^3(STP)/kg), nickel oxide(NiO) phase was detected on the specimen surface at temperature ranges between 290 and 350 . Nickel oxide phase appeared to be stable over a long period of time (21 hours) at 350 .
3. At the higher dissolved hydrogen concentration (30 cm^3(STP)/kg), chromium oxide hydroxide (CrOOH) phase was detected on the specimen surface at relatively low temperature ranging from 250 to 290 . Also, features attributed to the phase of NiO and $NiCr_2O_4$ were observed at 320 or higher.
4. Some unique observations were made, compared with earlier ex-situ results;
    A. CrOOH phase, undetected by ex-situ methods, was observed under most conditions.
    B. $NiFe_2O_4$ usually found in precipitate layer was not observed, conceivably due to the suppression of precipitate layers in this work.
5. NiO, Cr_2O_3 and $NiCr_2O_4$ phases were observed, in reasonable agreement with ex-situ results.
6. Ni/NiO equilibrium was determined as function of dissolved hydrogen concentration and temperature.
    A. Comparison of observed results with thermodynamic predictions showed a good agreement on Ni/NiO equilibrium at the temperature range from 250 to 350 degree C.

B. A good agreement was found between in-situ Raman results and those from contact electrical resistance (CER) measurements on Ni/NiO equilibrium.

7. From the result of this study, a new postulation that redox alteration between Ni metal and Ni can enhance oxide degradation presumably along grain boundaries and facilitate the percolation of oxidants to accelerate. A test of the postulation is planned using the in-situ Raman system.

ACKNOWLEDGEMENTS

The authors would like to express their gratitude to Dr. J. Maslar and Dr. W. Hurst of the National Institute of Standards and Technology, Gaithersburg, MD, USA. Professor Y.W. Kim of Seoul National University kindly helped electron microscope examinations. This work was supported by the National Nuclear Mid- and Long-Term R&D programs of the Korean Ministry of Science and Technology.

REFERENCES

1. J.M. Gras, “Stress corrosion cracking of steam generator tubing materials - review and assessment”, Parkins Symposium on Fundamentals Aspects of Stress Corrosion Cracking, TMS, 1992, p. 411.

2. T.M. Angeliu, P.L. Andresen and F.P. Ford, “Applying slip-oxidation to the SCC of austenitic materials in BWR/PWR environments”, Corrosion 98, NACE (1998), Paper No. 262.

3. T. Magnin, J-M. Boursier, D. Noel, R. Rios, and F. Vaillant, “Corrosion-deformation interaction during stress corrosion cracking of alloy 600 in primary water”, Proceedings of the 6th International Symposium on Environmental Degradation of Materials in Nuclear Power System – Water Reactors, TMS, 1993, p.669.

4. P.M. Scott and M. Le Calvar, “Some possible mechanisms of intergranular stress corrosion cracking of alloy 600 in primary water”, Proceedings of the 6th International Symposium on Environmental Degradation of Materials in Nuclear Power System – Water Reactors, TMS, 1993, p. 657.

5. P.M. Scott, “An Overview of internal oxidation as a possible explanation of intergranular stress corrosion cracking of alloy 600 in PWRs”, Proceedings of the 9th International Symposium on Environmental Degradation of Materials in Nuclear Power System – Water Reactors, TMS, 1999, p. 3.

6. G. Was, T.M. Angeliu, and J.K. Sung, “Deformation and intergranular cracking behavior of Ni-Cr-Fe alloys at high temperature”, Proceedings of the “Specialist Meeting on Environmental Degradation of Alloy600”, Airlie House, VA, April 1993, EPRI Report TR-104898, 1996, p. 24-1.

7. M.M. Hall, “Thermally activated low temperature creep and primary water stress corrosion cracking of NiCrFe alloys”, Proceedings of the “Specialist Meeting on Environmental Degradation of Alloy600”, Airlie House, VA, April 1993, EPRI Report

TR-104898, 1996, p. 6-1.
8. R.S. Pathania, and A.R. McIlree, “A review of the effect of hydrogen on stress corrosion cracking of alloy 600 in 360℃ water”, Proceedings of the 3rd International Symposium on Environmental Degradation of Materials in Nuclear Power System – Water Reactors, AIME, 1987, p. 551.
9. T. Cassagne and A. Gelpi, “Crack growth rate measurements an alloy 600 steam generator tubing in primary and hydrogenated AVT water”, Proceedings of the 8th International Symposium on Environmental Degradation of Materials in Nuclear Power System – Water Reactors, TMS, 1993, p.679.
10. C. Soustelle, M. Foucault and P. Combrade, “PWSCC of alloy 600: a parametric study of surface film effects”, Proceedings of the 9th International Symposium on Environmental Degradation of Materials in Nuclear Power System – Water Reactors, TMS, 1999, p. 105.
11. T. Cassagne, B. Fleury, F. Vaillant, O. De Bouvier, and P. Combrade, “An Update of the Influence of Hydrogen on the PWSCC of nickel base alloy in high temperature water”, Proceedings of the 8th International Symposium on Environmental Degradation of Materials in Nuclear Power System – Water Reactors, TMS, 1997, Vol. 1, p. 307.
12. D. Caron, PhD. Thesis, INSA-Lyon Scientific and Technical University, France, 2000.
13. D.M. Himmelblau, “Solubilities of inert gases in water 0℃ to near the critical point of water”, J. Chem. Eng. Data 5, 1 (1960): p. 10.
14. W.S. Hurst, M.S. Hodes, W.J. Bowers Jr., V.E. Bean, J.E. Maslar, and K.A. Smith, “Optical flow cell and apparatus for solubility, salt deposition and Raman spectroscopic studies in aqueous solutions near the water critical point”, Journal of Supercritical Fluids 22 (2002): p. 151.
15. J.H. Kim and I.S. Hwang, “Development of in-situ Raman spectroscopic system of surface oxide films of metals and alloys in high temperature water conditions”, *submitted to Nuclear Engineering and Design (2003)*.
16. J.E. Maslar, W.S. Hurst, W.J. Bowers Jr., J.H. Hendricks, and M.I. Aquino, “In situ Raman spectroscopic investigation of nickel hydrothermal corrosion”, Corrosion 58 (2002): p. 225.
17. J.E. Maslar, W.S. Hurst, W.J. Bowers Jr., and J.H. Hendricks, “In situ Raman spectroscopic investigation of stainless steel hydrothermal corrosion”, Corrosion 58 (2002): p. 739.
18. M.D. Cunha Belo et al., “Composition, structure and properties of the oxide films formed on the stainless steels 316L in a primary type PWR environment”, Corrosion Science 40 23 (1998): p. 447.
19. J.E. Maslar, W.S. Hurst, W.J. Bowers Jr., J.H. Hendricks, M.I. Aquino and I. Levin, “In situ Raman spectroscopic investigation of chromium surface under hydrothermal conditions”, Applied Surface Science 180 (2001): p. 102.
20. R.L. McCreery, Raman spectroscopy for chemical analysis, (Wiley-Interscience, 2000).
21. A.F. Well, Structural inorganic chemistry, 5th ed., (Oxford: Clarendon Press, 1984).
22. F.A. Cotton, and G. Wilkinson, Advanced inorganic chemistry: A comprehensive test, 5th ed. (New York, NY:Wiley, 1980).
23. R.G. Snyder, and J.A. Ibers, “O-H-O and O-D-O potential energy curves for

chromous acid", J. Chem. Phys. 36 (1962): p. 1356.
24. J.E. Maslar, W.S Hurst, T.A. Vanderah and I. Levin, "The Raman spectra of Cr_3O_8 and Cr_2O_5", J. Raman Spectrosc. 32 (2001): p. 201.
25. B.M. Weckhuysen, I.E. Wachs and R.A. Schoonheydt, "Surface chemistry and spectroscopy of chromium in inorganic oxides", Chem. Rev. 96 (1996): p. 3327.
26. J.B.B. Heyns, J.J. Cruywagen and K.T. Carron, "Raman spectroscopic investigation of chromium (VI) equilibrium-another look", J. Raman Spectrosc. 30 (1999): p. 335.
27. G. Michel and R. Machiroux, "Raman spectroscopic investigation of the $Cr_2O_4^{2-}$ /$Cr_2O_{47}^{2-}$ equilibrium in aqueous solution", J. Raman Spectrosc. 14 (1983): p. 22.
28. J.H. Kim, Ph. D. Dissertation, Seoul National University, Republic of Korea (2003)
29. J. Gui and T. M. Devine, "The influence of sulfate ions on the surface enhanced raman spectra of passive films formed on iron", *Corros. Sci. 36* (1994): p. 441.
30. C. A. Melendres, J. Acho and R. L. Knight, J. Electrochem. Soc. 138, (1991): p. 877.
31. T. Nakagawa, N. Totsuka, T. Terachi, and N. Nakajima, "Influence of dissolved hydrogen on oxide film and PWSCC of alloy 600 in PWR primary water," Journal of Nuclear Science and Technology 40, 1 (2003): p. 39.
32. "MULTEQ: Equilibrium of an electrolytic solution with vapor-liquid partitioning, Volume 3: Theory manual", EPRI NP-5561-CCML, Vol. 3, EPRI, Palo Alto, CA, 1992.
33. S.A. Attanasio, D.S. Morton, M.A. Ando, N.F. Panayotou and C.D. Thompson, "Measurement of the nickel/nickel oxide phase transition in high temperature hydrogenated water using the contact electric resistance (CER) techniques", Proceedings of the 10th International Symposium on Environmental Degradation of Materials in Nuclear Power System – Water Reactors, NACE, 2001.
34. E. Hillner, in: Zirconium in the Nuclear Industry: ASTM STP 633, Philadelphia, 1977, p. 211.
35. B.G. Park, I.S. Hwang, et al., "Corrosion induced clogging and plugging in water-cooled generator cooling circuit", International conference on water chemistry in nuclear reactors systems, Chimie 2002, Avignon, France, April 22-26, 2002.
36. D.S. Morton, S.A. Attanasio and G.A. Young, "Primary water SCC understanding and characterization through fundamental testing in the vicinity of the nickel/nickel oxide phase transition", Proceedings of the 10th International Symposium on Environmental Degradation of Materials in Nuclear Power System – Water Reactors, NACE, 2001.

TABLE 1. Chemical Composition of Alloy 600 Used in This Study (wt.%).

Element	Composition
C	0.06
Mn	0.26
Fe	8.31
S	0.001
Si	0.3
Cu	0.12
Ni	75.12
Cr	15.25
Al	0.16
Ti	0.36
Nb	0.04
P	0.09
B	0.02
N	0.01

TABLE 2.
Nominal Raman Peak Wavenumbers for Oxide Powders[a] Measured in Room Temperature Air Environment.

Oxide	This work[b]	Ref. A[c]	Ref. B[c]
NiO	1,074	<u>1,074</u> [16]	
	910	913 [16]	
	725	727 [16]	
	<u>532</u>	<u>535</u> [16]	<u>490</u> [16]
	400	370 [16]	
$NiFe_2O_4$	<u>702</u>	<u>705</u> [17]	<u>700</u> [18]
	654[sh]	655 [17]	655 [18]
	595	592 [17]	
	574	570 [17]	579 [18]
	492	488 [17]	490 [18]
	460	457 [17]	433 [18]
Cr_2O_3	610	613 [19]	585 [19]
	<u>550</u>	<u>552</u> [19]	554 [19]
	528	527 [19]	<u>488</u> [19]
	352	350 [19]	387 [19]
	302	300 [19]	352 [19]
$NiCr_2O_4$	<u>687</u>	685 [17]	<u>686</u> [18]
		616 [17]	
		585 [17]	
	550-560	554 [17]	
	<u>513</u>	<u>514</u> [17]	<u>512</u> [18]
	429	430 [17]	

[a] The most intense peak(s) in each spectrum is underlined.
[b] The wavenumber of a well-resolved peak has an associated uncertainty of ±2 cm^{-1}.
[c] The excitation laser with 647.1 nm wavelength was used.

TABLE 3.
Temperature and Exposure Time of Alloy 600 Specimen Prior to In-Situ Raman Spectra Measurements in High Temperature Water.

DH_2 (cc/kg)	Temperature (℃)	Total exposure time prior to first measurement at temperature (h)	Hold time at each temperature prior to first measurement (h)
30	250	28	2
	290	33.5	3
	320	42	7
	350-I	47.5	3.5
	350-II	69.5	20.5
1	250	40	33
	290	45	3
	320	48	2
	350-I	51	2
	350-II	74	23

TABLE 4.
Summary of Experimental Observations of Surface Oxide Phases Of Alloy 600 in 350℃ Water in Comparison with Literature Data at Each Dissolved Hydrogen Concentration.

	This work	Soustelle[11]	Caron[12]	Nakagawa[30]
Method	In-situ Raman	GDOS + EDS	XPS	Synchrotron XRD + TEM
Temperature (^{o}C)	350	360	330	320
Exposure time (hrs)	70	300	1869	1000
Oxide(s) at high DH_2	CrOOH Cr-Oxide $NiO+NiCr_2O_4$	Compact layer ($NiCr_2O_4$)+ Precipitates ($NiFe_2O_4$)	$NiCr_2O_4$	(Ni+Cr-rich) oxide + Precipitates ($NiFe_2O_4$)
Oxide(s) at low DH_2	CrOOH Cr-Oxide NiO	Compact layer ($NiCr_2O_4$)	NiO	NiO

TABLE 5.
Summary of in-situ Raman Observations and Thermochemical Predictions of Surface Oxide Phases of Alloy 600 in 350℃ Water with the Assumption of Different Oxides.

	Predicted at 350 °C			Observed at 350 °C
		With Ni spinels	Without Ni spinels	
DH_2 = 30cc/kg	With CrOOH	CrOOH $NiFe_2O_4$	CrOOH NiO	NiO $NiCr_2O_4$ CrOOH Cr-Oxide
	Without CrOOH	$NiCr_2O_4$ $FeCr_2O_4$	NiO $FeCr_2O_4$	
DH_2 = 1cc/kg	With CrOOH	CrOOH $NiFe_2O_4$	CrOOH NiO	NiO CrOOH Cr-Oxide
	Without CrOOH	$NiCr_2O_4$ $FeCr_2O_4$	NiO $FeCr_2O_4$	

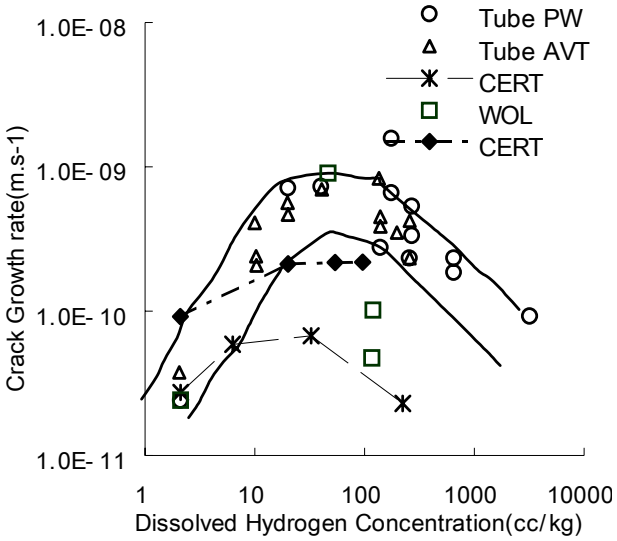

FIGURE 1. Influence of hydrogen concentration on the crack growth rate of PWSCC in Alloy 600 at 360℃.[10,11]

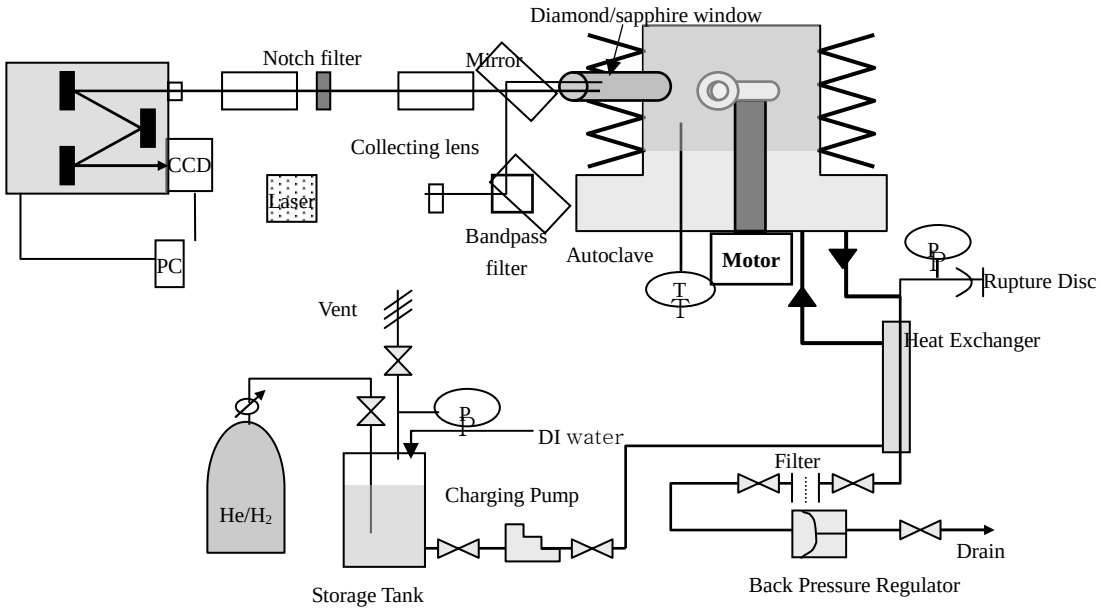

FIGURE 2. Layout of in-situ Raman spectroscopic measurement system in high temperature aqueous environment.

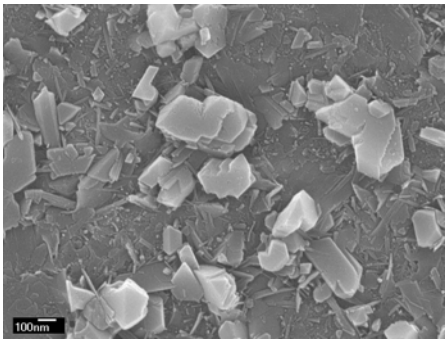

FIGURE 3. Field emission scanning electron micrographs of oxide film on Alloy 600 after 110 hours exposure in simulated PWR water.

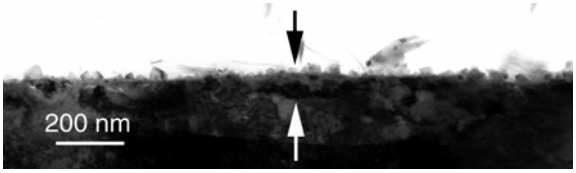

FIGURE 4. TEM micrographs of oxide film on Alloy 600 after 71 hours exposure in simulated PWR water.

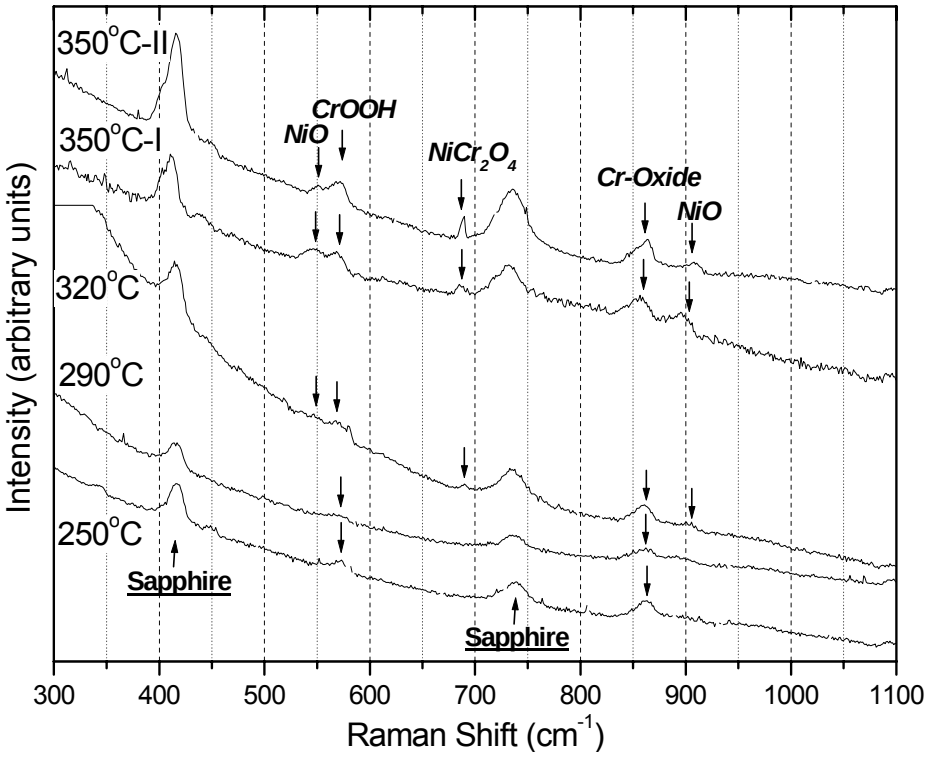

FIGURE 5. In-situ Raman spectra obtained for Alloy 600 by holding at 250, 290, 320 and 350℃, respectively, during heating up to 350 ℃ in PWR water condition with DH_2=30cc(STP)/kg.

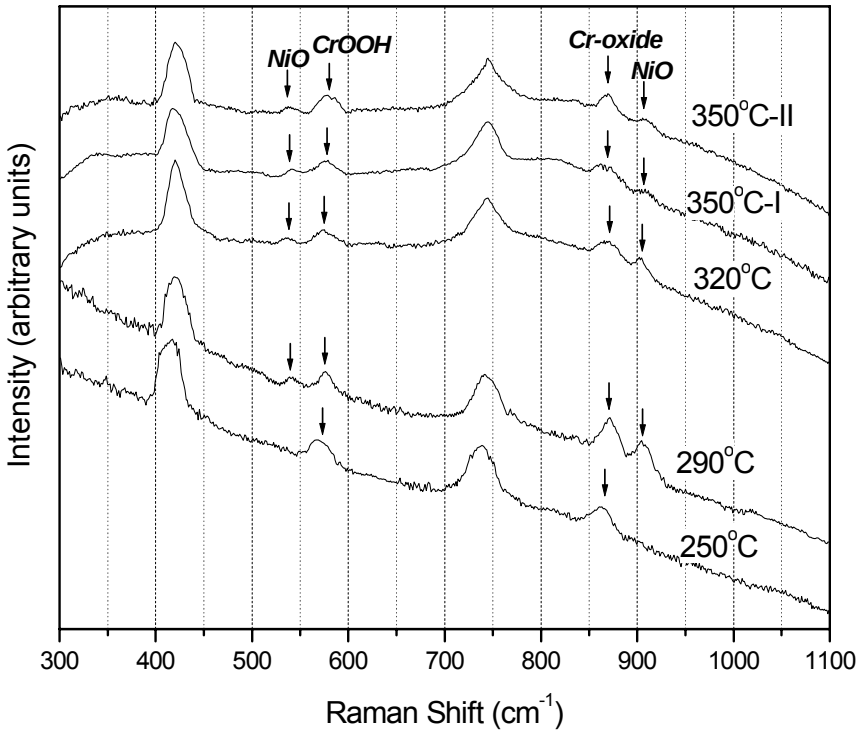

FIGURE 6. In-situ Raman spectra obtained for Alloy 600 by holding at 250, 290, 320 and 350℃, respectively, during heating up to 350℃ in PWR water condition with DH_2=1cc(STP)/kg.

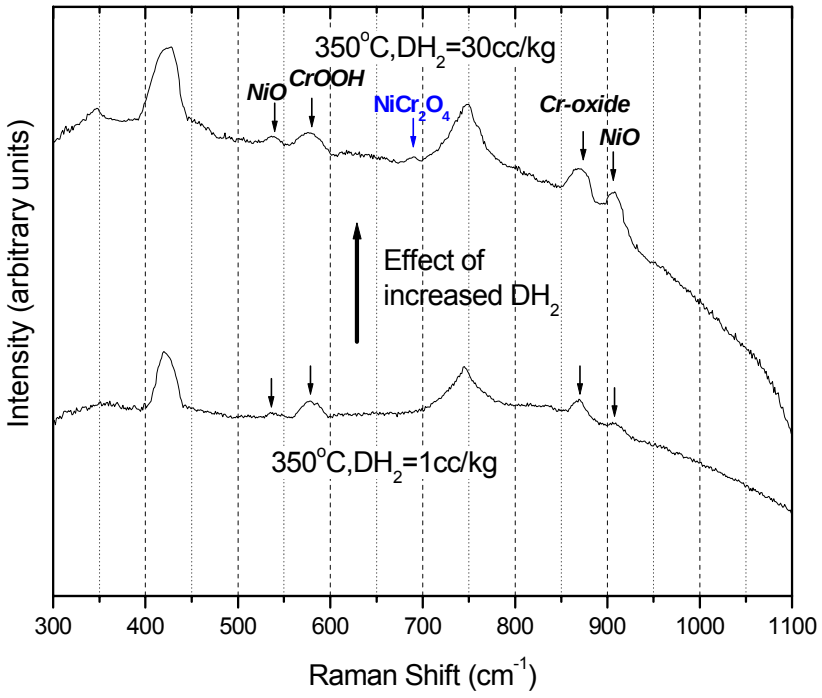

FIGURE 7. In-situ Raman spectra obtained for Alloy 600 at 350℃ in PWR water as the DH_2 in water was increased from 1 to 30 cc/kg.

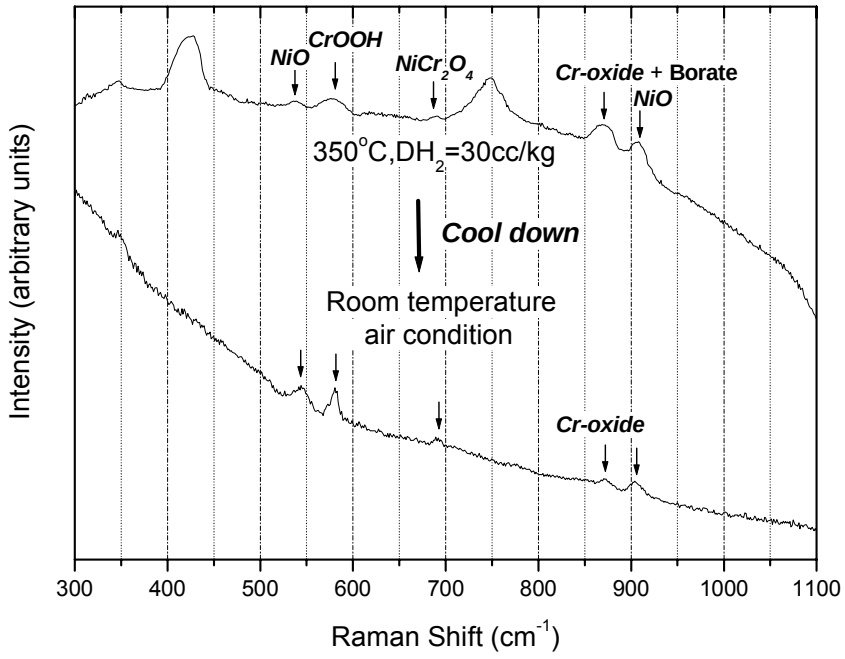

FIGURE 8. Comparison of Raman spectra obtained for Alloy 600 between by in-situ method at 350℃ in PWR water with DH_2 =30 cc/kg and by ex-situ method in room temperature and air condition.

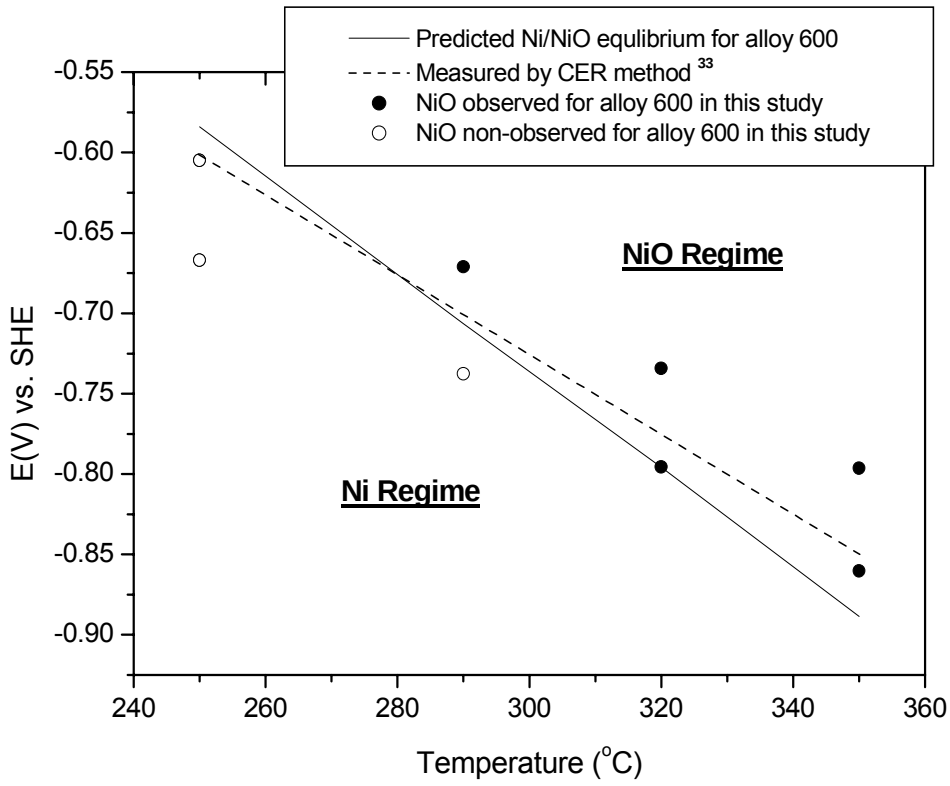

FIGURE 9. Summary plot on electrochemical potential for nickel in the Alloy 600 as a function of temperature.

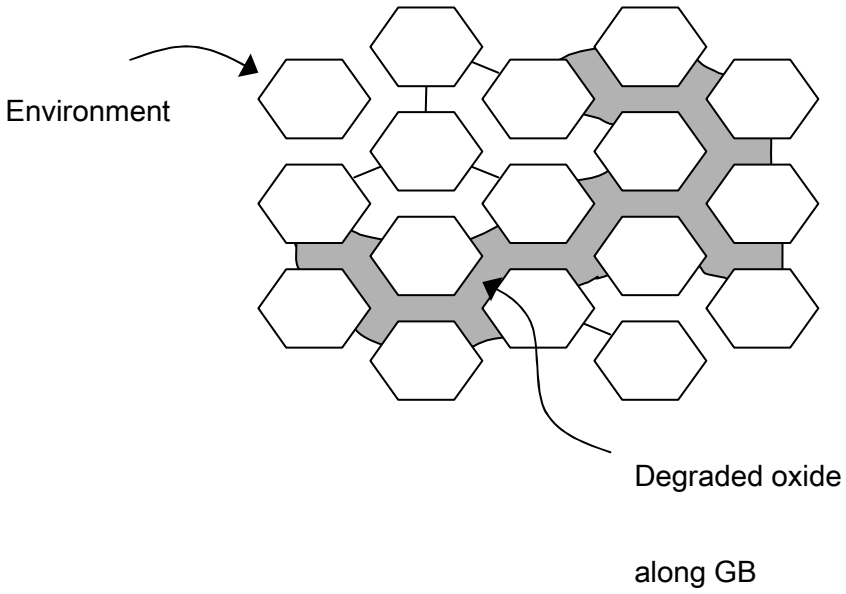

FIGURE 10. Postulated Redox-induced GB Oxide Degradation Mechanism.

Results of Accelerated SCC Testing of Alloy 82, Alloy 182 and Alloy 52M Weld Metals

R. J. Jacko, R. E. Gold, G. V. Rao,
Westinghouse Electric Company LLC
K. Koyama, Mitsubishi Heavy Industries, Ltd.
A. Kroes, Westinghouse Electric Europe

SUMMARY

Accelerated stress corrosion cracking tests were performed in a 400°C doped steam environment on weld metal specimens of Alloy 52M and Alloy 182. All specimens were tested as flat plates, bolt-loaded to strains of 0.35% and 1.0% in a four-point bent beam configuration. Alloy 600 specimens, prepared from archived sections of a CRDM nozzle, were included as control specimens. In exposure times equivalent to more than forty years at operating temperatures, Alloy 52M exhibited complete resistance to stress corrosion crack initiation. Stress corrosion cracking initiated in the Alloy 182 specimens in exposure times less than one-fifth the total exposure time of the Alloy 52M specimens. Crack initiation was also observed in the Alloy 600 control specimens.

In a separate but related evaluation, Alloy 82 and Alloy 182 weld metal specimens removed from the V.C. Summer reactor vessel nozzle safe-end that cracked in service in 2000 were tested in simulated primary water environments. Crack initiation tests were performed using four-point bent-beam specimens stressed in tension to loads equivalent to surface stresses of 400 and 500 MPa. These tests were performed at 360°C for total exposure times of 3522 hours. Crack initiation was not observed for any of the bent-beam specimens.

Crack growth rate tests were performed at 325°C on these weld metals using actively-loaded 0.5T-compact tension specimens. Nominal stress intensities of 20 and 35 MPa$\sqrt{m}$ were used. Careful post-test examinations indicated only the presence of minor welding defects. Only small differences were observed in the crack growth rates of the fatigue-precracked Alloy 82 and Alloy 182 compact tension specimens although the Alloy 82 specimens were tested with the weld dendrites in a more susceptible orientation.

INTRODUCTION

Three separate cracking events occurred in PWR reactor vessel outlet nozzle-to-pipe safe-end welds in 2000. These occurred at the Ringhals 3 and 4 units in Sweden and at the Summer PWR in the United States. Detailed destructive examinations were performed on specimens removed from the Ringhals 4 and Summer nozzles. The former examinations were done by

Studsvik AB in Sweden, and the latter examinations were done at the Westinghouse Science and Technology Department Remote Metallographic Facility.

At both Ringhals 4 and Summer, the full-section butt welds were made by "buttering" the face of the alloy steel nozzle with Alloy 182 and completing the weld with a multipass filler weld using Alloy 182 and/or Alloy 82. The Ringhals 4 degradation consisted of several deep axial cracks in the Alloy 182 weld (Ref. 1). At Summer, where considerable through-wall leakage had occurred, Westinghouse identified a 6.86-cm long axial crack on the OD surface, and several other indications on the ID surface of the weld (Ref. 2).

Repairs were made at Ringhals using Alloy 52M[1], and at Summer using Alloy 52 and Alloy 152. Weld qualification mockup preparations at Ringhals, involving both Alloy 52M and Alloy 182 multipass welds, provided test material for this program. The availability of a large ring section of the entire Summer circumferential nozzle weld afforded the further opportunity for stress corrosion cracking tests of the Alloy 82 and Alloy 182 welds from that plant. These materials were used for a variety of crack initiation and crack growth tests, the results of which are presented in this paper.

SCOPE OF THE EXPERIMENTAL PROGRAM

The research reported here was conducted to examine the following issues:

- Crack initiation in Alloy 52M (and controls of Alloy 182 and Alloy 600) used for the recent Ringhals repairs,
- Crack initiation in Alloy 82 and Alloy 182 weld metal specimens removed from the Summer outlet nozzle safe-end that cracked in 2000, and
- Crack growth rates in the Alloy 82 and Alloy 182 safe-end weld metals.

All crack initiation tests were performed using four-point bent beam specimens, and the crack growth rate tests were performed on actively-loaded 0.5T-compact tension specimens. A summary of the overall test matrix is shown in Table 1. Note that Alloy 182 was tested both from the Ringhals mockups and from the Summer nozzle safe-end.

The 400°C (752°F) crack initiation tests were performed in a doped steam environment, containing 30 ppm each of the chloride, fluoride and sulfate salts of sodium, in addition to a 76 kPa partial pressure (approximately 11 ppm) of hydrogen in 20 MPa steam. These four-point bent beam specimens were tested at top-surface strains of 0.35 and 1.0%, corresponding to average stresses in these materials of 360 MPa (52 ksi) and 500 MPa (73 ksi), respectively.

The 360°C (680°F) crack initiation tests were performed in simulated primary water [2.0 ppm Li, 500 ppm B, 30-35 cm^3 (STP) H_2/kg H_2O] with applied loads equivalent to surface stresses of

[1] Alloy 52M is a modified version of Alloy 52, the product used for gas tungsten arc, or gas metal arc, welding of Alloy 690 (Ref. 3).

400 and 500 MPa (58 and 73 ksi). The Summer Alloy 82 and Alloy 182 weld specimens were prestrained to permit testing at this stress level.

Table 1 - Overall Test Matrix

Material	Crack Initiation		0.5T-CT Crack Growth at 325°C
	400°C	360°C	
Alloy 52M [Ringhals]	X	---	---
Alloy 182 [Ringhals]	X	---	---
Alloy 600	X	---	---
Alloy 82 [Summer]	---	X	X
Alloy 182 [Summer]	---	X	X

Photographs showing typical test configurations for the 400°C tests are shown in Figure 1; the Ringhals Alloy 52M and Alloy 182 specimens were 9-mm thick. In addition to the Alloy 52M and Alloy 182 prepared for the Ringhals mockups, several Alloy 600 specimens were prepared from available CRDM archived material; these were tested as 3.8 mm thick plate in the four-point bent beam configuration. Photographs of the Summer weld specimens, loaded in preparation for the 360°C crack initiation tests are presented in Figure 2. The thickness of the Summer weld specimens used for these tests was in the range 2.4 to 3.2 mm.

Crack growth rate tests of the Summer Alloy 82 and Alloy 182 welds were performed at 325°C (617°F) in a simulated primary water environment containing 3.5 ppm Li, 1800 ppm B and 30-35 cm^3 (STP) H_2/kg H_2O. The specimens were fatigue pre-cracked in air at a stress intensity less than 15 MPa$\sqrt{m}$ and subsequently tested at stress intensities of 20 and 35 MPa$\sqrt{m}$. Crack growth was actively monitored *in situ* using the reverse DC potential drop method. Tests were conducted consistent with the guidelines specified in ASTM E399-90.

The specimens were periodically unloaded to a value 0.7 times the full applied load, in order to break any oxides that might compromise the accuracy of the DC potential drop measurements. The specimens were side-grooved in an attempt to keep the cracking generally in the intended plane. There is no standard terminology for the orientation of weld specimens. Adopting the ASTM terminology for plates, the Alloy 82 weld specimens were tested in the T-S direction. The crack direction was aligned with the dendrite direction in the Alloy 82 weld metal. Because of differences in the welding orientation for the Alloy 182 butter passes, the Alloy 182 butter passes were tested in the T-L direction where the crack growth direction was perpendicular to the dendrites.

TEST MATERIALS

The chemical concentrations for all test materials are summarized in Table 2. The chemical analyses reported for "Alloy 182 – Ringhals" and Alloy 52M were provided by Uddcomb

Table 2 - Chemical analyses for test materials

Element	Alloy 600	Alloy 182	Alloy 52M [NO6052]	Alloy 82 [N06082]		Alloy 182 [W86182]	
	WF 147	Ringhals	ERNiCrFe-7	Summer	ERNiCr-3	Summer	ENiCrFe-3
C	0.033	0.042	0.020		0.10 max		0.10 max
Si	0.29	0.43	0.03	0.13	0.50 max	0.73	1.0 max
Mn	0.78	6.63	0.92	3.29	2.5-3.5	6.88	5.0-9.5
P	0.009	0.004	0.003	n.d.	0.03 max	n.d.	0.03 max
S	0.001	0.002	0.001	n.d.	0.015 max	n.d.	0.015 max
Al			0.08	0.65		1.63	
B			0.004				
Cr	15.69	13.95	30.13	19.61	18.0-22.0	15.57	13.0-17.0
Cu	0.02	0.01	0.03	n.d.	0.50 max	n.d.	0.50 max
Fe	9.65	8.04	8.50	5.20	3.0 max	8.03	10.0 max
Mo			0.02				
Ni	73.07	68.90	60.10	69.01	67.0 min	64.61	59.0 min
Ti		0.47	0.22	0.60	0.75 max	0.93	1.0 max
Zr			0.006				
Nb + Ta		1.41	0.93	1.37	2.0-3.0	1.54	1.0-2.5
Co	0.18				0.12 max		0.12 max
Sources	Test Rpt.	Test Rpt.	Test Rpt.	EDS	ASME	EDS	ASME

Engineering, who manufactured the weld mockups for the Ringhals repair qualification program, and provided the materials tested (Ref. 4). The Alloy 600 material was from an archived CRDM penetration; this heat (WF147) had exhibited moderate resistance to stress corrosion cracking in previous testing. The microstructure of this material is shown in Figure 3, where it can be seen that a substantial density of carbide precipitation exists at current or prior grain boundaries.

Actual chemical analyses were not available for the Summer Alloy 82 and Alloy 182 weld metals. The values reported in Table 2 are those determined by EDS analyses performed on the scanning electron microscope; for comparison, the values from Section II of the ASME Code are shown beside these analyses. Some difference are noted; however, it was based on the analyses shown that supported the conclusion that the materials tested were in fact correctly identified (see, for example, the correspondence for Mn and Cr, two elements that vary significantly for these weld metals).

TEST RESULTS

Crack Initiation Tests - 400°C Doped Steam

The four-point bent beam specimens of Alloy 52M, Alloy 182 and Alloy 600 were tested at 400°C for a period equivalent to more than forty years of operation at the 322.8°C Ringhals outlet nozzle operating temperature. This time-correlation, with an acceleration factor of 195 in the doped steam environment, was derived from similar tests of Alloy 600 in which it was observed that in-service degradation after 89,000 effective full power hours at 317°C was essentially duplicated in 289 hours in doped steam [the resulting acceleration factor of 308 was adjusted to 195 to account for the temperature difference] (Ref. 5).

The results of the 400°C tests are summarized in Table 3. The times at which interim inspections were performed, and the equivalent efpy at the Ringhals service temperature, are shown in the left columns. As indicated, the terms “low” and “high” refer to the strain level.

Table 3 – Summary of crack initiation tests in the 400°C doped steam environment

Exposure Time		Alloy 52M		Alloy 182		Alloy 600	
AC, hours	Equiv. efpy	Low	High	Low	High	Low	High
124	2.8	0/2	0/2	0/2	0/2	0/2	0/4
214	4.8	0/2	0/2	--	2/2	--	--
269	6.0	0/2	0/2	0/2	2/2	0/2	1/4
418	9.3	0/2	0/2	--		0/2	1/4
450	10.0	0/2	0/2	2/2		--	2/4
598	13.3	0/2	0/2	2/2		0/2	3/4
889	19.8	0/2	0/2			0/2	3/4
1343	29.9	0/2	0/2			0/2	3/4
1801	40.1	0/2	0/2			0/2	3/4
2051	45.6	0/2	0/2			Not exposed	Not exposed

Low = 0.35% strain; High = 1.0% strain X/Y = no. with SCC/no. tested; AC = autoclave

After 2051 hours, crack initiation was not observed in any of the Alloy 52M specimens. In the inspection after a cumulative exposure of 1343 hours, short (0.16 and 0.20-mm in length) indications were observed on the surface of the two high-strain Alloy 52M specimens. These indications did not change in subsequent exposures. Subsequent metallographic cross-sectioning indicated these to be shallow hot-microfissures that were present from the weld preparation, but had not been clearly identified in the earlier examinations. Such hot cracks are generally distinguishable from shallow SCC by their characteristic rounded, as opposed to sharp, morphology. It was noted that these features did not serve as initiation sites for SCC, nor did they propagate during the tests.

Four Alloy 182 weld specimens were tested; two at low strain and two at high strain, Table 3. After a cumulative exposure of 214 hours (equivalent to 4.8 efpy in service), a number of cracks were observed in each of the high-strain specimens. These cracks ranged from as short as 0.25 mm to 3.0 mm in length. The low-strain specimens first exhibited stress corrosion cracking at the 450-hour interim inspection. During a subsequent 148-hour exposure, these cracks grew to a maximum length of 4.0 mm.

The Alloy 600 controls cracked only at the high-stress condition with the first failure occurring at 269 hours. Normally, it would be expected that the Alloy 600 specimens would crack before the Alloy 182 weld metal. However, this heat of Alloy 600 had previously exhibited moderately high resistance to stress corrosion cracking (Ref. 6).

Crack Initiation Tests - 360°C Primary Water

The four-point bent beam specimens prepared from the Summer Alloy 82 and Alloy 182 welds were exposed for a total of 3522 hours in the 360°C primary water environment. Careful post-test visual inspections did not reveal any indications of crack initiation. This exposure is equivalent to approximately 4.0 efpy at the Summer outlet nozzle temperature of 325.6°C; the cracking at Summer was detected after 14.3 efpy.

Crack Growth Rate Tests - 325°C Primary Water

At the conclusion of the crack growth rate testing, measurements made on the fracture surface using a combination of SEM fractography and optical microscopy to determine the rate of cracking. The reverse DC potential data were used to estimate trends in the SCC growth rate with time. Optical and scanning electron micrographs of the fracture surface of an Alloy 182 specimen is presented in Figure 4.

The measured crack growth rates determined for the Summer nozzle Alloy 82 and Alloy 182 weld metals are shown in Figure 5. Included in Figure 5 are curves corresponding to the 75th percentile data for Alloy 600 from MRP-55 (Ref. 7), and a preliminary EPRI model for crack

growth in Alloy 182 (Ref. 8). The current program results are within the range expected from previous industry experience.

Only small differences were observed between the Alloy 182 and Alloy 82 welds. Recall that there was a difference in specimen orientation between the Alloy 182 butter welds tested in the T-L orientation and the Alloy 82 welds tested in the T-S orientation. Crack growth rates have been reported to be 2 to 5 times higher (Refs. 9, 10) when the cracks were parallel to the dendrites (T-S) rather than perpendicular to the dendrites (T-L). The differences between the crack growth rates measured for Alloy 82 and 182 in the current program are well within the data scatter. However, if these materials were tested in the same orientation, the Alloy 82 growth rates may be one-half to one-fifth those of the Alloy 182 rates. It is concluded from these tests that the V. C. Summer CRDM nozzle weld metals do not exhibit unusually low resistance to environmental crack growth.

CONCLUSIONS

Crack Initiation - 400°C Doped Steam

- In four-point bent beam tests, Alloy 52M welds, prepared to simulate the Ringhals 4 field repairs of the reactor vessel outlet nozzle, exhibited complete resistance to stress corrosion crack initiation in laboratory exposure times exceeding 45 efpy equivalent service time. Small microfissures on the surface of the Alloy 52M welds, stressed in tension, did not serve as initiation sites for environmental degradation, nor did they propagate during the tests.

- Stress corrosion cracks initiated in specimens prepared from the Ringhals 4 Alloy 182 weld qualification mockups in exposure times less than one-fifth the total exposure time of the Alloy 52M specimens.

- Crack initiation was observed in specimens of archived Alloy 600 CRDM nozzle material in the doped steam environment.

Crack Initiation - 360°C Primary Water

- The four-point bent beam specimens prepared from the Summer Alloy 82 and Alloy 182 welds were exposed for a total of 3522 hours in the 360°C primary water environment with no indications of crack initiation. This exposure is equivalent to approximately 4.0 efpy at the Summer outlet nozzle temperature of 325.6°C.

- It is concluded that these materials do not exhibit unusually poor resistance to crack initiation in primary water environments

Crack Growth Rate Tests - 325°C Primary Water

- The results of crack growth rate tests of 0.5T-CT specimens prepared from the Summer reactor vessel outlet nozzle Alloy 82 and Alloy 182 safe-end weld metals, tested at stress intensities of 20 and 35 MPa$\sqrt{m}$, were consistent with the existing database.

- The crack growth rates measured in the Alloy 82 welds in the T-S orientation were similar to the crack growth rates reported on the Alloy 182 welds in the T-L orientation.

- These materials do not exhibit unusually low resistance to environmental crack growth.

REFERENCES

1. *Metallographic Examination of Cracks in Nozzle to Safe End Weld of Alloy 182 in Ringhals 4*, A. Jenssen et al., Studsvik Report 00/099, December 1, 2000.

2. "Metallurgical Investigation of Cracking in the Reactor Vessel Alpha Loop Hot Leg Nozzle to Pipe Weld at the V. C. Summer Station," Gutti Rao, Westinghouse Non-Proprietary Class 3 Report, WCAP-15616, Rev. 0, January 2001.

3. *Inconel™ Filler Metal 52M*, Preliminary Data Sheet, Special Metals Welding Products Company (undated specification sheet).

4. Communication and attached drawing EDSK437553B, J. Stotsberg, Uddcomb Engineering to R. J. Jacko, Westinghouse STD, 6 June 2002.

5. G. V. Rao, R. J. Jacko and A. R. McIree, "An Assessment of the CRDM Alloy 600 Reactor Vessel Head Penetration PWSCC Remedial Techniques", *Proceedings, Contributions of Materials Investigation to the Resolution of Problems Encountered in Pressurized Water Reactors*, Fontevraud V, pp. 93-105, SFEN, September 2002.

6. *Crack Growth and Microstructural Characterization of Alloy 600 PWR Vessel Head Penetration Materials*, Electric Power Research Institute, Palo Alto, CA, December 1997. EPRI TR-109136.

7. *Materials Reliability Program (MRP) Crack Growth Rates for Evaluating Primary Water Stress Corrosion Cracking (PWSCC) of Thick-Wall Alloy 600 Materials (MRP-55)*, Revision 1, EPRI, Palo Alto, CA: 2002. 1006695.

8. *Crack Growth of Alloy 182 Weld Metal in PWR Environments (PWRMRP-21)*, EPRI, Palo Alto, CA, June 2001. TR-1000037.

9. R. Pathania, A. R. McIlree and J. Hickling, "Overview of Primary Water Cracking of Alloys 182/82 in PWRS", *Proceedings, Contributions of Materials Investigation to the Resolution of Problems Encountered in Pressurized Water Reactors*, Fontevraud V, pp. 93-105, SFEN, September 2002.

10. F. Vaillant, Ph. Moulart, J-M. Boursier, C. Amzallag and J. Daret, "Crack Growth Rates in Thick Materials of Alloy 600 and Weld Metals of Alloy 182 in Laboratory Primary Water, Comparison with Field Experience", *Proceedings, Contributions of Materials Investigation to the Resolution of Problems Encountered in Pressurized Water Reactors*, Fontevraud V, pp. 107-116, SFEN, September 2002.

Figure 1 - Photographs of Alloy 52M (Upper 1 thru 4), Alloy 600 (600-1 thru-4), and Alloy 182- 4 (lower photo) bent beam test specimens. [Specimens with suffixes -1 and -2 were strained 0.35%; those with suffixes -3 and -4 wee strained 1.0%]

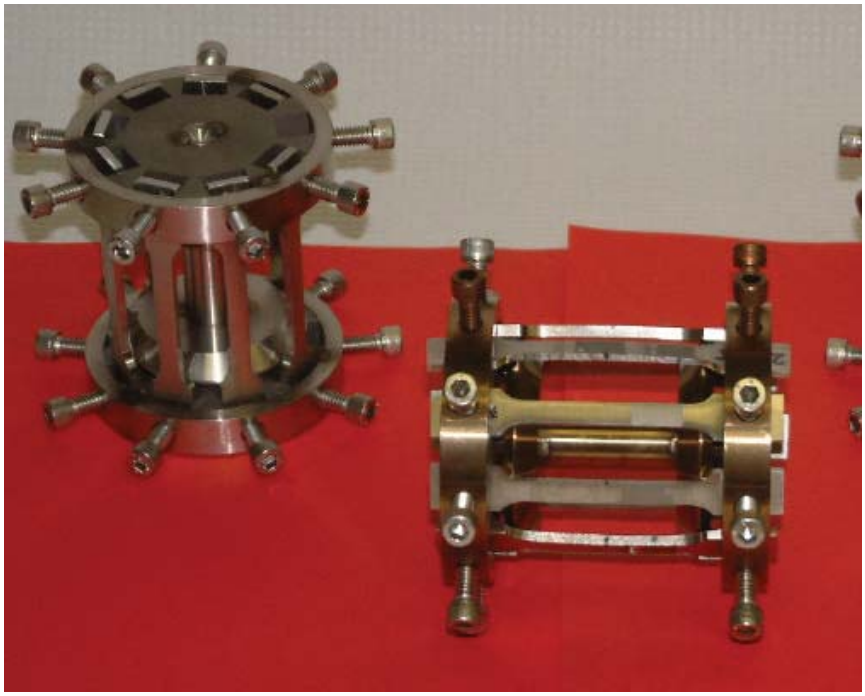

Figure 2 – Photographs showing the carousel-type arrangement used for the bent beam tests of the Summer Alloy 82 and Alloy 182 nozzle safe-end weld metals.

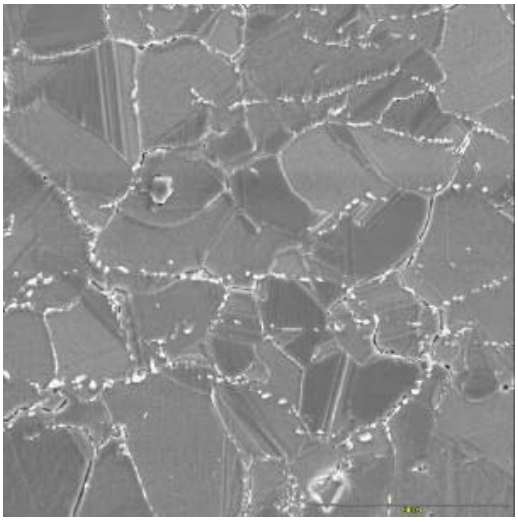

Figure 3 – Microstructure of Alloy 600 Heat WF147

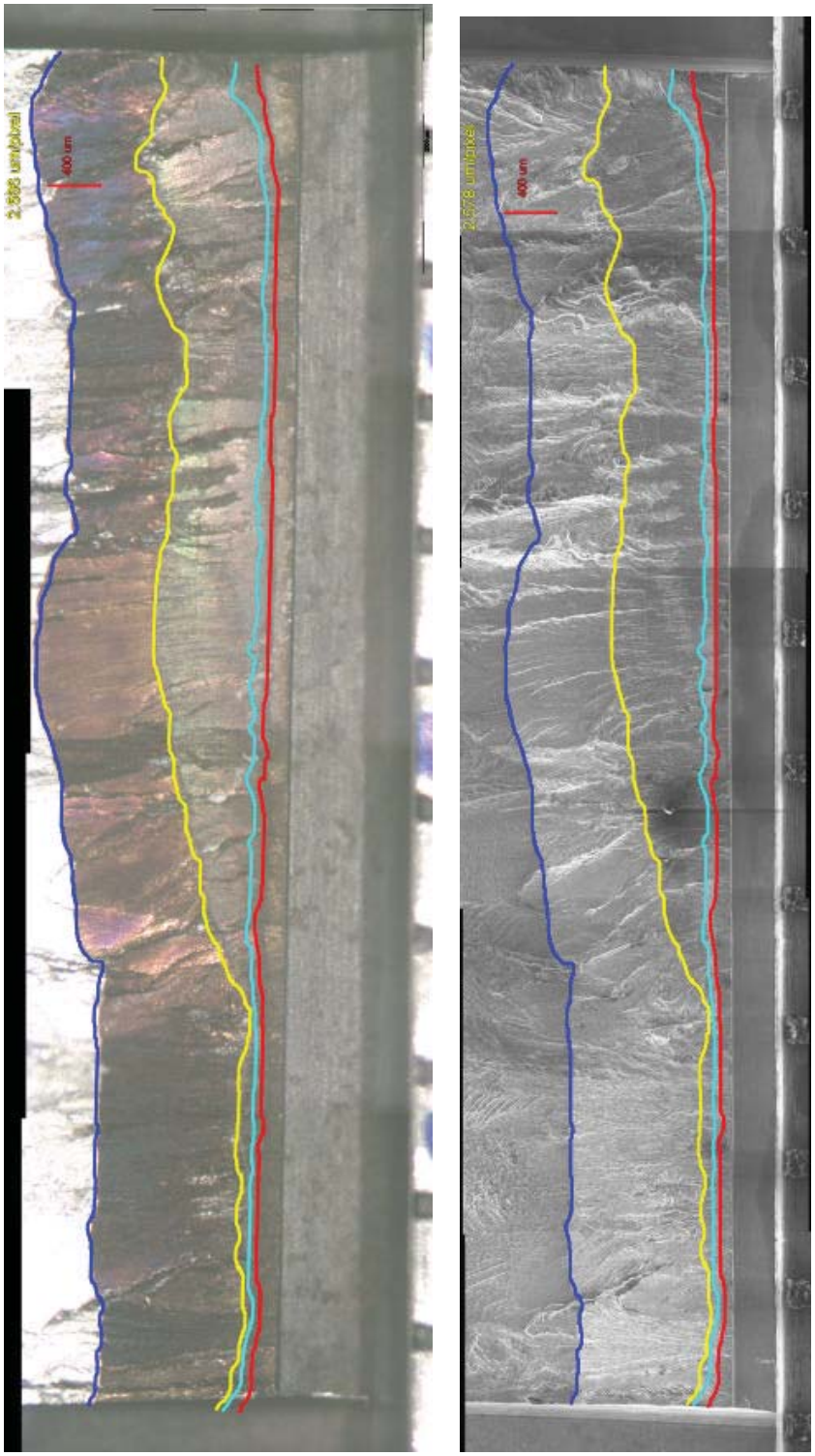

Figure 4 – Optical (top) and SEM (bottom) micrographs of an Alloy 182 crack growth specimen, showing the precrack and environmental crack extension across the face of the specimen.

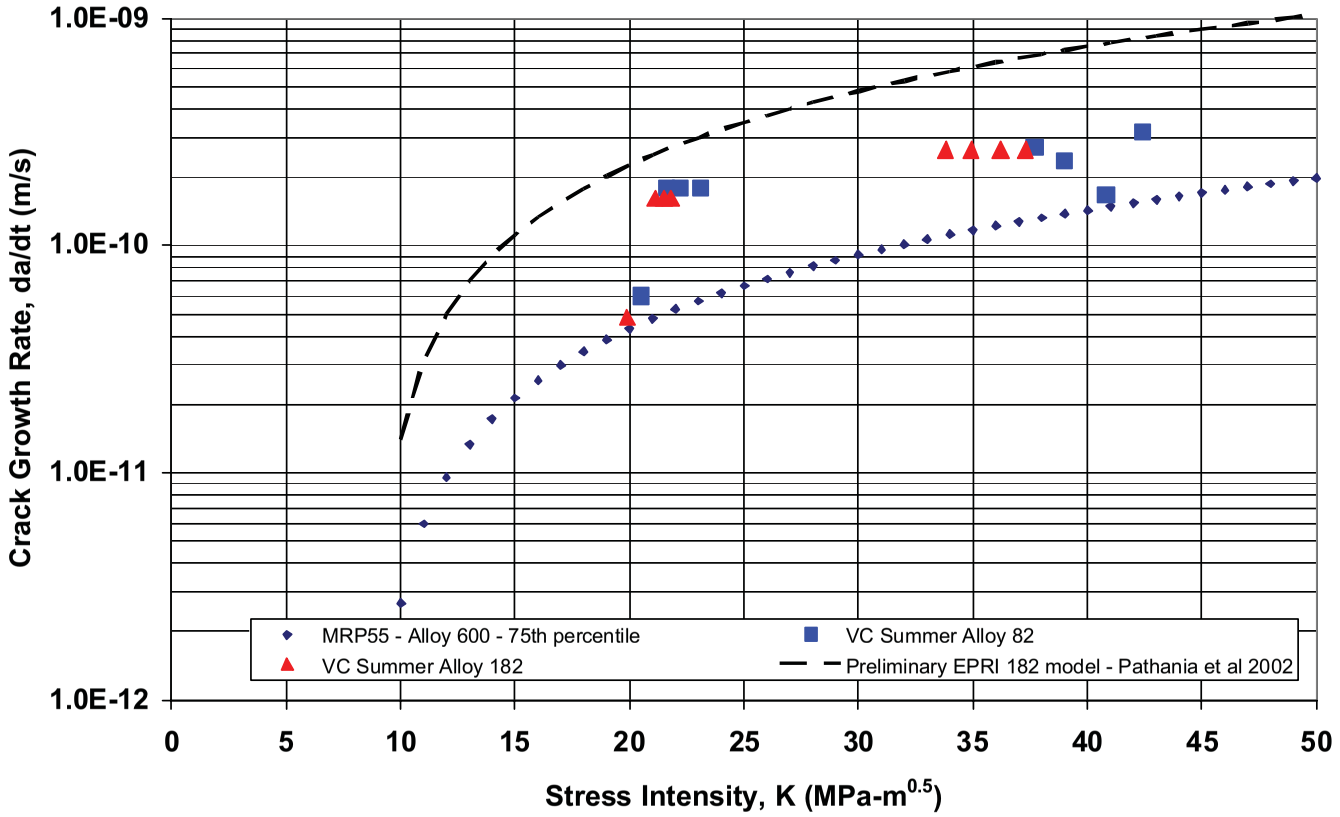

Figure 5 – Crack growth rate results for the Summer Alloy 82 and 182 weld metals compared with published data

Metallurgical Investigation and Root Cause Assessment of the Reactor Vessel Head Penetration Alloy 182/82 J-groove Weld Cracking in Rotterdam Vessels

G. Rao, Westinghouse Electric Company, Pittsburgh, PA
J. Bennetch, Dominion Generation,
G. Embring, Ringhals AB, Sweden, and
W. Gahwiller, Westinghouse Electric Company, Pittsburgh, PA

This Paper reviews the results of metallurgical investigation of cracking in the Alloy 182/82 J-groove welds of the Reactor Vessel Head Penetrations at North Anna 2 and Ringhal 2 Units to establish the origin and root cause of the cracking. The investigations were centered on boat samples containing cracking detected during scheduled outage inspections. The investigations included surface examinations, metallographic and fractographic assessments, chemistry and dilution assessments. Based on the results mechanistic and root cause assessments were conducted. Brief discussion of the repair methods employed for the cracks is also briefly provided.

The results of the investigations revealed the presence of two different types of cracking; namely, fabrication related hot cracking and service related PWSCC. Based on the results of the mechanistic assessments and a review of the fabrication records, the relation between the two types of cracking and their root cause of occurrence was established. The repair methods adapted for the two plants were discussed.

Manuscript was not available for publication in the Proceedings

The French Regulatory Experience and Views on Nickel-Base Alloy PWSCC Prevention and Treatment.

By

Guy TURLUER, Gérard CATTIAUX, Bernard MONNOT, (IRSN/DES), Fontenay-aux-Roses, FRANCE,
Institute for Radiological Protection & Nuclear Safety (IRSN)
http://www.irsn.fr/
Department of Safety Evaluation (DES)
guy.turluer@irsn.fr
Fax: + 33 1 47 46 10 14

and

David EMOND, Jacques REUCHET, Philippe CHARTIER (DGSNR/BCCN), Dijon, FRANCE
General Directorate for Nuclear Safety & Radiation Protection (DGSNR)
http://www.asn.gouv.fr/
Nuclear Steam Supply System Inspectorate (BCCN).
david.emond@asn.minefi.gouv.fr
Fax: + 33 3 80 29 40 88

Abstract

This paper presents the experience feedback and views of the French Regulatory Authority (ASN) and of the technical support institute (IRSN) on PWSCC prevention since the initiation in 1989 of the "Inconel Zones Review" requested by ASN to Electricité de France (EDF), the national operator of a fleet of 58 PWRs.
This proactive requirement, launched before the discovery, in September 1991, of the only CRDM nozzle leak in France, on Bugey unit 3, was then triggered by the recurrence of many alloy 600 rapid degradations and leaks, world wide, and also in France in the late 1980s, particularly on steam generator tubes and on some pressurizer penetrations.

Thus, the ASN requested that EDF, perform a comprehensive (generic) proactive assessment on all the nickel-base alloy components and parts of the main primary circuits, which of course included vessel head penetrations and bottom vessel head penetrations, and some other zones as a first priority.

This proactive "review" did, a minima, include the following tasks and actions:

- *Update and complete, by an extensive R&D program, the understanding and characterization of the Ni base alloys prone to PWSCC,*
- *Analyze the various materials, metallurgical features, mechanical stresses, and physicochemical conditions of the parts exposed to primary water, in order to predict the occurrence of PWSCC initiation and propagation,*
- *Provide a prioritization of the zones to be inspected,*
- *Implement by improved NDE techniques a practical inspection program on the 58 PWRs,*
- *Prepare and implement any needed mitigation actions as a result of the components conditions assessment.*

The present paper relates the main features of the French regulatory experience over more than 13 years and recalls the main principles of the assessment, which were applied by ASN. These principles, which are formalized in the current regulation rules revised in 1999, are briefly listed hereunder:

- *It is based on avoiding and preventing any leaking on the main primary circuit.*
- *In service inspections (ISI), including volumetric and surface NDE, have been agreed upon between ASN and EDF for all vessel head penetrations, with a re-inspection schedule.*
- *The preexisting regulatory hydraulic testing program was carefully implemented, which implied the removal of thermal insulation on the vessel heads.*
- *A comprehensive R&D program had to be conducted by EDF, the main progress reports and presentations had to be regularly submitted to DGSNR and IRSN staff.*

- *The assessment and the ranking of the sensitivity of the different nickel base alloy zones, derived from R&D and empirical models, would have to be confirmed by a comprehensive ISI program, including bottom head penetrations, steam generator partition plates, and more specific weld metal zones.*
- *ASN reviewed the various mitigations and preventive measures proposed by EDF, either temporary, such as leak detection systems, anti-ejections devices, interim repairs, or long term commitment of the French operator to replace in due time the vessel heads comprising the most affected CRDM penetrations.*

This paper also presents the ASN's follow up of the domestic and international feedback, such as the occurrence of PWSCC cracking (initiation and propagation) in the weld materials, whose occurrence is rather limited in France.

1. INTRODUCTION:

Ironically in a country where the sensitivity of alloy 600 to Stress Corrosion Cracking (SCC) in Pure Water, the source of a very long controversy across the Atlantic, was evidenced as early as 1959 in the French Atomic Energy Commission Laboratories in Saclay by Henri Coriou[1] and coworkers, and later confirmed repeatedly in unpolluted water and Primary Water[2] (hence the acronym PWSCC), it took a very long time and considerable industrial applications to realize that PWSCC was no longer a laboratory curiosity.
As recalled in an IRSN review paper in 1995[3], the recurrence of various worldwide numerous degradations of Steam Generator tubing and tube plugs by PWSCC, lead to the obvious conclusion that **the PWR industry was facing a generic SCC problem even in nominal primary water conditions**, on components or local zones submitted to high levels of residual and/or operational stresses which were not all covered in the past by regulatory NDE requirements and operational surveillance.

The advent of rapid through wall cracking for pressurizer penetrations in the USA, and in France, as early as the first fuel cycle for Inconel 600 instrument penetration nozzles of 1300 MWe units pressurizer in the late 1980s[4], together with the occurrence of circumferential through wall PWSCC cracking of thermally treated alloy 600 tubing on top of the tube sheet during the first fuel cycle in NOGENT unit in 1989[5], were perceived by EDF (the national operator of a fleet now amounting to 58 PWRs) and the French Safety Organizations (now DGSNR and IRSN) as severe warnings.

Consequently, at the strong request of the French Safety Authority (*Autorité de Sûreté Nucléaire)*, which will be referred to as ASN), a proactive approach to the "generic problem of "Inconel Zones" sensitivity to PWSCC" was launched by EDF and Framatome, without any delay as soon as 1989, under the name "Inconel Zone Review", which in fact was initiated and developed sufficiently ahead of time before the discovery in September 1991 of a leaking vessel head penetration on BUGEY unit 3[6] during its first regulatory decennial hydraulic test.

2. OBJECTIVES OF THE INCONEL ZONE REVIEW FOR THE FRENCH FLEET OF 58 PWRs

Actually the preliminary conclusions from the first version of the Inconel review submitted to ASN in summer 1991 did not rank the CRDM zones second to the pressurizer penetrations, but fourth in decreasing sensitivity, after the SG divider plate, and the vessel head vent central penetration[3].
This course of PWSCC events, the complexity and uncertainties to actually rank the sensitivities of the various zones and predict the occurrence of PWSCC crack initiation on actual components showed that the Inconel zone review should not remain an academic exercise and should be comprehensively restarted with a multiple integrated approach, with the following objectives, which had been requested by ASN:

- Review and document all the existing "Inconel zones" in contact with the primary water, characterize and rank their sensitivities toward PWSCC.

- Assess all the technical issues and data relevant to the fitness for service of the reviewed Inconel components in alloys 600, 182 and 82.
- Develop NDE inspection techniques and tooling.
- Implement timely a comprehensive NDE inspection program for the most PWSCC prone zones.
- Justify the various aspects of the Inconel zone review by a comprehensive R& D effort.
- Review and refine the descriptive PWSCC empirical models and input data to ensure a more reliable prediction and ranking of the Inconel zones crack initiation.
- Verify the specific "Inconel Zones" lifetime predictions by a sufficient amount of NDE inspection, either full scale or according to an agreed sampling rate.
- Anticipate any further degradation of these zones and perform a safety assessment for each zone in case of failure or leaks caused by through wall cracking.
- Prepare for mitigation techniques including PWSCC prone components repairs or replacements.

All those stringent and comprehensive requirements developed in the early nineties were justified to guarantee both safety and availability of a large fleet of 58 PWRs, should an untimely treated generic degradation plague most units, which have generic common design and construction features (fleet effect), but also some differences as described briefly in § 4.
Most of those early requirements, devised to master PWSCC issues, are forerunners for the new more general regulatory rules which has been further developed, expanded and formalized recently in a new ministerial order on November 10 th, 1999, devoted to the surveillance in operation, which revised and replaced Part III of the initial ministerial order of February 26 th, 1974.

3. MAIN REGULATORY FEATURES AND PRINCIPLES TO ENSURE THE INTEGRITY OF THE MAIN PRIMARY CIRCUITS DURING OPERATION

3.1) General features

In France, these principles are now formalized in one document, dedicated to the surveillance in operation of the main primary and secondary circuits, referred to as "the ministerial order of November 10th, 1999", (supplemented by a ministerial circular that explicates it and provides guidance for its implementation), which revised and replaced Part III of the initial ministerial order of February 26 th, 1974, which, otherwise dealt then mostly with the design and fabrication aspects of the main nuclear pressure retaining components.

The new ministerial order emphasizes and describes more thoroughly the responsibility of the operator to maintaining the integrity of the main primary and secondary circuits during operation, which implies the assurance that the pressure boundaries would retain their properties, in operation and under various ageing processes, to confine the primary and secondary fluids**.**
This means principally:

- **Precluding the occurrence of leaks** other than those leaks, normally collected, allowed by conception in some joints (pumps for example).
- **Excluding the presence and development of flaws whose noxiousness might be excessive in normal, incidental, or accidental operating conditions,** thus preventing break and any uncontrolled and "unmonitored" leaks, whatever the degradation mechanisms which might be involved.

Consequently, the operator is in principle required to repair every flaw, which could lead to a break or a leak during operation and take appropriate measures to prevent the recurrence of those damages to the secondary and primary circuit.

One exception to the principle of precluding any leak was allowed for some steam generators tube bundles with a large number of tiny (a few mm long but some through wall) longitudinal cracks usually by PWSCC at the roll transition, with very low leak rates, where it was impossible to identify the tubes (to be plugged) contributing most to the overall leakage.
This exception would only hold for SG regularly inspected by sensitive NDE techniques capable to detect and size accurately defects whose degradation mechanisms, orientation and kinetics are fully identified

such as axial PWSCC cracks at the roll transition, namely on steam generators which follow a low leak rule management pending the SG replacement**,** knowing that all SG are equipped with continuous N16 leak monitoring.

The recently formalized French main regulatory principles to be applied are the following:

The operator has to anticipate and take into account, in service, any possible form and/or mechanism of degradation and their combinations, which might affect the integrity of the components of the primary circuit, (such as thermal ageing, embrittlement, creep, fatigue, erosion, wear, corrosion, Stress Corrosion Cracking [SCC], Corrosion fatigue [CF], and other environmental effects including, local chemistry, operational, residual stresses, gamma and neutron irradiation effects…), in particular, through the careful analysis of:

- **Design files** (i.e. stress analysis report of complex assemblies, reinvestigating relevant materials properties),
- **Fabrication records**, materials deviations from conformity and batch specific features,
- **Complex loads or environmental conditions,** for example: thermal fatigue caused by mixing fluids, Stress Corrosion Cracking (SCC) and/ or Corrosion Fatigue (CF), or particularly in singular complex locations,
- **Operation feedback analysis**, both domestic and international, such as materials properties alterations, investigating the cause and magnitude of flaws or indications detected by NDE, which should be further characterized on removed components, parts or samples affected by the given degradation,
- **Components or parts failure/degradation reporting and analysis,**
- **Through appropriate R & D programs,** needed to identify the conditions of occurrence of the degradation mechanisms, and evaluate the quantitative effect of the influential parameters on the degradation kinetics.

The different zones of the main primary system have then to be ranked according to their sensitivity to the different damages taken into consideration, in particular, when establishing maintenance and In Service Inspection (ISI) programs, which have to be submitted with justifications to ASN**.**

3.2) In Service Inspection (ISI):

According to the French regulation, an in-service inspection program has to be defined, for the various types and categories of zones and must be devised and implemented in view of a preventive policy, in order to avoid the failure or loss of integrity, whether it be a leak or the break of the component.
The operator must take the necessary measures to detect early enough the anticipated degradations, in general flaws, adapt the tools and select the proper NDE techniques to implement the regulatory required ISI program capable to detect those flaws before they reach a critical size.

The new regulation provides some differences of treatment with regard to ISI requirements according to two broad categories of zones, respectively **"sensitive zones"** & **"non sensitive zones"**.

"Sensitive zones":
They may belong to the following categories:

- Zones identified as sensitive from the design and safety overall studies,
- Zones where, from the domestic and international experience feedback, the occurrence of degradations are proven or most likely to occur, which usually imply the implementation of a specific maintenance and in service Inspection program,
- Zones where the environmental stressors are complex involving usually some specific combinations of factors among those, mechanical, physicochemical, hydraulic, thermal factors…

The operator has to:

- Determine which zones are sensitive,
- Define their localization and their extension,
- Identify and characterize the degradation mechanism,

- Determine the flaw critical size (with security margins).

The preventive nature of the ISI program implies that it be applied to all the sensitive zones on all components and units of the French PWR fleet concerned by the considered degradation process. The ISI program and schedule depends on the critical size and the growth rate of the defects, in order to make sure the flaw can be detected prior it reaches the critical size. Thus, the utility has to choose the appropriate NDE method and performances and to make a **qualification** of the method.
Two types of qualification are considered:

- **A "specific" qualification**, when the characteristics of the suspected flaws are known, and usually have already been observed and measured on real components,
- **A "general" qualification",** when flaws are suspected, but not yet observed.

During the ISI program implementation, if an indication is detected, the utility has to issue a **deviation** report with deviation analysis, which is usually followed by either a specific justification for its innocuousness, a proposal for a temporary or a definitive repair, or replacement of the part.

Precursor zones: under specific conditions however, some "precursor sensitive zones" might be selected for a first round of inspections within a population of zones of similar sensitivity to a given degradation.
To be considered a precursor, a sensitive zone has to be fully representative with some anticipation of its family of sensitive zones. In other words, the zones of this family must be subject to the same degradation mechanisms, which would occur in the same circumstances, except that the **precursor zone's** rate of degradation initiation must be significantly more precocious and its flaw propagation rate faster than the other zones of its family.
Of course, an extension rule has to be defined in the ISI program that sets down additional NDE to be done on the family, if degradation is detected on the precursor zone.

"non sensitive zones":
For the zones, "a priori judged non sensitive zones"**,** the French regulation requires that some sample checking be performed on non-sensitive zones. ISI in these zones aims at collecting information in order to confirm the conclusions of the degradation sensitivity analysis, in other word at verifying that there are no flaws.

3.3) Periodic requalification for the primary circuit components:

This principle, which was already included in the original ministerial order from February 26th, 1974, and lead to the discovery of the Bugey 3 CRDM penetration degradation and small leak, has been maintained and further developed in the new surveillance ministerial order and implementation circular that stipulates:

The components must be submitted to periodic requalification steps, which include:

- **A complete visit of the primary circuit**
- **A hydro test at least at 1.2 times (207 bar) the design pressure (172.5 bar)** instead of the normal operating pressure (155 bar),
- **An examination of the safety dedicated circuits and set ups.**

A first primary circuit requalification is required no later than 3 years after the first fuel core loading followed by periodic requalifications at ten year intervals, usually during the "extended decennial outages".
The requalification regulatory requirements to be performed at last during the decennial outages constitute an important step, since all the primary circuit is concerned and, in particular, thermal insulation should be removed for visual, video inspections and leak detection:

- **For an overall in-depth defense policy against unanticipated flaws and degradations,**
- **For an extensive review of the fitness for continued service,**
- **Following the implementation of maintenance or replacement operations, on components or parts.**

3.4) French Nuclear Safety Decisions:

The Advisory Group on Nuclear Pressure Vessels (SPN) has studied four times the issue of Inconel zones in France: first in April 1994, then in 1996, in 1997 and the last time in March 2000. The final French nuclear safety decision[1] was published **(http://www.asn.gouv.fr)** and sent to the French utility in March 2001. The requests refer much to the "ministerial order of November 1999". The main requests are the following:

- **Steam generator partition plate:** inspection of the weld of the partition stub (without stress relieving treatment) and triple point zone, of 26 SGs, and one SG with many loose part impacts, and 9 other random SGs, before 2008,
- **Bottom vessel head penetrations**: inspection of all penetrations with UT and ET on twelve reactor vessels before 2008,
- **M shaped core support pads**: an inspection method is being developed and qualified in order to detect and size possible PWSCC cracks. The method must be used during the 30 year outage,
- **Local Inconel repairs in vessel nozzle inner radius**: inspection of Inconel 182 repairs in hot leg nozzle inner radius must be done during the 30 year outage (17 nozzles in 7 reactor vessels) and an inspection method to detect and size cracks in cold leg nozzle inner radius must be performed and qualified.

4. INITIAL FEATURES OF INCONEL ZONES TROUGHOUT THE 4 MAIN FRENCH PWR SERIES

The present fleet of the 58 PWRs, now in operation in France, commissioned for industrial service from 1977 to 1999 were in fact designed and constructed, as part of standardized series, during a crash program initiated in the early 1970s, which did not allow easily for early major materials modifications, which the experience feedback might have suggested. Partly as a result of the Westinghouse patent, applied by Framatome, some Nickel base alloy parts made of Alloy 600 and of related weldments made from Alloys 182 & 82, have been extensively used in the primary circuits of the French PWRs, some of which ensuring the integrity of the pressure retaining boundaries. These are schematically shown in the following figure:

[1] Décision BCCN/MP/ARn°/010067, *March 05/2001,on ASN web site (http://www.asn.gouv.fr) "Zones en alliage "Inconel 600" sur les réacteurs à eau sous-pression d'EDF. Programme de maintenance"*

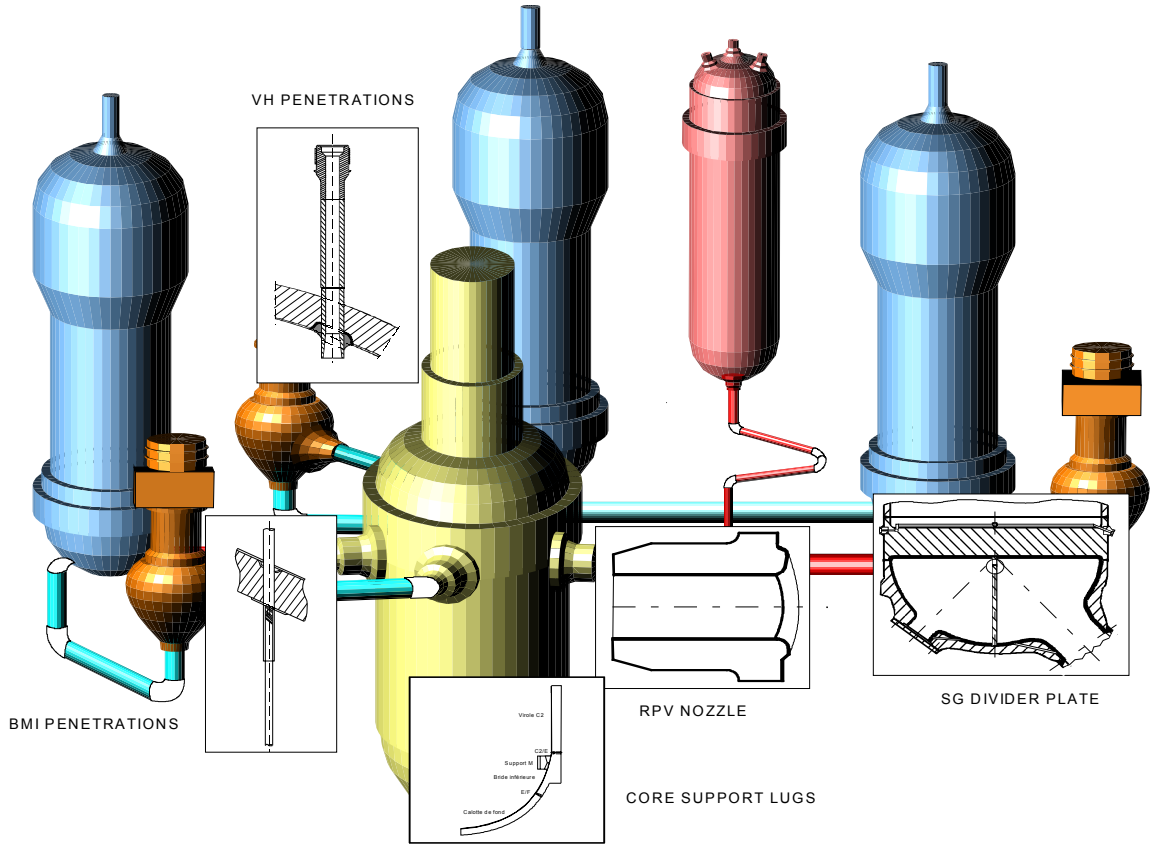

Figure 1, *by courtesy of EDF, (this conference[12])*
Showing the main Inconel Zones locations in the primary circuit and some close-ups

The main 4 series of PWR units had initially, with a few exceptions, at the design stage the following features:

- **Vessel Head Penetrations for Control Rod Drive Mechanisms (CRDM)** were made from thick forged alloy 600 bars and welded with alloy 182 without any post weld stress relief treatment. The first units whose vessel head penetrations were constructed in the workshop with alloy 690 are the latest 4 N4, 1450 MWe units,
- **Vessel Bottom Head Penetrations, (namely Bottom Mounted Instrumentation [BMI] Penetrations)** having a smaller diameter, were made from hot rolled alloy 600 bars welded with alloy 182, but were submitted to a 600 °C treatment, normally typically needed for low alloy components stress relief. Only the last 2 N4 units were originally constructed with alloy 690 penetrations,
- **Central Vessel Head Vent Penetrations,** usually made from the same hot rolled alloy 600 bars used for BMI, were not stress relieved at all,
- **Steam Generator divider plates**, normally made of alloy 600, are welded to the channel head partition stub with alloy 182 without any stress relief treatment,
- **Steam generator tubing (SGT)** made from alloy 600 MA or later on more recent units with more SCC resistant alloy 600 TT, with the exception of the last 5 units which benefited from alloy PWSCC resistant 690 SG tube bundle,
- **Some Bimetallic junctions** between the ferritic components (Reactor Vessel, Pressurizer, Steam generators) and main stainless steel primary loops piping, as a standard were made of

stainless steel, except for the last three N4 reactor vessel safe end/to the main coolant piping Dissimilar Metal Welds (DMW) made by a hot alloy 82 wire TIG process,

- **Pressurizer penetrations** (heater sleeves, and instrumentation nozzles) normally made in 316L stainless steel, except for the 1300 MWe units, whose instrumentation nozzles made of alloy 600 did fail rapidly within the first to the fourth fuel cycle, and were replaced by 316 L penetrations in the 1990s,
- **M shaped core support pads** in alloy 600 welded to the vessel walls with alloy182, and then submitted to the vessel stress relief treatment.
- **Some repaired underclad defects in some vessel nozzles** were repaired with alloy 182 & stress relieved in plant with the vessel;

The main specific differences and features among the 4 PWR series were the following:

- The oldest 6 CPO units (3 loops, 900 MWe) on the sites of Fessenheim & Bugey commissioned in the years 1977-1979, including Bugey 3 (1978) initially equipped with Mill Annealed Alloy 600 SG tubing, operated under hot upper vessel plenum conditions **at the estimated temperature of 315°C.**
- 28 CP1- CP2 units (3 loops, 900 MWe), commissioned in the years 1981-87, some of which were equipped initially with Alloy 600 TT Steam Generator tubing (SGT), operated initially under low temperature upper vessel plenum **(estimated around 290 °C).**
- 20 P4-P'4 units (4 loops 1300MWe), commissioned in the years 1984-93, all with Alloy 600 TT SGT (except Penly unit 2 and Golfech 2, with alloy 690 SGT), were initially operated under high temperature upper plenum **(estimated at 315-320°C)**. As opposed to the general use of AISI 316 L stainless steel for the pressurizer penetrations for the other series, the P4-P'4 series was equipped with pressurizer instrumentation penetrations made of alloys 600 welded with alloy 182, which failed rapidly by PWSCC between the first and fourth fuel cycle and consequently were replaced by 316 L penetrations.
- 4 N4 units (4 loops, 1450 MWe) commissioned in the years 1996-1999, initially designed with alloys 600/182 & 82 penetrations for the vessel heads were re-equipped before commissioning with alloys (690/52 & 152) vessel head penetrations. The last 2 N4 units were built with alloy 690 Bottom Mounted Instrumentation (BMI) Penetrations Their original Steam Generators were designed with alloy 690 tubing.
- However on three N4 units, stress relieved **D**issimilar **M**etal **W**elds (DMW) were made with alloy 82, joining the reactor vessel to the cold and hot leg primary circuit piping, instead of the otherwise general use in France of stainless steel for DMWs.

5. THE TREATMENT OF THE VESSEL HEAD PENETRATIONS IN FRANCE, IN RELATION WITH THE ASN POSITIONS

The implementation of the "Inconel Zones Review" has been performed in various stages since the discovery of the BUGEY 3 CRDM penetration leak in 1991, with the benefits of the CRDMs failure investigations, the first assessment of the penetration deformations induced by welding, and the results of a first round of CP0 units NDE inspections.

5.1) Lessons learned from the Bugey 3 failure investigation[7]:

Risk of OD circumferential SCC re-initiation and cracking:

The examinations of the failed Bugey 3 penetration T54, which entailed a very low leak rate, less than 1 kg per hour, characterized by primary ID initiated longitudinal cracks, did show, that once some crack got through wall above the weld, they could later trigger in the outer annulus between the vessel bore and the penetration, a new PWSCC like secondary OD cracking process, this time of circumferential orientation, more critical in terms of safety consequences.

Risk assessment of potential leaks:
This incipient form of OD re-initiated circumferential degradation, in case of a continuously low rate leakage, difficult to detect in operation, as observed in Bugey 3, also exemplified at a more advanced stage of propagation some ten years later on Oconee in the USA was then judged safety significant so as to potentially entail a control rod ejection event.
This added to the original concern that **uncontrolled higher leak rates would, in worst case conditions, entail rapid wastage or erosion corrosion processes to the vessel low alloy steel, as observed in the USA on ferritic components and lately on Davis Besse vessel head.**
Those field examples world wide, of various primary water leaks, demonstrate, just like laboratory or mock-up corrosion tests, that the damages incurred by low alloy steel could vary in a very large range (typically from zero for dry salts conditions, up to some cm/year, or possibly more than 10 cm/year in case of erosion corrosion), as a function of the leak rate and leak thermo-hydraulic conditions on hot vessel walls.
IRSN, which reviewed some early data and crude models supplied and analyzed by EDF trying initially to demonstrate the acceptability in terms of safety of some leak scenarios, realized the complexity and uncertainty of the simplistic and fragile assumptions that had to be made in such a complex location in order to predict the consequences of a leak[8].
IRSN, came to the conclusions that the defense-in-depth concept should be applied in order to preclude the occurrence of through wall longitudinal cracks, whose leak rate would remain uncontrolled, usually difficult to detect early enough under the insulations, and whose consequences could not be mastered and would ultimately worsen the safety scenarios, involving the risk of a control rod ejection.

5.2) Strategy of leak prevention: precluding the occurrence of through wall cracking

Consequently, after consultation of IRSN, of the Standing Groups of Experts for Reactor Safety (GPR) and of the Standing Nuclear Section (SPN), the Safety Authority required that the main immediate course of action to treat the Inconel vessel penetration in France should be based on the principle of preventing any further penetration leak, with a safe margin. This requirement strongly oriented the "Inconel Zones Review" actions toward the implementation of a comprehensive NDE program as the base line for the Inconel Zones treatment.

5.3) First stage of the "Inconel Review"

In 1991, the only available PWSCC data base source was derived from the laboratory testing and field experience worldwide on SG tubing**,** characterized by a strong dependence of time to cracking with temperature between the hot leg and cold leg, and a well recognized scatter due the "Inconel" heat to heat variations. 6 oldest 900 MWe (CP0) units with a supposedly high temperature plenum estimated then at around **315 °C**, would be affected with a sufficient lead time with regard to the following 900 MWe units (CP1- CP2) operating at a "low temperature plenum" estimated in the range **288-290 °C.**
The then younger twenty 1 300 MWe (P4-P'4) hot plenum units, whose temperature was estimated in the range **315-320°C**, were initially considered "too young" to be inspected on a first priority. In other words, only time/temperature and absence or presence of a final stress relief treatment were considered to rank the "Inconel Zones".
However, with the agreement of EDF, ASN requested additional NDE investigations on a sampling basis for the initially judged low risks units.

5.4) Development and refinement of the "Inconel Review":

From 1991 on, both EDF and the ASN agreed that the first crude PWSCC descriptive models had to be reviewed, refined and include:

- **The intrinsic metallurgical and PWSCC sensitivity characteristics of thick forged or hot rolled alloy 600 materials:** as closely as possible, those materials should be representative of the French CRDM, vent, and bottom head penetrations, and thoroughly assessed with regard to the effect of the heats characteristics, the chemical composition, and the history of the thermo-mechanical treatments (derived from the fabrication records),

- **A more accurate estimation of the stress fields and their uncertainties**, particularly in the singular geometries of the penetrations on the components, as fabricated, and a reasonable assessment of the superficial stresses left behind by the final fabrication process**.**

ASN emphasized that the paramount sensitivity of the time to crack initiation t_i on the actual surface and bulk stress level σ influencing t_i at the power (σ^n, with n = 4 ± ?), should be recognized and expressed in terms of uncertainties for the estimation either of t_i, or of the relative stress index. Hence the need to perform:

- **A more accurate determination of the temperature dependence for PWSCC initiation time,**
- **A more accurate evaluation of the actual Inconel zone wall temperature at the location of the highest stresses,**
- **A more realistic revision of the empirical description of the time to initiation**, taking into account the results of the extensive Inconel zones characterizations and the PWSCC initiation experimental results on relevant material. The implementation of the latter goal required a considerable R & D effort on conventional SCC specimen but also on mock-ups and weld assemblies in order to determine the stress fields and stress magnitudes[9].

Use of PWSCC initiation deterministic models as a predictive tool?

An improved empirical PWSCC initiation model was needed, for integrating the various R &D data, NDE field return of experience, international feedback, but, above all, since the operator wanted to base some of its inspection priorities on a credible determination of precursor zones.

The data thus collected would be compared, and expressed either in terms of either relative susceptibility indexes, or of relative life time projections, for providing general guidance and priorities for subsequent NDE program, rather than for predicting absolute time to first cracking occurrence.

Actually the effects of stochastic processes involved in crack initiation are particularly noticeable for nickel base alloys PWSCC, already characterized by long incubation times and a large scatter of time to crack initiation.

Even if the main PWSCC controlling parameters are well determined, as for example in carefully controlled laboratory conditions, where stresses and materials conditions can be mastered, the times to initiation for the various individual identical specimen can be largely distributed over large time scale factors which may range up to factors of 10, possibly 100.

Consequently, assuming that the stress level and metallurgical PWSCC sensitivity are known on the as fabricated component, the determination of the absolute time to cracking for a particular "Inconel Zone" cannot be ascertained from the empirical deterministic models [3] without taking into account very large time brackets. Ultimately, the final uncertainty brackets, whether expressed in time to crack initiation estimates or zone sensitivity indexes should also include the uncertainty levels arising from the estimation of the stress, temperature, metallurgical PWSCC sensitivity factors for a given component as fabricated.

Consequently, ASN and IRSN held the views that:

- The aggregate uncertainties in using the PWSCC initiation predictive models, compounded by only best estimates for key input data such as superficial stress levels and material susceptibility indexes, should be fully and clearly expressed before relying on assumed time to cracking figures based on mathematical calculations to assess the PWSCC risk of cracking,
- Essential information such as crack orientation, location, number, size, depth, which are badly needed can only be obtained by the recourse to a comprehensive NDE (incipient surface crack detection, and volumetric detection and sizing) inspection program,
- In addition, the confrontation of NDE results and component PWSCC initiation predictions should be used to further validate and improve the realism and the reliability of the empirical models as it has been practiced several times by EDF and Framatome in the development of the Inconel zone review[9,10],
- A full NDE inspection program should be performed on a 100 % basis for the most PWSCC prone components or alternatively on a sampling basis for less sensitive components, as initially guided and prioritized by the best validated PWSCC models, awaiting for a completion of a NDE based condition assessment of the various zones.

5.5) Focus on the implementation of a comprehensive Inspection Program[11].

The review by ASN and IRSN of the "Inconel Zones" technical assessment and treatment strategy, made by EDF, lead the operator to focus its investigations and main actions toward the implementation of a preventive maintenance approach based on actual Inconel zones early flaw detections and sizing by NDE.

Extension of the initial NDE program to youngest or supposedly less sensitive units:

The assumed time to cracking high dependence on temperature, derived from early PWSCC initiation models based on laboratory tests performed mostly in more aggressive conditions (High temperature range, even in contaminated steam, on severely stressed specimen like "Reverse U Bends") lead to the belief that low temperature plenum units (288-290 °C) would be less concerned by PWSCC occurrence**.**

However, the application of the principle of precaution, first initiated on a random sampling basis to the supposedly low risk (only assessed by temperature/ operating time considerations) lead to the discovery in the field (in BLAYAIS unit 1), that crack initiation times and propagation rates did not seem to follow such a strong temperature dependence as it could be anticipated by the "predictive PWSCC models" based on laboratory experiments.

Consequently, ASN and EDF agreed not to further differentiate between the data obtained from the various series, all the more that the majority of plant (20 P4-P'4 units), which initially operated at a high temperature plenum, were progressively converted to low temperature plenums.

Thus, a complete first fleet status assessment for all the vessel head penetrations conditions with regard to cracking by PWSCC would have to be performed, whatever the assumed penetration wall temperature.

EDF reviewed recently the temperatures estimates, following some additional thermo hydraulic investigations, with the benefits of thermometric instrumentations on some CRDM penetrations, confirmed that the "cold plenum penetration wall temperatures were close to 290 °C, but re-estimated the hot plenum wall temperatures at the level of the weld at values close to 300 °C, thereby reducing the temperature difference estimates to only 10 °C[12]**.**

Most vessel heads were found affected by a small ratio of cracked penetrations, mostly peripherically located, where the residual stresses were estimated the highest**.** Some young 1300 MWe units just like Cattenom did exhibit cracking as soon as after 30 000 hours of operation, whereas one the oldest French units (Fessenheim) did only show a first incipient crack after some 130 000 hours of operation[12]**.**

Since Vessel penetration cracking by PWSCC could not be at once mitigated for all vessel heads, re-inspection schedules had to be determined:

- First, by the previous PWSCC degradation state assessed by NDE,
- Second, by the input of maximum CGR derived from laboratory testing and from some field crack propagation data of shallow cracks left in service, sized by UT at periodic intervals.

5.6) Crack growth rates (CGR) data as a function of relevant materials, temperature range and stress fields;

A crack growth rate database was progressively constituted by EDF and Framatome, mainly for the base metal with the involvement of various European laboratories, and compared with worldwide data.

This allowed to include a reasonable scatter band either obtained from experimental laboratory testing and/or by periodic sizing using the Ultrasonic NDE for some field cracks left in service in some units, in particular mostly on BLAYAIS unit 1,and some other units which operated from the beginning in cold plenum conditions[13]**.**

This set of data allowed EDF with the agreement of ASN to define objective criteria **(in terms of maximum CGR)** to safely leave in place acceptable flaws or cracks and set crack dimensions thresholds beyond which penetration repair or replacement ought to be performed.

The maximum in depth CGR measured in service (in Blayais 1) was 3.7 mm per one-year fuel cycle (8000 hour) whereas most of mean CGR values were in the order of magnitude of 1.5-2 mm per year [12, 13], though many instances of crack arrest have also been observed.
Typically, one can expect some scatter, or uncertainties in determining the CGR (da/dt) as a function of the assumed Stress Intensity level K_1, as shown on figure 2, comparing field data to some upper bound laboratory data.

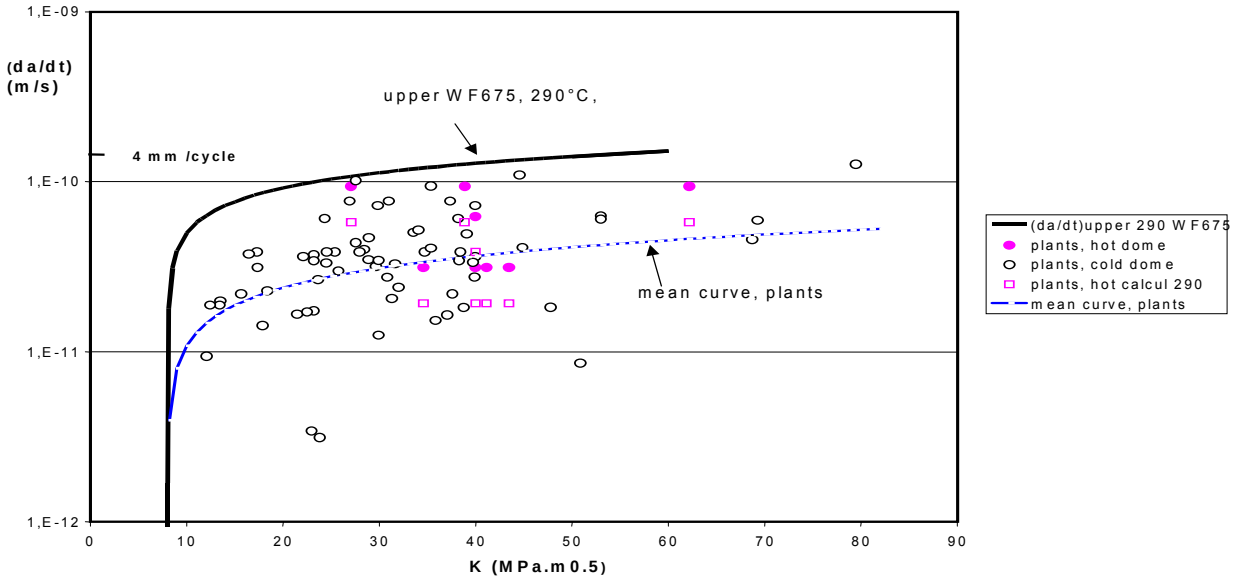

Fig. 2: Comparison between laboratory and field experience *(by courtesy of EDF, this conference ref.[12]),*
Showing the representation of CGR versus the estimated K values for field and laboratory data, expressed either at the assumed temperatures respectively of 300°C and 290°C, some data being converted to 290°C.

5.7) Present NDE inspection program criteria, now in a phase of renewed inspection regime;

The present inspection interval rules, now proposed by EDF, which has been approved by ASN on the basis of the CGR data obtained from the R &D program and from the field operational experience, are derived on a maximum (in depth) CGR of 4 mm/8 000 hours as follows, respectively for a standard 12 month or prolonged 18 month fuel cycle:

Previous status of Vessel Head degradation	**Interval between 2 consecutive Inspections or action, as a function of the length of the Fuel cycle**	
	12 months	**18 months**
No previously detected cracks	3 years intervals	2 cycles
3 mm <Crack depth < 5 mm	2 years intervals	1 fuel cycle
Crack depth > 5 mm	1 year interval	
When the remaining sound penetration ligament < 4mm	Immediate replacement of the vessel head	

In the present situation, the maximum crack depth left in service is not currently exceeding 5 mm.

5.8) Mitigation measures:[15]

Various mitigating measures have been proposed by EDF both as short term measures and for the long term treatment, which have been carefully examined by the French Safety Authority and IRSN, some of them being considered as interim measures: the most significant step being**:**

- Upper plenum temperature reduction,
- A speeded up qualification of base metal alloy 690 and related weld materials alloys 52 and 152 for penetration applications in line with the SG replacement applications already under way,
- Implementation of alloys 690/ 152 & 52 for vessel head penetrations on newly built units. (4 N4 units) and for BMI on the last 2 N4 units,
- Vessel Head replacement by new one with Alloy 690 penetrations welded with alloys 152/52,
- Reliance on a comprehensive NDE program to ensure that no further CRDM leak would occur, awaiting the complete replacement of the vessel heads.

Interim measures:

Pending the implementation of those long-term countermeasures, some other interim measures have been temporarily accepted by ASN in the initial transient periods in the early 1990s, such as:

- Temporary measures for CRDM leak detection using N13 gamma counting systems capable of detecting a leak rate of about 1 kg per hour, if placed in the vicinity of the most suspected penetrations,
- Temporary installation of anti-ejection devices,
- Temporary CRDM repairs.

Those temporary equipments and repairs have been later dismantled or removed as soon as the vessel heads were replaced, or when the routine NDE program was put in place, giving the assurance that PWSCC induced leakage could be excluded.

5.9) Vessel Head Replacements:

Very early in the review of the long term solutions which were discussed between EDF and DGSNR and IRSN, many interim measures have been accepted by ASN, taking into account EDF's pledge to suppress the root cause of PWSCC by elimination of the most PWSCC prone zone and replace the vessel heads using this time alloy 690 penetration material, resistant if not immune to PWSCC associated with 30 % Cr rich weld materials, 152 & 52 alloys.

The relatively young age of the French fleet, the financial and radiation exposure constraints and the logistic burden of repeating regularly full scale NDE assessments of the vessel head integrity over a long period of time, drove also obviously EDF to implement timely a planned vessel head replacement policy.

In addition to the first replacement of Bugey 3 vessel head, some reactor vessels in the Bugey 4, Paluel 4 and Flamanville I units, were repaired in 1992.

In practice, the repair process has been abandoned in favor of the program to replace progressively the most affected, vessel heads, usually with some anticipation with regard to the replacement criteria.

So far, 42 vessel heads out of 54 original alloy 600 containing heads have been replaced, which provides a definite improvement to significantly reduce the risks of pressure boundary failure and leaks from PWSCC.

This approach is also comforted by the positive results of the inspection of the Replacement Steam Generators (RSG) equipped with a tube bundle in alloy 690 TT, put into service since 1990 (Dampierre 1), expecting now in 2003 a fleet of 11 units with RSG (33 SG) adding to the existing 6 units (24 SG) originally equipped with alloy 690 tube bundle, so altogether, 57 SG for 17 units.

5.10) Inspection of Replaced Vessel Heads with Alloy 690 Penetrations:

Some inspections of the oldest replacement vessel heads have been programmed to confirm the anticipated good behavior of the Alloy 690 penetrations and the soundness of the welds:

- In 2002, the full inspection by NDE of the BUGEY 3 replaced vessel head took place and did not reveal any defect.
- The inspections of 2 other "old" replacement vessel heads respectively for Blayais unit 2 and Gravelines unit 4 which have been recently performed in 2003.did confirm, so far, the expected good resistance to PWSCC.

6. THE PRESENT STATUS OF THE INCONEL ZONE TREATMENT

After some 13 years of "Inconel Zones" treatment and review and continuous assessment of the, so far, remaining un-replaced 12 vessel heads, there is a reasonable confidence that the CRDM penetration PWSCC problem will be soon definitively settled in France in the coming years.

Therefore the present focus is being laid upon the next priority zones as defined by the ranking of the Inconel review based on the fabrication records, the material sensitivity to PWSCC, and the evaluation of the stress state.

Presently the Inconel Review has already been implemented in priority on:

- The Bottom Vessel Heads **(BVH),** also called the Bottom Mounted Instrumentation **(BMI)** Penetrations,
- The Steam Generator Partition Plate and its welded zones.

The examination or other Inconel Zones, which will be processed in more details at a later stage, will not be reported here, since EDF is currently reviewing the safety consequences, the need for NDE capabilities and for tooling adaptations, and in some cases, feasibility studies for possible repairs or mitigation techniques.

6.1) Bottom Mounted Instrument (BMI) Penetrations:

The Inconel Review concerning the BMI reveals the following favorable characteristics and some particular cases**:**

- The BVHP materials are estimated intrinsically more homogeneous, less PWSCC sensitive by a factor close to 4 than most of the CRDM penetration base metal heats, due to a different fabrication process, as determined by PWSCC experiments, on O rings representative of the bottom penetrations and on welded mock-ups,
- The 600 °C stress relief post weld treatment, intended essentially for the low alloy steel welded structure stress relief, reduces somewhat also the residual stress level of the penetrations,
- A small number of BVHP have been replaced after this partial stress relief, and did not benefit of any final stress relief at all, some others were submitted to some mechanical straightening up after the vessel post weld treatment.

BMI Penetrations NDE inspections:

Although a large investigation has been performed to assess the metallurgical features, the level of residual stresses in all situations (stress relieved, non stress relieved replacement penetrations or repaired after the vessel stress relief), in order to anticipate any unforeseen degradation, it has been decided in France to proceed initially on a sampling basis to the **inspection by NDE of all the bottom penetrations of some vessels,** with a priority to the units which comprise penetrations zones replaced or repaired after the stress relief [14]**,** such as BUGEY 3 (14 penetrations out of 50).

These inspections by NDE techniques are aiming at:

- Detecting, localizing and sizing potential cracks initiated from the Internal Diameter or alternatively on the outer BMI walls, whose orientation may be longitudinal or circumferential,
- Detecting flaws, which may be localized at the weld/BMI penetration interface, possibly due to welding defects of the type "lack of fusion", which may cause, according to their numbers and distributions, some partial leak path along the interface.

The following schematic drawing represents the extent of the anticipated BMI zones covered by the NDE:

- **1** search zone for OD initiated cracks,
- **2** zone where interfacial [weld/penetration] weld defects may appear,
- **3** search zone for ID initiated cracks) .

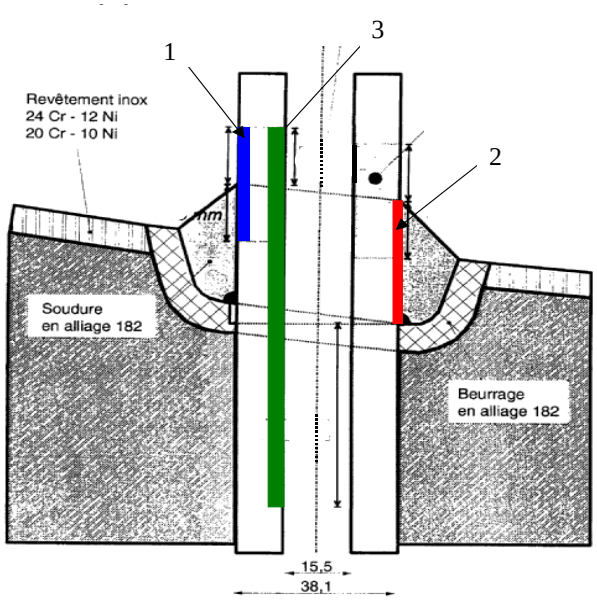

Figure 3, showing schematically the BMI zones covered by NDE examinations

The following NDE techniques have been implemented as follows:

- Eddy Current are being used to detect ID initiated cracks, whereas UltrasonicTestings (UT) are implemented for both detection and sizing,
- OD initiated cracks can only be detected and sized by UT,
- 0 degree longitudinal waves UT are used to detect and size the possible weld defects at the BMI penetration/weld interface,
- High-resolution remote video inspections are also implemented for local singular examinations.

So far 15 BVH inspections have been performed (including the 1992, 94, 97 re-inspections on Bugey 3) using eddy current and ultrasonic techniques together with high definition video examination.
So far, on the selected 12 older units comprising non-stress relieved penetrations, **no indications characteristic of PWSCC have been found**, although some "non-surface breaking" indications could be detected and related to the fabrication stage.

Continued Inspection Schedule:
Presently and in the near future, a continued inspection and re-inspection schedule is planned by EDF until year 2008, at the initiative of an ASN decision issued in 2001, following the recommendation of the Advisory Group on Nuclear Pressure Vessels (SPN), which required:

- **The NDE inspection of 12 BVH at higher risk of PWSCC, some before year 2005, the remainder till year 2008,**
- **The periodicity for two successive NDE should not exceed ten years,**
- **In the frame of the preparation of the third complete visit (usually performed during the third decennial extended outage), taking into account the latest experience feedback, the operator would have to submit to ASN, for approval, a complete BVH penetration inspection schedule for the whole fleet.**

Preparation for mitigation and repair measures:
In line with the objectives of the "Inconel Review" the operator has undertaken by anticipation, some pre studies to assess the feasibility of some mitigating measures; such as penetration plugging, repairs, or replacements, which should be further studied and submitted to ASN, some of them being already qualified.
N13 Leak monitoring:

From 1994 on, the N13 leak monitor system, previously installed in Bugey 3, for the vessel head surveillance, has been temporarily reinstalled under the bottom of the vessel to monitor any leak close to the 14 non stress relieved penetrations, to check its performance, and serve as a reference for further developments or installations, if need be.

6.2) Steam Generator Partition Plate (SGPP):

Although a postulated leak by PWSCC would not pose an immediate safety risk, the non stress relieved SGPP plate zone close to the alloy 182 welds (in particular at the so called triple point), represents in the Inconel Zone Review performed by EDF, a precursor zone relative to the stress relieved RBHP. The SGPP can be rather easily inspected and deliver information on incipient cracking, thereby alerting the attention for other Inconel zones to be further inspected. This could be the case for namely the Reactor Bottom Head Penetrations materials that followed a final fabrication process by hot rolling very similar to the basic process for the SGPP.
Hence the commitment of EDF to inspect by dye penetrant technique, retired SG partition plates, and until year 2008, the 26 SG in service, also deemed precursor zones.

7. FUTURE PROSPECTS AND NEEDS

So far, in the "Inconel zones review" and its treatment in France, the focus has been laid mainly on base metal degradations as they appeared in the field, in particularly in the vicinity of highly stressed zones, which in many cases are adjacent to welds, in complex geometries.
Consequently, laboratory investigations were initially more developed to assess the base material and component behavior toward PWSCC, although some similar laboratory works are now in progress in France[15,16] and worldwide to better assess the PWSCC sensitivity of the weld materials intrinsically, with or without the effect of various stress relief states.

7.1) Focus in the future for Weld metal behavior:

In France, so far, the satisfactory resistance to PWSCC of the alloys 182 and 82 weld buttering and deposits in the field is not yet fully understood, if we take into account the proved sensitivity of alloy 182, comparable to alloy 600, assessed world wide at the laboratory stage.
Furthermore, a detailed analysis of the worldwide return of experience concerning PWSCC cracking initiations and propagations observed abroad (in particular the USA and Sweden for the Dissimilar Metal Welds made with alloy 182), and also recently in the USA in some CRDM welds themselves will be needed and followed with care by EDF and the French Nuclear Safety.

7.2) Need to better assess the PWSCC temperature dependence, in the low temperature range:

From the French experience perspective, where most of the highest temperature zones with no stress relief are in the process to be fully treated or replaced, the future focus should be placed on lowest temperature zones, on a better assessment of the temperature dependence of both PWSCC initiation and propagation, since the weak apparent difference observed in the field between "hot" and "cold " plenum Vessel Head Penetrations cracking has not been fully understood. **Some clarification in that area would help to refine the prediction of bottom head penetrations and give more confidence to define the In Service Inspection needs and priorities.** One possible explanation might arise from a "smaller than initially anticipated temperature difference in the field" (refer to § 4), between hot & cold plenum wall temperatures, in the order of 10 °C, instead of some 25-30 °C[12].

7.3) Ageing and life extension issues:

In the prospect of ageing issues, and life extension, safety organizations and operators would need some further data and hard facts from the operational experience and NDE status of oldest components in the world to better anticipate in the long term the PWSCC behavior of so far un-replaced components, which might be less sensitive to cracking than presently vessel head penetrations. For that purpose, ASN is

ready to follow up and take benefits from the experience feedback given by some failure investigations performed in the world, and in particular in welded zones (North Anna 2) and on a South Texas Project unit 1, for the Bottom Vessel Head penetrations.

7.4) Hence some suggestions for continued emphasis on the following areas of investigation to fully exploit worldwide return of experience:

- Review and refine the assessment of temperature dependence for both crack initiation and propagation from 325, 290 down to 250 °C,
- Review with more accuracy the assumed wall temperatures and perform measurements relevant to the actual components wall temperature,
- Improve and extend the laboratory database for crack propagation as a function of temperature, down to temperatures around 290 °C, and below, in particular for weld materials, as it has been proposed within an international specialists group "ICG-EAC",
- Review the characteristics of the Bottom Head Penetrations (metallurgical features, residual stress, temperature) and NDE results of those units that have been inspected following the suspicion of bottom vessel leaks such as South Texas unit 1,
- Take into account the possible accelerating effect on PWSCC crack initiation and propagation of superimposed low frequency cyclic loading/unloading, or ripple load effect, in particular for the low temperature components[17].
- Improve, as already initiated by EDF, the characterization of superficial cold work and superficial residual stresses, both for laboratory PWSCC database, and component stress assessment, since the superficial stresses are controlling the time to initiation,
- Express both laboratory and plant CGR data not only in terms of mean CGR, but above all in terms of maximum CGR, since it is important to preclude any unanticipated through wall cracking and leak occurrence,
- For safe plant operation, more emphasis should be given to the improvement of crack initiation anticipation methodology and to the early detection of incipient cracks in plants, since, so far, a great emphasis has been given to crack CGR extrapolations from laboratory data.

7.5) Suggested focus for improving the PWSCC return of experience worldwide:

From the French perspective, the recurrence of PWSCC initiation and propagation in the welds themselves observed abroad would constitute a unique source of return of experience, when the detailed characteristics of the materials, stresses, and environmental conditions are available in order to better predict the behavior of similar materials as they age.
A closer attention should be paid to the NDE results, the In Service Inspection programs in the world concerning the Bottom Head Penetrations, their results, and the qualification of repair methods.

8. CONCLUSIONS

- **Precluding leakage**:
  From the very beginning in 1991, the French Safety Authority did not accept the principle proposed by some operators in the world to allow leakage through the vessel penetrations and rely solely on boric acid deposits inspection as a means to detect the degraded components, since the safety consequences of a leak would strongly depend on the evolution of the leak rate, thus left uncontrolled, under thermal insulation,
  Past experience, the Oconee and Davis Besse cases, illustrate the fact that some leak conditions would worsen the mere safety case of a longitudinal near through wall ID initiated crack,
  Actually, waiting for a leak to occur under insulation materials, all the more in absence of sensitive leak detectors, would not provide an early warning with regard to the PWSCC status of a given component, or PWR fleet, to anticipate timely the necessary corrective or mitigation measures.

- **Regulatory hydro test**:
  The first and only, early discovery of a CRDM penetration leak, in France, on Bugey unit 3 in 1991, during the decennial outage, was made possible by the French regulation requirement that a hydraulic testing, at 207 bars, be performed after 10 years of operation, implying in principle the removal of the thermal insulation and visual inspection of the external pressure retaining boundary. The hydro test did fulfil its goal as an in-depth-defence disposition to detect any through wall defect of the pressure retaining boundary which was unanticipated or at least not covered by a specific periodic maintenance and surveillance program,

- **Considerable R&D to support PWSCC initiation prediction:**
  The Bugey 3 event has triggered a steady and considerable investigation effort by EDF and Framatome in France[3,12], which started by the reactivation of the proactive project named "Inconel Zones Review" requested by the French Nuclear Safety organisations.
  An enlarged data base has been established to describe empirically a relative relationship between crack initiation, temperature; heat characteristics, surface "effective" stresses, taking also into account some effects of the mechanical surface treatment. It has been achieved through a comprehensive PWSCC laboratory investigation carried out mainly on a large number of heats of alloy 600 base metal representative of vessel penetrations and other thick components and also on some alloy 82, 182 weld materials.
  In a complete review of the various PWSCC prone Inconel Zones for all the 58 PWRs, EDF and Framatome have tried to feed the estimates of the above quoted parameters in the PWSCC model and derived some estimates of the time to "detectable crack initiation" mainly for the purpose to determine "precursor zones" and relative zones ranking,

- **Limitations of PWSCC prediction to Inconel Zones ranking:**
  Despite the sophistication of the descriptive PWSCC models lately developed by EDF and Framatome-ANP, which in turn require the input of Inconel zones PWSCC characteristics " as fabricated" and their uncertainties difficult to quantify, IRSN and DGSNR concluded that this "predictive approach alone " could not provide a reliable absolute prediction of time to cracking or time for inspection, but rather constitute a rationale to integrate and compare PWSCC data, and essentially a guide and a ranking tool to set priorities for the definition of the In Service Inspection (ISI) program,

- **Recourse to extensive ISI:**
  Instead, a policy of comprehensive implementation of the NDE techniques was judged as a necessary step to ensure safe and controlled soundness of components since the predictability of PWSCC initiation is confronted to large uncertainties. Once the degradation status of the PWSCC prone components are established from ISI, a flexible re-inspection program can be adjusted, **using the upper bound values for crack propagation,**

- **Timely replacement of the PWSCC affected Vessel Heads:**
  The necessity to repeat a rigorous NDE program all over the remaining life time of the reactor constitutes an incentive for the operator to resort to a more definitive timely mitigation by eliminating the most PWSCC prone zones by component total or partial replacement, as exemplified by EDF policy to replace timely all the vessel heads equipped with alloy 600/182 penetrations,

- **Bottom Head Mounted Instrumentation (BMI) Penetrations:**
  An increased attention should be paid to review the present ISI requirements in all countries (sampling rate, NDE periodicity for stress relieved and non-stress relieved bottom penetrations) in the light of some leaks and crack suspicions discovered abroad, pending confirmation that PWSCC is involved in the degradation of those Inconel zones.

9) REFERENCES

1 **H. Coriou, L Grall, et al**. , *corrosion fissurante sous contrainte de l'inconel dans l'eau à haute température",* 3° colloque de métallurgie-corrosion, CEN Saclay, France, (Amsterdam, North Holland Publishing Company, p. 161, 1959),

2 **J. Blanchet, H. Coriou, L. Grall, C. Otter, G.Turluer**, *"Influence de la contrainte, des traitements thermiques et des couplages sur la fissuration intergranulaire des alliages inconel 600 et X 750"*, (Journal of Nuclear Materials, vol.55, pp. 187, 1975), also published in English as *"Historical Review of the Principal Research Concerning the Cracking of Nickel Base Austenitic Alloys",* (Proceedings of the International Conference on SCC and Embrittlement of Iron Base Alloys, June 1973, Firminy, ed. R. W. Staehle et al., NACE, Houston),

3 **G. Turluer***, "Status of Alloy 600 Components Degradations By PWSCC in France; Incentives and Limitations of Life Prediction, as viewed by a Nuclear Safety Body"*, Proceedings of International Symposium on Plant Aging and Life Prediction of Corrodible Structures, May 15-18, 1995, Sapporo, Japan, (R. N. Parkins Editor, pp 273-283),

4 *"Small Primary Coolant Leak at a Pressurizer Instrumentation Nozzle, Generic (PWR), France, 1989"*, IRS 1010-60, OECD/NEA

5 *"Cracks in Steam Generator Tubes, Generic (PWR), France, 1989"*, IRS 1607-60, OECD/NEA/Incident Reporting System,

6 *"Discovery of a Leak on the Reactor Vessel Head During the Decennial Primary Circuit Hydraulic Test",* IRS 1232.00 to 04, Bugey 3, PWR, France, Sept. 23, 1991, OECD/NEA/Incidents Reporting System, Issy les Moulineaux, France,

7 **J. Economou, A. Assice, F. Cattant, J. Salin, M. Stindel;** *"Contrôles et expertises métallurgiques de traversées de couvercle de cuve",* proceedings of the Fontevraud 3 International Symposium on "Contribution of Materials Investigation to the Resolution of Problems Encountered in PWR, 1994,Vol. 1, pp 197-208,

8 **D. You, D. Féron, G. Turluer;** *" Experimental Simulation of Low Rate Primary Coolant Leaks, For the Case of Vessel Head Penetrations Affected by Through Wall Cracking"*; proceedings of the international conference **"Chimie 2002",** on "Water Chemistry in Nuclear Reactors Systems", Avignon, France, 22-26 April 2002,

9 **C. Amzallag, S. Le Hong, C. Pagès, A. Gelpi; "***Stress Corrosion Life Assessment of Alloy 600 PWR Components, ",* Proceedings of Ninth Internat. Symp. on Environmental Degradation of Materials in Nuclear Power Systems Water Reactor, pp 243-250, (1999),

10 **P. Scott, C. Benhamou;** *"An Overview of Recent Observations and Interpretation of ICGSCC in Nickel base Alloys in PWR Primary Water";* proceedings of Tenth International Conference on Environmental Degradation of Materials in Nuclear Power Systems-Water Reactors, Lake Tahoe, August 2000,

11 **J. Salin**, *"NDE advances due to 5 years of Inconel Zones"*, EPRI PWSCC workshop, Daytona Beach, 1997, USA,

12 **F. Champigny, C. Amzallag, F. Chapelier, F. Vaillant;** *"Maintenance Strategy of Inconel Systems Components in PWR Primary Water in France".* This conference,

13 **C. Amzallag, F. Vaillant;** *"Stress Corrosion Cracks Propagation rates in Reactor Vessel Penetrations in Alloy 600",* proceedings of Ninth International Symposium on Environmental Degradation of Materials in Nuclear Power Systems Water Reactor, pp 235-241, Newport Beach (1999),

14 **J. Samman, J. Salin,** *"Keeping Vigilance for RPV Penetration Cracks; Improved NDT Tools for SCC in Bottom Head Penetrations"*, Nuclear Engineering, Vol. 41, n° 505, August 1996,

15 **C. Amzallag, J. M. Boursier, C. Pages, C. Gimond; "***"Stress Corrosion Life Assessment of 182 & 82 Welds used in PWR Components,* proceedings of Tenth International Conference on Environmental Degradation of Materials in Nuclear Power Systems-Water Reactors, Lake Tahoe, August 2001,

16 **S. Le Hong, J. M. Boursier, C. Amzallag, J. Daret; "***Measurement of SCC Growth Rates in Weld Alloys 182 in Primary Water";* proceedings of Tenth International Conference on Environmental Degradation of Materials in Nuclear Power Systems-Water Reactors, Lake Tahoe, August 2001,

17 **F. Vaillant, J. M. Boursier, C. Amzallag, J. Chambredonde, J. Daret, C. Bosch;** *"Influence of Cyclic Loading on Crack Growth Rates of Alloy 600, in Primary Environment: an Overview".* Proceedings of 11th International Conference on Environmental Degradation of Materials in Nuclear Power Systems-Water Reactor, Stevenson, Washington State, USA, August 2003.